Constraint-based Analysis for Comparison of Thermal Performance in Various Buoyancy-driven Enclosures

Thesis submitted by
Abhinav Saha

Doctor of Philosophy (Engineering)

Department of Mechanical Engineering
Faculty Council of Engineering and Technology
Jadavpur University
Kolkata, India

2023

1. Title of the thesis:	**Constraint-based Analysis for Comparison of Thermal Performance in Various Buoyancy-driven Enclosures**
2. Name, Designation & Institution of the Supervisor/s:	**1. Dr. Nirmal Kumar Manna** Professor Department of Mechanical Engineering Jadavpur University Kolkata –700032, India **2. Dr. Koushik Ghosh** Professor Department of Mechanical Engineering Jadavpur University Kolkata –700032, India **3. Dr. Nirmalendu Biswas** Assistant Professor Department of Power Engineering, Salt Lake Jadavpur University Kolkata –700106, India
3. List of Publications:	**Journal Publications:~** 1. **Abhinav Saha**, Aranyak Chakravarty, Koushik Ghosh, Nirmalendu Biswas, and Nirmal K. Manna, 2022. Role of obstructing block on enhanced heat transfer in a concentric annulus. *Waves in Random and Complex Media*, pp. 1-25. doi:10.1080/17455030.2022.2106386. 2. **Abhinav Saha**, Nirmal K. Manna, Koushik Ghosh and Nirmalendu Biswas, 2022. Analysis of geometrical shape impact on thermal management of practical fluids using square and circular cavities. *The European Physical Journal Special Topics*, *231*(13-14), pp. 2509-2537. doi: 10.1140/epjs/s11734-022-00593-8.

3. **Abhinav Saha**, Nirmalendu Biswas, Nirmal K. Manna, and Koushik Ghosh, 2022, Impact of Linear Heating Profiles on Nanofluidic Convection in Enclosure, *Heat Transfer Engineering*. (Accepted)

Book Chapter:

1. **Abhinav Saha**, Nirmal K. Manna, and Koushik Ghosh, 2022. Influence of Non-uniform Heating Profiles on Free Convection Entropy Generation Inside an Enclosure Filled with Nanofluid. *In Recent Advancements in Mechanical Engineering: Select Proceedings of ICRAME 2021, Springer Nature*, pp. 1-13.

2. Abhinav Saha, Nirmalendu Biswas, Nirmal K. Manna, and Koushik Ghosh, 2023, Influence of various linearly heating profiles on buoyancy-driven flow in an enclosure filled with nanofluid, *Fluid Mechanics and Fluid Power, Select Proceedings of FMFP 2021, Springer Nature,* pp. 345-350.

International Conference Publications:~

1. **Abhinav Saha**, Nirmalendu Biswas, Nirmal K. Manna, and Koushik Ghosh, 2022. Effect of non-uniform heating on thermal performance of an enclosure filled with nanofluid. *Materials Today: Proceedings*, *56*, pp.179-185. doi:10.1016/j.matpr.2022.01.062.

2. **Abhinav Saha**, Nirmalendu Biswas, Nirmal K. Manna, and Koushik Ghosh, 2022. Thermal analysis of buoyancy-driven flow in a square enclosure filled with porous medium. *Materials Today: Proceedings*, *63*, pp.185-191. doi:10.1016/j.matpr.2022.02.451.

3. **Abhinav Saha**, Nirmalendu Biswas, Koushik Ghosh, and Nirmal K. Manna, 2022. Thermal management with localized heating on enclosure's wall during thermal convection using different fluids. *Materials Today: Proceedings*, *52*,pp.391-397.
doi:10.1016/j.matpr.2021.09.069.

	4. **Abhinav Saha**, Nirmal K. Manna, Koushik Ghosh, 2021.Thermal Hydraulic Analysis of Natural Convection in a Solar Collector Filled with Nanofluid. *In 2021 Innovations in Energy Management and Renewable Resources (52042), IEEE*, pp.1-6. doi: 10.1109/IEMRE52042.2021.9387014. 5. **Abhinav Saha**, Nirmal K. Manna, and Koushik Ghosh, 2021. Analysis of nanofluid based natural convection in a square cavity applying corner heating and cooling. In *IOP Conference Series: Materials Science and Engineering,* IOP Publishing, 1080 (1), p. 012049. doi:10.1088/1757-899X/1080/1/012049.
4. List of Patents	NIL
5. List of Presentation in National / International Conference:	**Paper presentation:~** 1. **Abhinav Saha**, Nirmalendu Biswas, Nirmal K. Manna, Koushik Ghosh, Impact of linearly varying heating temperature profiles on nanofluidic thermal convection in an enclosure, *4th International Conference on Advances in Mechanical Engineering (ICAME-2022)*, 24th – 26th March 2022, SRM Institute of Science and Technology, Tamil Nadu, India. 2. **Abhinav Saha**, Nirmalendu Biswas, Koushik Ghosh, Nirmal K. Manna, Thermal analysis of buoyancy-driven flow in a square enclosure filled with porous medium**,** *4th International conference on Advances in Mechanical Engineering and Nanotechnology (ICAMEN-2022),* 18th – 19th February 2022, Manipal University, Jaipur, India. 3. **Abhinav Saha**, Nirmalendu Biswas, Koushik Ghosh, Nirmal K. Manna, Effect of non-uniform heating on thermal performance of an enclosure filled with nanofluid, *International conference on Materials, Machines and Information Technology – 2022 (ICMMIT-2022)*, 24th - 25th January 2022, Amity University, Jharkhand, India. 4. **Abhinav Saha**, Nirmalendu Biswas, Nirmal K. Manna, Koushik Ghosh, Influence of various linearly heating profiles on buoyancy-driven flow in an enclosure filled with nanofluid, *Proceedings of the 48th National Conference on Fluid Mechanics and Fluid Power (FMFP-2021)*, 27th -29th December 2021, BITS Pilani,

	Rajasthan, India
	5. **Abhinav Saha**, Nirmal K. Manna, Koushik Ghosh, Influence of non-uniform heating profiles on free convection entropy generation inside an enclosure filled with nanofluid, *2nd International Conference on Recent Advancements in Mechanical Engineering (ICRAME-2021)*, 7th - 9th February 2021, at National Institute of Technology Silchar, India.
	6. **Abhinav Saha**, Nirmal K. Manna, Koushik Ghosh, Thermal Hydraulic Analysis of Natural Convection in a Solar Collector Filled with Nanofluid, *IEEE International Conference on Innovations in Energy Management and Renewable Resources (IEMRE-2021)*, 5th - 7th February 2021, IEM, Kolkata, India.
	7. **Abhinav Saha**, Nirmal K. Manna, Koushik Ghosh, Effect of Non-Uniform Heating on Natural Convection and Entropy Generation in a Square Enclosure Filled with Nanofluid, *International Conference on Materials and Technology (Material TECH-2021)*, 9th - 10th January 2021, National Institute of Technology Raipur, India.
	8. **Abhinav Saha**, Nirmal K. Manna, Koushik Ghosh, Analysis of nanofluid based natural convection in a square cavity applying corner heating and cooling, *3rd International Conference on Advances in Mechanical Engineering and its Interdisciplinary Areas (ICAMEI-2021)*, 6th January 2021, CEM, Kolaghat, India.
	Best Paper Award:
	1. **Abhinav Saha**, Nirmalendu Biswas, Nirmal K. Manna, Koushik Ghosh, Impact of linearly varying heating temperature profiles on nanofluidic thermal convection in an enclosure, *4th International Conference on Advances in Mechanical Engineering (ICAME-2022)*, 24th – 26th March 2022, SRM Institute of Science and Technology, Tamil Nadu, India.

"Statement of Originality"

I **Abhinav Saha** registered on **28.06.2016** do hereby declare that this thesis entitled **"Constraint-based Analysis for Comparison of Thermal Performance in Various Buoyancy-driven Enclosures"** contains literature survey and original research work done by the undersigned candidate as part of Doctoral studies.

All information in this thesis have been obtained and presented in accordance with existing academic rules and ethical conduct. I declare that, as required by these rules and conduct, I have fully cited and referred all materials and results that are not original to this work.

I also declare that I have checked this thesis as per the "Policy on Anti Plagiarism, Jadavpur University, 2019", and the level of similarity as checked by iThenticate software is **2 %**.

Signature of Candidate:

Date : 9/03/2023

Certified by Supervisor(s):

(Signature with date, seal)

1. 09/03/2023

PROFESSOR
Mechanical Engineering Deptt
Jadavpur University
Kolkata - 700 032

2. 09/03/2023

PROFESSOR
Mechanical Engineering Deptt
Jadavpur University
Kolkata - 700 032

3. 09/03/2023

Dr. Nirmalendu Biswas
Assistant Professor
Department of Power Engineering
Jadavpur University
Salt Lake Campus, Kolkata-700 106

CERTIFICATE FROM THE SUPERVISORS

This is to certify that the thesis entitled "**Constraint-based Analysis for Comparison of Thermal Performance in Various Buoyancy-driven Enclosures**" submitted by **Shri ABHINAV SAHA** who got his name registered on **28ᵗʰ June, 2016** for the award of Ph. D. (Engineering) degree of Jadavpur University, is absolutely based upon his own work under the supervisions of **Dr. NIRMAL KUMAR MANNA, Dr. KOUSHIK GHOSH and Dr. NIRMALENDU BISWAS** that neither his thesis nor any part of the thesis has been submitted for any degree/diploma or any other academic award anywhere before.

Manna 09/03/2023

**1. Signature of the Supervisor
and date with Office Seal**
PROFESSOR
Mechanical Engineering Deptt
Jadavpur University
Kolkata - 700 032

Koushik Ghosh 09/03/2023

**2. Signature of the Supervisor
and date with Office Seal**
PROFESSOR
Mechanical Engineering Deptt
Jadavpur University
Kolkata - 700 032

Biswas. 09/03/2023

**3. Signature of the Supervisor
and date with Office Seal**

Dr. Nirmalendu Biswas
Assistant Professor
Department of Power Engineering
Jadavpur University
Salt Lake Campus, Kolkata-700 106
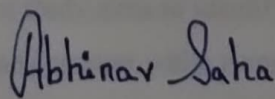
Dedicated to My Beloved Parents

ACKNOWLEDGEMENTS

Date:..09/03/2023..

Abhinav Saha

_____

(Abhinav Saha)

ABSTRACT

In modern times, thermal systems in the form of enclosures or cavities are widely used in various applications. As the demand for energy-efficient miniature devices continues to grow, passive cooling systems operated by natural convection have become a popular choice. However, the heat transport physics in these systems is significantly affected by various factors such as geometry, boundary conditions, and multi-physical processing parameters. Therefore, thermal management is critical, especially in designing thermal systems involving higher performance, miniaturization, and passive cooling methods.

Passive cooling systems relying on natural convection have emerged as a viable solution for efficient heat dissipation in various applications. For instance, designing electronic devices with higher performance and miniaturization requires effective thermal management. However, understanding the heat transport physics in these systems requires taking into account various factors, such as geometry, boundary conditions, and processing parameters. The buoyancy-induced flow in enclosures is diverse and multidisciplinary, encompassing fluid mechanics, heat transfer, and materials science.

Although there is a vast amount of literature available on convective thermal systems, none of them has thoroughly examined the impact of geometrical shape. For the past few decades, researchers have been striving to develop energy-efficient thermal devices, which have led to numerous studies on passive cooling applications utilizing buoyancy-driven flow. However, despite the abundance of literature on buoyancy-driven flow in thermal systems, there is a noticeable gap in research on constraint-based thermal analysis.

This current work presents a novel approach to constraint-based thermal analysis, which is applied to analyze the heat transfer characteristics of various-shaped enclosures. The objective is to develop a methodology for comparative performance analysis of thermal systems involving different geometries for buoyancy-driven flow in enclosures, considering recent advancements such as nanofluid and magneto-hydrodynamics (MHD). The present study aims to identify the most efficient geometric shape from a thermal performance viewpoint while using the same heat input and working fluid volume. To assess thermodynamic irreversibility in thermal systems, the entropy generation for MHD nanofluidic convection is

evaluated. The entire work focuses on heat transport, fluid flow, heat transfer, and irreversibility production during MHD nanofluid flow in the constraint-based analogous square, trapezoidal, triangular, and annular thermal systems. Annular systems have been extensively researched in terms of their application in heat-exchanging devices, particularly buoyancy-driven convection.

The study focuses on typical regular geometric shapes such as square, circular, trapezoidal, and triangular geometries, along with square and circular annuli. To evaluate the performance of various enclosure-shaped thermal systems, the square-shaped configurations have been selected as the base cases. Classical differential heating configurations are chosen for this constraint-based performance analysis of the chosen problems. The study also considers the effect of magnetic fields and nanofluids on buoyancy-driven flow. The practical working fluids used in the study are air, water, and CuO-water nanofluid. The formulated problems for this study include buoyant flow in (1) equivalent square and circular thermal systems, (2) MHD flow in equivalent square and circular thermal systems, (3) MHD flow in equivalent square and trapezoidal thermal systems, (4) MHD flow in equivalent square and triangular thermal systems, and (5) MHD flow in equivalent square and circular annular thermal systems. For the trapezoidal case, a series of several trapezoidal-shaped systems of identical fluid volume and heating load however varying cooling surfaces are investigated, and the triangular–shaped system is treated as a special case of a trapezoidal-shaped system where one parallel length approaches zero. Two cases of alternative circular annuli are analyzed against the performance of a base square annulus.

In this study, the flow is assumed laminar, steady, incompressible, and two-dimensional, and the Boussinesq approximation. The fluid and heat flow describing governing equations are solved numerically using a Computational Fluid Dynamics (CFD) tool, and local and global performance parameters are computed from the solved variables. The Nusselt number is used to measure the rate of heat transfer, and entropy generation is considered to identify the efficacious thermal system. The study focuses on the effects of Rayleigh number (Ra), Hartmann number (Ha), magnetic field angle, and nanofluid concentration on the thermal performance of various thermal systems. The Rayleigh number quantifies the ratio of buoyancy and viscosity forces, while the Hartmann number represents the ratio of electromagnetic forces to

viscous forces. These dimensionless numbers play an essential role in the heat transport physics of buoyancy-driven flow.

Following the same set of governing equations and numerical approach, the afore-stated five problems are analyzed, by comparing with the base case, using the local flow features (streamlines, isotherms, heatlines, and entropy generation contours), and global performance parameters (maximum magnitudes of streamfunction and heatfunction, heat transfer performance parameter, and the average Nusselt number). The findings of this study provide insights into the thermal behavior of various-shaped enclosures under buoyancy-driven flow conditions. The analysis shows that the circular-, trapezoidal-, and triangular-shaped enclosures offer superior thermal performance compared to the traditional square-shaped enclosure. The circular annular thermal system also shows better thermal performance than its equivalent square annular system. Obtained results are explained from the fundamental physics. Each problem is devoted to a chapter for the systematic presentation of various parametric results exploring the effects of Rayleigh number (Ra), Hartmann number (Ha), magnetic field angle, and nanofluid concentration.

In conclusion, the present study proposes a constraint-based methodology for comparative performance analysis of various-shaped thermal enclosures under buoyancy-driven flow conditions. The study includes the effects of magnetic fields and nanofluids on heat transfer and irreversibility production in thermal systems. The findings provide insights into the thermal behavior of various-shaped enclosures and identify the most efficient geometric shape from a thermal performance viewpoint. The results can be applied to a wide range of engineering and industrial applications, from the design of cooling systems in electronics to the optimization of energy systems.

TABLE OF CONTENTS

LIST OF FIGURES

LIST OF TABLES

NOMENCLATURE

B	Magnetic fields (N A^{-1} m^{-1})
e_x, e_y	Unit vectors in Cartesian coordinate
C_p	Specific heat at constant pressure (J Kg^{-1} K^{-1})
E	Electric field (Vm^{-1})
Ec	Eckert number
F_L	Force (N)
g	Acceleration due to gravity (m s^{-2})
H	Cavity height /Length scale (m)
Ha	Hartmann number
J	Current density (A m^{-2})
k	Thermal conductivity (W m^{-1} K^{-1})
MNS, VNS	Magnetic and viscous entropy generation
n	Normal outward direction
Nu	Average Nusselt number
p	Dimensional pressure (N m^{-2})
P	Dimensionless pressure
Pr	Prandtl number
q	Electric charge (C)
Ra	Rayleigh number
S	Entropy generation (W m^{-3} K)
NS	Entropy generation (dimensionless)
T	Temperature (K)
u, v	Velocity components in Cartesian space (m s^{-1})
U, V	Dimensionless velocity components
x, y	Cartesian coordinates (m)
X, Y	Dimensionless coordinates

Greek symbols

α	Thermal diffusivity (m^2 s^{-1})
β	Thermal expansion coefficient (K^{-1})
χ	Fluid-flow performance parameter
η	Heat transfer performance parameter

Θ	Dimensionless temperature
θ_r	Temperature ratio reference parameter
γ	Magnetic field orientation (degree)
μ	Dynamic viscosity (N s m^{-2})
v	Kinematic viscosity (m^2 s^{-1})
ρ	Density (kg m^{-3})
ϕ	Cavity inclination angle (degree)
Φ	Irreversibility distribution parameter
ζ, ξ	Nanoparticle volume fraction
ψ	Dimensionless stream function
Π	Dimensionless heat function
σ	Electric conductivity (Sm^{-1})

Subscripts

An	annular
c	cold
Cir	circular
f	base fluid
h	hot
l	local
m	magnetic field
max	maximum
min	minimum
Sq	square
t	total
tg	thermal gradient
v	viscous dissipation

Chapter – 1

Literature Survey, Scope of Work, and Outline of Thesis

1.1 Motivation

Nowadays, various electronic appliances such as mobile phones, laptops, desktops, and tablets are essential for daily activities and operate primarily on spontaneous buoyancy-driven flow. These appliances generate heat as a by-product and require cooling, which is achieved by transferring heat from its source to a suitable sink, such as ambient air. From natural physics, the temperature variation causes fluid flow due to its density change, which means that natural convection is inherently present in all fluid-based natural events and thermal systems/devices. The number of applications utilizing natural convection, such as electronic/electrical components/devices, textile/food processing, solar collectors/dryers, heat transfer equipment, and heating/cooling of buildings, is increasing day by day. However, low-power application devices operating on buoyancy-driven flow (or natural convection) face challenges for further improvement. This is due to the fact that the low-power application devices, which are essentially small electronics, usually face the following challenges when it comes to managing heat transfer via natural convection. The heat transfer by convection depends upon surface area, temperature difference, and heat transfer coefficient. In buoyancy-induced flow, the temperature difference is small. Furthermore, the surface area of micro-devices is limited. This means that the rate of thermal energy transport is governed by the heat transfer coefficient. The heat transfer coefficient is affected by numerous factors such as fluid type, flow velocity, flow type, geometry and orientation, and so on. The dependence of heat transport on a large number of parameters makes designing low-power application devices highly challenging. These facts motivate the present work in the area of buoyancy-driven flow.

1.2 Survey of Literature

The current importance of buoyancy-driven flow can be realized from its publication trend. The data of Figure 1 is taken from Scopus website from 2001 to 2021. According to statistics from the Scopus repository, the trend of buoyancy-driven flow research in closed/confined domains, such as cavities or enclosures is increasing day-by-day.
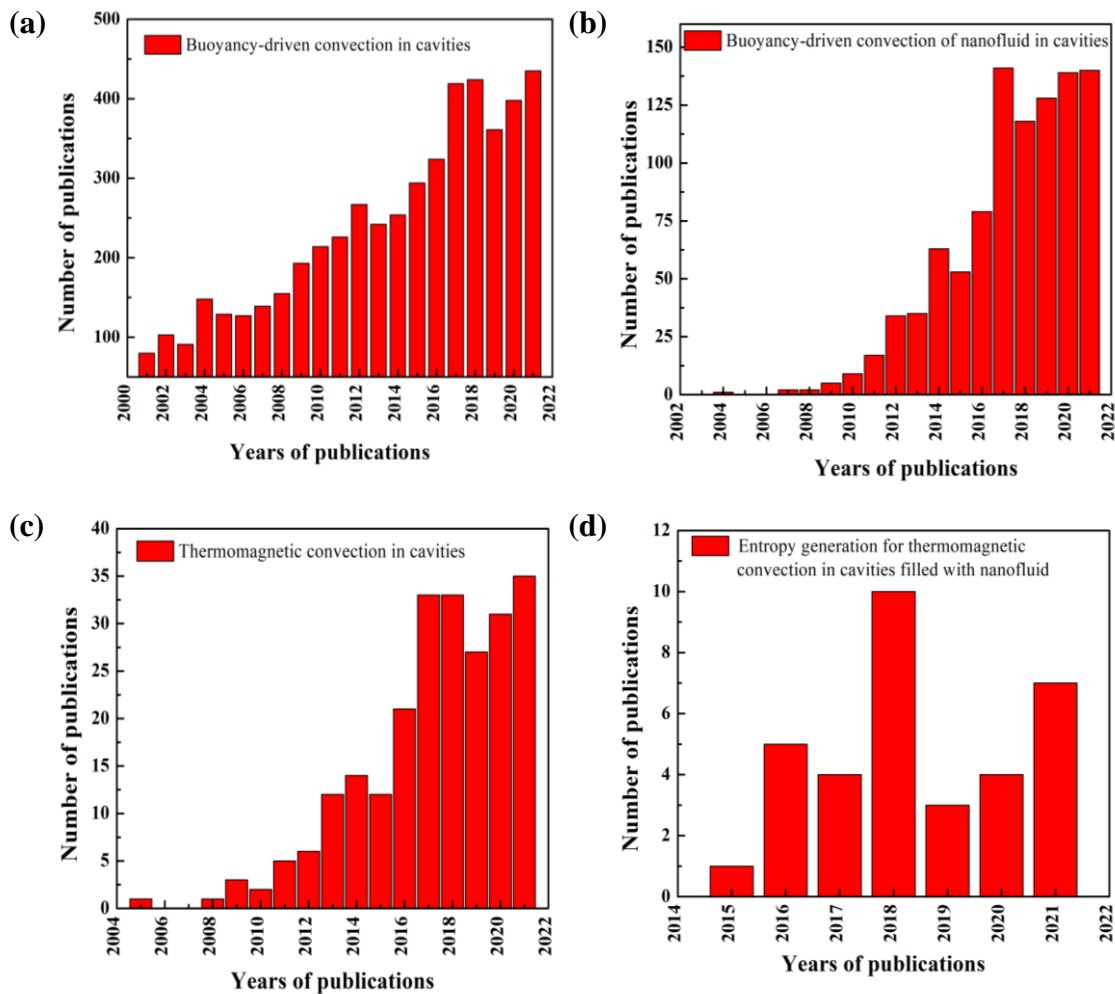
Figure 1.1 Trends of published articles on buoyancy-driven convection in enclosures.

It reveals that buoyancy-driven convection in enclosures is gaining unprecedented interest (Figure 1.1a) due to its diverse range of applications. Effective heat transport is an important issue for widespread industrial and engineering applications, such as air conditioning and ventilation, crystal growth, micro-fuel cells, nuclear reactors, energy storage, solar-based applications (like solar energy, ponds, lakes, and reservoirs), etc. Therefore, a significant volume of studies has focused on natural convection problems, as shown in Figure 1.1a, which justifies the need for a

strong understanding of flow and heat transfer to meet practical applications. However, the studies of buoyancy-driven flow using nanofluids (Figure 1.1b), magnetic fields (Figure 1.1c), and their influences on entropy generation (Figure 1.1d) are relatively fewer and recently growing day-by-day. Therefore, the present work is formulated in magneto-nanofluidic natural convection after a careful review of a bulk volume of pioneering, fundamental, numerical, and experimental works as detailed systematically in the following subsections.

1.2.1 *Earlier works on buoyancy-driven flow*

Buoyancy-driven convection in enclosed regions has been extensively studied, with numerous works available in the literature, including pioneering studies, fundamental investigations, and current research trends. Many experimental and numerical studies have examined the impact of key parameters such as Rayleigh number (Ra), Prandtl number (Pr), aspect ratio (*A*), and cavity inclination angle (ϕ) (Dropkin and Somerscales 1965; Hollands and Konicek 1973; Ozoe et al. 1975; Holland et al. 1976; ElSherbiny et al. 1982; Lartigue et al. 2000; Ampofo and Karayiannis 2003; Henderson et al. 2007; Biswas et al. 2016a).

Dropkin and Somerscales (1965) investigated the effect of Ra, Pr, and ϕ on buoyancy-induced convection in two parallel plates experimentally and developed a correlation to calculate heat transport in terms of the Nusselt number (Nu). Hollands and Konicek (1973) determined the critical Ra regulating the stability of inclined air layers in conduction experimentally and found that the value of the critical Ra obtained for the horizontal position is within 1% of the accepted value (1708). Ozoe et al. (1975) experimentally studied the impact of Ra, *A*, and ϕ on buoyancy-driven convection inside a long rectangular channel and found that the greatest and least heat transport occurs at $\phi = 0°$ and 180°, respectively. Additionally, the critical tilt angle was found to be a strong function of *A* and a weak function of Ra.

Elsherbiny et al. (1982) conducted experimental work to study the impact of Ra, *A*, and ϕ on laminar buoyancy-driven convection and presented correlations to compute convective heat transport based on their experimental findings. Ampofo and Karayiannis (2003) conducted an experiment with exceptional precision to measure the free convection of air in a square-shaped enclosure at a fixed Ra ($= 1.58 \times 10^9$), which provided benchmark data that could be used to validate numerical methodologies. Lartigue et al. (2000) investigated buoyancy-induced flow in a

rectangular enclosure with a high aspect ratio both numerically and experimentally and reported that multicellular convection cells are formed for a high aspect ratio.

Henderson et al. (2007) performed an experimental and numerical investigation of free convection in an integrated collector storage solar water heater consisting of air and water cavities. The results showed that Benard convection cells are formed, consistent with the findings of Lartigue et al. (2000). These experimental and numerical works provide a detailed understanding of buoyancy-driven convection in enclosed regions and are essential for developing and validating numerical models.

Natural convection has been a topic of interest for both numerical and experimental studies. The literature contains many pioneering numerical studies on this topic, such as Globe and Dropkin's (1959) proposed the first correlation to compute heat transport through natural convection in a bottom-heated enclosure. Ayyaswamy et al. (1973) studied the boundary layer regimes for tilted rectangular enclosures and proposed a correlation to compute the average Nusselt number (Nu) based on their obtained results. They found that for sufficiently high Ra, a rescaling of the results for $\phi = 90°$ could be applied for cavity inclination angles (ϕ) ranging from 70° and 90°. Catton et al. (1974) used the Galerkin technique to solve for buoyancy-driven flow and heat transfer in a tilted rectangular slot, while Yin et al. (1978) studied the free convection of air in a temperature-controlled rectangular cavity for different aspect ratios ($4.9 \leq A \leq 78.7$). Yin et al. proposed correlations to compute convective heat transfer based on their results, which showed a maximum deviation of 7.8% from the obtained data.

De Vahl Davis and Jones (1983) later examined the effect of several non-dimensional parameters, namely, Ra and Pr, on buoyancy-driven convection inside a differentially heated square-shaped cavity. Their results showed that Ra had a larger influence on thermal convection than Pr. This article is considered as a benchmark for future research. In summary, extensive numerical and experimental studies have been conducted on natural convection, and many correlations have been proposed to compute convective heat transfer based on their findings.

Over the years, many studies have been conducted to investigate thermal convection in enclosures. These studies have considered a variety of enclosure shapes and configurations, fluids, boundary conditions, numerical techniques, and other non-dimensional parameters. Enclosure configurations such as square, rectangular, trapezoidal, triangular, circular, quadrantal, and elliptical have been examined in these

studies (de Vahl Davis 1983; Mukhopadhyay 2010; Biswas et al. 2021; Saha et al. 2021a; Saha et al. 2022a; Patterson and Imberger 1980; Oztop and Abu-Nada 2008; Biswas et al. 2016; Lam et al. 1989; Varol et al. 2009; Sen et al. 2022; Salmun 1995; Basak et al. 2009a; Chatterjee et al. 2022; Nag et al. 2022; Kuehn and Goldstein 1976; Saha et al. 2022b; Chatterjee et al. 2023; Manna et al. 2023; Tayebi et al. 2020a; Tayebi et al. 2020b; Yadav et al. 2022). Additionally, some studies have investigated natural convection in more complex geometries, such as C-shaped, L-shaped, and T-shaped enclosures (Mansour et al. 2014; Mliki et al. 2017; Karimi and Ghasemi 2012; Nia et al. 2020; Hussein et al. 2016; Sen and Inam 2021). However, several scholars have also published review articles on buoyancy-induced convection in enclosures, providing a wealth of information (Choi and Kim 2012; Das et al. 2017a; Rahimi et al. 2018; Abdulkadhim et al. 2021). The majority of studies of buoyancy-driven convection utilized streamlines and isotherms to investigate the local fluid flow and heat transfer characteristics (Mukhopadhyay 2010; Mahapatra et al. 2013; Saha et al. 2022a).

Prior to the concept of heatline, the convective heat transport mechanisms were mostly studied using isotherms. However, Kimura and Bejan (1983) developed the heatline technique to visualize and analyze the convective heat flow. Heatlines provide the pictorial depiction of the thermal energy flow for convective heat transport systems, whereas isotherms are unable to provide such information. The heatline technique is a valuable tool for analyzing and visualizing. It not only the direction but also the intensity of heat flow in a region. The heatline technique serves as the most effective tool for illustrating thermal energy transfer in the two-dimensional computational domain with complex heat-fluid patterns (Sharma et al. 2015; Biswas et al. 2015; Biswas and Manna 2017; Manna et al. 2019; Biswas et al. 2021a,b; Mondal et al. 2022; Mandal et al. 2022; Chatterjee et al. 2023; Mondal et al. 2023).

Heatlines are pathways via which heat is transported by convection and/or conduction from the hot wall (source) to the cold wall (sink). The direction of thermal energy transfer is represented by the positive/negative signs of the heat function. The positive sign signifies counter-clockwise motion, whereas the negative sign denotes clockwise motion. The rate of transport of thermal energy within the passage remains unchanged. Costa (1999) presented a comprehensive perspective of heatline approaches for visualizing two-dimensional transport processes. In addition to

pioneering investigations, several researchers investigated convective heat transport utilizing the heatline technique (Dalal and Das 2008; Varol et al. 2008; Basak et al. 2009a; Basak et al. 2009b; Ramakrishna et al. 2013; Biswas et al. 2016; Mahapatra et al. 2018).

The buoyancy-driven convection in a complex cavity using the heatline method was presented by Dalal and Das (2008). They looked into the influence of surface waviness and found that the presence of undulations had a minor impact on thermal energy transport. Basak et al. (2009a) investigated the impact of Rayleigh number (Ra) and Prandtl number (Pr) on the visualization of heat flow in triangular enclosures subjected to buoyancy-induced convection. They found that as Ra and Pr values rise, heatlines get denser, indicating improved heat transport. Basak et al. (2009b) investigated the effect of non-uniform heating of trapezoidal enclosures subjected to natural convection utilizing the heatline concept. They found that in the case of non-uniform heating, the total heat transfer rates are lower.

In recent years, there has been a growing demand for efficient thermal devices with rapid heat transfer from various systems such as solar devices, machinery, electrical equipment, and electronic components and devices. To increase the rate of heat transfer in free convection, researchers have turned to the use of nanofluids. The growing interest in this field is evidenced by the number of articles published on nanofluid-based natural convection, as shown in Figure 1.1b. The data for the figure was collected from the Scopus repository. As a result, the focus of research on buoyancy-induced flow has shifted from conventional fluids to nanofluids.

1.2.2 Earlier works on buoyancy-driven nanofluid flow

The superior heat transfer properties of nanofluids have garnered a lot of attention in various fields, particularly in applications where efficient heat dissipation is essential. This includes systems with low energy consumption, excellent durability, and low operational noise, such as nuclear reactors, heat exchangers, and solar collectors, among others. This is evidenced by the large number of articles published in this field (Figure 1.1b). The high surface-to-volume ratio of nanoparticles in nanofluids enhances their thermo-physical properties, resulting in better thermal energy transport than conventional fluids (Khanafer et al. 2003; Oztop and Abu-Nada 2008). The concept of nanofluids was first introduced by Choi and Eastman (1995), who blended nano-sized particles with base liquids to create a superior heat transfer

fluid. The low thermal conductivity of conventional fluids, such as air and water, makes them ineffective at dissipating heat quickly. Therefore, increasing the thermal conductivity of these fluids improves heat transport (Pak and Cho 1998; Lee et al. 1999).

Modeling nanofluid-based natural convection can be performed using a single-phase model or a two-phase model, as revealed by the literature review. For low concentrations of nanoparticles, the single-phase model treats nanofluids as homogeneous single-phase fluid. This model assumes that the suspended nanoparticles and base fluid flow at the same velocity due to their small size and low concentration. Additionally, the solid-liquid combination can be approximated to act as a traditional single-phase fluid when local thermal equilibrium is taken into account, with properties that must be assessed from its components. However, Ding and Wen (2005) observed that the assumptions made in the single-phase model might not always be accurate, particularly for Peclet numbers (Pe) above 10.

Numerous articles have investigated convective heat transfer models for nanofluids using a single-phase model. Most of these studies have found that the presence of nanoparticles enhances heat transport (Khanafer et al. 2003; Jou and Tzeng 2006; Oztop and Abu-Nada 2008; Abu-Nada and Oztop 2009). Khanafer et al. (2003) presented a numerical benchmark article on buoyancy-driven convection in a square-shaped enclosure filled with nanofluid and investigated the impact of Grashof numbers (Gr) and volume fractions (ζ) on thermal energy transport. They found that the heat transfer rate increases with an increase in Gr and ζ, and proposed a correlation to estimate the average Nusselt number (Nu) in terms of Gr and ζ.

Oztop and Abu-Nada (2008) studied the influence of aspect ratio (*A*) on nanofluid-based free convection and reported that nanofluid-enhanced heat transport is more pronounced at low *A* values than at high *A* values. Abu-Nada and Oztop (2009) investigated the impact of tilt angle (ϕ) on buoyancy-induced flow and heat transfer in a square cavity using Cu-water nanofluid and found that minimum heat transport occurs at $\phi = 90°$. In addition to these parameters, other studies have examined the influence of heater dimensions and position (Aminossadati and Ghasemi 2009; Saha et al. 2022b), non-uniform heating (Oztop et al. 2012; Saha et al. 2022c), and other factors on thermal energy transfer. Single-phase models are typically used for low concentrations of nanoparticles, but particle distribution becomes non-uniform at high Peclet numbers (Ding and Wen 2005).

Few articles in the literature have reported a decrement in heat transfer with an increase in ζ. Abouali and Falahatpisheh (2009) numerically examined the thermal convection of nanofluid in vertical annuli and proposed a correlation to estimate heat transfer. They found that the Nu declines with an increase in ζ values. Similarly, Rashmi et al. (2011) performed numerical simulations of the buoyancy-induced flow of nanofluids and found a decrement in thermal energy transport with an increase in the value of ζ.

The literature reports that there are two important parameters in the single-phase model for nanofluids: thermal conductivity and fluid viscosity. However, different authors used different correlations to estimate these values, leading to variations in numerical results. To predict thermal conductivity and viscosity, several models have been proposed in the literature.

Maxwell (1983) proposed the model to predict the thermal conductivity of the nanofluids. There are several models in the literature that may be used to compute the thermal conductivity of nanofluids. However, the majority of the model is an enlarged version of the classical Maxwell model. These models are based on the assumption that the nanoparticles are in a static state and that heat transfer occurs solely through conduction. Later, Jang and Choi (2004) extended the model by including the conduction and convection modes of heat transfer in nanofluids. According to Shukla and Dhir (2008), the thermal conductivity of nanofluids is the combined effect of conduction and convection (produced by the Brownian movement of the nanoparticles). However, the mobility of nanoparticles is too sluggish to carry large amounts of heat transfer due to Brownian motion through nanofluids according to Keblinski et al. (2002). As a result, the thermal conductivity due to Brownian motion is ignored in the current study.

In the year 1952, the Brinkman model extended the first equation proposed by Einstein's equation in the year 1906 for use with moderate particle concentration. He considered the effect of the addition of solute molecule to an existing continuous medium of particle concentrations less than 4 %. In the present work, we have used the Brinkman model which was more accepted among the researchers (Khanafer et al. 2003; Abu-Nada 2009; Sheikholeslami et al. 2016).

As a result, the Maxwell model and the Brinkman model are commonly used for thermal conductivity and viscosity, respectively (Maxwell 1873; Pak and Cho 1998; Yu and Choi 2003; Chon et al. 2005; Brinkman 1952; Batchelor 1977; Wang et

al. 1999). Abu-Nada and Chamkha (2010) investigated the impact of thermal conductivity and viscosity models on buoyancy-induced convection in an enclosure and found that the viscosity model is more important than the thermal conductivity model for convective heat transfer.

Several researchers have attempted to build convective heat transfer models for nanofluids using a two-phase model with nano-sized particles in the solid phase. However, it is debatable whether the traditional two-phase model can accurately predict the fluid motion and heat transfer of nanofluids. Multiple factors, including gravitational force, nanoparticle-fluid friction, the particles' dispersion, Brownian effects, etc., might influence the motion and heat transport of a nanofluid. Therefore, while modeling nanofluid motion and heat transfer, the slip velocity between the fluid and the nanoparticles cannot be ignored.

Buongiorno (2006) carried out an in-depth examination of convective transport in nanofluids, considering various slip mechanisms. According to the findings, only thermophoresis and Brownian diffusion are significant slip mechanisms. The two-phase approach considers the mobility of solid and fluid molecules separately, providing extensive information on the mixture's liquid and solid phases. Multiple multiphase concepts have been developed and used to understand fluid motion and predict heat transfer. A significant number of multiphase flow publications used mixture theory to analyze flow patterns and heat transport of nanofluids (Akbarinia and Laur 2009; Bianco et al. 2011).

According to a study of the literature, buoyancy-induced convection of nanofluid using a single-phase model may predict the rate of heat transfer more precisely than a two-phase model. Saghir et al. (2016) conducted a comparative study of single-phase and two-phase models in a square-shaped enclosure filled with nanofluid. They performed numerical investigations using both models and compared the results to the available experimental data in the literature. The authors found that the single-phase model produced results that were more consistent with the experimental results than the two-phase model. However, the two-phase approach offers detailed information about the liquid and solid phases of the mixture.

Several experimental studies have been conducted to investigate the effect of nanofluids on buoyancy-driven convection in enclosures. Putra et al. (2003) experimented to assess the effect of nanofluid on free convection in a horizontal cylinder and observed a substantial reduction in the rate of heat transfer at high

nanoparticle concentrations. Ho et al. (2010) studied the buoyancy-induced fluid motion and thermal energy transport of nanofluid in a square cavity and reported that the rate of heat transfer improves at low volume fractions ($\zeta = 0.1\%$) with a maximum improvement of 18% compared to pure water. However, for $\zeta > 2\%$, there is a decrease in the rate of heat transfer. Hu et al. (2014) examined the fluid motion and thermal energy transport of Al_2O_3-water nanofluid in a square cavity and found that the thermal energy transfer of nanofluid increases at low nanoparticle concentration ($\zeta = 0.25$) and decreases at high concentration ($\zeta = 0.77$) compared to pure water. Torki and Etesami (2019) investigated the influence of tilt angle (ϕ) and volume fraction of SiO_2 nanoparticles on buoyancy-induced fluid motion and thermal energy transmission in a rectangular cavity. They reported that increasing the nanoparticle concentration had no significant effect on convective heat transport at low concentration. The maximum heat transfer occurs at $\phi = 0°$. While the experimental studies provide insight into the behavior of nanofluids, numerical studies are also essential for a more comprehensive understanding of fluid flow and heat transfer mechanisms.

A survey of the literature shows that the use of nanofluids to enhance convective heat transfer is still a subject of debate, with conflicting findings on their effectiveness. However, most numerical studies have found that nanofluids can significantly improve heat transport compared to traditional fluids. Experimental studies, on the other hand, have reported that high concentrations of nanoparticles can reduce heat transmission, while low concentrations can improve it. The discrepancy between numerical and experimental results can be attributed to the impact of thermal conductivity and viscosity on convective heat transfer in nanofluids. The addition of nanoparticles to the base fluid increases both heat conductivity and viscosity; however, the viscosity can have opposing effects on the Nusselt number depending upon nanoparticle concentration. Overall, it is clear that heat transport is enhanced at low nanoparticle concentrations. Several review articles are available that discuss the impact of nanofluids on buoyancy-induced convection in enclosures.

Current research in this field focuses on using an external magnetic field to drive the natural convection of nanofluids in cavities, leading to a trend in publications on thermomagnetic convection in enclosures. However, the number of articles on this topic remains limited, indicating that there is still significant potential for research in this area. Figure 1.1c shows the trend of publication on MHD-based

buoyancy-driven convection in enclosures using nanofluids, based on data from the Scopus repository.

1.2.3 *Buoyancy-driven convection in presence of magnetic fields*

The current shift in technological innovation has resulted in the development of magnetic components and gadgets with superior thermal performance. Such components include electronic gadgets, cooling systems, magnetic storage devices, and sensors, among others. To ensure that these devices function optimally, the study of buoyancy-induced convection in the presence of the magnetic field is necessary. This study is known as magnetohydrodynamics (MHD), and it involves the study of the influence of a magnetic field in a moving electrically conducting fluid. The presence of a magnetic field in a moving electrically conducting fluid creates an electromagnetic force, also known as the Lorentz force. The presence of Lorentz force in the flow domain during buoyancy-induced convection alters the flow pattern and temperature distribution, making it crucial to study its effects (Oztop et al. 2013).

A substantial amount of numerical research on MHD-based natural convection is available. The majority of researchers look into the impact of magnetic fields on various enclosure shapes/configurations, non-dimensional parameters, the inclination of a cavity (ϕ), magnetic field strength, magnetic field inclination (γ), and so on. The impact of magnetic field on different geometrical configurations, namely, rectangular (Wang et al. 2017; Giwa et al. 2020a), triangular (Mahmoudi et al. 2012; Rahman 2016; Dogonchi et al. 2019), circular (Sheikholeslami et al. 2012; Tayebi et al. 2021), trapezoidal (Mahmoudi et al. 2013; Bondareva et al. 2015), etc. was studied by several researchers. Several authors studied the effect of several non-dimensional parameters, namely Rayleigh number (Ra), and Hartmann number (Ha) on thermo-magnetic convection (Nemati et al. 2012; Kefayati 2014; Selimefendigil and Öztop 2015). They reported that heat transfer during buoyancy-induced convection (Nu) increases with a rise in Ra, and declines with a rise in Ha.

Several researchers (Bourantas et al. 2014; Mamourian et al. 2016; Zhang and Che 2016; Balla et al. 2017; Shahriari et al. 2019) examined the influence of tilt angle of enclosure on MHD-based thermal convection flow. Bourantas et al. (2014) studied MHD-based thermal convection flow in a tilted enclosed space occupied with a micropolar nanofluid. They reported that the magnetic field intensity and orientation

had a substantial effect on the fluid motion and temperature distribution. Mamourian et al. (2016) investigated the effect of tilt angle on MHD-based buoyancy-induced flow in a square-shaped enclosure and found that the Nu was more susceptible to tilt angle than that of the Ha value. Zhang and Che (2016) investigated the impact of tilt angle on MHD-based buoyancy-driven convection in a cavity having various heat sources. The results show that for a high value of Ra (= 10^5), the Nu declines initially as the tilt angle increases to a particular tilt angle and then rises with further increment in tilt angle at a low value of Ha. Whereas for a high value of Ha, the Nu increases first as the tilt angle increases to a specific value and then declines with a further increase in tilt angle. Balla et al. (2017) examined MHD-based buoyancy-induced flow in an inclined square-shaped enclosure occupied with a porous media saturated with nanofluid. The results indicate that the minimum and maximum heat transfer occur at $\phi = 0°$ and $45°$, respectively. Shahriari et al. (2019) applied the lattice Boltzmann method (LBM) to simulate MHD-based free convection of CuO-water nanofluid inside an inclined wavy cavity and found that the Nu changes with tilt angle, while the minimum values of Nu occur at $\phi = 60°$.

Several authors studied the impact of magnetic field inclination (γ) in buoyancy-driven convection (Mansour and Bakier 2015; Manna et al. 2022). The buoyancy-driven convection in a square enclosure in the presence of an inclined magnetic field was examined by Mansour and Bakier (2015). They found that the maximum heat transfer occurs at $\gamma = 90°$.

Several other factors affect thermomagnetic convection, including surface waviness (Biswas et al. 2021a), non-uniform heating (Mejri et al. 2014; Sheikholeslami et al. 2014a; Manna et al. 2021a), and obstruction (Selimefendigil and Öztop 2015; Mallick et al. 2021). Additionally, Manna and Biswas (2021b) recently developed a novel visualization technique for MHD-based convection known as magnetic force vectors. There are also numerous review articles available on MHD-based buoyancy-induced convection in enclosures, providing a wealth of information on the topic (Hemmat et al. 2020; Giwa et al. 2020b; Molana et al. 2020).

In addition to assessing flow strength and thermal energy transfer in an enclosure, it is critical to estimate entropy generation (EG) in a thermodynamic system for system design. However, the number of studies published on entropy production in thermo-magnetic convection using nanofluids is limited (Figure 1.1d), leaving ample opportunity for further research in this area.

1.2.4 *Entropy generation in buoyancy-driven convection*

The concept of entropy generation (EG) is crucial in assessing the irreversibility of a thermodynamic system and is essential in optimizing system design (Bejan 1979). The rate of EG indicates the level of molecular randomness at the microscopic level and is proportional to the amount of waste energy produced by energy loss. Entropy generation comprises of the irreversibilities associated with heat transport between the system and its surroundings, friction (or viscous effects), and other elements such as internal heat generation and magnetic fields. Reducing entropy generation is essential in improving thermal system performance as higher values of entropy production indicate less efficient processes, equipment, or systems (Ilis et al. 2008).

Numerous fundamental studies have examined the influence of non-dimensional parameters on entropy production (Batyas 2000; Oliveski et al. 2009; Sarkar et al. 2021). Baytas (2000) numerically examined the impact of Ra, varying from 10^2 to 10^4, on entropy production of free convection in an inclined porous enclosure and found that as the Rayleigh number (Ra) declines; heat transfer irreversibility surpasses fluid friction irreversibility. Ilis et al. (2008) studied the effect of aspect ratio (*A*) on free convection. Oliveski et al. (2009) investigated the impact of Ra, *A*, and irreversibility ratios (*Φ*) on EG in a rectangular enclosure subjected to buoyancy-driven convection and found that the total EG rises as the value of Ra, *A*, and *Φ* increases.

Sarkar et al. (2021) numerically studied EG in a semi-elliptical enclosure subjected to buoyancy-driven convection and found that EG due to viscous dissipation is insignificant compared to EG due to heat transfer, which is consistent with Mukhopadhyay (2010). The studies cited above demonstrate that understanding the influence of non-dimensional parameters on entropy production in convection is crucial for optimizing system design.

Several articles in the literature explore the effect of nanofluid on entropy generation (EG) in cavities experiencing natural convection. Researchers have found that the overall EG increases with a rise in the Rayleigh number (Ra) and nanoparticle size, but decreases with increasing nanoparticle concentration (*ζ*) (Esmaeilpour and Abdollahzadeh 2012; Cho 2014; Mahian et al. 2014; Kefayati 2015; Kolsi et al. 2016; Ashorynejad and Hoseinpour 2017; Cho 2020). Mahian et al. (2014) investigated

buoyancy-induced convection in a solar collector containing Al_2O_3-water nanofluid and found that rough tubes produce significantly more EG than smooth tubes. Mamourian et al. (2016) studied the effect of a constant magnetic field on EG in cavities filled with Al_2O_3-water nanofluid and found that for a fixed Hartmann number (Ha), the net EG increases with the inclination angle of the enclosure up to 30°, and then decreases.

Literature reviews show that EG is strongly influenced by several parameters, including Ra, Pr, Ha, the inclination of the cavity (φ) and magnetic field (γ), heating profiles (Malik and Nayak 2017; Sahin 2020), discrete heating (Mukhopadhyay 2010; Das and Basak 2017b), and obstructions (Mahmoodi and Sebdani 2012; Mahapatra et al. 2013), as well as nanoparticle concentration (ζ). Several excellent review papers in the literature have studied the effect of EG on thermal convection in enclosures. Oztop and Al-Salem (2012) provided a comprehensive review taking into account various enclosure shapes; Sciacovelli et al. (2015) published a review on the use of EG analysis in various engineering applications. Biswal and Basak (2017) provided a review on EG during thermal convection in different cavities and processes involving diverse practical uses.

In addition, the literature survey indicates that the number of studies published in the field of entropy production in thermo-magnetic convection utilizing nanofluid is limited (Figure 1.1d). Thus, there is still a lot of room for research in this field (Biswas et al. 2021a).

1.3 Major observations from the Literature survey

In summary of the literature review, the following common observations can be listed as follows:

- The fluid flow, heat transfer, and entropy generation are influenced by a variety of factors such as the geometry and orientation of enclosures, heating and cooling conditions, their locations, types of working fluids, the presence of different physics, etc.
- The flow, heat transfer, and entropy generation are primarily governed by the Rayleigh number Ra, Prandtl number Pr, Hartmann number Ha, and the inclination of a cavity (ϕ) and magnetic field (γ).

- The interdependence of these parameters generates different heat transfer and flow characteristics and makes room for future research related to specific or newer applications.

1.4 Scope and Objective of the Present Study

The present study aims to address the research gap in the area of buoyancy-driven flow in enclosures. Various enclosures have been investigated in earlier works, but there has been no discussion on the most efficient geometric shape from a thermal performance viewpoint. To fill this gap, a novel constraint-based methodology is developed to compare the thermal performance of different thermal systems and geometries. This study establishes equivalency statements and evaluates the local and global thermal characteristics of various buoyancy-driven flow geometries with respect to a referenced (base) thermal system/geometry. The goal is to identify the most efficient geometric shape that utilizes the constraints of the same heat input (or heating surface area) and working fluid volume, and possibly the same cooling surface area for certain problems. The current work considers typical regular geometric shapes such as square, circular, trapezoidal, and triangular geometries, along with square and circular annulus. As a result, the following equivalent problems are formulated to explore the importance of the newly proposed constraint-based approach for the comparative analysis of buoyancy-driven flow in various typical enclosures as listed below.

Problem 1 - Buoyant flow in an equivalent square (base case) and circular thermal systems: In this problem, the classical differentially heating configuration (DHC) is used with practical working fluids such as air, water, and CuO-water nanofluid. The constraints for this study are equal fluid volume, equal heating and cooling surfaces, and equal cavity inclinations.

Problem 2 - MHD flow in equivalent square and circular thermal systems: This problem builds on the first problem by considering the magneto-hydrodynamic flow of CuO-water nanofluid for different strengths and inclinations of the imposed magnetic field. The evaluation of entropy generation is used to assess thermodynamic irreversibility in the base and alternative thermal geometries. The constraints for this study are identical fluid volume, heating and cooling surfaces, and magnetic field strength and inclination.

Problem 3 - MHD flow in equivalent square and trapezoidal thermal systems: This study is similar to the second problem but uses a series of trapezoidal-shaped thermal

enclosures with different cooling surfaces while keeping the fluid volume and heating surface constant.

Problem 4 - MHD flow in equivalent square and triangular thermal systems: This study is an extension of the third problem, focusing on the special or limiting case of the trapezoidal enclosure.

Problem 5 - MHD flow in equivalent square and circular annular thermal systems: In this problem, the approach of constraint-based analysis is applied to annular flow geometries (square and circular) with identical heating surfaces at the inner walls. Based on the equivalency of fluid volume or cooling surface, two different circular annulus geometries are assessed along with the reference square annular enclosure.

The detailed objectives for examining the global and local thermal characteristics and associated entropy generation for no-MHD and MHD nanofluid flow in constraint-based equivalent systems of the above-mentioned problems are:

- To **examine** the influence of **geometrical shape** (square, trapezoidal, triangular, and circular) on **system thermal performance** subjected to **buoyancy-driven flow** applying the **constraints** of equal fluid volume, and equal heating surfaces.

- To **examine** the impact of **magnetic field** on thermo-fluid flow pattern and heat transfer.

- To **scrutinize** the effect of **nanofluid flow** on thermo-fluid flow pattern and heat transfer.

- To **inspect** the heat flow mechanism in various geometrical shapes by using Bejan's **heatlines**.

- To **evaluate** the **thermodynamic irreversibility** of different thermal systems considered in the present work.

- To **assess** the **improved heat transfer** caused by different geometrical configurations in comparison to the base case (square-shaped geometries).

- To **compare** the local flow features and heat transport behaviors using different visualization means like streamlines, isotherms, and heatlines.

The importance of identifying an efficient thermal system from a geometrical shape point of view is understandable in the practice of thermal system design. Therefore,

the outcomes of this novel constraint-based natural convection analysis would be useful to thermal system engineers and researchers.

1.5 Organization of the Present Work

Although the studied problems are different, they share the same governing equations and solving methodologies. The mathematical formulation, numerical procedure, and rigorous validation studies are presented cohesively in **Chapter 2**. Subsequent **Chapters 3-6** address the different problems studied and present their findings and results logically. The final chapter (**Chapter 7**) provides a comparative assessment of heat transfer performance for equivalent buoyancy-driven thermal enclosures, as well as a discussion of the present work's contribution and future scope. The reference list is provided afterwards. The details of grid structure of different problems are presented in the **Appendix** which is provided at the end of the document.

Chapter – 2

Mathematical Treatment and Numerical Procedure

2.1 Introduction

This chapter presents the mathematical modeling of the buoyancy-driven flow influenced by a magnetizing field within a confined space. The governing equations, along with the boundary conditions, are solved numerically using a Computational Fluid Dynamics (CFD) tool. Local and global parameters are then visualized from the solved data. Additionally, a general overview of the finite element method (FEM) is provided. The accuracy of the solver is verified through a rigorous validation study in which several numerical and experimental results available in the literature are simulated.

2.2 Governing equations of buoyancy-driven flow

This study focuses on investigating buoyancy-driven flow within an enclosed space, with Figure 2.1 representing the base case. In the figure, the cavity inclination angle (ϕ) is measured from the x-axis. Other alternative thermally equivalent enclosures are detailed in subsequent chapters. The enclosed area can be filled with practical fluids such as air, water, or specially engineered fluids like nanofluids, which are created by blending nano-sized particles in a liquid. Nanofluids are assumed to behave like Newtonian single-phase fluids, with the base fluid and nanoparticles in thermal equilibrium. The nanoparticles are assumed to be uniform in shape, travel at the same velocity as the fluid due to their small size and low concentration, and exist as a homogenous mixture without sedimentation.

The present simulation considers a laminar, steady, and incompressible, flow inside an enclosed space filled with either regular fluids or nanofluids. The current numerical simulation is carried out using two-dimensional geometry, with the assumption that the depth of the cavity in the third dimension is sufficiently large. This reduces computational time and resources. The Boussinesq approximation is utilized to calculate the buoyant force term in the momentum equation, considering the density variation with temperature, while the other thermo-physical properties are assumed to

be constant. However, the simulation does not consider the induced electric current, Joule heating, viscous dissipation, or radiation. As the magnetic Reynolds number is low, the induced magnetic field is neglected compared to the applied magnetic field. The conservation laws of continuity, momentum, and energy regulate fluid motion and heat transport equations in the present study.
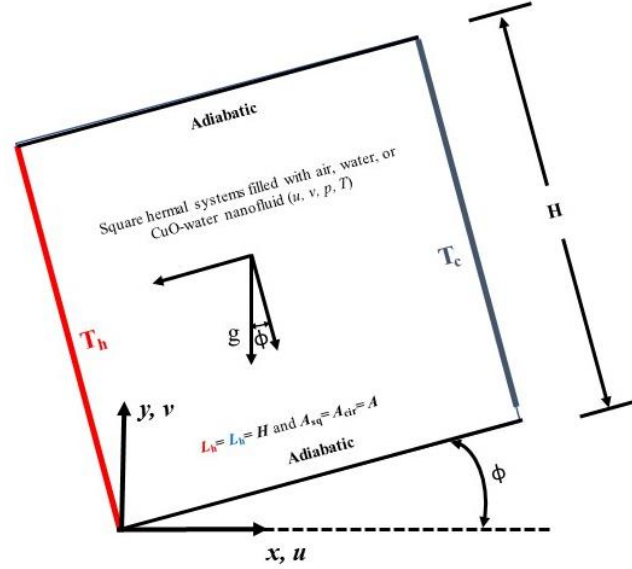
Figure 2.1 Pictorial representation of the base problem.

The dimensional form of governing equation subjected to buoyancy-driven flow under the aforementioned assumptions is presented as follows:

$$\frac{\partial u}{\partial x} + \frac{\partial u}{\partial y} \tag{2.1}$$

$$\rho\left(u\frac{\partial u}{\partial x} + v\frac{\partial u}{\partial y}\right) = -\frac{\partial p}{\partial x} + \mu\left(\frac{\partial^2 u}{\partial x^2} + \frac{\partial^2 u}{\partial y^2}\right) + \rho g \beta (T - T_c)\,\sin\phi \tag{2.2}$$

$$\rho\left(u\frac{\partial v}{\partial x} + v\frac{\partial v}{\partial y}\right) = -\frac{\partial p}{\partial y} + \mu\left(\frac{\partial^2 v}{\partial x^2} + \frac{\partial^2 v}{\partial y^2}\right) + \rho g \beta (T - T_c)\,\cos\phi \tag{2.3}$$

$$\rho C_P\left(u\frac{\partial T}{\partial x} + v\frac{\partial T}{\partial y}\right) = k\left(\frac{\partial^2 T}{\partial x^2} + \frac{\partial^2 T}{\partial y^2}\right) \tag{2.4}$$

where the symbols u and v correspond to the directional velocity components; p, T, g, ϕ and γ are respectively the static pressure, temperature, gravitational acceleration, and cavity and magnetic field angles. Fluid properties utilized here are densityρ,

viscosity μ, volumetric thermal expansion coefficient β, and thermal conductivity k of the working fluids.

When a magnetic field is applied to the buoyancy-driven flow, an additional force known as the electromagnetic (or Lorentz) force acts on the thermal system. For two-dimensional problems, the applied external magnetic field of the intensity $\left(\vec{B} = B_x \vec{e_x} + B_y \vec{e_y}\right)$ of constant magnitude $B = \sqrt{B_x^2 + B_y^2}$ is considered homogeneous. The electric current J is defined as $J = \sigma\left(\vec{V} \times \vec{B}\right)$. The electromagnetic force F is defined as $F = J \times \vec{B}$. The electromagnetic force acting on an infinitesimal volume of fluid carrying a charge (q) and a current density (J) can be represented as follows:

$$\vec{F}_L = q\vec{E} + \vec{J} \times \vec{B} \tag{2.5}$$

$$\vec{F}_L = q\vec{E} + \sigma(\vec{V} \times \vec{B}) \times \vec{B} \tag{2.6}$$

where E and B represent the electric and magnetic fields, respectively. The corresponding force can be divided into two components: the Coulomb force, which accounts for the electric field, and the Lorentz force which accounts for the magnetic field. When there is no electric field, the Lorentz force can be expressed as follows:

$$\vec{F}_L = \sigma(\vec{V} \times \vec{B}) \times \vec{B} \tag{2.7}$$

Under the aforementioned assumptions, the dimensional forms of the flow-regulating momentum equations of buoyancy-driven flow in the presence of a magnetic field, are expressed as

$$\rho\left(u\frac{\partial u}{\partial x} + v\frac{\partial u}{\partial y}\right) = -\frac{\partial p}{\partial x} + \mu\left(\frac{\partial^2 u}{\partial x^2} + \frac{\partial^2 u}{\partial y^2}\right) + \rho g\beta(T - T_c)\ \sin\phi$$
$$+ \sigma B^2(v\sin\gamma\cos\gamma - u\sin^2\gamma) \tag{2.8}$$

$$\rho\left(u\frac{\partial v}{\partial x} + v\frac{\partial v}{\partial y}\right) = -\frac{\partial p}{\partial y} + \mu\left(\frac{\partial^2 v}{\partial x^2} + \frac{\partial^2 v}{\partial y^2}\right) + \rho g\beta(T - T_c)\ \cos\phi$$
$$+ \sigma B^2(u\sin\gamma\cos\gamma - v\cos^2\gamma) \tag{2.9}$$

The present computations are carried out in a non-dimensional form. Therefore, the dimensional form of governing equations of MHD buoyant flow are transformed to their dimensionless forms. The used non-dimensional variables are as follows:

$$(X,Y) = \frac{(x,y)}{H}, \quad (U,V) = \frac{(u,v)}{(\alpha_f / H)}, \quad P = \frac{p}{\rho(\alpha_f / H)^2}, \quad \theta = \frac{(T - T_c)}{(T_h - T_c)} \tag{2.10}$$

In the above equation, H stands for the length scale. As the characteristic velocity is missing in the case of natural convection heat transfer, the diffusion velocity scale (α_f/H) is selected to obtain a dimensionless velocity term in the governing equations. The evolved dimensionless numbers are Rayleigh number (Ra), Prandtl number (Pr), and Hartmann number (Ha) (based on fluid properties such as kinematic viscosity v_f, thermal diffusivity α_f, electrical conductivity σ_f) and defined as

$$\Pr = v_f / \alpha_f, \quad \mathrm{Ra} = g\beta_f (T_h - T_c)H^3 / v_f \alpha_f, \quad \mathrm{Ha} = BH\sqrt{\sigma_f / \mu_f} \tag{2.11}$$

The resulting non-dimensional governing equations in the presence of an inclined magnetic field (with respect to the horizontal axis) and an inclined cavity (with respect to horizontal axis) are derived as

$$\frac{\partial U}{\partial X} + \frac{\partial V}{\partial Y} = 0 \tag{2.12}$$

$$\left(U\frac{\partial U}{\partial X} + V\frac{\partial U}{\partial Y} \right) = -\frac{\partial P}{\partial X} + \Pr\frac{v}{v_f}\left(\frac{\partial^2 U}{\partial X^2} + \frac{\partial^2 U}{\partial Y^2} \right) + \frac{(\rho\beta)}{\rho\beta_f}\mathrm{Ra}\,\Pr\theta\sin\phi$$
$$+ \Pr\mathrm{Ha}^2\frac{\sigma\,\rho_f}{\sigma_f\rho}(V\sin\gamma\cos\gamma - U\sin^2\gamma) \tag{2.13}$$

$$\left(U\frac{\partial V}{\partial X} + V\frac{\partial V}{\partial Y} \right) = -\frac{\partial P}{\partial Y} + \Pr\frac{v}{v_f}\left(\frac{\partial^2 V}{\partial X^2} + \frac{\partial^2 V}{\partial Y^2} \right) + \frac{(\rho\beta)}{\rho\beta_f}\mathrm{Ra}\,\Pr\theta\cos\phi$$
$$+ \Pr\mathrm{Ha}^2\frac{\sigma\,\rho_f}{\sigma_f\rho}(U\sin\gamma\cos\gamma - V\cos^2\gamma) \tag{2.14}$$

$$\left(U\frac{\partial\theta}{\partial X} + V\frac{\partial\theta}{\partial Y} \right) = \frac{\alpha}{\alpha_f}\left(\frac{\partial^2\theta}{\partial X^2} + \frac{\partial^2\theta}{\partial Y^2} \right) \tag{2.15}$$

The thermophysical properties of a nanofluid are dependent on its constituents. In the final set of governing equations (2.12-2.15), property ratios are present when a nanofluid is used as the working fluid. In these equations, the subscript 'f' represents the pure or base fluid, and there is no subscript for the nanofluid or working fluid. For pure fluid cases such as air or water, these property ratios are equal to 1. However, for nanofluid cases, the values of these ratios differ. The properties of water and nanoparticles are taken from standard literature sources to evaluate the properties of

nanofluids (Sheikholeslami et al. 2014; Mliki et al. 2016). The properties of nanofluids are estimated using the following correlations.

$$\rho = (1-\zeta)\rho_f + \zeta \rho_s \qquad\qquad (2.16)$$

$$(\rho c_p) = (1-\zeta)(\rho c_p)_f + \zeta(\rho c_p)_s \qquad\qquad (2.17)$$

$$(\rho\beta) = (1-\zeta)(\rho\beta)_f + \zeta (\rho\beta)_s \qquad\qquad (2.18)$$

The dynamic viscosity of the nanofluid is proposed by Brinkman (1952). Maxwell (1983) postulated the thermal and electrical conductivities of nanofluids, respectively.

$$\mu = \mu_f(1-\zeta)^{-2.5} \qquad\qquad (2.19)$$

$$k = k_f\left[\frac{(k_s + 2k_f) - 2\zeta(k_f - k_s)}{(k_s + 2k_f) + \zeta(k_f - k_s)}\right] \qquad\qquad (2.20)$$

$$\sigma = \sigma_f\left[1+\frac{3(\sigma_s/\sigma_f - 1)\zeta}{(\sigma_s/\sigma_f + 2) - (\sigma_s/\sigma_f - 1)\zeta}\right] \qquad\qquad (2.21)$$

It should be noted that the viscosity and thermal conductivity of the nanofluid considered in this study do not include the effects of Brownian motion. While several studies have examined the impact of thermophoresis and Brownian motion in nanofluid flow, and again several studies also exist which have not considered these effects. Therefore, these effects are not considered in the present simulation.

The boundary conditions for the numerical simulation are determined based on the problem description shown in Figure 2.1. The walls of the stationary cavities are rigid, and the fluid-bounding walls are set to $U = V = 0$. The thermal conditions include the cold portion ($\theta = 0$) and hot portion ($\theta = 1$) and insulation ($\partial\theta/\partial n = 0$) along the system's boundaries.

2.3 Performance analysis parameters

To estimate the local heat transfer characteristics, the local Nusselt number ($\mathrm{Nu_l}$) is defined using the normal temperature gradient (n implying the normal outward direction). After solving the flow governing equations in terms of primitive dimensionless variables, thermal and flow performance parameters are computed using the solved variables. The Nusselt number is considered to be the most important

global performance parameter, which measures the rate of heat transfer. It is defined by

$$\text{Nu}_1 = -\frac{k}{k_f} \frac{\partial \theta}{\partial n}\bigg|_{\substack{\text{heater,}\\\text{cooler}}} \tag{2.22}$$

The mean or average Nusselt number is computed by integrating the local Nu over the active surface as

$$\text{Nu} = \int_0^S \text{Nu}_1 \, dS \bigg/ \int_0^S dS \tag{2.23}$$

The evolved circulation strength is computed by utilizing the stream function (ψ), which follows the form of the Poisson equation as

$$\frac{\partial^2 \psi}{\partial X^2} + \frac{\partial^2 \psi}{\partial Y^2} = \frac{\partial U}{\partial Y} - \frac{\partial V}{\partial X} \tag{2.24}$$

The value of ψ is set to zero (0) on all boundary walls, with the maximum or minimum value of ψ indicating the highest flow strength established in the enclosures. Isocontours of ψ, commonly referred to as streamlines, illustrate flow patterns within confined thermal systems. These streamlines may depict a clockwise (CW) circulation with $-\psi$ and/or a counter-clockwise (CCW) circulation with $+\psi$.

The heatfunction (Π equation and heatlines are used for comparative performance analysis of various buoyancy-driven enclosures, similar to the stream function (ψ) and streamlines, for understanding the heat flow mechanism. The maximum or minimum value of Π indicates the highest heat transfer strength in the enclosures. The heat transfer can be clockwise (CW) with $-\Pi$ or counter-clockwise (CCW) with $+\Pi$ circulation. The equation of Π is expressed as

$$\frac{\partial^2 \Pi}{\partial X^2} + \frac{\partial^2 \Pi}{\partial Y^2} = \frac{\partial(\theta U)}{\partial Y} - \frac{\partial(\theta V)}{\partial X} \tag{2.25}$$

The value of Π is set to zero for the bottom adiabatic wall. For all other walls, the normal heat flux is properly computed. This heat function is obtained from the heat-transporting steady-state energy equation (Biswas et al. 2016).

Although ideal operations or processes are reversible, irreversibility arises during real operations or processes. In the case of MHD buoyant flow systems, it is

necessary to identify an effective thermal system. The presence of fluid flow and finite temperature gradients in the thermal system generates thermodynamic irreversibility, which is commonly known as entropy generation (EG). The local entropy production (S_l) is caused by irreversibilities in heat transfer (S_{tg}), fluid friction (S_v), and the magnetic force effect (S_m). These are represented by the first, second, and third terms of the following dimensional form, respectively (Tayebi and Chamkha, 2020; Manna et al. 2023).

$$S_{loc} = S_{tg} + S_v + S_m$$

$$= \overbrace{\frac{k}{T^2}\left[\left(\frac{\partial T}{\partial x}\right)^2 + \left(\frac{\partial T}{\partial y}\right)^2\right]}^{S_{tg}} + \overbrace{\frac{\mu}{T}\left[2\left(\frac{\partial u}{\partial x}\right)^2 + 2\left(\frac{\partial u}{\partial y}\right)^2 + \left(\frac{\partial u}{\partial y} + \frac{\partial v}{\partial x}\right)^2\right]}^{S_v}$$

$$+ \overbrace{\frac{\sigma B^2}{T}\left(u\sin\gamma - v\cos\gamma\right)^2}^{S_m} \tag{2.26}$$

By transforming it into its non-dimensional form (as NS_{tg}, NS_v, and NS_m, respectively) the dimensionless local entropy production rate (NS_l) is expressed are evaluated as

$$NS_l = S_l / (k_f / H^2) = NS_{tg} + NS_v + NS_m$$

$$= \overbrace{\frac{1}{(\theta + \theta_r)^2}\frac{k}{k_f}\left[\left(\frac{\partial\theta}{\partial X}\right)^2 + \left(\frac{\partial\theta}{\partial Y}\right)^2\right]}^{NS_{tg}}$$

$$+ \overbrace{\frac{Ec\,Pr}{(\theta + \theta_r)}\frac{\mu}{\mu_f}\left[2\left(\frac{\partial U}{\partial X}\right)^2 + 2\left(\frac{\partial V}{\partial Y}\right)^2 + \left(\frac{\partial U}{\partial Y} + \frac{\partial V}{\partial X}\right)^2\right]}^{NS_v} \tag{2.27}$$

$$+ \overbrace{\frac{Ec\,Pr\,Ha}{(\theta + \theta_r)}\frac{\sigma}{\sigma_f}(U\sin\gamma - V\cos\gamma)^2}^{NS_m}$$

where the Eckert number (Ec) and a reference temperature ratio parameter (θ_r) are calculated from the published article by Mukhopadhyay (2010).

$$Ec = \alpha_f^2 / H^2 C_{Pf}(T_h - T_c) = \sqrt[3]{(g\alpha_f\beta_f)^2 / (T_h - T_c)}\,Pr^{-2/3}\,Ra^{-2/3}$$
$$\theta_r = T_c / (T_h - T_c) \tag{2.28}$$

The global estimation of total entropy generation (*NS*), the integration of NS_l over the entire domain is performed as

$$NS = \iint NS_l dXdY \tag{2.29}$$

Furthermore, the efficacy of a specific geometry in comparison to the base case (square geometry) is evaluated employing the heat transfer and fluid-flow performance parameters represented by η and χ, respectively. It is defined as follows:

$$\eta = (Nu_{specific\ case} - Nu_{base\ case}) / Nu_{base\ case} \tag{2.30}$$

$$\chi = (\psi_{specific\ case} - \psi_{base\ case}) / \psi_{base\ case} \tag{2.31}$$

2.4 Numerical procedure

The conservation laws of fluid motion and heat transfer are governed by a system of nonlinear partial differential equations (PDEs). However, exact solutions for complex problems in the industry are often difficult to ascertain due to the irregularity or arbitrariness of geometries.
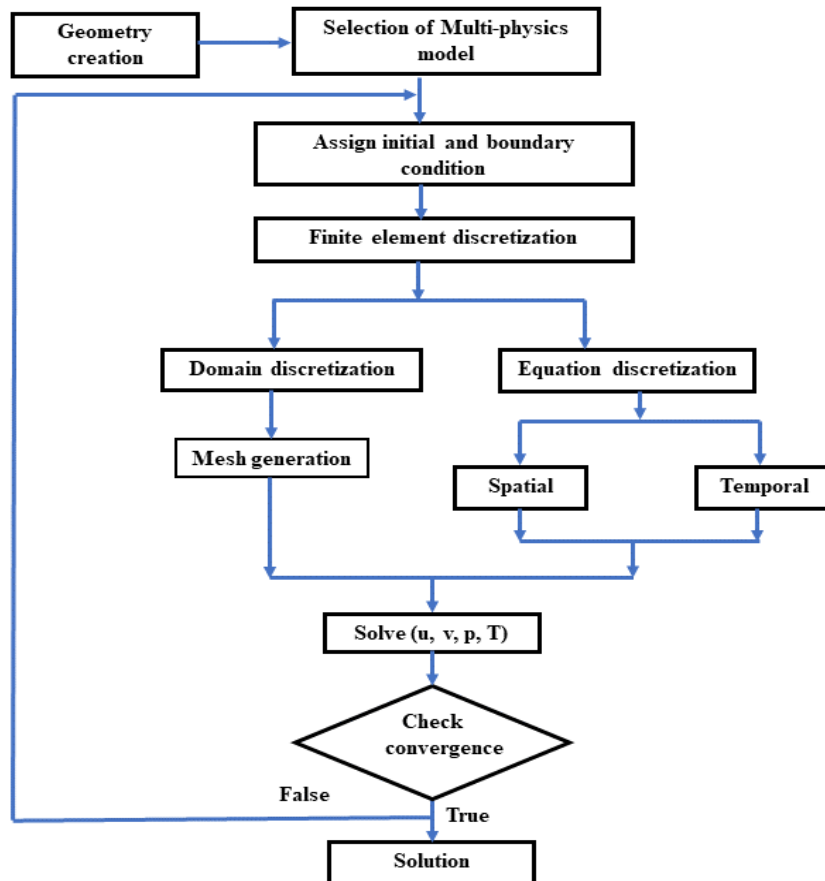
Figure 2.2 Flow chart of finite element method.

Therefore, numerical approaches such as the finite element method (FEM) can be used to derive approximate solutions. The FEM aids in computing solutions by

26

dividing the flow geometry into smaller interconnected sub-regions, which allows complex partial differential equations to be simplified into linear or nonlinear simultaneous equations. To apply the FEM, the mathematical equations (2.12)-(2.15) of the problem were numerically solved, invoking the Galerkin technique with specified weighted function for the considered mesh. The finite element analysis is carried out using commercial COMSOL Multiphysics software. The linear equations were then collected to form a matrix, and an iterative process was used to solve the evolved equations using the LU decomposition algorithm and the Newton-Raphson method. The term "residual" is used to check the convergence. The solutions were considered converged when the residuals were minimized less than 10^{-4}. The flow chart for the FEM approach is depicted in Figure 2.2.

2.5 Validation studies

The present numerical technique has been validated by solving published problems related to buoyancy-driven thermo-fluid flow with different flow geometries and boundary conditions. This was done to evaluate the reliability of the employed numerical techniques.

The current study compared its numerical technique with both the numerical solution of de Vahl Davis and Jones (1983) and the experimental results of Ho et al. (2010). The comparison was made for Ra values ranging from 10^3 to 10^6 at Pr = 0.71. Table 2.1 shows a comparison of the highest absolute velocities in the *X* and *Y* directions, the absolute value of the streamfunction, and the mean Nusselt number (Nu) between the current simulation and the benchmark numerical solution of de Vahl Davis and Jones (1983). The current results showed a strong agreement with the Nu and the streamfunction, with maximum deviations of nearly 1% and 0.5% respectively from the benchmark solution.

Table 2.1 Comparison of maximum velocities in the X and Y directions, streamfunction, and Nu for different Ra at Pr = 0.71 with benchmark solution of de Vahl Davis and Jones (1983).

Ra	de Vahl Davis and Jones (1983)				Present results			
	U_{max}	V_{max}	$\|\Psi\|_{max}$	Nu	U_{max}	V_{max}	$\|\Psi\|_{max}$	Nu
10^3	3.649	3.697	–	1.118	3.651	3.699	1.176	1.118
10^4	16.179	19.617	–	2.243	16.193	19.636	5.077	2.247
10^5	34.73	68.59	9.612	4.519	43.886	68.264	9.634	4.537
10^6	64.63	219.36	16.750	8.880	128.814	218.185	16.931	8.925

Additionally, the current study compared its results with the experimental published data of Ho et al. (2010) for pure water (Pr = 5.65) with temperature variations ranging from 2°C to 10°C, as shown in Figure 2.3. The current results were found to be in good agreement with the Nu values from the experimental data, with a maximum difference of less than 1%. Thus, both comparative analyses demonstrate that the current numerical technique is capable of accurately capturing flow features and heat transport of free convection in a square enclosure.
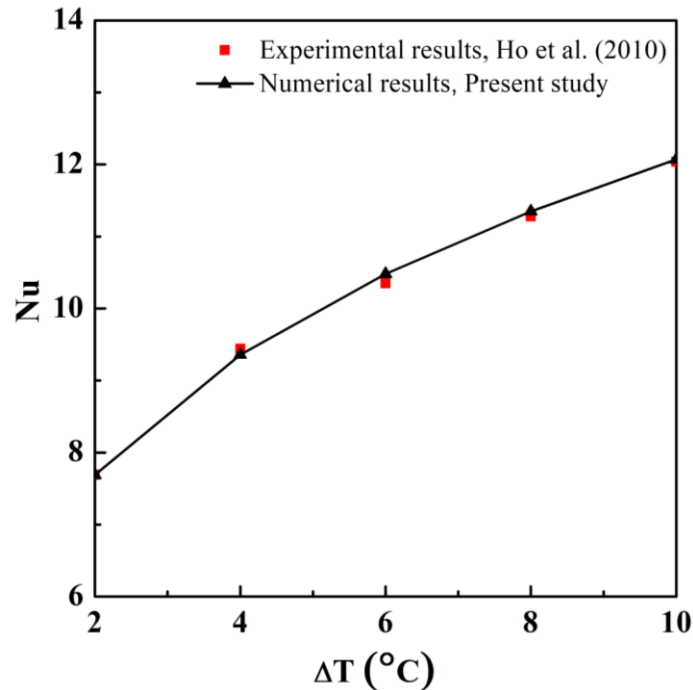
Figure 2.3 Comparison of Nu with experimental Nu of Ho et al. (2010) for pure water (Pr = 5.65).

The present numerical technique is also validated using the experimental work of Kuehn and Goldstein (1976) and the computational results of Yoo (1998) to validate buoyancy-driven convection in the cylindrical annulus. Figure 2.4 compares the local Nusselt number variations at the inner cylindrical surface (Nui) and outer cylindrical surfaces (Nuo) for Ra = 5×104 and L/Di = 0.8, where L = (Ro – Ri) represent the gap width, computed from the present numerical simulation, with the experimental benchmark results of Kuehn and Goldstein (1976). The highest discrepancy in the Nu value from the experimental data is less than 5%.

28
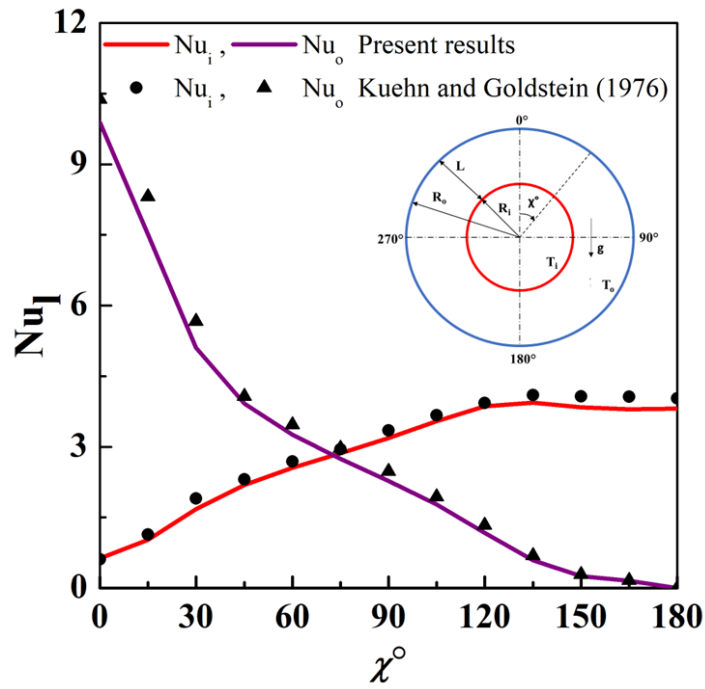
Figure 2.4 Assessment of Nu$_l$ with experimental work of Kuehn and Goldstein (1976).

The existing computational model's capability to numerically evaluate convective thermo-fluid flow in a circular annulus is demonstrated by comparing the variation of Nu computed from the present simulation with the numerical results of Yoo (1998) for different Ra in the range of 10^3 to 10^5 at Pr = 0.7 and $\varepsilon = 0.5$ in Figure 2.5. The maximum deviation of Nu of the inner cylinder is less than 1%.
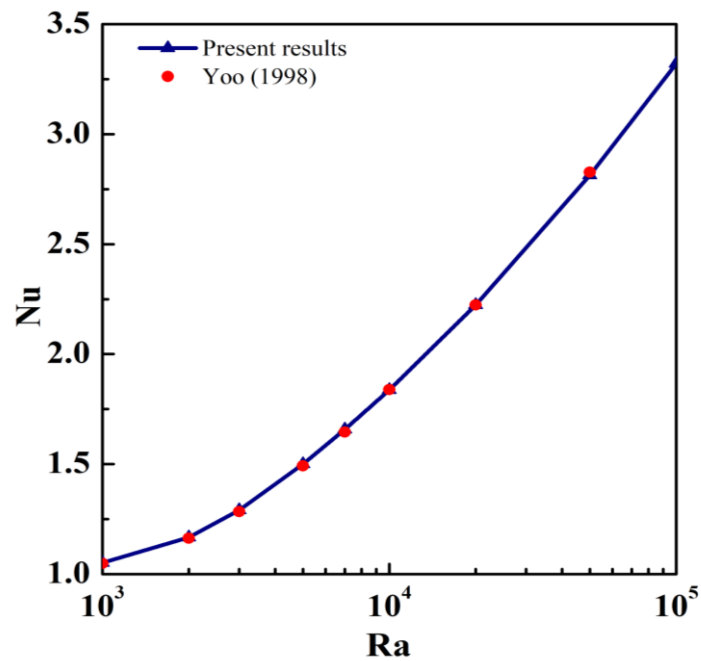
Figure 2.5 Comparison of Nu with Yoo (1998) for different Ra at Pr = 0.7.

The accuracy of the numerical methodology for simulating buoyancy-driven nanofluid-based flow in a square enclosure was also confirmed by comparing it with the numerical findings of Khanafer et al. (2003) and the experimental results of Hu et al. (2014) and Torki and Etesami (2019). In their numerical study, Khanafer et al. (2003) presented a correlation to estimate the mean Nusselt number (Nu) in a square enclosure containing a Cu/water nanofluid based on the Grashof number (Gr) and nanoparticle volume fraction (ζ). The present results were compared with the correlation developed by Khanafer et al. (2003) for varied Gr (=10^3, 10^4, and 10^5) and ζ (= 0, 0.01, 0.02, 0.03, 0.04, and 0.05) at Pr = 6.2. The current results showed strong agreement with a maximum discrepancy of less than 5% from the numerical benchmark study of Khanafer et al. (2003), as shown in Figure 2.6.
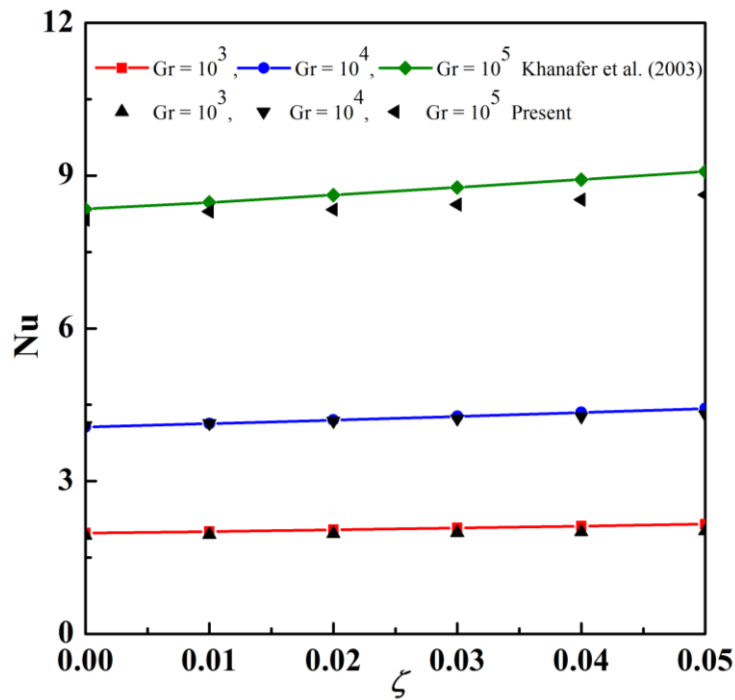
Figure 2.6 Comparison of Nu with Khanafer et al. (2003) for different Gr and ζ.

The present numerical result is validated against experimental studies conducted by Hu et al. (2014), and Torki and Etesami (2019). The comparison of current results with the experimental results of Hu et al. (2014) is presented in Table 2.2 for a square cavity filled with pure water (ζ = 0) and Al_2O_3/water nanofluid (ζ = 0.25). The maximum deviation of Nu obtained from the present simulation with experimental data is 17.27% and 16.19% for pure water and nanofluid, respectively, observed at higher Ra. This comparison shows that the present numerical methodology is within an acceptable limit.

Moreover, the current numerical approach is compared with the experimental results of Torki and Etesami (2019) as shown in Table 2.3 for a square enclosure filled with pure water ($\zeta = 0$) and SiO$_2$/water nanofluid ($\zeta = 0.01\%$). The maximum deviation of the present results from the experimental results is 7.29% and 2.8% for pure water and nanofluid, respectively. The comparison of the present results with the numerical and experimental data demonstrates that the current numerical approach can accurately predict heat transport in a buoyancy-driven flow in an enclosure.

Table 2.2 Comparison with Hu et al. (2014) for different Ra, and ζ.

Ra $\times 10^7$	Nu for pure water ($\zeta = 0$)			Ra $\times 10^7$	Nu for nanofluid ($\zeta = 0.25$)		
	Hu et al. (2014)	Present results	% Error		Hu et al. (2014)	Present results	% Error
2.48	19.041	22.204	14.25	3.09	20.555	23.612	12.95
3.63	20.757	24.587	15.58	4.02	21.962	25.324	13.27
4.56	22.009	26.126	15.76	4.81	22.908	26.579	13.81
5.53	23.052	27.504	16.19	5.73	23.553	27.839	15.40
6.28	23.539	28.454	17.27	6.41	24.037	28.682	16.19

Table 2.3 Comparison of Nu with Torki and Etesami (2019) for different Ra, and ζ.

Ra $\times 10^7$	Nu for Pure water ($\zeta = 0$)			Ra $\times 10^7$	Nu for Nanofluid ($\zeta = 0.01\%$)		
	Torki and Etesami (2019)	Present results	% Error		Torki and Etesami (2019)	Present results	% Error
0.95	16.503	14.994	0.06	0.93	16.784	14.895	-2.68
1.54	18.071	17.100	5.68	1.66	19.546	17.447	-2.04
1.77	18.814	17.769	5.88	1.98	20.577	18.312	-2.37
3.81	21.411	21.922	2.33	3.97	22.186	22.189	0.02
7.35	24.455	26.378	7.29	7.19	25.485	26.218	2.80

The current numerical model is compared to the published result of Ghasemi et al. (2011) to evaluate the reliability of numerical methodologies for predicting heat transfer for magnetohydrodynamic buoyancy-induced convection in enclosures. This study involves a square flow domain with side heating and cooling, filled with Al$_2$O$_3$/water nanofluid, and subjected to a horizontal magnetic field. The comparison is carried out for different Ra ($= 10^3, 10^4, 10^5,$ and 10^6), ζ ($= 0, 0.02,$ and 0.04) at Ha $= 30$, and the outcomes of Nu and ψ_{max}, computed from the present simulation, are compared with the numerical solution of Ghasemi et al. (2011). The results show good agreement with the Nu and ψ_{max} solution of Ghasemi et al. (2011), with

maximum deviations of less than 10.6% and 17.5%, respectively (Table 2.4 and Table 2.5). The comparison is further extended for varied Ha (= 0, 15, 45, and 60) and ζ (= 0, 0.02, and 0.04) at Ra = 10^5, and the comparison of Nu and ψ_{max} are presented in Tables 2.6 and 2.7, respectively. The present result shows nice agreement with the Nu and ψ_{max} solution of Ghasemi et al. (2011), with maximum deviations of less than 7.3% and 13.5%, respectively. These comparison studies demonstrate that the present numerical technique can predict magnetohydrodynamic buoyancy-driven flow and heat transfer in an enclosure.

Table 2.4 Comparison of Nu with Ghasemi et al. (2011) for distinct Ra at Ha = 30.

Ra	Ghasemi et al. (2011)			Present results		
	$\zeta = 0$	$\zeta = 0.02$	$\zeta = 0.04$	$\zeta = 0$	$\zeta = 0.02$	$\zeta = 0.04$
10^3	1.002	1.060	1.121	1.002	1.002	1.002
10^4	1.183	1.212	1.249	1.182	1.163	1.147
10^5	3.150	3.138	3.124	3.138	3.032	2.930
10^6	7.907	7.979	8.042	7.812	7.548	7.292

Table 2.5 Comparison of ψ_{max} with Ghasemi et al. (2011) for different Ra, ζ at Ha = 30.

Ra	Ghasemi et al. (2011)			Present results		
	$\zeta = 0$	$\zeta = 0.02$	$\zeta = 0.04$	$\zeta = 0$	$\zeta = 0.02$	$\zeta = 0.04$
10^3	0.128	0.119	0.11	0.127	0.128	0.129
10^4	1.193	1.123	1.057	1.191	1.207	1.221
10^5	5.71	5.682	5.642	5.693	5.878	6.062
10^6	14.088	14.293	14.495	13.939	14.430	14.928

Table 2.6 Comparison of Nu with Ghasemi et al. (2011) for different Ha, ζ at Ra = 10^5.

Ha	Ghasemi et al. (2011)			Present simulation		
	$\zeta = 0$	$\zeta = 0.02$	$\zeta = 0.04$	$\zeta = 0$	$\zeta = 0.02$	$\zeta = 0.04$
0	4.738	4.820	4.896	4.720	4.803	4.880
15	4.143	4.179	4.211	4.127	4.209	4.287
45	2.369	2.342	2.317	2.361	2.419	2.478
60	1.851	1.831	1.815	1.845	1.896	1.948

Table 2.7 Comparison of ψ_{max} with Ghasemi et al. (2011) for different Ha, ζ at Ra = 10^5.

Ha	Ghasemi et al. (2011)			Present simulation		
	$\zeta = 0$	$\zeta = 0.02$	$\zeta = 0.04$	$\zeta = 0$	$\zeta = 0.02$	$\zeta = 0.04$
0	11.053	11.313	11.561	11.014	11.275	11.522
15	8.484	8.615	8.734	8.457	8.733	9.005
45	3.825	3.729	3.629	3.813	3.922	4.031
60	2.518	2.518	2.415	2.614	2.677	2.740

The present study aims to evaluate the accuracy of the entropy generation (EG) employed to obtain irreversibility in the flow domain. The results of EG are presented in a non-dimensional form and compared with the numerical outcomes of Ilis et al. (2008) and Oliveski et al. (2009). Ilis et al. (2008) computed EG in a square enclosure for different Ra values (10^3, 10^5) with a fixed value of irreversibility distribution parameter ($\Phi = 10^{-4}$). The comparison of EG results with Ilis et al. (2008) is presented in Table 2.8. The highest value of EG owing to heat transfer, fluid friction, and overall entropy production computed from the present simulation is compared with the numerical published results of Ilis et al. (2008). The current EG results show good agreement with those of Ilis et al. (2008), with maximum deviations of less than 0.6%, 6.3%, and 6.1% for the maximum value of the rate of EG owing to heat transfer (NS_{tg}), fluid friction (NS_v), and total entropy production (NS), respectively.

Table 2.8 Comparison of EG with Ilis et al. (2008) for different Ra at Φ (= 10^{-4}).

Ra	Ilis et al. (2008)			Present study		
	max(NS_{tg})	max(NS_v)	max(NS)	max(NS_{tg})	max(NS_v)	max(NS)
10^3	2.27	0.25	2.29	2.272	0.251	2.291
10^5	61.03	563.20	597.11	60.658	598.775	633.278

The current EG results are further validated against the results of Oliveski et al. (2009), as shown in Table 2.9. Results are compared in a square enclosure for a wide range of Ra values (10^3–10^7) at various Φ (= 10^{-2}, 10^{-4}). The current results match well with Oliveski et al. (2009), with a maximum error of less than 5%. Both comparisons clearly illustrate that the existing numerical methodology can accurately estimate EG in a buoyancy-driven flow in an enclosure.

Table 2.9 Comparison of EG with Oliveski et al. (2009) results for various Ra and Φ.

Ra	NS at $\Phi = 10^{-2}$			NS at $\Phi = 10^{-4}$		
	Oliveski et al. (2009)	Present study	% Error	Oliveski et al. (2009)	Present study	% Error
10^3	4.602	4.579	0.49	1.182	1.153	2.48
10^4	108.071	106.052	1.87	3.308	3.285	0.69
10^5	2063.512	1922.829	6.82	24.607	23.720	3.61
10^6	37413.970	36583.440	2.22	395.064	376.200	4.77
10^7	714386.200	694785.300	2.74	7436.892	7065.809	4.99

The validity of the heatline solution used to visualize and investigate 2-D convective heat flow, is assessed in this study. Heatlines generated from the current solution are compared to the benchmark article published by Kimura and Bejan (1983), which is shown in Table 2.10. The comparison is performed in a square enclosure, and the maximum value of the heat function (Π_{max}) is evaluated for distinct Ra values of 140 and 1.4×10^5 at Pr = 7. The maximum variation of Π_{max} obtained from the current solution from Kimura and Bejan's (1983) pioneering work is 5.87%. This comparison analysis demonstrates that the present numerical technique can accurately capture heatlines solutions for buoyancy-driven flow.

Table 2.10 Comparison of Π_{max} with benchmark result of Kimura and Bejan (1983) at Pr = 7.

Ra	Π_{max} for different Ra at Pr = 7		
	Kimura and Bejan (1983)	Present solution	% Error
140	1.004	1.003	0.11
140000	5.548	5.223	5.87

Additionally, the solution technique has been compared to experimental results obtained from a PIV (Particle Image Velocimetry) experiment involving a fluid-filled enclosure with a bottom-protruded heater. The experimental results were successfully reproduced by the solution technique, as reported by Biswas et al. (2016a), which demonstrates a good match. Furthermore, the solution technique has been repeatedly verified in solving various types of thermal-fluid coupled problems, including natural convection (Biswas et al. 2020b), forced convection (Biswas et al. 2012), mixed convection (Biswas et al. 2015a; 2015b; 2017), thermomagnetic

convection (Manna and Biswas 2018; Biswas et al. 2021a; 2021b; Biswas et al. 2022), and bioconvection (Biswas et al. 2020b; Biswas et al. 2022; Biswas et al. 2023). The corresponding validation results are reported elsewhere, confirming the reliability of the present numerical technique.

2.6 Grid independence test

The grid independence test was conducted to ensure that the numerical simulations were not significantly affected by the mesh size. This test is crucial to ensure the accuracy and reliability of the simulations. Mesh generation in two-dimensional problems was executed using the Finite Element Method (FEM) in COMSOL Multiphysics software, and the mesh structures for various geometries are shown in Appendix (Figure A). The details of the mesh studies are indicated in Appendix (Table A). These results provide information about the mesh size, average Nusselt number (Nu), and minimum stream function (ψ_{min}) for different meshes and geometries. This rigorous grid independence testing ensures the reliability of the numerical simulations conducted in the study.

2.7 Conclusions

A series of comparative analyses of buoyancy-induced convection in different geometrical configurations using a range of fluids (such as air, water, nanofluid), and magnetic field are demonstrated above in this chapter. It includes both the experimental and numerical solutions reported by different authors, and overall, a good agreement was found during these validation studies. It encourages conducting new simulations for buoyancy-driven convection in various geometrical shapes, fluids, and boundary conditions, by applying a novel constraints-based (volume and length) approach. These studies are discussed in subsequent chapters, omitting the mathematical formulation and numerical procedural parts for individual problems, to avoid repetition.

Chapter – 3

Geometrical constraint-based performance analyses of equivalent square and circular thermal systems using air, water, and CuO-water nanofluid

3.1 Introduction

In modern times, enclosure or cavity-shaped thermal systems are widely used in various applications. As the demand for energy-efficient miniature devices continues to grow, the study of passive cooling systems operated by natural convection has reached its limit. The geometry, boundary conditions, and multi-physical processing parameters significantly affect the heat transport physics in a thermal system. Consequently, a vast amount of published works exists on the broad area of buoyancy-driven flow, as detailed in Chapter 1 and shown in Figure 1.1. However, there is a shortage of research works on constraint-based thermal analysis. Geometrical parameters such as the volume of the system or the length of the active heating or cooling surface can be utilized as constraints to analyze different shapes of the system cavities. In this chapter, as a first attempt, a novel constraint-based approach is applied to analyze two popular classical geometrical shapes, square and circular cavities, under similar heating configurations.

3.2 Background earlier works

The impact of geometrical shape on the thermal performance of a system cannot be overstated, especially in light of the demands of emerging energy technologies. To address adequately this issue, a sufficient volume of fundamental research on geometrical shapes is necessary. Despite the vast pool of research works available in the open literature on convective thermal systems, none of them have critically addressed the issue of geometrical shape. The development of energy-efficient thermal devices has been an ongoing effort over the last few decades, driving many published works in the area of passive cooling applications using buoyancy-driven flow (Banerjee et al. 2008; El Omari et al. 2011; Faraji et al. 2020). Energy efficiency, heat transfer augmentation, or the average Nusselt number (Nu) is sought after in these kinds of thermal systems and applications. The utilization of system

geometries with in-built heater and cooler layouts is common in various applications, including solar collectors, electronic cooling, food processing, and drying technologies (Henderson et al. 2007; Rahimi et al. 2018; Hussien et al. 2021). The buoyancy-driven convective processes are sensitive to the geometrical shape (of enclosure/cavity) and heater-cooler layout. Previous studies have focused on understanding thermal behaviors under various parametric influences (Ra, Gr, Pr, Re, Ri, Ha, etc.) for a single geometrical shape. Despite numerous reports on various cavity shapes, including regular (such as square, circular, trapezoidal, etc.) and irregular (such as C-shaped, H-shaped, etc.) geometries, no comparison with any classical shape has been provided in the literature. As a result, it is challenging to understand the benefits or drawbacks of modified or uncommon cavity shapes. In light of this gap in the literature, the present study is designed to explore buoyancy-driven systems' thermal behaviors using a novel constraint-based approach. Therefore, to provide a comprehensive background, some typical buoyancy-driven studies that are closely related to the present work are discussed further.

The area of buoyancy-involved phenomena has seen a significant increase in research volume, with relatively few pioneering works laying the mathematical and conceptual foundation stones (Dropkin and Somerscales 1965; Kuehn and Goldstein 1976; ElSherbiny et al. 1982; Ostrach 1988; Incropera 1988). Recent studies focus on more sophisticated/complex phenomena, such as those involving nanofluids (Biswas et al. 2018; Dutta et al. 2019; Chatterjee et al. 2022), hybrid nanofluids (Suresh et al. 2012; Manna et al. 2021; Biswas et al. 2021a; 2022a), magnetic fields (Dogonchi et al. 2018; Ghalambaz et al. 2019; Biswas et al. 2020a; Ghalambaz et al. 2020; Manna and Biswas 2021; Hamzah et al. 2021), porous medium (Bejan et al. 2004; Biswas and Manna 2017a; Biswas et al. 2016; 2021a), microorganisms (Biswas et al. 2020b; 2021b; 2021c), complex geometries (Yao 2006; Hussain and Öztop 2021), embedded obstructions (Sahoo et al. 1993; Mallick et al. 2021), and others. Convective heat transport has been visualized and analyzed using the heatline approach by several researchers (Biswas and Manna 2017b; Das and Basak 2017; Mahapatra et al. 2018; Lukose and Basak 2019).

In addition to these studies, numerous review articles are available that provide a wealth of knowledge in this field (Tian and Zhao 2013; Sarkar et al. 2015; Kabeel et al. 2015; Das et al. 2017; Giwa et al. 2021). Karki et al. (2022) studied buoyant convection in a rectangular cavity heated at the bottom and cooled at the top,

considering practical fluids (like nanofluid, air, or water). Gokulavani et al. (2020) investigated the impacts of centrally located heated baffle orientation in an alternatively designed ventilation enclosure. Recently, Gokulavani et al. (2022) demonstrated thermal convection in a hybrid nanofluid flowing porous open cavity using injection/suction. These studies are crucial for understanding different shades of flow behaviors and thermal characteristics. These investigations also contribute to the design and operation of various thermal systems and devices and justify the need for further exploration and development in buoyancy-based convection for future technical potentialities.

This work focuses on the effect of geometrical shapes, specifically targeting square and circular cavities. The differentially heated cavity (DHC), which is a recognized benchmark classical problem (de Vahl Davis and Jones, 1983), has been widely used for the validation of numerical works. This DHC has square geometry, a left wall that is hot, a right wall that is cold, and the other walls that are adiabatic. Various studies have investigated the heat transfer characteristics of DHC under different physical conditions such as magnetic fields, porous medium, nanofluids, non-Newtonian fluids, and heat generation. However, there are relatively few studies that have addressed the thermal performance of perfectly circular geometries, and none of these studies have considered differentially heated configurations similar to the DHC. Consequently, the findings of the existing studies are scattered and challenging to assimilate, making it difficult to select optimal geometrical shapes for the design and operation of buoyancy-driven systems. Therefore, this study aims to compare the thermal behaviors of the DHC with a perfectly circular cavity under the constraint-based analysis approach.

A significant volume of studies on natural convection has been conducted and individual studies on square and circular cavities have been examined. However, a comparison of thermal efficacy between the two shapes has not been made, and the degree of difference in thermal characteristics has not been evaluated. Furthermore, it is not known which system would be more effective if the orientation changes. This research study utilizes a novel constraint-based analysis to compare the thermal performance of a square cavity and a circular cavity. The analysis considers identical areas and heating/cooling lengths to understand the impact of geometrical shapes on thermo-fluid phenomena. The study's findings hold significance in designing practical thermal systems that operate on air, water, and nanofluids, especially while

considering the relocated heat sources and heat sinks during inclined cavity positions. The results of this fundamental study can assist in designing single and multi-physical thermal systems for various applications. Additionally, this new approach to analysis could offer a new research direction for the optimal design of thermal systems and heater-cooler arrangements.

3.3 Problem formulation

Figure 3.1 illustrates the thermal systems corresponding to the square and circular geometries. The evolution of the equivalent circular configuration from the square geometry is also shown in the figure. The classical problem of the differentially heated cavity (DHC) in the square geometry is depicted in Figure 3.1a, while its equivalent circular cavity is presented in Figure 3.1b. These geometries can be referred to as CDHSC (Classical Differentially Heated Square Cavity) and EDHCC (Equivalent Differentially Heated Circular Cavity). The mesh structures for the CDHSC and EDHCC geometries are shown in Figures A1 (a) and (b), respectively, in the Appendix. The mesh details, provided in Appendix, are summarized in Tables A1 (a) and (b). The constraints for the equivalency of the two geometries are as follows: (i) same volumes or cross-sectional areas ($A_{sq} = A_{cir} = A$), (ii) equal heating and cooling lengths ($L_h = L_c = H$), and (iii) the heater and cooler located at identical positions. Based on these constraints, the circular cavity is similar to the square cavity in all aspects except its geometrical shape. The primary objective of this investigation is to analyze the effects of the geometrical shape on the thermal performance and fluid flow induced by thermal gradient based buoyancy flow. The results of this study can provide significant insights to thermal system analysts and designers.
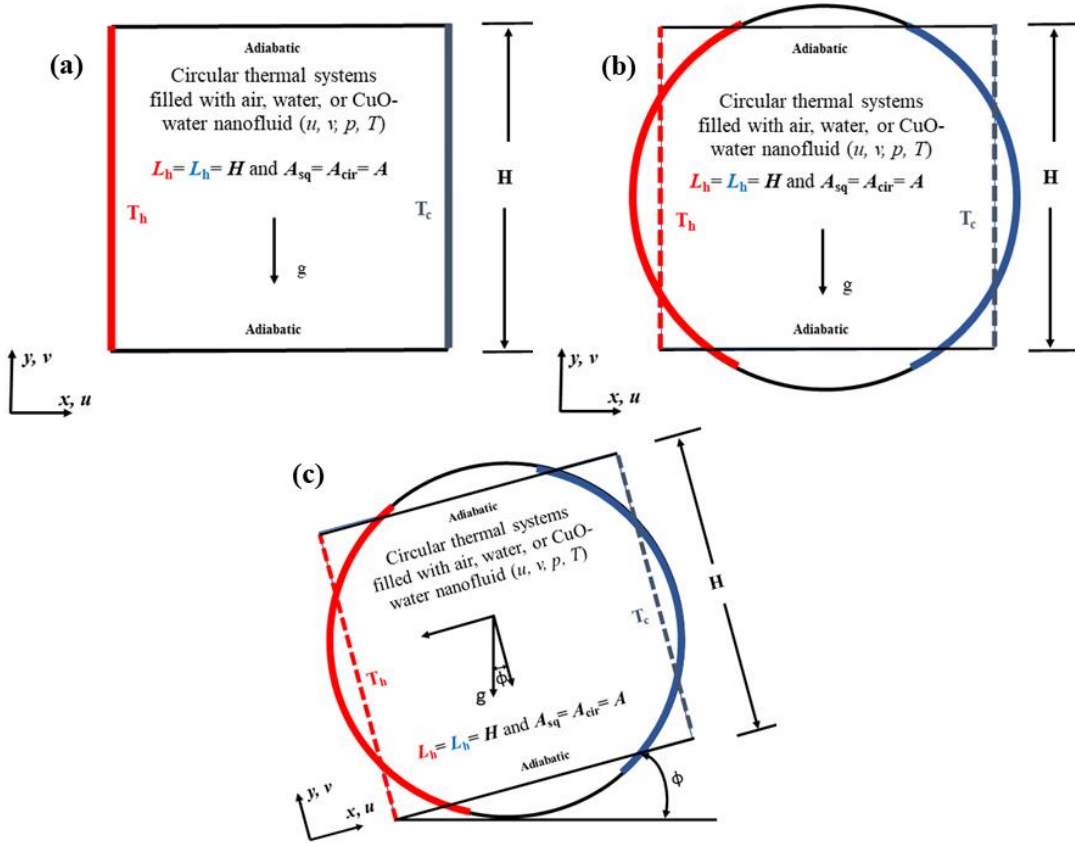
Figure 3.1 Constraint-based problem definition: (a) square shape (CDHSC), (b) circular shape (EDHCC), and (c) their tilted arrangements.

The non-isothermal fluid flow in these systems is modeled and solved mathematically by using a CuO-water nanofluid with fine nanoparticles (~1−5 μm) at a diluted concentration ($\zeta = 0$−3%) to ensure a single-phase homogeneous flow model and prevent agglomeration and sedimentation. The study is conducted under steady flow conditions at 300 K, and the Ra (10^6) within the laminar regime is used with the Boussinesq approximation. To account for cavity inclination scenarios, the momentum balance equations are utilized, decomposing the gravity-involved buoyancy term into the sine and cosine components expressed in Eqs. (2.13) and (2.14). The cavities are analyzed in an upright posture, while the direction of the buoyancy force (or gravity) is rotated for different values of ϕ. This is a nonlinear, velocity-coupled temperature problem, with the thermal conductivity and specific heat of CuO nanoparticles adopted from the literature (Mliki et al. 2017; Sheikholeslami et al. 2014). The details of mathematical formulation, numerical treatment, and validation studies are discussed comprehensively in Chapter 2. For CDHSC and

EDHCC, the system performance parameters in this thermal design analysis are the Nusselt number (Nu) and the minimum/maximum stream function (ψ).

3.4 Results and Discussion

In this study, the thermal performance of square and circular systems is analyzed under constraint-based conditions using three different fluids for various parameters. The range of parameters includes $\phi = 0–85°$, $Ra = 10^3–10^6$, and Pr values of 0.71 (air) and 5.83 (water and nanofluid). The results are presented systematically in separate subsections for easy comprehension.

3.4.1 *Ra impacts on flow features*

Figures 3.2−3.4 illustrate the impact of Rayleigh number (Ra) on anisothermal fluid flow in buoyant square and circular enclosures for air, water, and CuO-water nanofluid-based systems. These plots show the effect of cavity shape on flow structures at Ra values ranging from 10^4 to 10^6. The arrowhead lines in Figure 3.2 depict the direction of fluid circulation in corresponding streamlines, while the contours are normalized using the maximum $|\psi|$ magnitude that measures the flow strength. The normalized ψ ranges from 0−1, with values of 0 at all the walls and -1 or 1 at the core of the circulation. The study results indicate a clockwise single circulation in both of the thermal cavities, with increasingly congested streamlines around the active walls as Ra values increase. This congestion indicates high convective flow over the walls and the formation of a thinner velocity boundary layer, resulting in the horizontal stretching of streamlines in the core zones, which is particularly notable at $Ra = 10^6$. At high Ra values, the impact of cavity shape becomes more evident, underscoring the importance of considering geometric shapes when studying these systems.
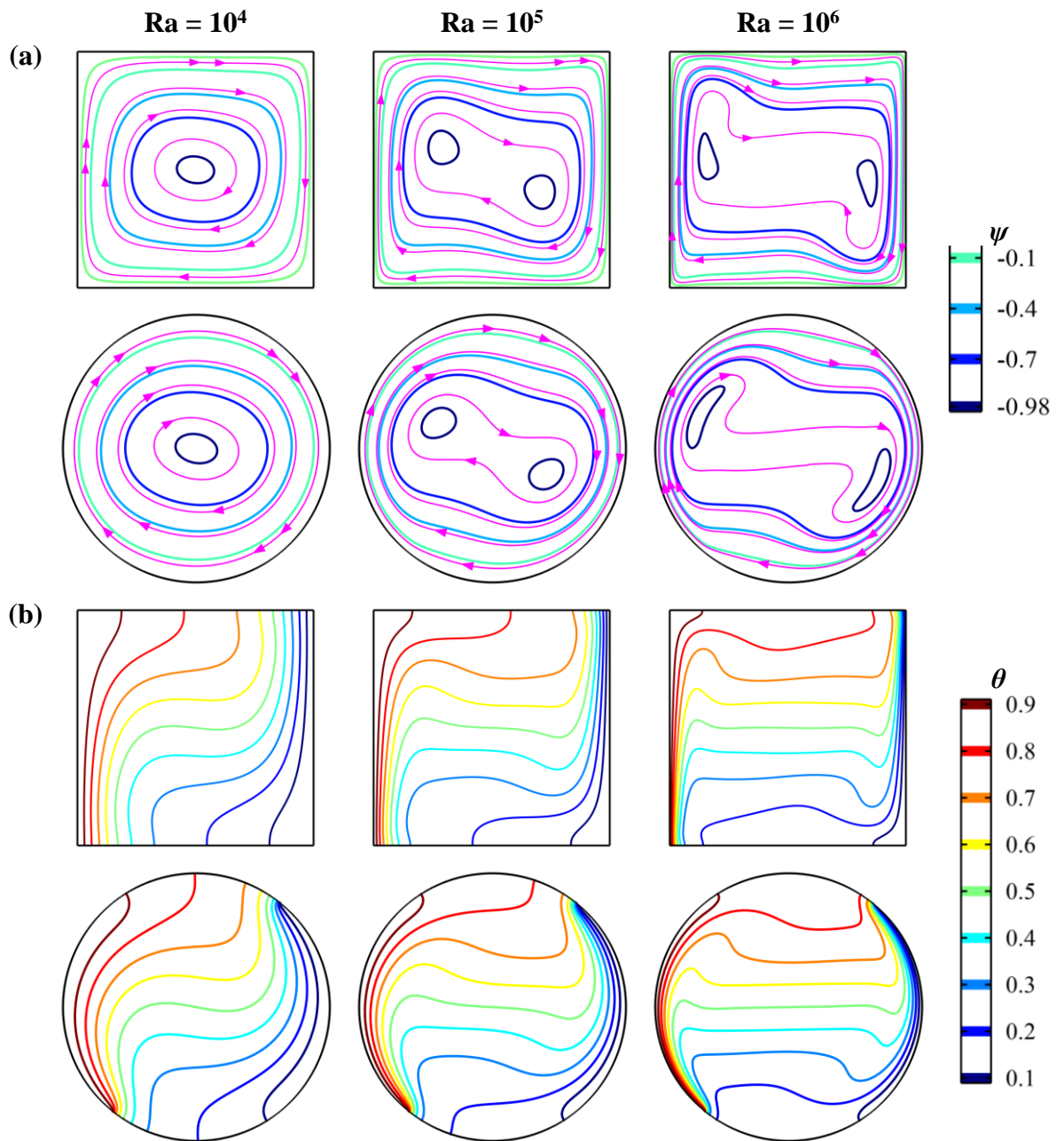
Figure 3.2 Effects of Ra on air-based thermal systems' streamlines (a) and isotherms (b)
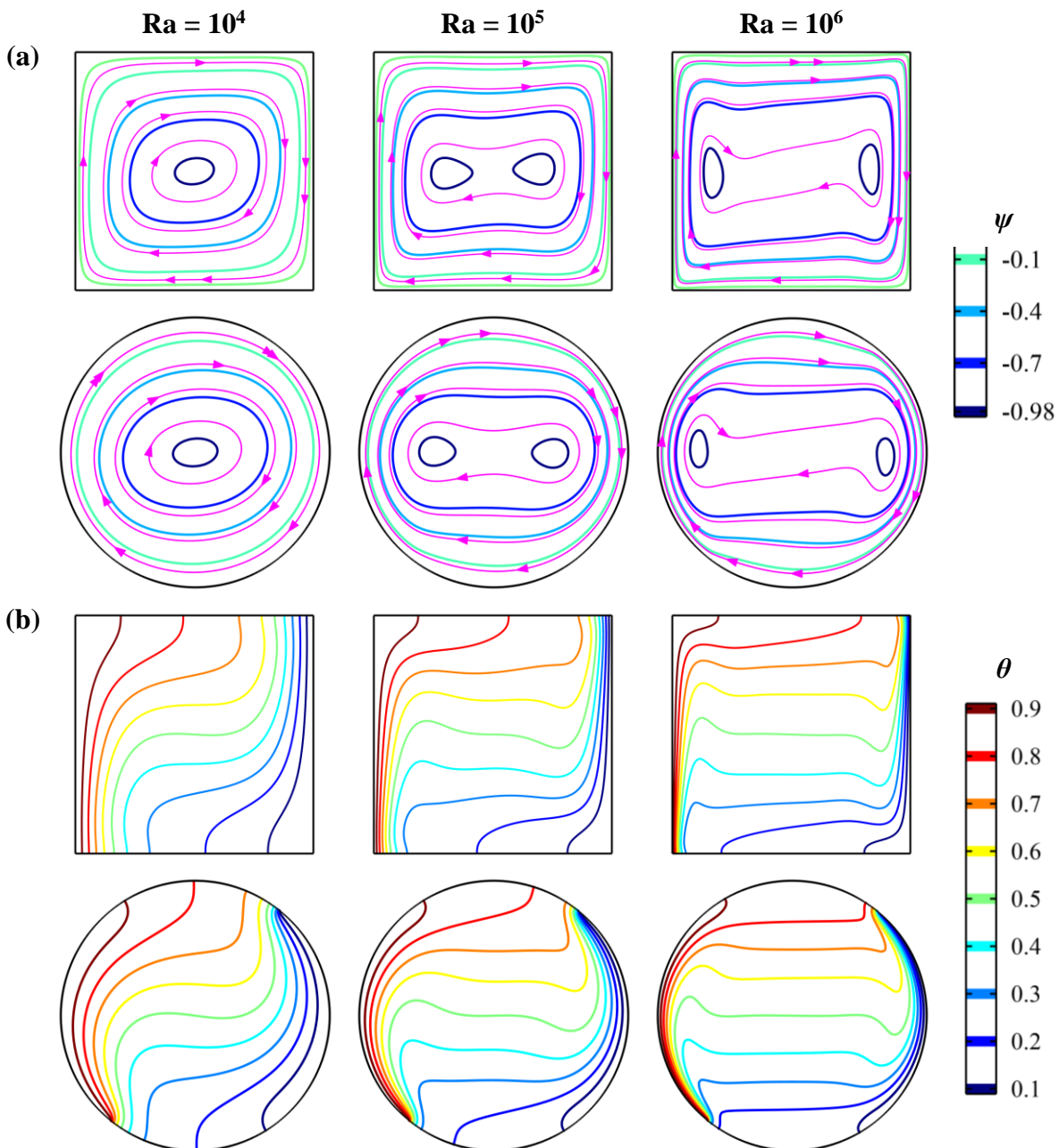
Figure 3.3 Effects of Ra on water-based thermal systems' streamlines (a) and isotherms (b).

The study highlights the role of established circulations in dictating static temperature distributions. The isotherms in Figure 3.2b reveal that as Ra increases, the lines become less vertical and take on a long horizontal stretch in the middle. When only thermal conduction governs the thermofluid flow at lower Ra values, perfectly active-wall parallel isotherms emerge. Additionally, the study emphasizes the impact of cavity shape on static temperature distributions, with the isotherm lines orienting differently in the two cavities. At Ra = 10^4, the isotherm lines are more

vertical or S-shaped, while at Ra = 10^5 and 10^6, they take on a long-horizontal middle stretch.
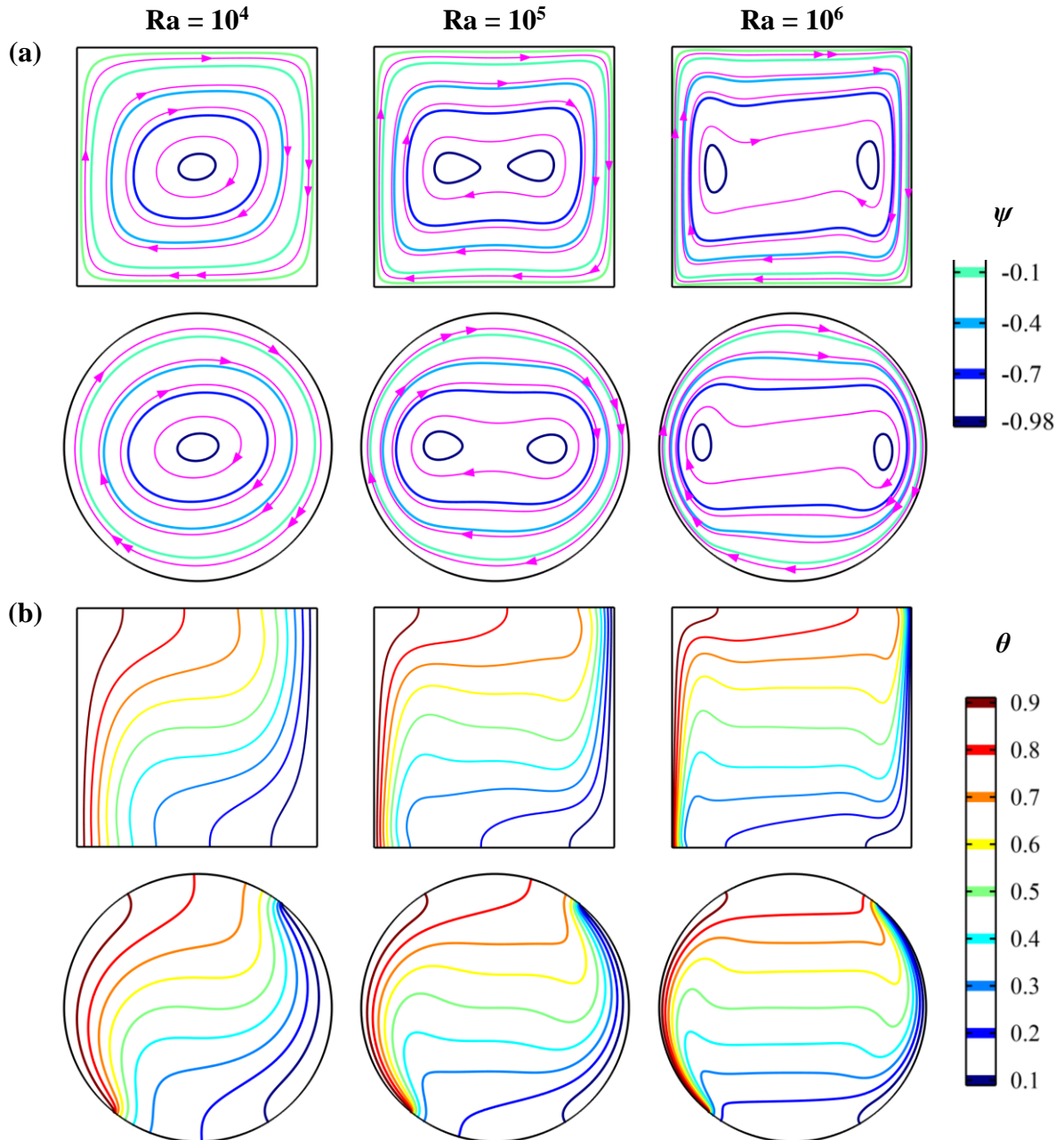
Figure 3.4 Effects of Ra at ζ = 3% on CuO/water-based thermal systems' streamlines (a) and isotherms (b).

The streamlines and isotherms maintain their features when the operating fluid is something other than air, although their sizes and shapes are adjusted accordingly. The innermost horizontal core appears to rotate in the clockwise (CW) direction, a phenomenon observed in both water-based systems (Figure 3.3) and nanofluid-based systems (Figure 3.4).

3.4.2 *Effects of cavity orientation (ϕ)*

In this study, the effect of cavity inclination on thermofluid flow features in thermally equivalent different shaped cavities has been investigated using both air and CuO-water nanofluid-based systems. The study has focused on understanding the impact of varying Ra and ϕ on fluid circulation and local static temperature distribution.

Figures 3.5–3.12 illustrate the effects of cavity inclination on the evolved thermofluid features flow in CDHSC and EDHCC at different Ra ranging from 10^4–10^6, using streamlines and isotherms for air and CuO-water nanofluid-based systems. The row- and column-wise variation of Ra and ϕ (= 25-85°) is depicted in the figures. At lower Ra values, the fluid circulation exhibits a single clockwise circulation similar to that of the upright cavity, as seen in Figure 3.5. However, at ϕ = 25°, as the thermal gradient increases with increasing Ra, the strength of fluid circulation increases markedly, and the circulating cell is stretched diagonally at Ra = 10^5, followed by the separation of the inner circulations cell at Ra = 10^6, resulting in the formation of one pair of inner circulations cells positioned diagonally. A similar trend of circulation patterns and increasing circulation strength is observed for ϕ = 45°, while a marked change in the circulation patterns is observed at ϕ = 70°, revealing a single clockwise circulation irrespective of any Ra values, and the circulation strength jumps into a double value ($|\Psi_{min}|$ = 73.631) at Ra = 10^6. However, there are no significant changes in the circulation pattern at ϕ = 85°, except for the formation of minor two corner circulation cells at Ra = 10^6. A similar pattern of fluid circulation is observed for the EDHCC case in Figure 3.6, where the circulation strength becomes maximum ($|\Psi_{min}|$ = 94.779) at ϕ = 85° and Ra = 10^6, corresponding to the higher convective flow.

The local temperature patterns in Figures 3.7 and 3.8 are also found to be affected by the cavity inclination and Ra values. The isotherms are parallel to the heating and cooling walls however markedly distorted for the rest portions, particularly at higher Ra, as the thermal gradient increases. The congested isotherms over the active sidewalls indicate a thinner thickness of the thermal boundary layer along with higher heat transfer. The isotherms change significantly with ϕ, following the fluid circulation patterns. At higher Ra and ϕ = 70°, the circular-shaped isotherms

evolve. The isotherm portrait is more complicated for the EDHCC case with the curved wall.
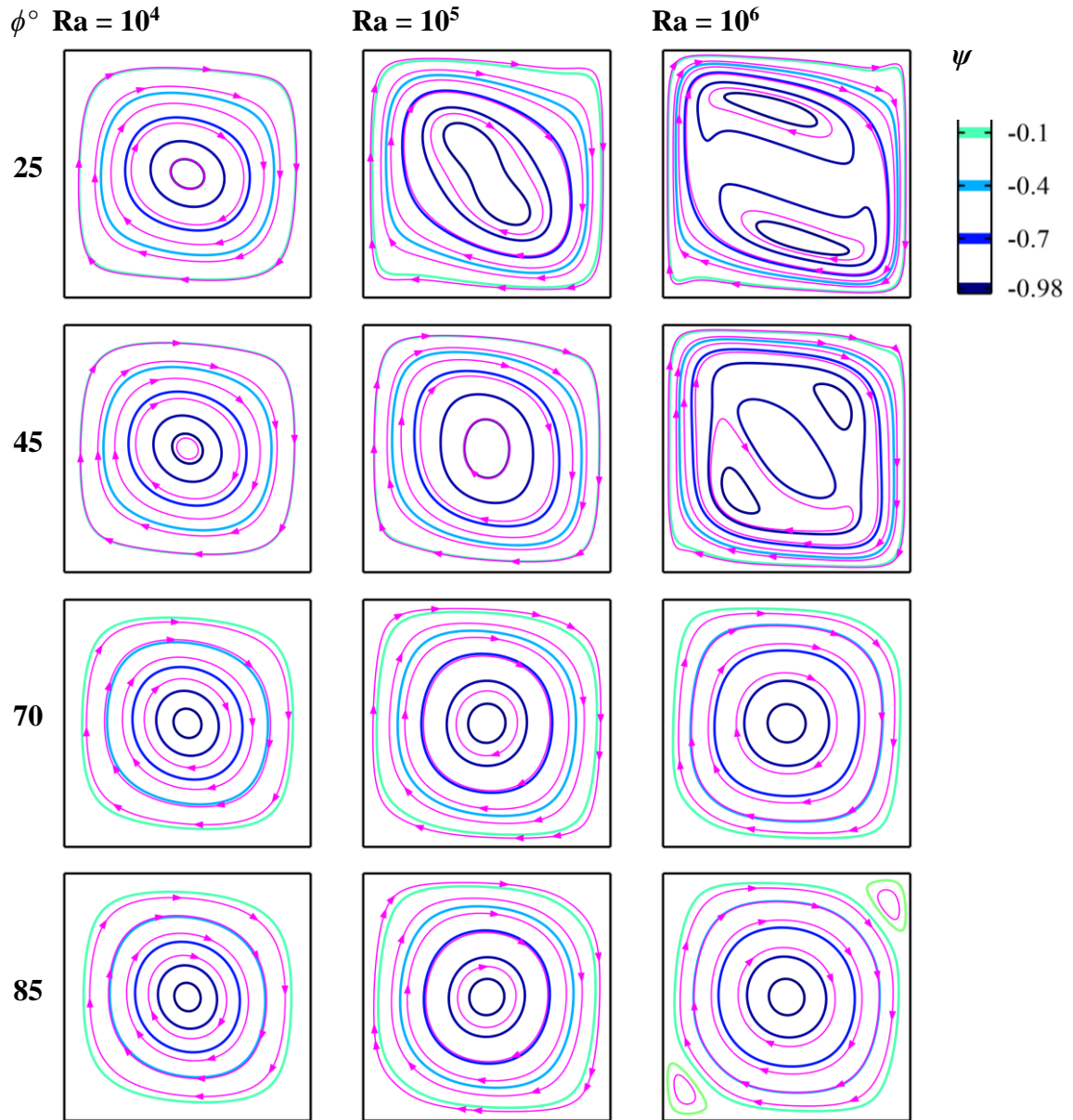
Figure 3.5 Cavity inclination impact on streamlines of the air-based thermal square system.

The findings of this study reveal interesting and novel insights into the thermofluid flow features with varying cavity inclination angles and Ra values. The results may have potential applications in various industrial processes that involve heat transfer and fluid flow in inclined cavities with a discrete heating-cooling arrangement.
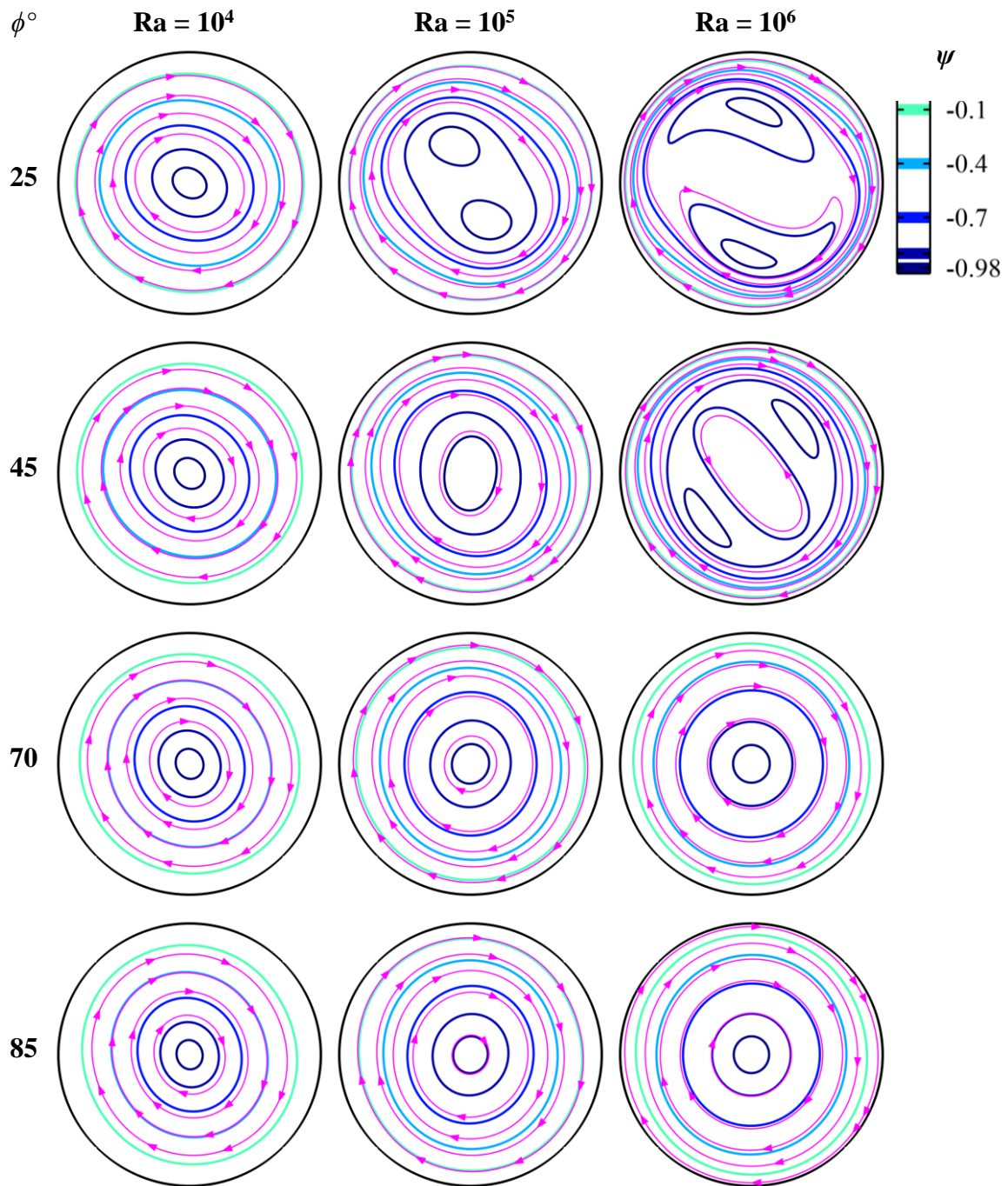
Figure 3.6 Cavity inclination impact on streamlines of air-based thermal circular systems.
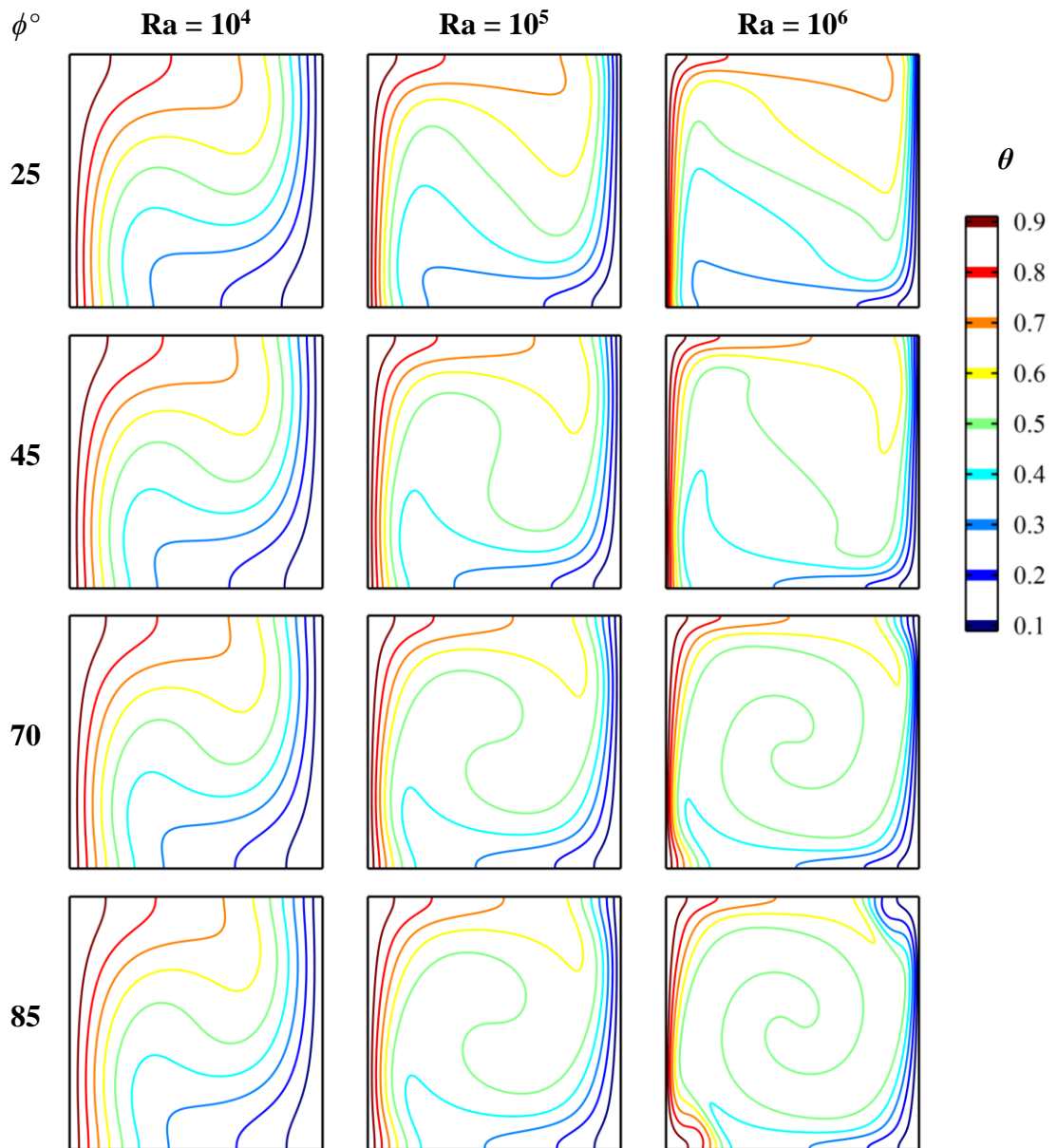
Figure 3.7 Cavity inclination impact on isotherms of air-based thermal square systems.
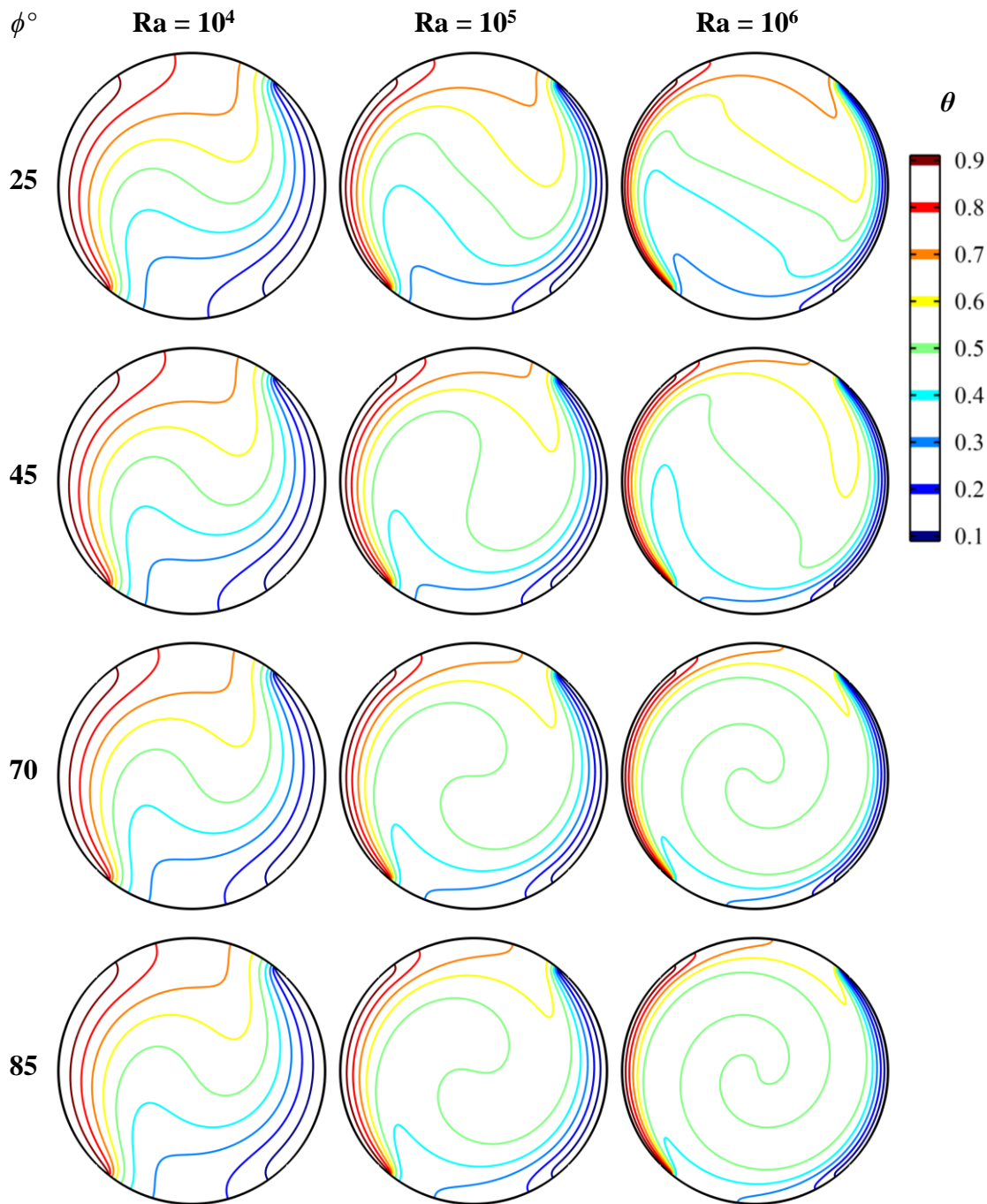
Figure 3.8 Cavity inclination impact on isotherms of air-based thermal circular systems.

Figures 3.9 to 3.12 present the cavity orientation effects on the thermal-flow features in CDHSC and EDHCC operating on CuO/water-based nanofluid with a 3% volume fraction. Here, Rayleigh numbers (Ra) range from 10^4 to 10^6 and inclination angles (ϕ) change from 25° to 85°. At $\phi = 25°$, with augmenting Ra, the fluid circulation in CDHSC is observed to stretch diagonally, accompanied by two tiny circulation cells and clockwise circulation. At higher inclination angles ($\phi = 45°$ to

85°), the circulation patterns change significantly, with a transition from diagonally stretched to circular circulation at Ra = 10^5. Interestingly, at Ra = 10^6, the twisted circulating cell changes from left to right inclination as the angle increases to $\phi = 85°$, with a maximum stream function value of 54.019. In EDHCC, the circulation patterns show similar patterns as in CDHSC, except for the curvature effect on the surroundings, with a maximum stream function value of 52.193 at Ra = 10^6 and $\phi = 85°$. The temperature distribution changes following the circulation patterns.
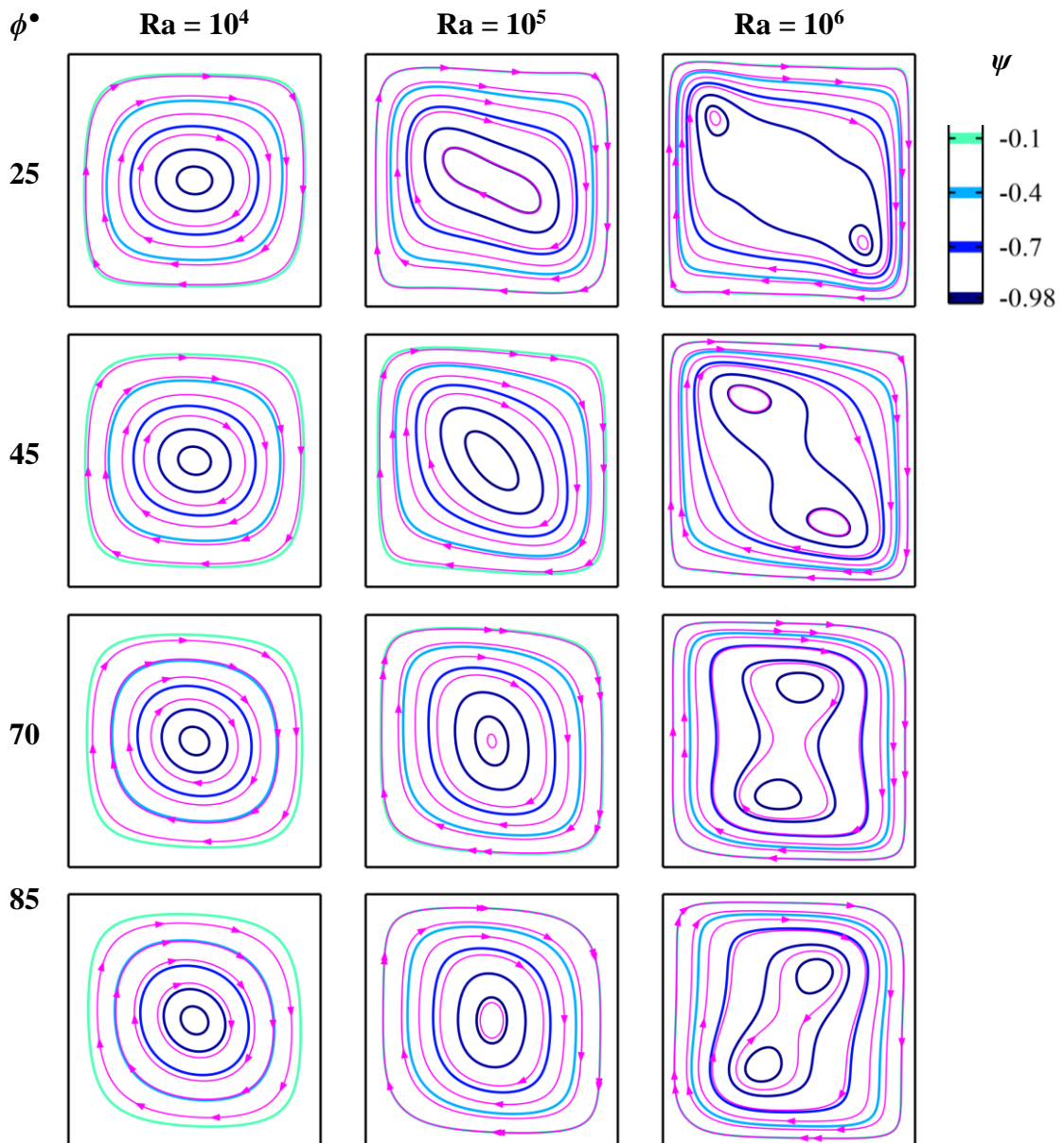
Figure 3.9 Cavity inclination impact on streamlines: CuO/water-based ($\zeta = 3\%$) square thermal system.
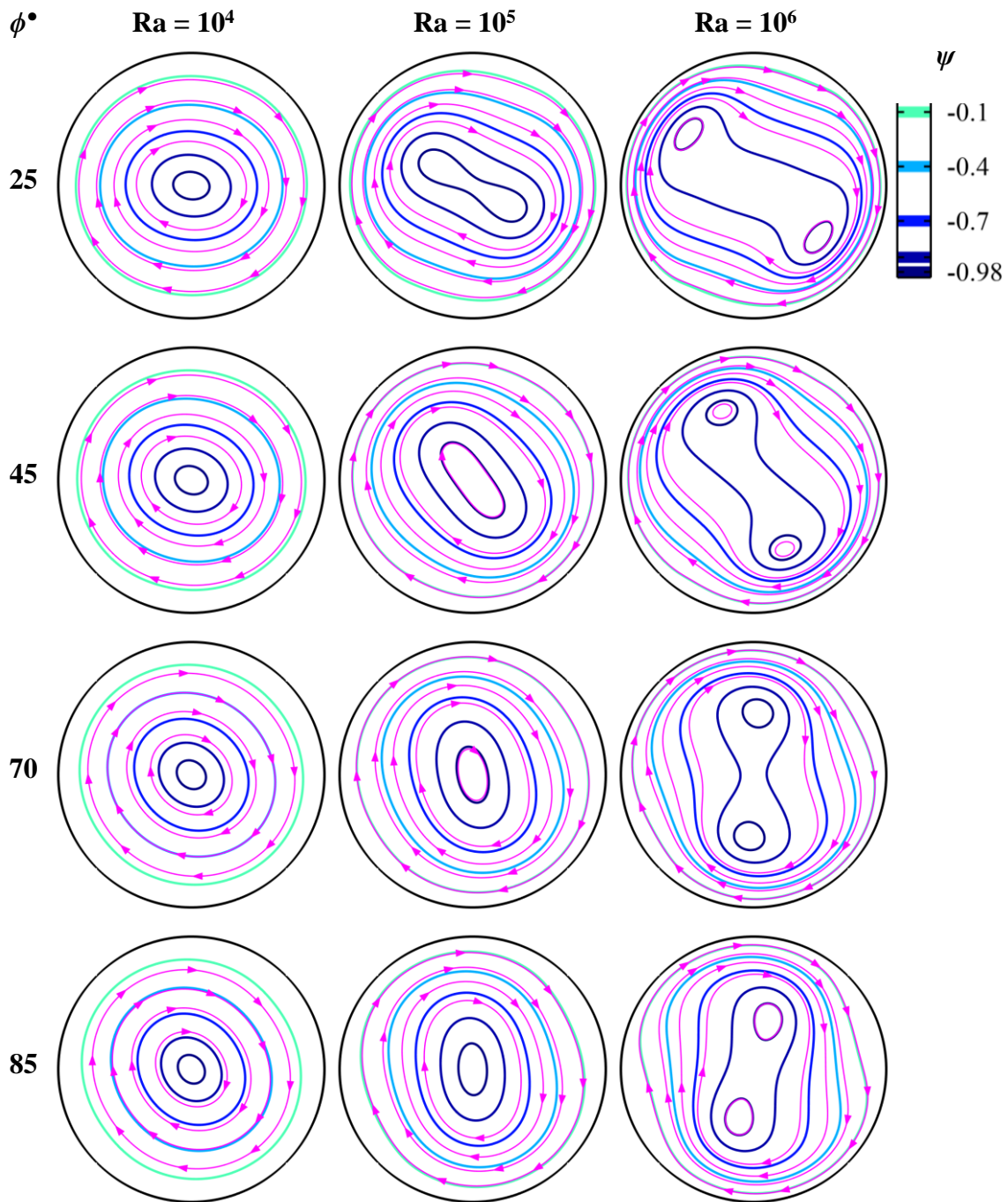
Figure 3.10 Cavity inclination impact on streamlines: CuO/water-based (ζ = 3%) circular thermal system.

Figure 3.11 Cavity inclination impact on isotherms: CuO/water-based (ζ = 3%) square thermal system.
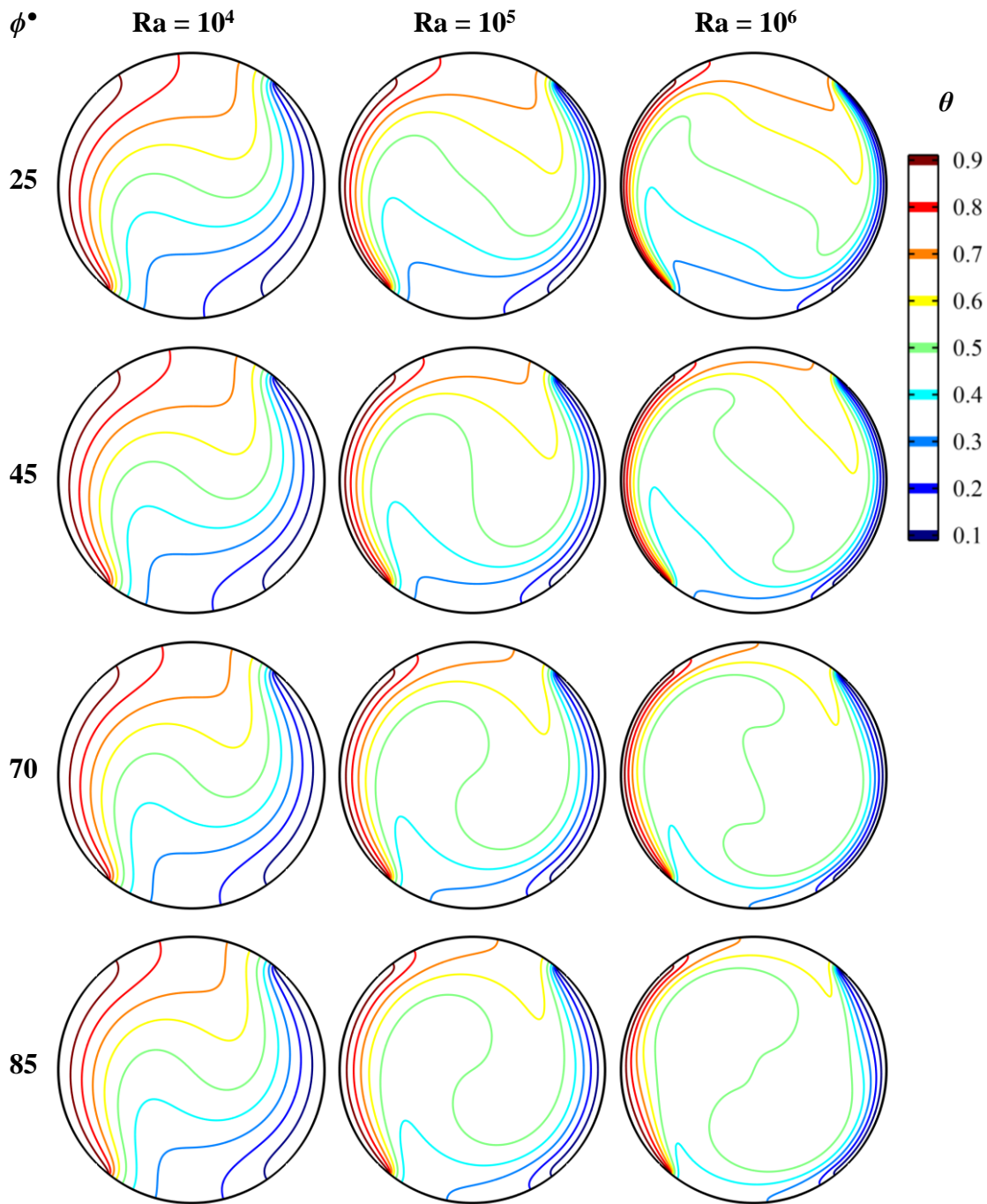
Figure 3.12 Cavity inclination impact on isotherms: CuO/water-based ($\zeta = 3\%$) circular thermal system.

3.4.3 *Sectional analyses of flow structures (U, V, θ)*

The local variations of velocities (U, V) and temperature (θ) profiles at horizontal and vertical planes are analyzed to understand the flow physics in Figures 3.13 to 3.16. Figure 3.13a demonstrates the *V*-velocity component about the mid-horizontal plane at Y = 0.5 for CDHSC for the air-based system with Ra = 10^4 to 10^6 and cavity orientation (ϕ = 0°, 45°, 70°, and 85°). The flow takes place along the

vertical sidewalls, resulting in a peak value of velocity (at $X = 0$ and 1) in the flow direction due to the formation of the boundary layer. The magnitude of $+V$ and $−V$ increases with increasing Ra for the upright cavity ($\phi = 0°$), as the entire buoyancy force acts vertically. This V-profile also shows a wavy pattern when multiple circulation cells evolved in the systems. The cavity inclination when changes from $\phi = 0°$ to 45°, 70°, and 85°, both $± V$ increase markedly at Ra $= 10^6$ because of the higher convective flow. As ϕ substantially increases, the vertical hot wall is going to the bottom and the cold wall to the top and it augments buoyant force and thereby flow velocity. Similar observations are found for the EDHCC case (in Figure 3.13b); however, the peak value of velocity shifts away from the sidewalls. The cavities at $\phi = 85°$ yield the highest V-velocity. The V-velocity is relatively less for CDHSC due to the corner separation.

(a) V for air-based square cavity

(b) V for air-based circular cavity

(c) U for air-based square cavity

(d) U for air-based circular cavity
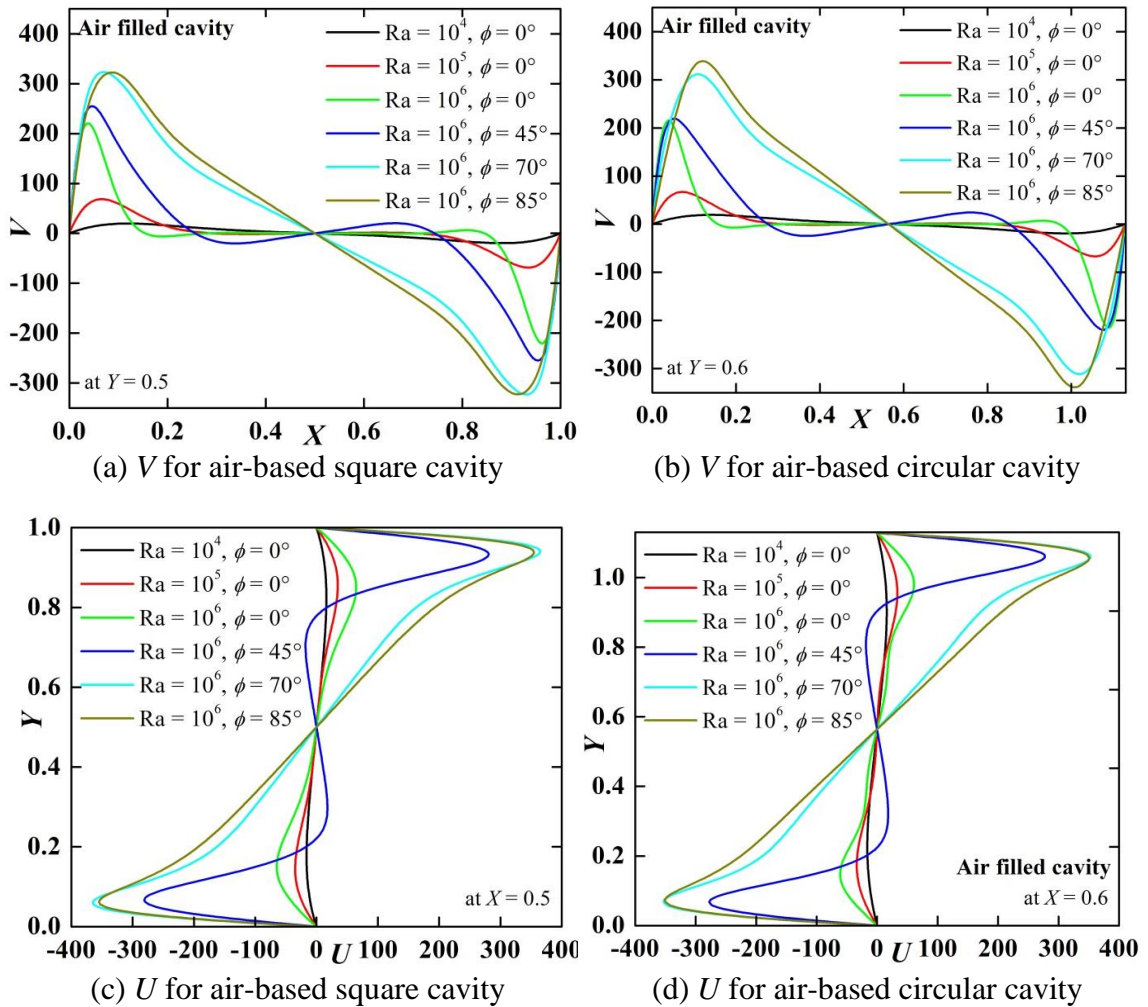
Figure 3.13 Ra-ϕ effect on sectional U and V plots in air-based CDHSC and EDHCC.

(a) Mid-horizontal θ for square cavity

(b) Mid-horizontal θ for circular cavity

(c) Mid-vertical θ for square cavity

(d) Mid-vertical θ for circular cavity
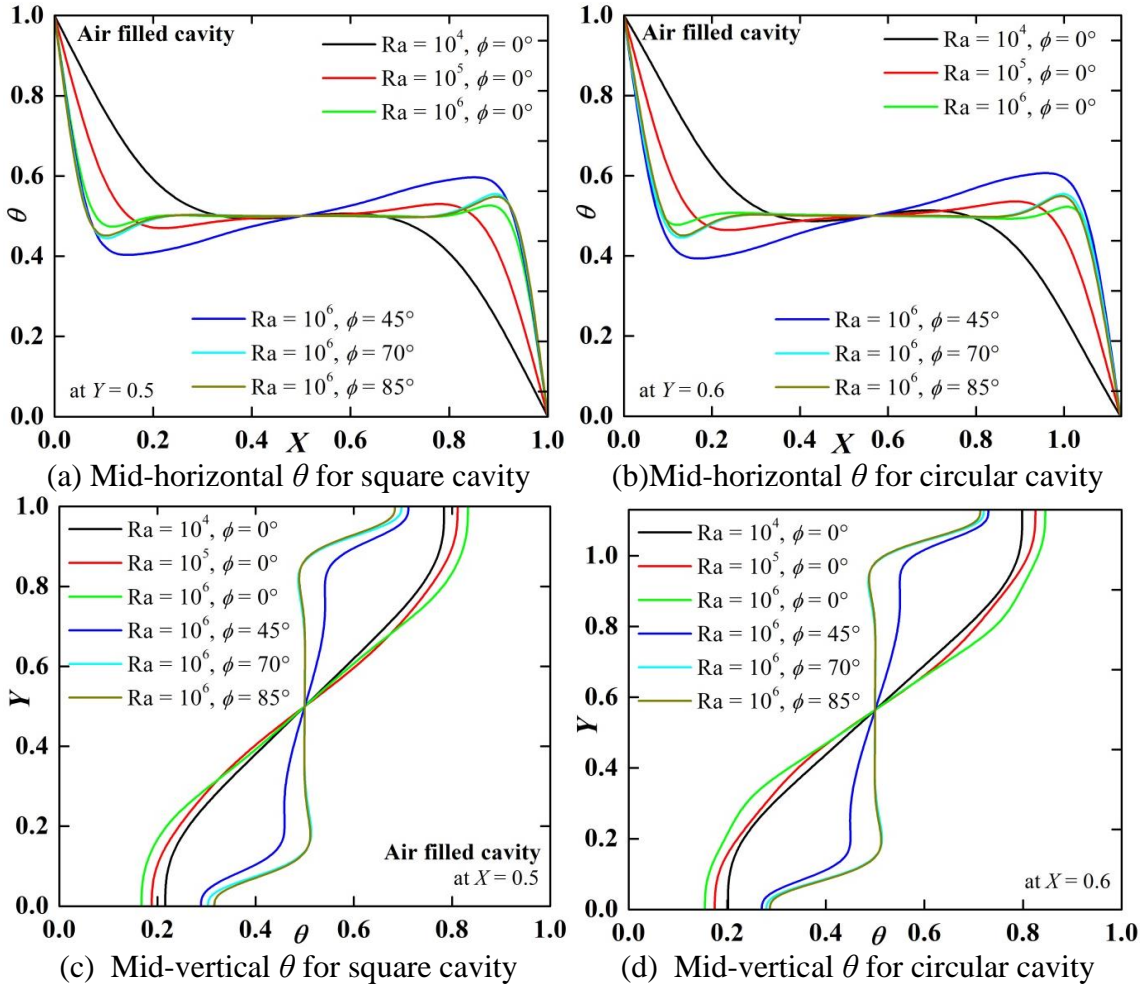
Figure 3.14 Ra-ϕ effect on sectional θ plots in air-based CDHSC and EDHCC.

Figures 3.13c and 3.13d illustrate the *U*-velocity profile at the mid-vertical plane at different Ra and ϕ. Similar to the *V*-profile, the velocity peaks are located near the top and bottom walls and its magnitude is high at higher Ra. The *U*-velocity profile is almost the same for CDHSC and EDHCC except for the peak shifting. The *U*-velocity enhanced significantly as ϕ increased at higher Ra values. Interestingly, the wavy *U*-profile is due to the formation of multi-circulations cells (which appears in Figures 3.5 and 3.6).

Temperature profiles are taken at the midplanes to assess changes in the thermal field, as shown in Figure 3.14. While there are minor variations in magnitudes, the θ-profiles for both CDHSC and EDHCC cases are similar. The differential heating between the left and right sidewalls is clearly reflected in the θ values of $\theta = 1$ (at $X = 0$) and 0 (at $X = 1$). Figure 3.14a depicts significant changes in the mid-horizontal θ-profiles as Ra and ϕ change. Monotonic change is noted at low Ra, due to a thermal conduction-dominated system. However, with enhanced flow

velocity, some distortions appear near the vertical walls due to the thermal boundary layer. At Ra = 10^6 with $\phi = 85°$, the static temperature (θ) shows a decrement near the left wall, and then it increases and falls suddenly near the right cold wall. This fact is justified by the distorted isotherms (indicated in Figures 3.7 and 3.8). Similarly, the vertical sectional temperature is illustrated in Figures 3.14c and 3.14d. As reflected in these figures, it is apparent that the temperature at the bottom is less than the temperature at the top of the cavities. However, when the cavity inclined, the θ profile changed significantly due to changes in the flow structures within the cavities.

(a) *V* for water-based square cavity

(b) *V* for water-based circular cavity

(c) *U* for water-based square cavity

(d) *U* for water-based circular cavity
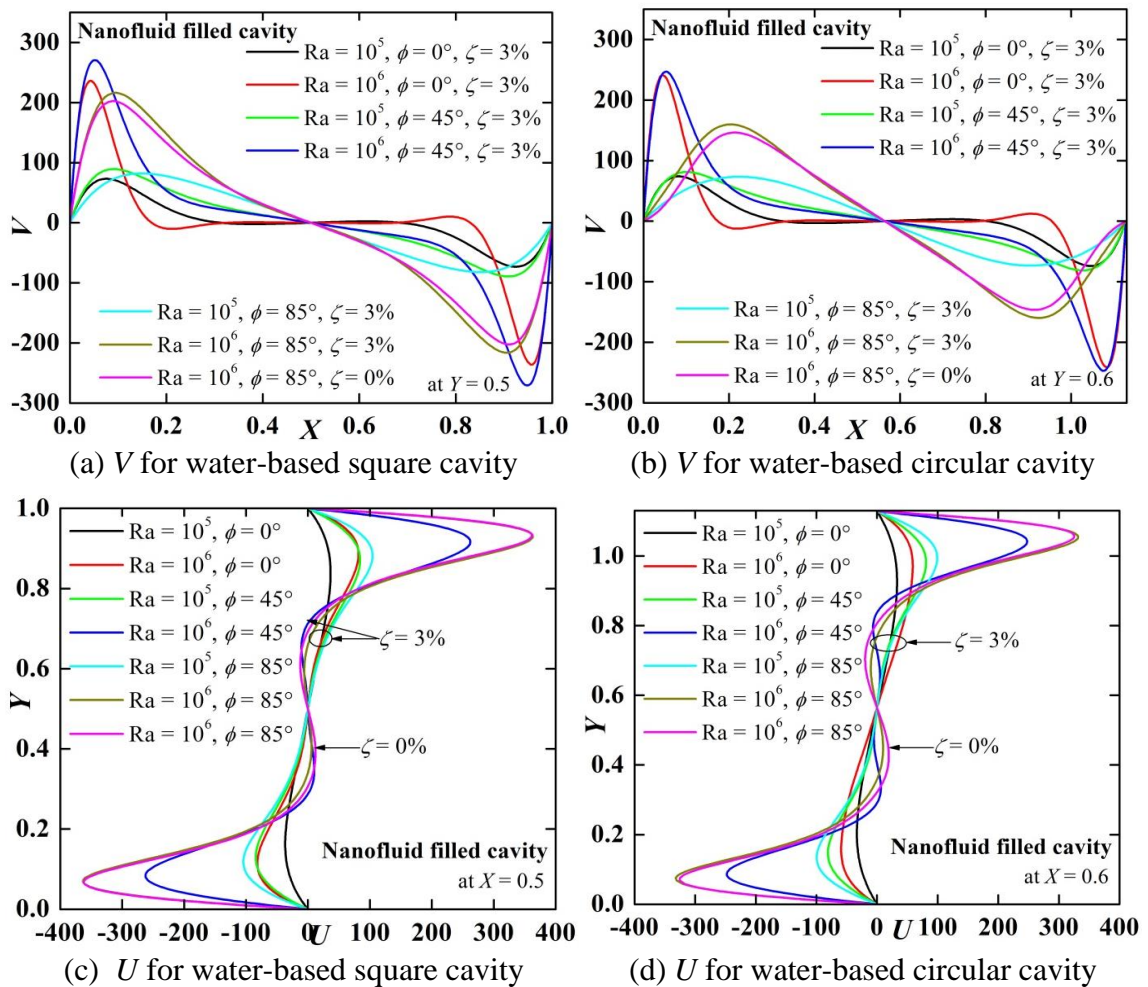
Figure 3.15 Ra-ϕ effect on sectional *U* and *V* plots in water-based CDHSC and EDHCC.

Similar analyses are conducted for water-based systems (CDHSC and EDHCC) in Figures 3.15 and 3.16, which demonstrate (*U*, *V*) and θ midplane profiles. Overall observations are similar to those for the air-based system, but changes are more pronounced for water and nanofluid systems. The peaks of *V* and *U* velocities are higher for the nanofluid cases due to higher convective flow and heat transfer. The results show a higher velocity with $\phi = 45°$, $\zeta = 3\%$, and Ra = 10^6. The sectional

temperature plots in Figure 3.16 show similar but distinct profiles with changes in Ra, ϕ, and ζ. The temperature peak locations are different for EDHCC and CDHSC cases.

(a) Mid-horizontal θ for square cavity   (b) Mid-horizontal θ for circular cavity

(c) Mid-vertical θ for square cavity   (d) Mid-vertical θ for circular cavity
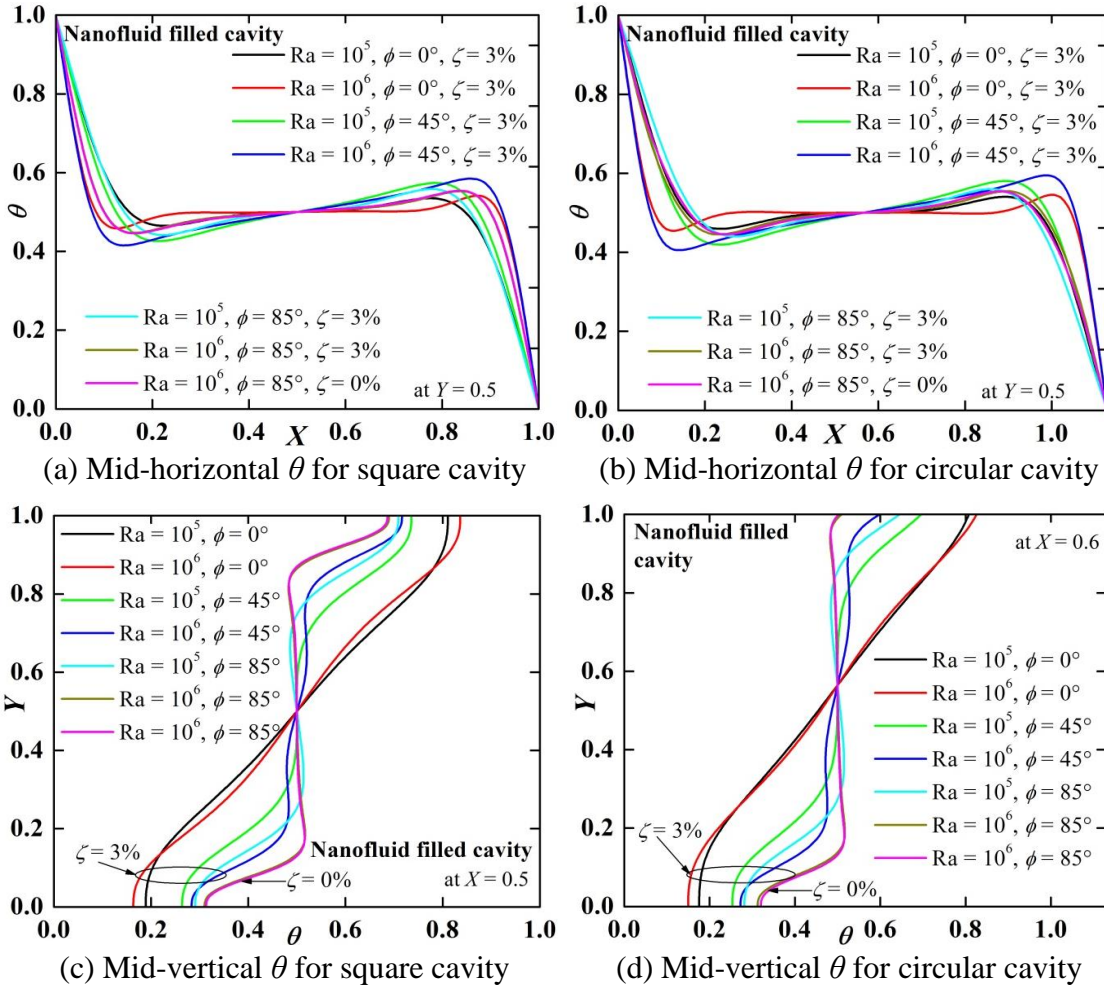
Figure 3.16 Ra-ϕ effect on sectional θ plots in water-based CDHSC and EDHCC.

3.4.4 *Analysis of global parameters (Nu, ψ_{min})*

This section discusses the global heat transfer characteristics using the average Nusselt number (Nu) and the minimum streamfunction for a specific set of controlling parameters (Ra, ϕ, ζ). Figure 3.17 shows the effect of changing Rayleigh numbers (Ra) on Nu at ϕ = 0º for CDHSC and EDHCC cases. At lower Ra values, heat transfer is dominated by conduction, resulting in lower Nu values. As Ra increases, convective heat transfer becomes dominant, leading to increased thermal energy transport from the heat source to the heat sink as indicated by higher Nu values. EDHCC exhibits higher Nu values due to stronger fluid circulation, as indicated by the maximum stream function (ψ_{max}) in Figure 3.18a. Overall, the geometry of EDHCC is more effective in facilitating better heat transfer for a given fluid volume and surface area.

Figure 3.17b shows the variation of Nu with increasing Ra for CDHSC and EDHCC cases with water and CuO water nanofluid as working media. The inclusion of CuO nanoparticles in the water results in a further improvement in the effective thermal conductivity of the working medium, leading to higher heat transfer rates. The nanofluid-filled circular-shaped cavity consistently exhibits higher Nu values. This is also an interesting finding for a given working fluid volume and heater-cooler length.

(a) Ra effect for air-based systems   (b) Ra effect for water-based systems

(c) Inclination effect for air-based systems   (d) Inclination effect for water-based systems
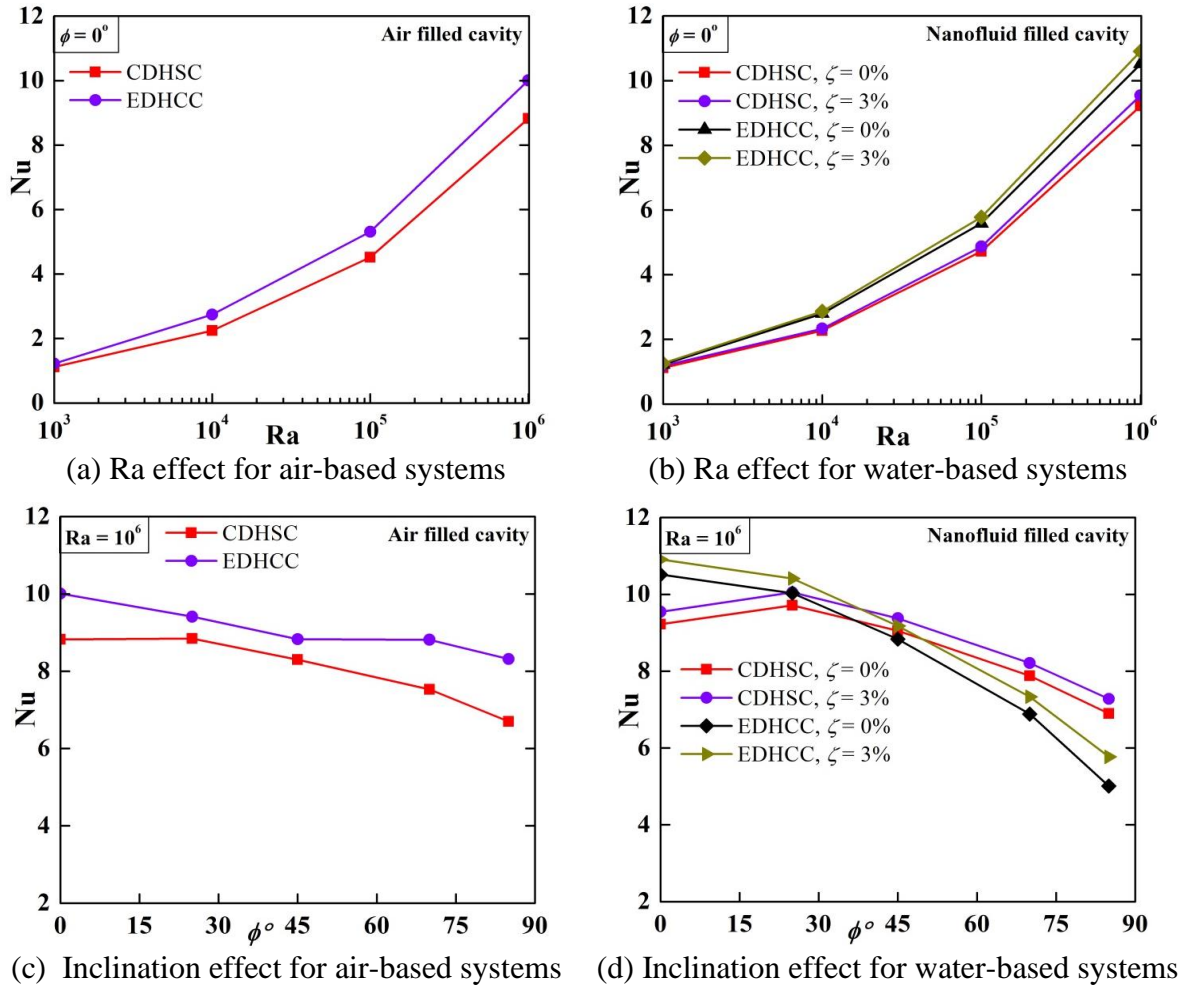
Figure 3.17 Ra-ϕ impact on Nu of CDHSC and EDHCC for different fluids.

The effect of cavity orientation on thermal performance is also analyzed. The magnitude of Nu is higher for EDHCC compared to CDHSC, irrespective of any orientation of the cavity, due to its stronger fluid velocity. A sudden boost in Nu values of EDHCC is observed when the orientation changes from $\phi = 45°$ to $70°$, due to the change in multicellular flow structures at lower ϕ values and in single circulation at higher ϕ values. The wall frictional resistance is relatively less for EDHCC, which magnifies the difference when the circulation becomes stronger.

59

However, the variation of global heat transfer characteristics shows a decreasing trend as ϕ increases, with a more significant decrease observed in CDHSC compared to EDHCC. According to Fig. 3.17 (d), the maximum value of Nu for a circular cavity is obtained at 0°, whereas the maximum value of Nu for a square cavity is attained at 22.5°. This discrepancy can be explained with the help of isotherms. The component of buoyant force changes as the cavity is titled, causing the flow pattern and isotherm to change. It is observed for square cavities that Nu values increase as the cavity is titled from 0° to 22.5° and afterward, it decreases. A close inspection of the isotherm reveals that it becomes overpopulated when the cavity is titled from 0° to 22.5° and then diminishes. In the case of a circular cavity, however, the Nu monotonically decreases with cavity inclination. Further analysis is conducted with water and CuO water nanofluid (Figure 3.17) as the working medium. The inclusion of nanoparticles always shows an enhanced heat transfer compared to pure water.

(a) Ra effect for air-based systems

(b) Ra effect for water-based systems

(c) Inclination effect for air-based systems

(d) Inclination effect for water-based systems
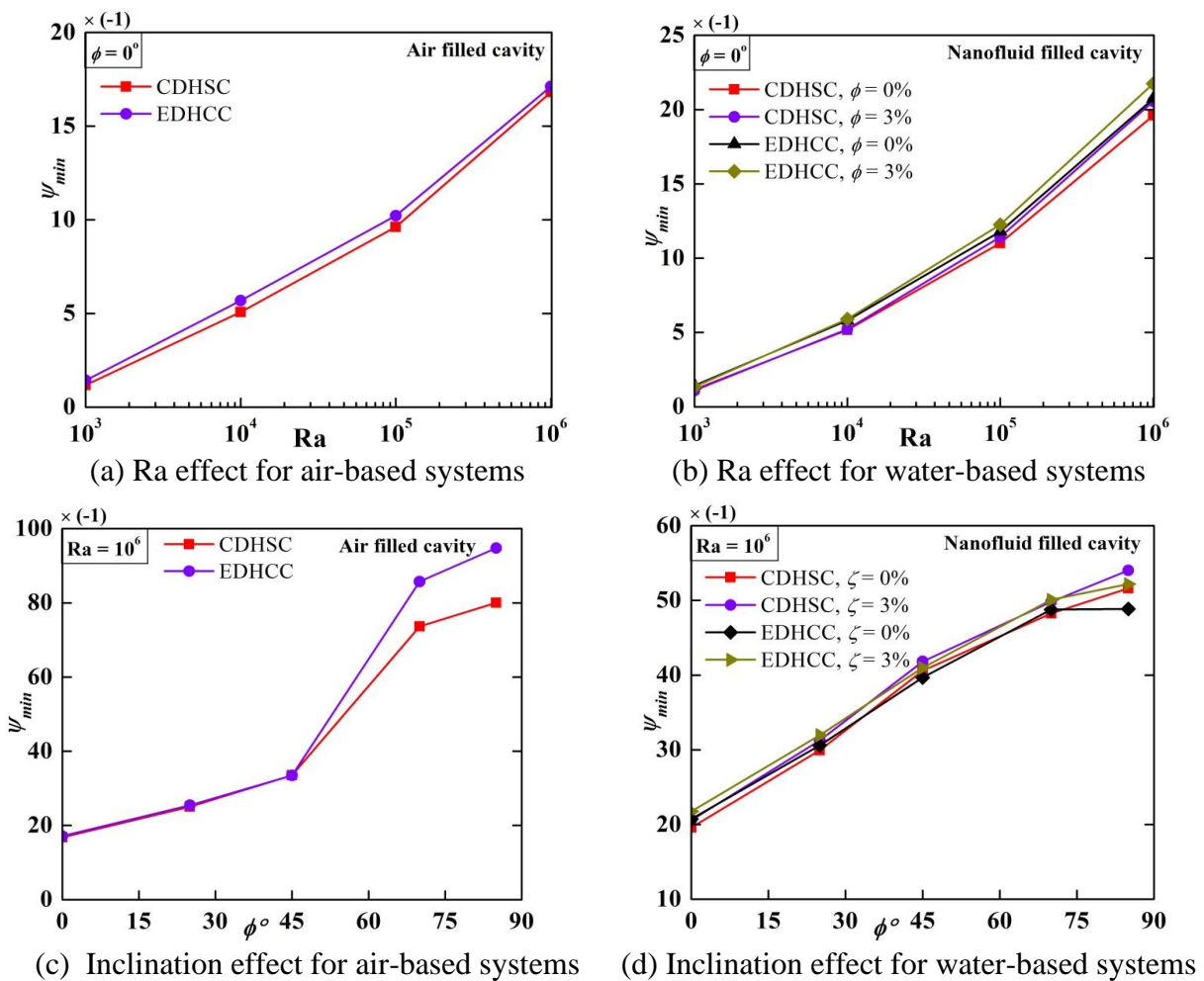
Figure 3.18 Ra-ϕ impact on ψ_{min} of CDHSC and EDHCC for different fluids.

The circulation strength (ψ_{max}) increases monotonically with ϕ (Figure 3.18d). In contrast, a monotonous decreasing trend of Nu with increasing ϕ is noted for the circular-shaped cavity (EDHCC). The study confirmed that the choice of cavity shape and orientation, working fluid, and nanoparticle concentration dictate the thermal performance of a confined thermal system. Overall, the analysis demonstrated that the geometrically modified circular inclined cavity is a better choice. The enhancements in heat transfer with air and nanofluid are up to 24.11% and 15.19% (with inclined cavity) using nanofluid.

Table 3.1 Performance of the air-based circular thermal systems (EDHCC)

Ra	$\phi = 0°$	$\phi = 25°$	$\phi = 45°$	$\phi = 70°$	$\phi = 85°$
(a) Heat transfer Nu (% enhancement in Nu)					
10^3	1.27 (13.6)	1.29 (14.2)	1.26 (14.1)	1.16 (12.1)	1.10 (10.0)
10^4	2.58 (15.0)	2.81 (14.6)	2.84 (14.6)	2.73 (14.7)	2.56 (14.8)
10^5	4.95 (9.4)	5.15 (10.8)	5.10 (12.6)	4.97 (15.5)	4.70 (16.6)
10^6	9.19 (4.1)	9.41 (6.3)	9.02 (8.7)	8.90 (18.3)	8.44 (24.11)
(b) Fluid flow $|\psi|_{max}$ (% enhancement in $|\psi|_{max}$)					
10^3	1.43 (21.9)	1.54 (23.5)	1.42 (25.8)	0.87 (31.6)	0.25 (35.9)
10^4	5.69 (12.1)	7.45 (13.1)	8.40 (13.6)	8.69 (14.0)	8.22 (14.2)
10^5	10.22 (6.3)	14.65 (4.9)	20.59 (5.4)	28.16 (12.0)	29.37 (12.5)
10^6	17.12 (1.8)	25.45 (1.7)	33.48 (- 0.1)	85.75 (16.5)	94.78 (18.4)

Table 3.2 Performance of the water-based circular thermal systems (EDHCC)

Ra	$\phi = 0°$	$\phi = 25°$	$\phi = 45°$	$\phi = 70°$	$\phi = 85°$
(a) Heat transfer Nu (% enhancement in Nu)					
10^3	1.27 (13.6)	1.29 (14.2)	1.26 (14.1)	1.16 (12.1)	1.10 (10.0)
10^4	2.61 (14.7)	2.86 (13.9)	2.89 (13.5)	2.75 (13.4)	2.57 (13.4)
10^5	5.13 (8.6)	5.44 (7.4)	5.24 (6.7)	4.78 (6.5)	4.31 (5.7)
10^6	9.55 (3.6)	9.97 (2.6)	9.21 (1.7)	7.65 (-2.9)	6.01 (-12.9)
(b) Fluid flow $|\psi|_{max}$ (% enhancement in $|\psi|_{max}$)					
10^3	1.43 (21.9)	1.54 (23.4)	1.42 (25.7)	0.87 (31.6)	0.25 (35.9)
10^4	5.81 (12.5)	7.56 (12.7)	8.47 (12.9)	8.71 (12.9)	8.19 (12.9)
10^5	11.80 (7.1)	16.97 (6.6)	21.23 (4.4)	25.64 (5.1)	25.67 (3.6)
10^6	20.74 (5.8)	30.59 (2.2)	39.68 (-2.3)	48.77 (1.1)	48.85 (-5.3)

The quantitative details of the findings are presented in Tables 3.1–3.3 for air-, water-, and nanofluid-based systems. The study focused on the estimation of global parameters, such as the average Nusselt number (Nu) and the maximum absolute

streamfunction magnitude ($|\psi|_{max}$ = -ψ_{min}). The data for the circular thermal system (EDHCC) are compared with the base square thermal system (CDHCC) by percentage enhancement figures in brackets. The circular geometry outperforms the square geometry. The high enhancement occurs with the equivalent circular thermal system undergoing natural convection using air irrespective of cavity tilting (Table 3.1). At higher cavity angles ($\phi > 45°$), the magnitude of the streamfunction becomes substantially high for all working fluids. The trend of Nu decreases after a certain inclination angle that depends on the Rayleigh number, although the streamfunction magnitude almost increases monotonically at higher Ra (Ra $> 10^3$) for all working fluids. For water-based systems (Tables 3.2 and 3.3), the flow velocity (Figure 3.15) and streamfunction magnitude are relatively less due to the enhanced fluid and nanofluid viscosity. The enhancement in cavity inclination shows a decreasing trend of approximately 13.8 % at Ra = 10^4 and 6.8% at Ra = 10^5 for water-based systems.

Table 3.3 Performance of 3% CuO-water nanofluid-based circular thermal systems (EDHCC)

Ra	$\phi = 0°$	$\phi = 25°$	$\phi = 45°$	$\phi = 70°$	$\phi = 85°$
(a) Heat transfer Nu (% enhancement in Nu)					
10^3	1.35 (12.9)	1.36 (13.3)	1.33 (13.0)	1.25 (11.2)	1.21 (9.9)
10^4	2.70 (15.1)	2.96 (14.3)	3.00 (14.0)	2.86 (13.8)	2.67 (14.0)
10^5	5.34 (9.1)	5.67 (7.9)	5.48 (7.3)	5.03 (7.3)	4.56 (6.8)
10^6	9.98 (3.9)	10.41 (2.9)	9.62 (2.0)	8.10 (-1.9)	6.69 (-8.7)
(b) Fluid flow $|\psi|_{max}$ (% enhancement in $|\psi|_{max}$)					
10^3	1.34 (22.6)	1.41 (24.1)	1.27 (26.3)	0.74 (30.8)	0.20 (33.1)
10^4	5.90 (13.2)	7.58 (13.3)	8.42 (13.4)	8.56 (13.5)	7.98 (13.7)
10^5	12.25 (7.2)	17.55 (6.5)	21.98 (5.0)	26.22 (5.7)	26.21 (4.6)
10^6	21.75 (5.8)	31.96 (2.3)	40.99 (-2.0)	50.08 (30.5)	52.19 (-3.4)

It is observed from Table 3.3 that the heat transfer parameter is positive in most of the cases, showing enhancement of heat transfer in circular cavities, while it is negative in a few cases (for = 70° and 85° at Ra = 10^6), showing a deterioration in heat transfer of circular cavities compared to square cavities. When nanoparticles are added to the base fluid, they improve both thermal conductivity and viscosity. When the increase in thermal conductivity outweighs the increase in viscosity, heat transport increases; otherwise, it diminishes. The decrease in heat transfer parameters in the aforementioned situation could be attributed to the greater impact of viscosity than thermal conductivity.

3.4.5 *Heatline visualization*

Figures 3.19 and 3.20 depict the heatlines in CDHSC and EDHCC at different Ra and ϕ. Heatlines represent the direction of heat flow within the system. These lines span from the left to the right wall and trace the paths of heat transport from the heat source to the heat sink.
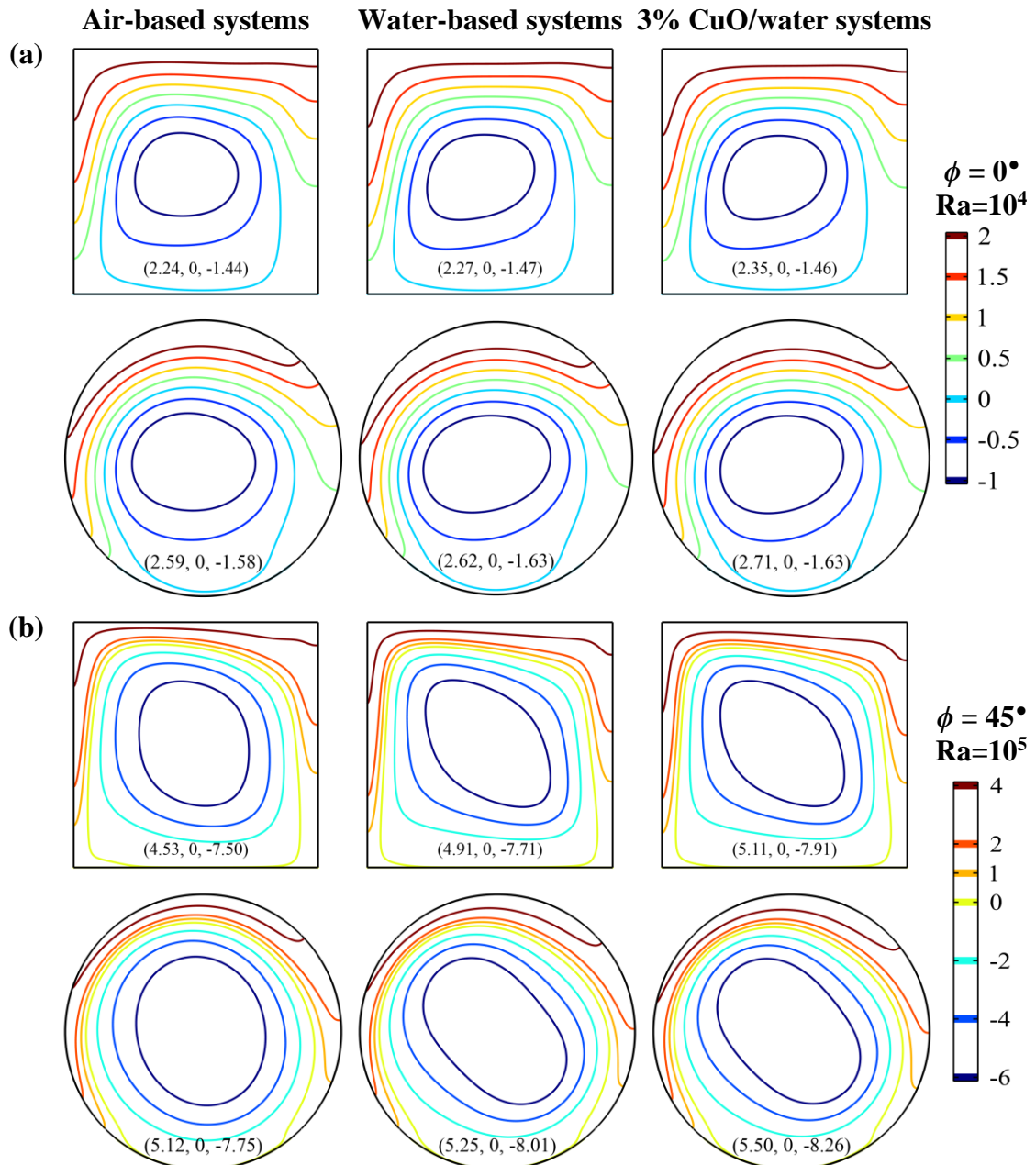
Figure 3.19 Heatlines for different thermal systems: (a) ϕ = 0•, Ra = 10⁴; (b) ϕ = 45•, Ra = 10⁵.

In each corridor, the rate of heat flow remains constant, but the local intensity of the combined heat flux may vary if the width of the flow passages is uneven. The rotation of hot working fluid in confined systems creates a heat flow circulation or an energy-recirculation cell. The magnitude of the heat function within the brackets

changes depending on the operating parameters and cavity shapes. The maximum value occurs at the top adiabatic wall, while the minimum value corresponds to energy recirculation.
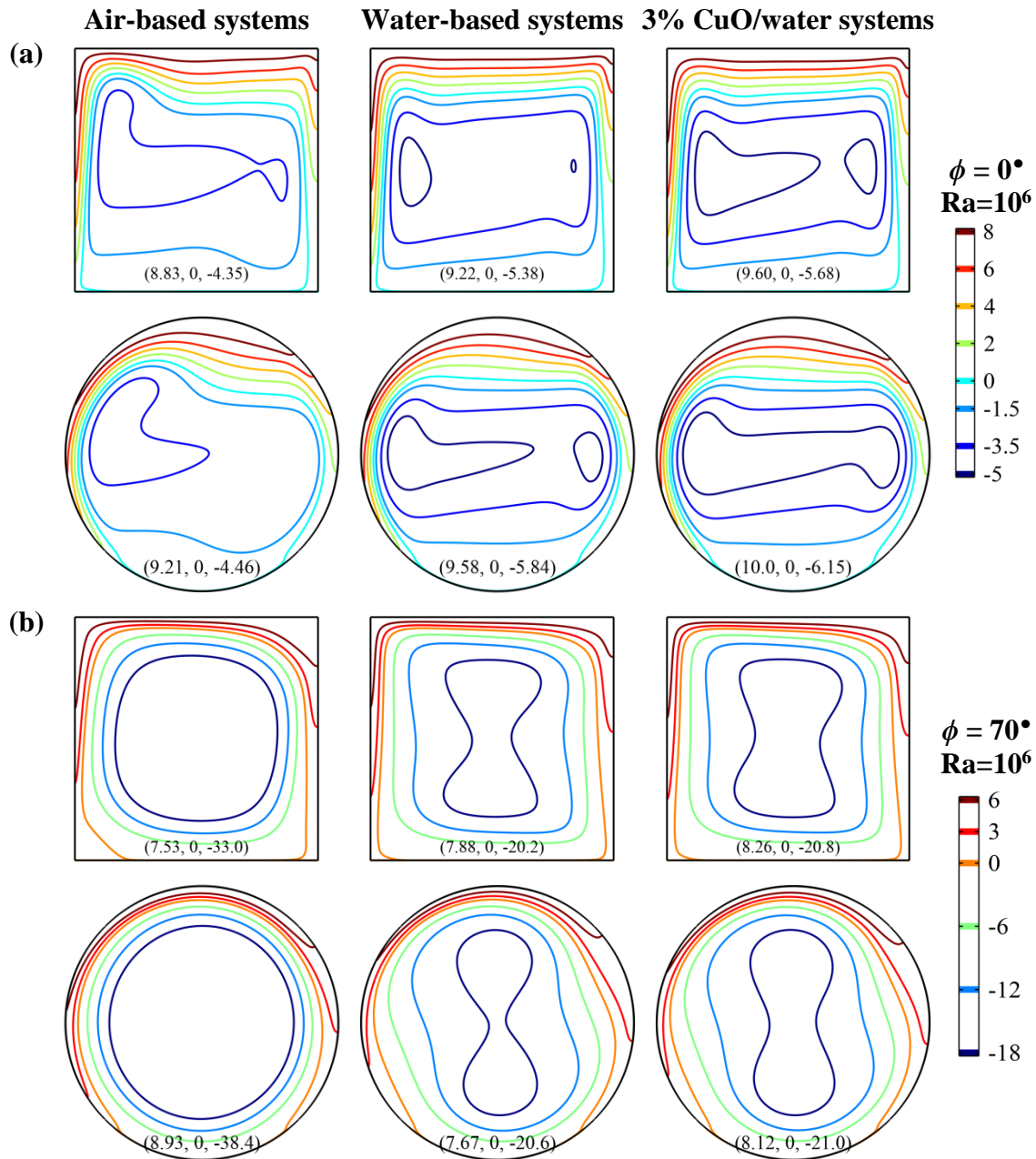
Figure 3.20 Heatlines for different thermal systems at Ra = 10^6: (a) $\phi = 0^\bullet$, (b) $\phi = 70^\bullet$.

The results shown in Figure 3.19a illustrate the heatlines at Ra = 10^4 and $\phi = 0°$, with a maximum contour value of 2 near the top wall and a clockwise energy circulation cell of -1. The size and shape of heatlines with the same value differ for the three fluids considered. Similar observations were made for all other results at

different Ra and ϕ. Figures 3.19 and 3.20 demonstrate that the heat flow in equivalent circular systems is consistently higher, regardless of the working fluid, due to lower flow resistance. Fluids with higher thermal conductivity enable more efficient heat transport and transfer.

3.5 Conclusions

In conclusion, the present constraint-based analysis has provided valuable insights into the thermal performance of square and circular cavities. The following points summarize the key findings:

1. Flow structures adapt to available volumes and system perimeters, regardless of the working fluid.
2. Circular cavities outperform square cavities due to lower surface friction; smoother turns, and an increased overall height that enhances buoyancy force.
3. Geometrically modified circular cavities can achieve up to 24.11% heat transfer enhancement with air and up to 15.19% with nanofluid, compared to square cavities.
4. The equivalent circular thermal system is more efficient at $Ra = 10^4$ and 10^5, with heat transfer enhancements of around 15% for air.
5. A heatline visualization is a useful tool for analyzing heat flow patterns, which are influenced by Rayleigh number and cavity inclination, regardless of a working fluid.

These findings can assist system developers in making decisions about a particular cavity shape for optimal thermal performance.

Chapter – 4

Heat transport and accompanying irreversibility during MHD nanofluid flow in constraint-based equivalent square and circular thermal systems

4.1 Introduction

The current research builds upon the work presented in the previous chapter by exploring the effects of magnetohydrodynamic (MHD) nanofluid flow in both the equivalent square and circular thermal systems. The thermal performance analysis of these systems is carried out in an upright position, and the study also includes an estimation of thermodynamic entropy generation (EG). To provide context for this research, a brief literature survey of the current topic is presented before discussing the new aspects of the study.

4.2 Relevant background works

In modern civilization, thermal systems/devices are extensively used in numerous applications. To enhance their performance and create energy-efficient alternatives, new studies on evaluating the performance of such systems are necessary. Among the various thermal systems, those operated using natural convection face challenges in achieving heat transfer enhancement, leading to a vast number of fundamental studies in this area as discussed in Chapter 1. The geometry of thermal systems significantly affects their thermal performances, and different system geometries have been investigated over the years (Hussien et al. 2021). However, relatively few works deal with comparative studies of different geometries. Moreover, the concept of equivalent systems for any comparative investigation has been overlooked in earlier studies. The same system volumes or active heater (and cooler) lengths for the system geometries under comparative assessment are rarely considered. It is vital to analyze which specific geometrical shape is more efficient than the other shapes with the same equivalent geometrical parameters in designing thermal systems. The present work addresses this issue and considers two of the most

commonly used classical geometric shapes, square and circular for the magnetohydrodynamic (MHD) nanofluid flow. The current work is an extension of the initial effort presented by Saha et al. 2022 in the absence of a magnetic field.

Buoyancy-driven convection in the presence of magnetic fields is a crucial area of research, given the current trend in technological innovation, which has led to the development of magnetic components and gadgets with superior thermal performance. The study of magnetohydrodynamics (MHD) is necessary to ensure that these devices function optimally, and it involves the study of the influence of a magnetic field in a moving electrically conducting fluid. The presence of a magnetic field in a moving electrically conducting fluid creates an electromagnetic force, also known as the Lorentz force. This force alters the flow pattern and temperature distribution during buoyancy-induced convection, making it crucial to study its effects.

Several researchers have studied the impact of magnetic fields on different geometrical configurations, such as rectangular (Wang et al., 2017; Giwa et al., 2020a), triangular (Mahmoudi et al., 2012; Rahman, 2016; Dogonchi et al., 2019), circular (Sheikholeslami et al., 2012; Tayebi et al., 2021), trapezoidal (Mahmoudi et al., 2013; Bondareva et al., 2015), among others. Several researchers have studied the effect of non-dimensional parameters, such as Rayleigh number (Ra), and Hartmann number (Ha), on thermo-magnetic convection (Nemati et al., 2012; Kefayati, 2014; Selimefendigil and Öztop, 2015). Researchers have reported that heat transfer during buoyancy-induced convection increases with a rise in Ra and declines with a rise in Ha.

Several authors studied the impact of magnetic field inclination (γ) in buoyancy-driven convection (Mansour and Bakier, 2015). The buoyancy-driven convection in a square enclosure in the presence of an inclined magnetic field was examined by Mansour and Bakier (2015), who found that the maximum heat transfer occurs at $\gamma = 90°$. Factors affecting thermomagnetic convection include surface waviness (Biswas et al., 2021a), non-uniform heating (Mejri et al., 2014; Sheikholeslami et al., 2014a; Manna et al., 2021a), and obstruction (Selimefendigil and Öztop, 2015; Mallick et al., 2021). Recently, Manna and Biswas (2021b) developed a novel visualization technique for MHD-based convection known as magnetic force vectors.

Entropy generation (EG) is a crucial concept in evaluating the irreversibility of thermodynamic systems and optimizing their designs. Heat transfer irreversibilities, fluid friction irreversibilities, internal heat generation, and magnetic fields are among the irreversibilities associated with EG. Higher values of EG indicate less efficient processes, equipment, or systems. Understanding the impact of non-dimensional parameters on EG in convection is crucial for optimizing system design. Studies have investigated the influence of Ra and Ha on EG in buoyancy-driven enclosures (Malik and Nayak 2017; Sahin 2020; Mukhopadhyay 2010; Das and Basak 2017b). The results show that at low Ra values, irreversibility due to heat transfer dominates, while at high Ra values, irreversibility due to fluid friction dominates. Literature reviews on EG have been published, including a comprehensive review by Oztop and Al-Salem (2012) and reviews by Sciacovelli et al. (2015) and Biswal and Basak (2017) on the use of EG analysis in various engineering applications and during thermal convection in different cavities and processes involving diverse practical uses, respectively.

The objective of this research work is to investigate the heat transport and accompanying irreversibility during MHD (Magneto-hydrodynamic) nanofluid flow in constraint-based equivalent square and circular thermal systems. While several studies have been carried out on MHD nanofluid flow, the impact of geometrical shapes on the heat transfer and accompanying irreversibility has not been explored in detail, especially in constraint-based equivalent square and circular thermal systems. The study aims to compare the thermal efficiency of equivalent square and circular thermal systems, considering identical heating/cooling lengths and fluid flow areas. The investigation will also analyze the impact of magnetic field strength, nanoparticle concentration, and accompanying irreversibility. The findings of this study will have practical implications in designing optimal thermal systems for various applications, including nuclear reactors, heat exchangers, and electronic cooling systems. Furthermore, the proposed constraint-based analysis approach is expected to be an original contribution and may open new avenues for designing optimal thermal systems and nanofluid flow control mechanisms.

4.3 Problem formulation and solution

In order to investigate the impact of geometrical shape on the thermal performance of an MHD nanofluidic system, two equivalent systems, a square cavity, and a circular cavity, were examined as shown in Figure 4.1 with dotted and solid

lines, respectively. The classical configuration of differential heating (DH) was used, with the left wall heated at T_h and the right wall cooled at T_c (Figure 4.1a). The two dissimilar thermal systems were made equivalent by applying the following constraints: (a) same volume/area for both the systems, (b) same heater length, (c) same cooling length, and (d) identical arrangement of the heater and cooler. The height of the square cavity, H, was used as the length scale. Based on the concept of an equivalent system of the same area, the diameter and perimeter of the circle became $H\sqrt{4/\pi}$ and $H\sqrt{4\pi}$, respectively. The small mismatch in the perimeters of the circular and square cavities ($H\sqrt{4\pi}$ and $4H$, respectively) was adjusted through the inactive adiabatic walls of the cavities. All active wall lengths of both systems followed the constraint of $L_h = L_c = H$. Furthermore, the midpoints of the heater and cooler of the circular cavity were strictly located on its mid-horizontal plane. The present study and its findings are potentially meaningful to thermal system developers as it explores the impact of thermal system shape on transport phenomena. These two equivalent differentially heated square and circular cavities were addressed as EDHSC and EDHCC in further discussion. The mesh architecture and the number of elements used for square and circular geometries is same as discussed in the preceding Chapter 3.

(a)

(b) Physical ranges of parameters

Description	Study range
CuO-water nanofluid	Working fluid
Nanofluid Concentration	$\zeta = 0\text{-}3\%$
Equivalent geometries	EDHSC, EDHCC
Buoyancy effects	Ra $= 10^3 - 10^6$
Magnetic field strengths	Ha $= 0-100$
Magnetic field angles	$\gamma = 0-180°$
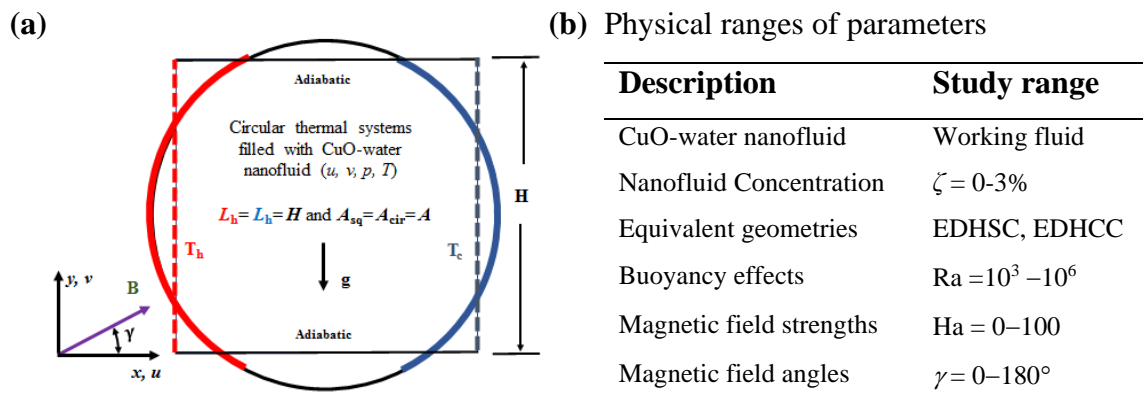
Figure 4.1 Equivalent thermal systems: (a) square (EDHSC) and circular (EDHCC) shapes, and (b) physical ranges of studied parameters.

Figure 4.1b summarizes the details of the involved physics and the ranges of operating parameters considered for this investigation. The study utilizes two equivalent systems filled with a highly diluted CuO-water nanofluid (nanoparticles' volume concentration $\leq$ 3%). Natural convection drives the fluid flow in the equivalent systems due to differential heating, which is modeled by the Rayleigh

number (Ra). Externally generated magnetic fields, simulated by the Hartmann number (Ha), are used to moderate the flow process. Usually, the magnetic force acts as a flow damper. This constraint-based study characterizes the thermal performance of two different shapes of thermal systems and helps in the decision-making process for choosing one over the other. The objectives of the present investigation include the identification of an efficient thermal system over the operating parametric spaces by analyzing the thermal buoyancy impact and magnetic damping effect. Both the strength (mesmeasured through Ha) and angle (γ) of the magnetic field are taken into account. The source-to-sink heat transport mechanism is investigated using heatlines. Moreover, an entropy-based analysis of system irreversibility is also addressed.

Based on the references (Biswas et al. 2018; Chatterjee et al. 2023), the flow of a diluted CuO-water nanofluid ($\zeta = 0\text{–}3\%$) is mathematically modeled using the homogeneous model and the Boussinesq approximation. The assumption of no agglomeration/sedimentation is considered. The reference temperature of 300 K is used along with constant properties of pure-water and nanofluids. The investigation also considers the effects of the strength and inclination of the magnetic field along with different buoyancy strengths. The problem is nonlinear and involves coupled flow physics of fluid flow and heat transfer in the presence of magnetic force. Therefore, the mathematical formulation and numerical handling follow the necessary treatments as discussed in Chapter 2. The numerical solution to the problem involves the application of no-slip and no-penetration wall boundary conditions ($U = V = 0$) along with constant temperatures ($\theta = 1$ and $\theta = 0$) for the heater and cooler walls, respectively. Additionally, zero adiabatic wall gradient ($\partial\theta/\partial n = 0$) is enforced on the adiabatic walls.

4.4 Results and Discussion

This section presents the results and analyses of the MHD nanofluid flow work systematically in five subsections. The effects of Rayleigh and Hartmann numbers (Ra and Ha) and magnetic field orientation (γ) on the flow patterns, sectional velocity and temperature profiles, irreversibility generation, and global performance parameters are addressed. Comparative assessments of the thermal-flow aspects of equivalent square and circular enclosures are presented to understand the impact of geometric shapes on the thermal systems' local and global characteristics. This helps in making a robust and flow-physics-oriented decision for appropriate shape design.

4.4.1 *Effects of Rayleigh and Hartmann numbers*

The effects of Rayleigh and Hartmann numbers on the anisothermal flow fields for the equivalent buoyant enclosures are analyzed first in Figures 4.2 to 4.4 presenting streamlines, isotherms, and heatlines respectively. The study is conducted for various Rayleigh numbers (Ra = 10^4–10^6) at a fixed magnetic field inclination (γ = 25°) for Hartmann numbers Ha = 10 and 70. Arrowhead lines of the streamlines in Figure 4.2 illustrates the direction of fluid circulation in corresponding streamlines and their contours are normalized using the maximum |ψ| magnitude that measures the flow strength. The normalized ψ ranges from 0-1 for counter-clockwise flow (or 0 to -1 for clockwise flow). Due to the confined flow domain, |ψ/ equals 0 at all the walls and -1 or 1 at the core of the circulation. As Ra values increase, the streamlines become more congested around the active walls, indicating a high convective flow over the walls and the formation of a thinner velocity boundary layer.

The results of the study demonstrate a clockwise single circulation in both of the thermal cavities. As Ra values increase, the streamlines become more congested around the active walls, indicating a high convective flow over the walls and the formation of a thinner velocity boundary layer. This results in the horizontal stretching of streamlines near the core zones, which is particularly prominent at Ra = 10^6. The impact of the cavity's geometric shape becomes more evident at high Ra values (= 10^6).
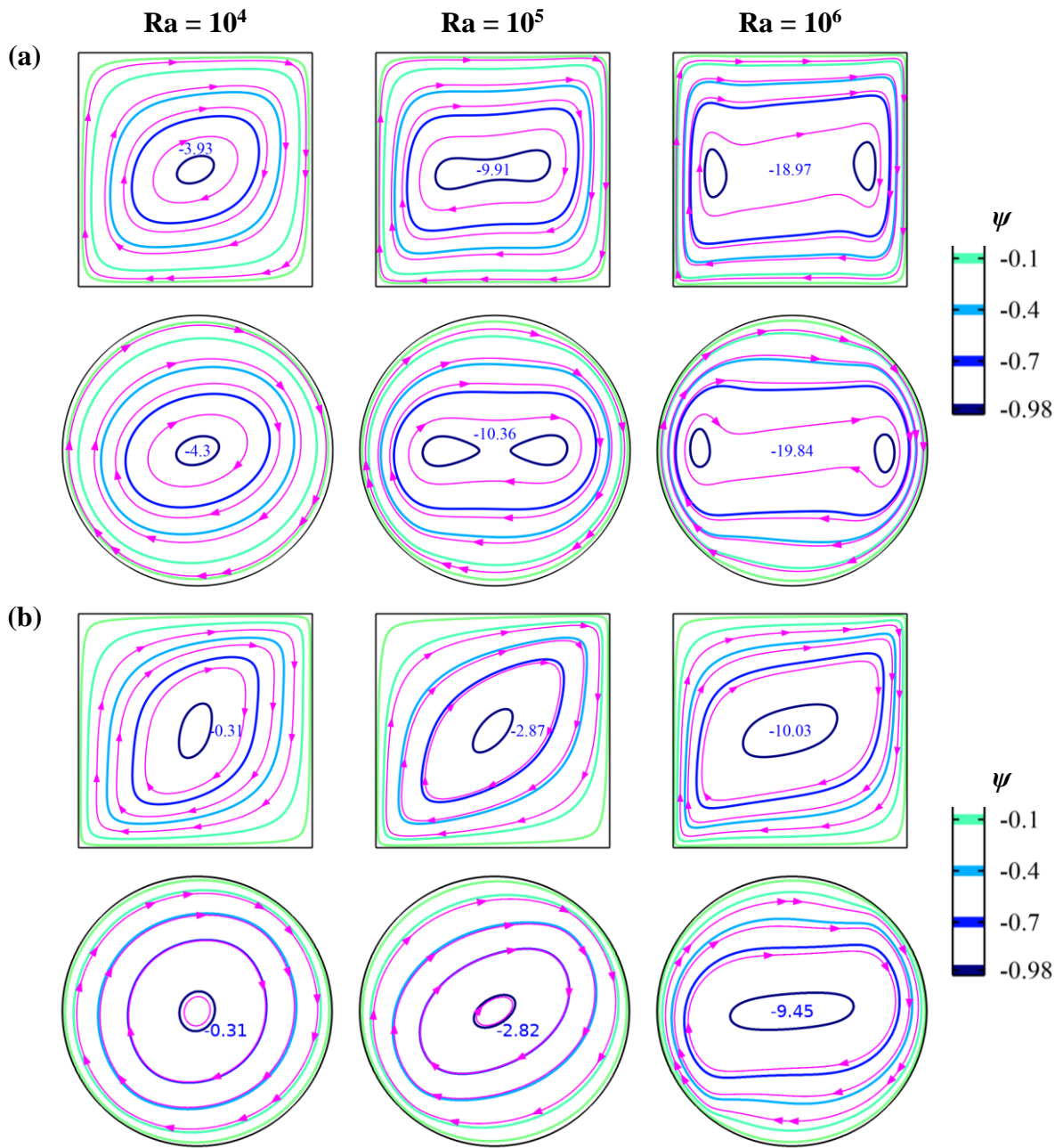
Figure 4.2 Effects of Ra on thermal systems' streamlines (within square and circular domains) for $\gamma = 25°$ and $\zeta = 1\%$: (a) Ha = 10, and (b) Ha = 70.

The effect of established circulations on static temperature distributions is made clear by the isotherm lines in the two cavities (Figure 4.3). As Ra increases from 10^4 to 10^5 and 10^6, the lines become less vertical and take on a longer, horizontal middle stretch. At lower Ra values, when only thermal conduction governs the thermofluid flow, isotherms develop parallel to the active walls. Furthermore, the qualitative differences due to the change in cavity shape are easily noticeable.
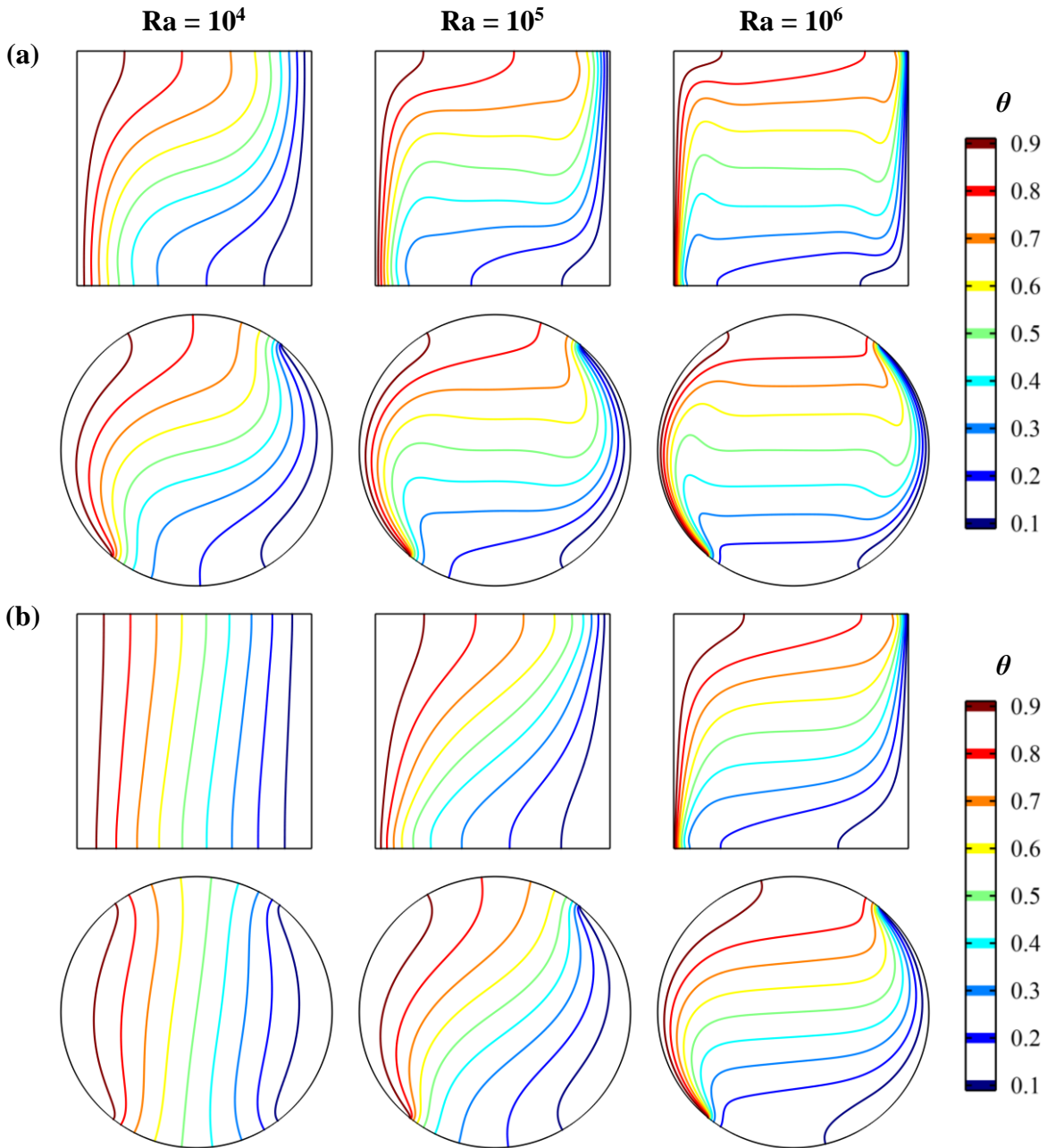
Figure 4.3 Ra effects on thermal systems' isotherms (within square and circular domains) for $\gamma =$ 25° and $\zeta = 1\%$: (a) Ha = 10, and (b) Ha = 70.

Figures 4.2b and 4.3b show the significant effect of higher Ha (= 70) on isotherms. The flow-damping effect of the imposed magnetic field reduces the stronger convective flow at higher Ra (for example, Ra = 10^5 or 10^6). As a result, not only does the circulation strength decrease, but it also has a strong impact on the static temperature distribution in the system. Therefore, the horizontal isotherms observed at Ha = 10 are transformed into 'S'-shaped patterns at Ha = 70. The coupling between fluid flow and heat transport physics plays a significant role in the observed behavior. As the fluid flow is affected by the magnetic field, it changes the heat transfer

mechanisms and alters the static temperature patterns. This coupling effect is an important consideration in the study of magnetoconvection-based thermal systems.
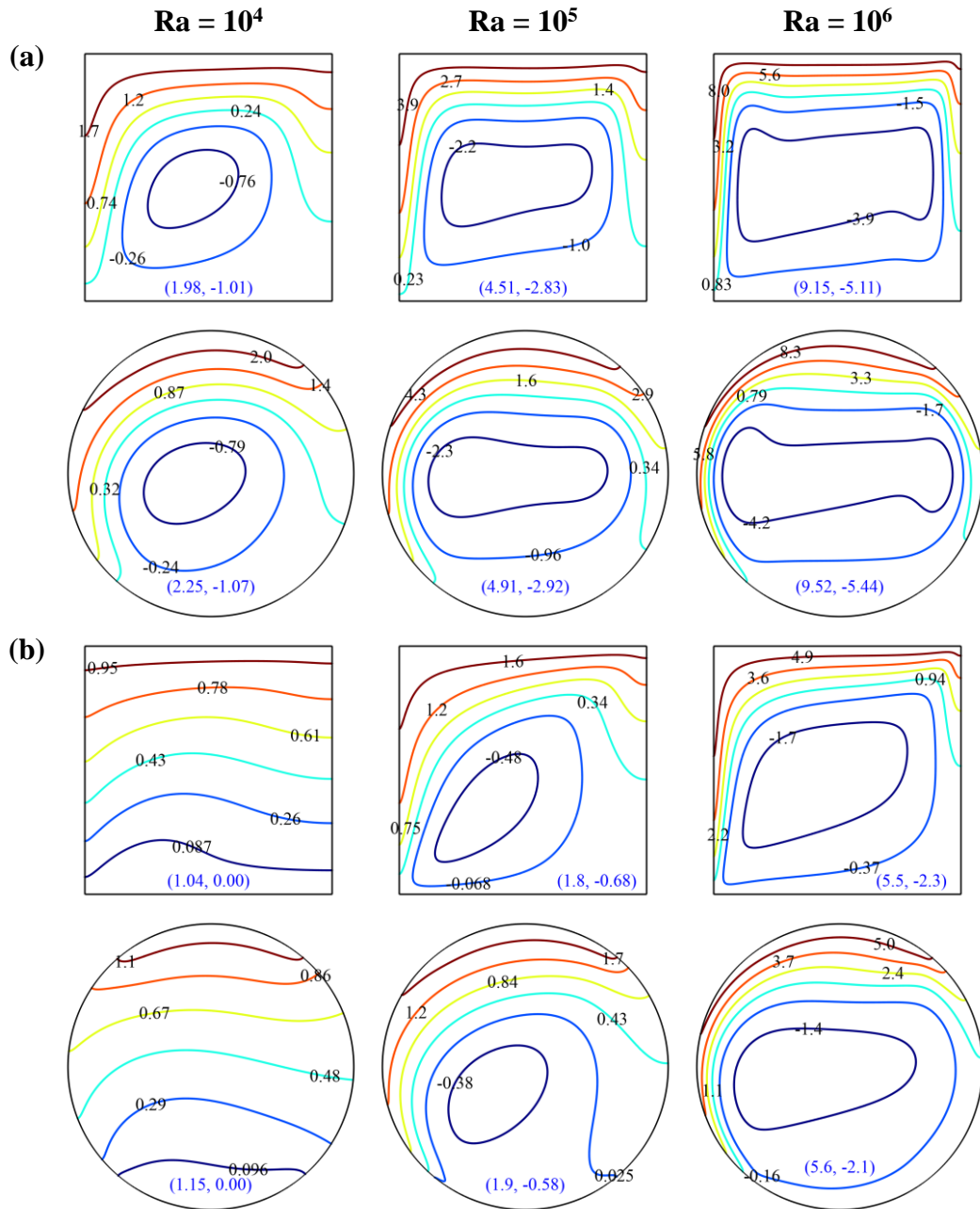
Figure 4.4 Effects of Ra on thermal systems' heatlines (within square and circular domains) for γ = 25° and ζ = 1%: (a) Ha = 10, and (b) Ha = 70

Figure 4.4 provides a visual representation of the heatlines in EDHSC and EDHCC, where heatlines represent the flow of heat instead of fluid flow. The lines extend from the left wall to the right wall and illustrate the paths of heat transport from the left source to the right sink. Within a particular corridor, the heat flow rate remains constant, while the local intensity of the combined heat flux varies if the width of flow passages is not uniform. The rotation of hot working fluid within

confined systems gives rise to a heat flow circulation, also known as an energy-recirculation cell. The magnitude of the heat function within the brackets changes with the operating parameters and cavity shapes, where the maximum value corresponds to the top adiabatic wall, and the minimum value relates to energy recirculation.

The results presented in Figure 4.4 demonstrate that the magnetic field substantially dampens heat transport from Ha = 10 to Ha = 70, regardless of Ra values. The energy-recirculation cells also weaken as Ha increases. The geometric shape has a significant impact on heat flow. With the circular domain, the contour values of the heat function increase, although the volume and heating/cooling length of the square and circular domains are identical.

4.4.2 *Effects of magnetic field orientation (γ)*

In this section, the effects of magnetic field orientation ($\gamma = 0-180°$) on the streamlines, isotherms, and heatlines at different Ra (10^4-10^6) are presented for both the square thermal system (EDHSC) in Figures 4.5 to 4.7 and the circular thermal system (EDHCC) in Figures 4.8 to 4.10. The results show that all the flow patterns in Figures 4.5 to 4.10 appear rotated with increasing γ, with Figures 4.5 and 4.8 prominently revealing this fact at lower Ra = 10^4. This is because the magnetic force is divided into the *X* and *Y* components and acts in the opposite direction of the buoyant force. At $\gamma = 0°$, the entire magnetic force acts only in the vertical direction, but as γ increases, a horizontal component is added, reducing the strength of the vertical component and rotating the flow structures in the clockwise direction. The rotating feature of flow structures loses prominence particularly at Ra = 10^6 when the counteracting buoyant force becomes stronger. Secondly, the fluid and heat flow is found stronger at $\gamma = 45°$ when Ra = 10^4 and 10^5, but it is stronger at $\gamma = 90°$ when Ra = 10^6, due to lesser MHD dampening effect, as for this case, the Lorentz force is a function of *U*-component of velocity only. The coupled physics for static temperature distribution (Figures 4.6 and 4.9) and heat flow (Figures 4.7 and 4.10) take their shape accordingly to the fluid flow structures depicted in Figures 4.5 and 4.8.

Comparing the results of the square and circular systems, it is clear that, under constraint-based consideration of geometrical shape, the fluid flow, heat flow, and heat transfer are enhanced in the case of circular geometry for all combinations of

flow parameters. One reason for this is that smoother flow-turning causes lesser hydraulic resistance against the flow.
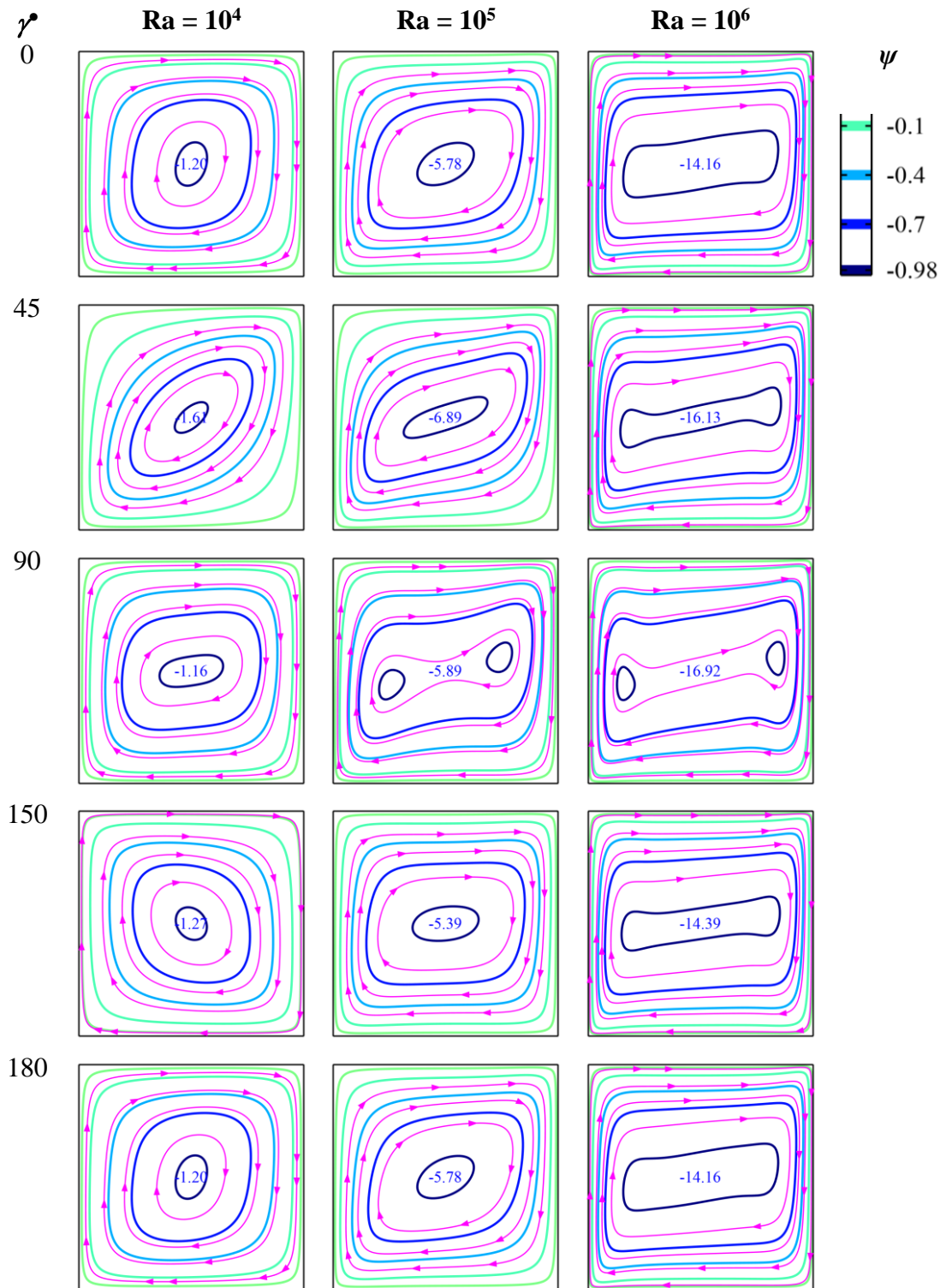
Figure 4.5 Magnetic field inclination effects on streamlines of the square thermal system.
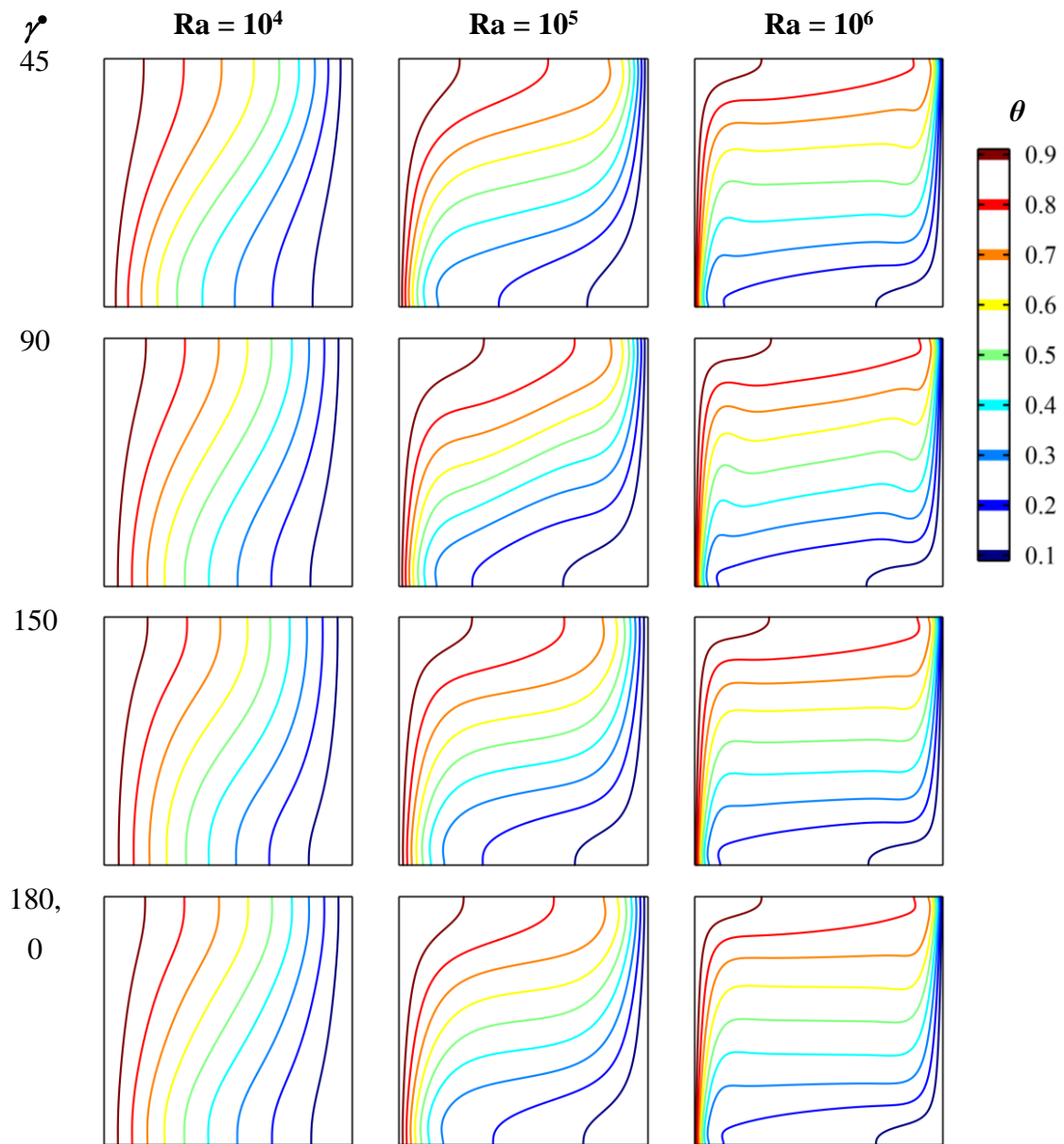
Figure 4.6 Magnetic field inclination effects on isotherms of the square thermal system.
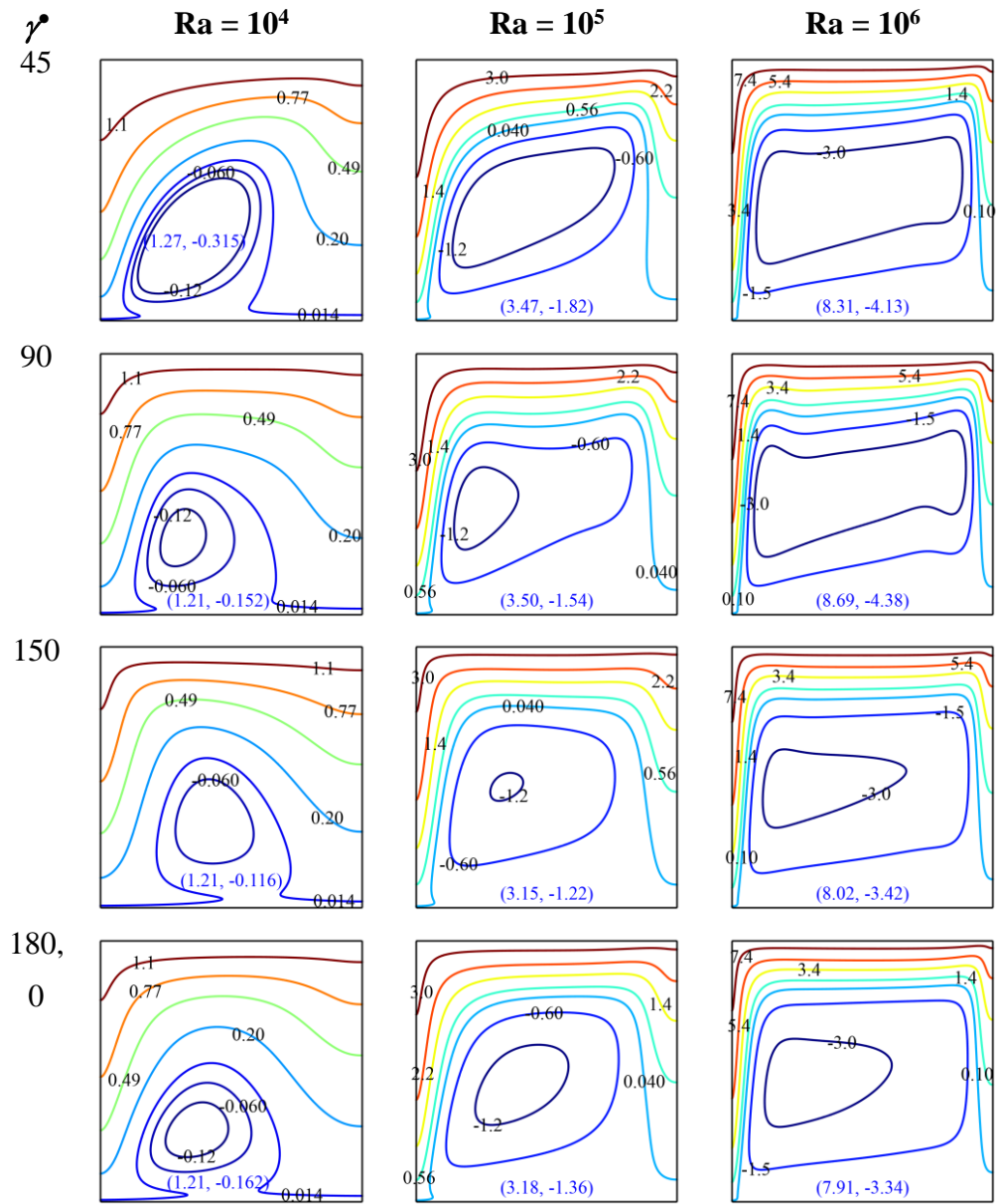
Figure 4.7 Magnetic field inclination effects on heatlines of the square thermal system.
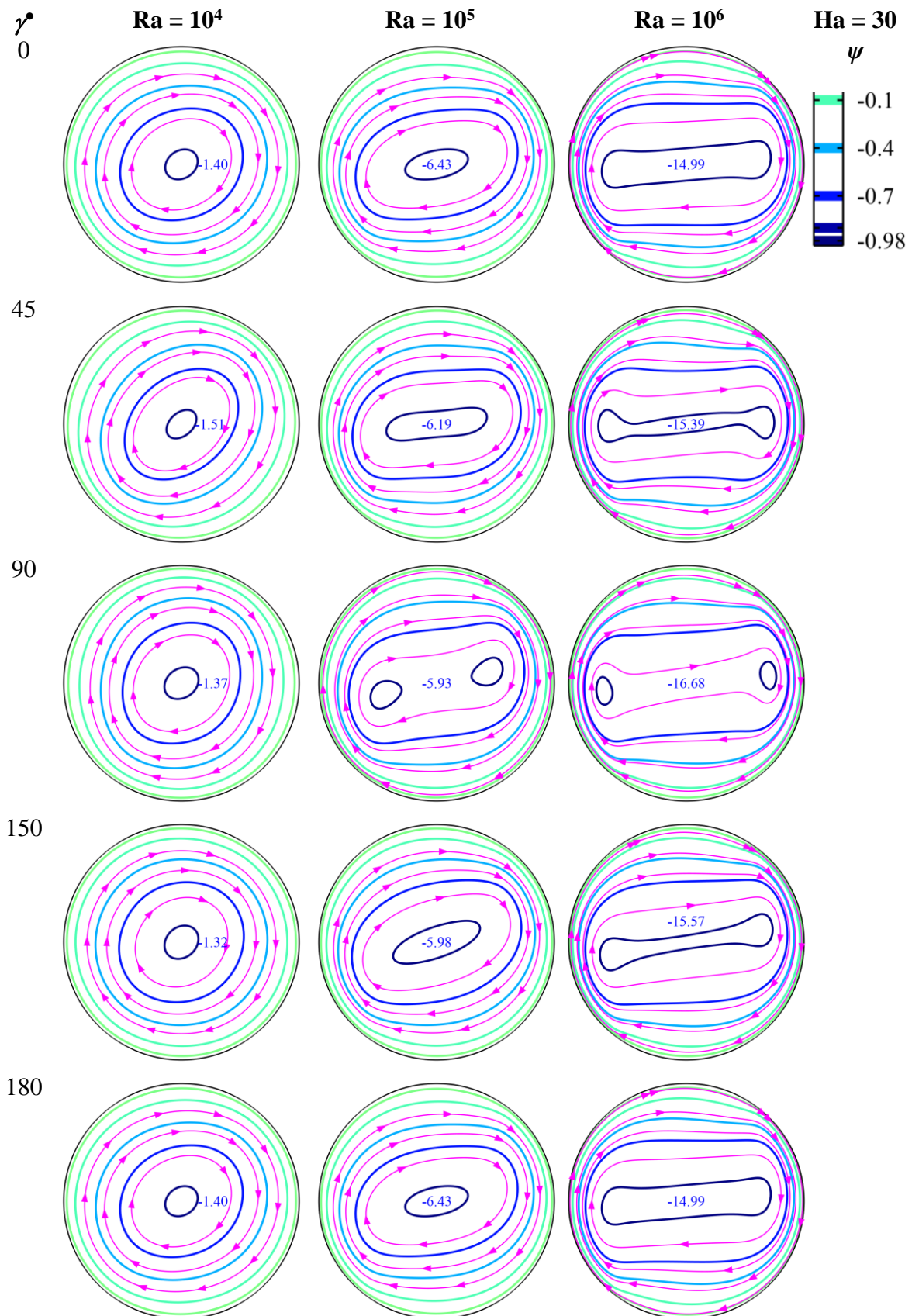
Figure 4.8 Magnetic field inclination effects on streamlines of the circular thermal system.
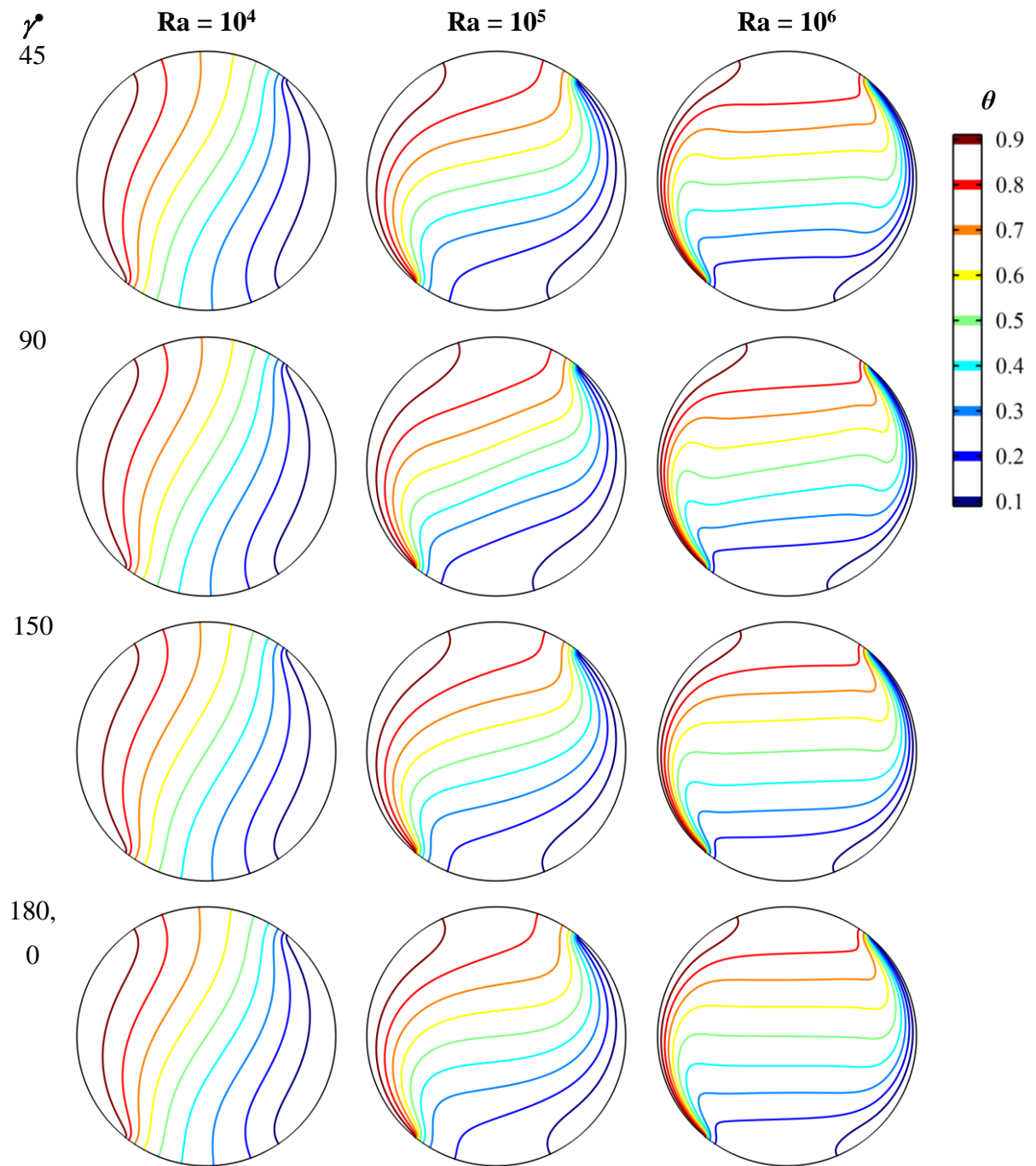
Figure 4.9 Magnetic field inclination effects on isotherms of the circular thermal system.
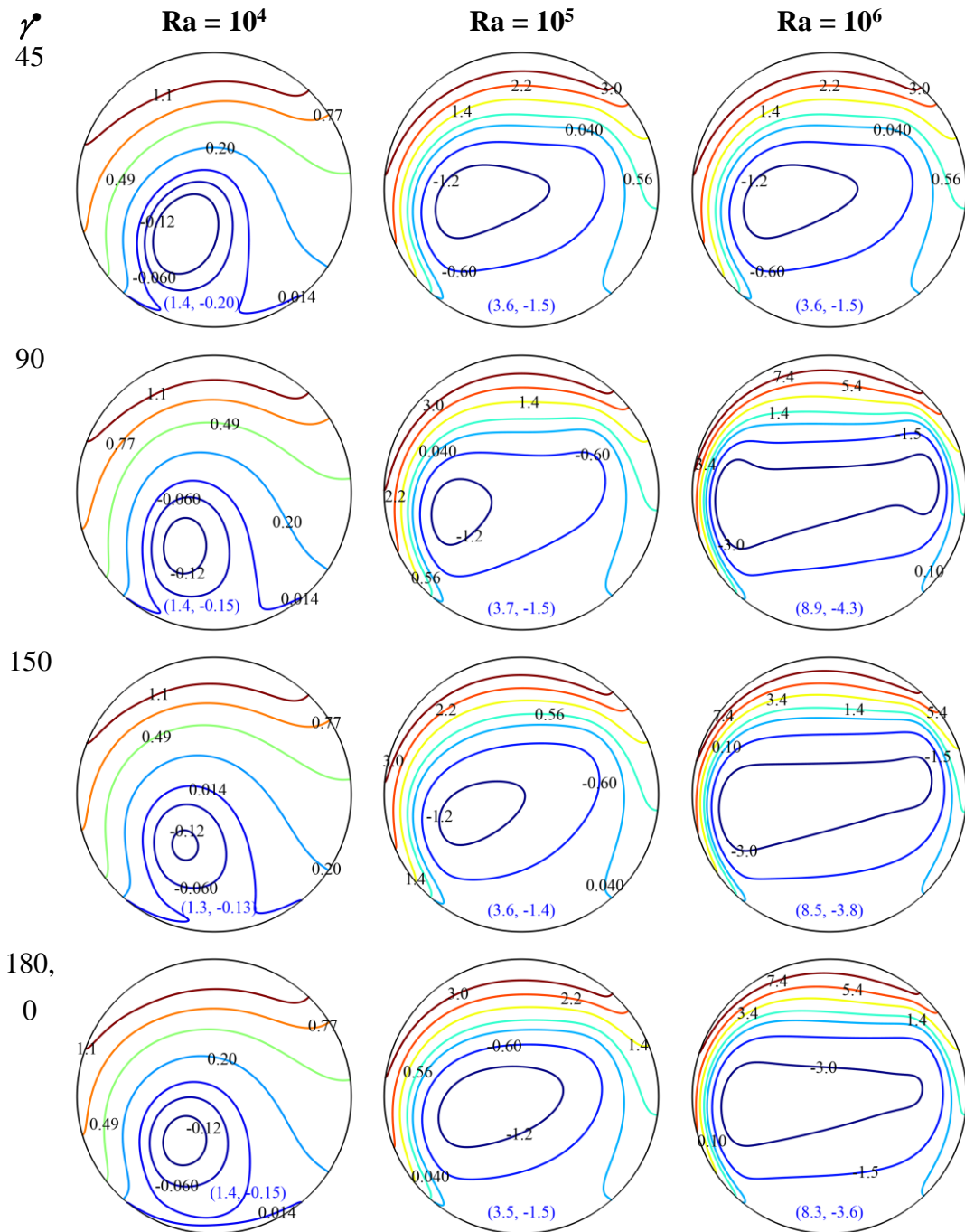
Figure 4.10 Magnetic field inclination effects on heatlines of the circular thermal system.

4.4.3 *Sectional analyses of flow structures (U, V, θ)*

In order to understand the in-depth flow physics of the equivalent thermal systems (EDHSC and EDHCC) and assess the effect of the magnetic field, sectional analyses of velocities (*U*, *V*) and temperature (*θ*) profiles at the horizontal and vertical planes are conducted. These analyses are performed with fixed Ra = 10^6 and various Ha (= 0, 50, 100) and field angles *γ* (= 0, 45, 90, 150°) for both systems. The mid-

velocity components are shown in Figures 4.11 and 4.12, while the mid-temperature profiles are in Figures 4.13 and 4.14. The impacts of different Ha at γ = 0° and Ha = 100 at various field angles are remarkable.

(a) *V* for square cavity

(b) *V* for circular cavity

(c) *U* for square cavity

(d) *U* for circular cavity
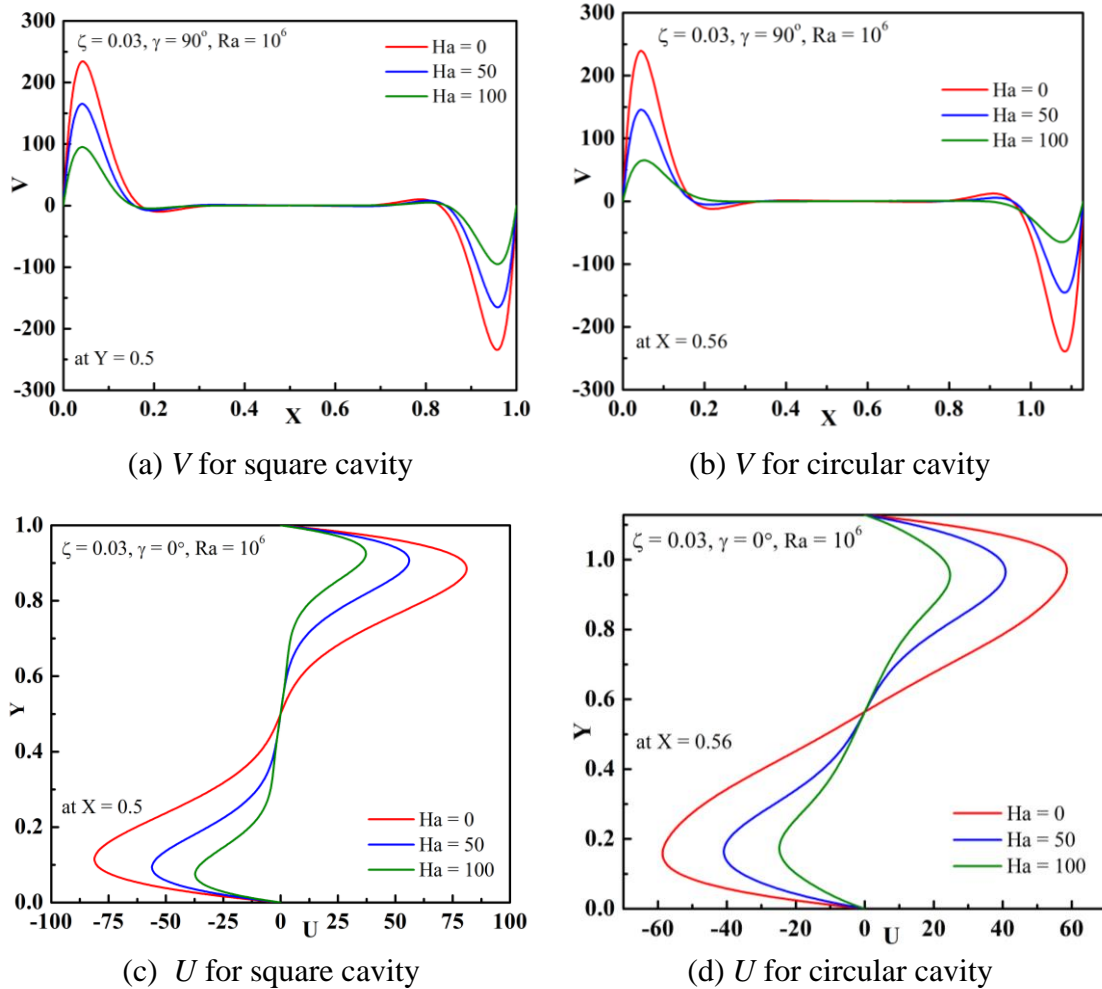
Figure 4.11 Effect of Ha and cavity shape on sectional *U* and *V* plots in EDHSC and EDHCC.

Figure 4.11 illustrates the mid-vertical velocity (*V*) components at *Y* = 0.5 for EDHSC and at *Y* = 0.56 for EDHCC. It shows that near-wall boundary layer formation occurs over a short distance of 0.2 extents, with the upward flow at the left wall (*X* = 0) and downward flow at the right wall (*X* = 1). The magnitude of the peak velocity decreases, resulting in thicker boundary layers, as expected with an increase in Ha. The mid-horizontal velocity (*U*) component takes a sinusoidal shape, especially at Ha = 0 for the circular system. For other values of Ha, the *U*-velocity peaks are located near their walls (at *Y* = 0 and 1) similar to the *V*-velocity profiles. However, the magnitude of the *V*'s peaks is substantially higher than the *U*'s peaks as the active walls are located on the sidewalls, participating in heat transfer and the main driving flows evolved thereon.

(a) *V* for square cavity

(b) *V* for circular cavity

(c) *U* for square cavity

(d) *U* for circular cavity
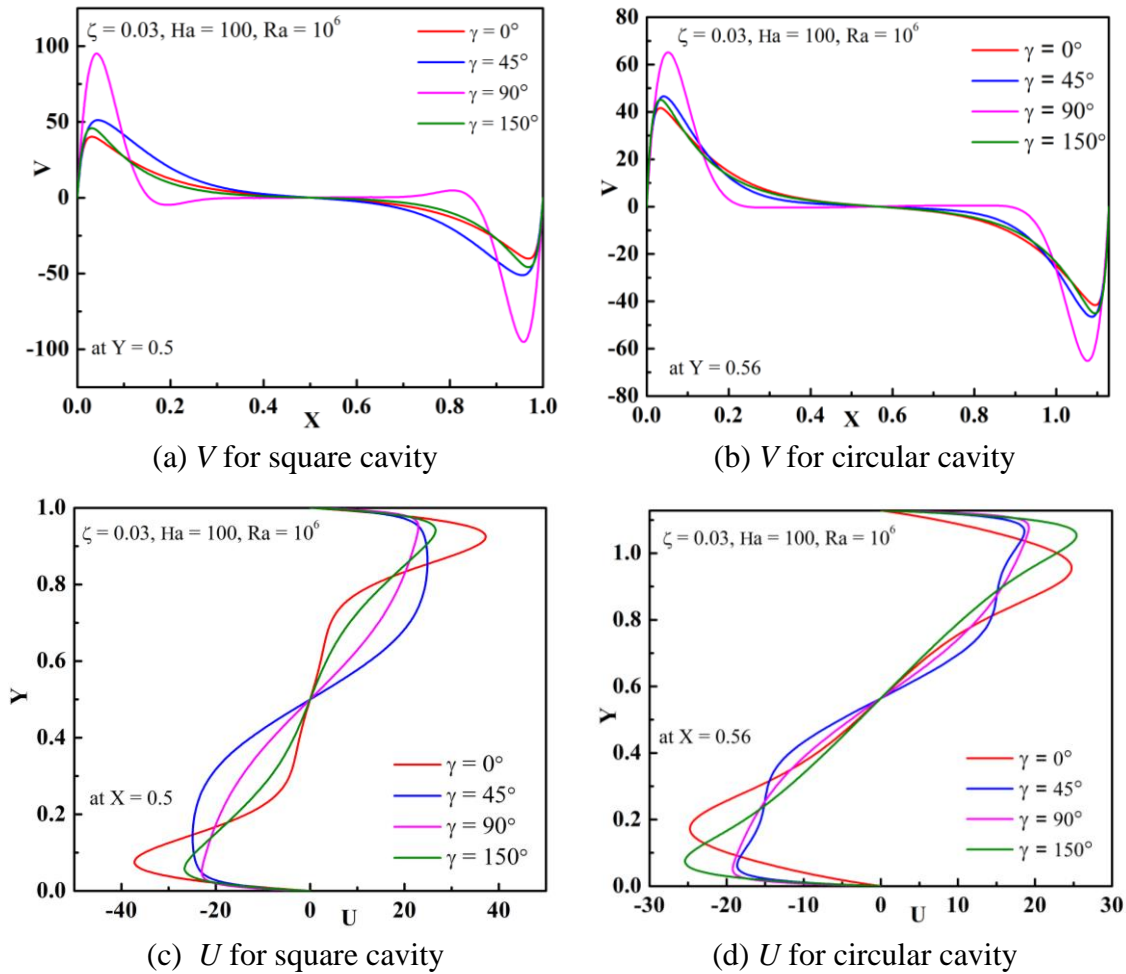
Figure 4.12 Effect of γ and cavity shape on sectional *U* and *V* plots in EDHSC and EDHCC.

Figure 4.12 illustrates the different profiles of *V*- and *U*-velocity components when the field angle γ changes from 0° to various angles (45°, 90°, and 150°), compared to their previous presentation on various Ha. The magnitudes of all velocity peaks substantially reduce (become half or less) compared to the previous figure. Except for $\gamma = 0°$ in the case of *U*-velocity and $\gamma = 90°$ in the case of *V*-velocity, all other angles, the changes in peak magnitudes of velocity are comparatively less. Although the *V*-velocity maintains their profiles similar at various values of γ, the drastic changes are noted in the case of the *U*-velocity profiles. Different *U*-patterns evolve when γ changes, and the changes in patterns, particularly at $\gamma = 45$ and 90°, are well marked. The effects of geometric shapes are also prominent, which is clearly realizable from Figures 4.12c and 4.12d. The reason behind these observations could be realized from the force effect. The substantial change in magnetic force component in the horizontal direction takes place with γ, as it also involves both *U* and *V* components of velocity.

The mid-plane temperature profiles were obtained from the simulated results to complement the velocity profiles, as depicted in Figures 4.13 and 4.14. The temperature boundary layers' formation is clearly observed in Figures 4.13a and 4.13b, where the left wall is hot and the right wall is cold. It can be seen that the temperature, represented by θ, sharply decreases from $\theta = 1$ near $X = 0$, reaching $\theta = 0.5$ at the middle of the geometries, followed by a continued sharp fall to $\theta = 0$ near $X = 1$.

(a) Mid-horizontal θ for square cavity (b)Mid-horizontal θ for circular cavity

(c) Mid-vertical θ for square cavity (d) Mid-vertical θ for circular cavity
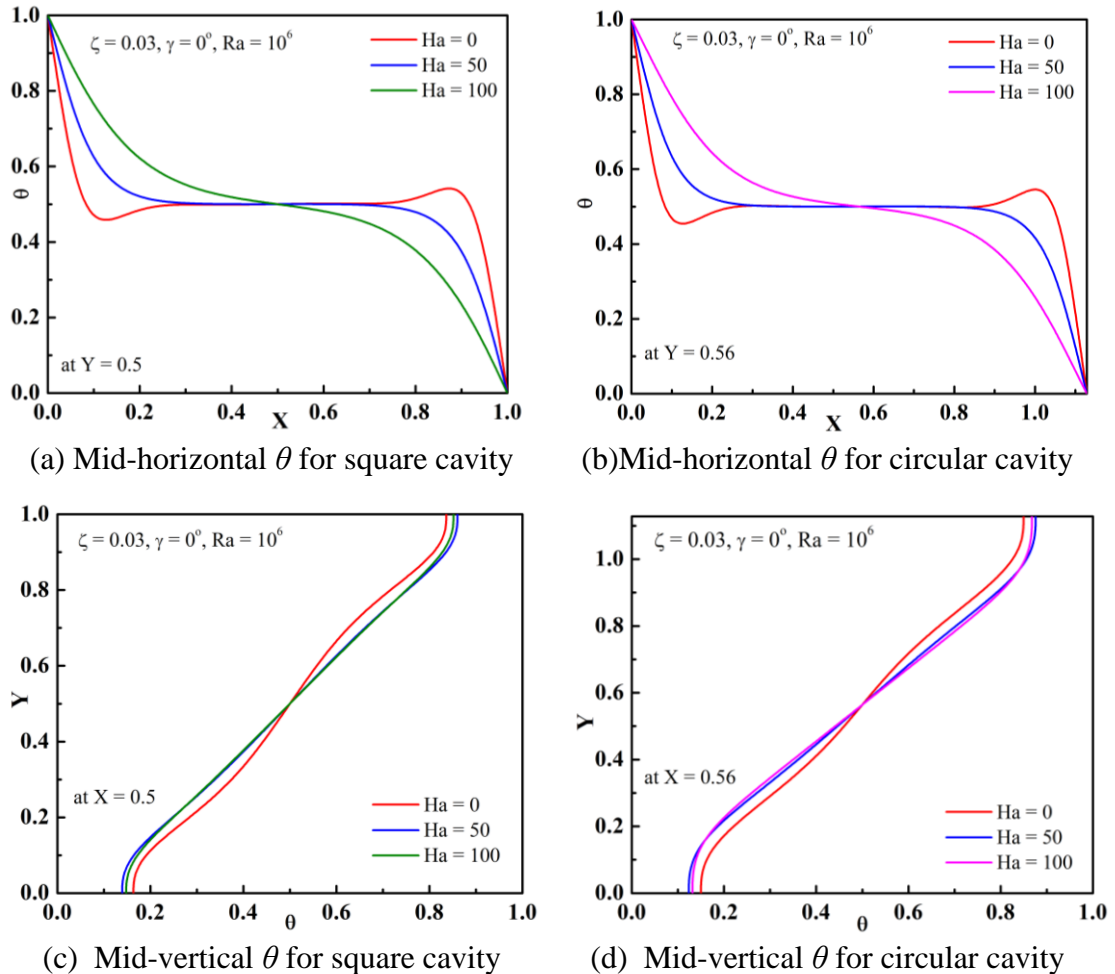
Figure 4.13 Effect of Ha and cavity shape on sectional θ plots in EDHSC and EDHCC.

The effect of the Hartmann number on the mid-horizontal θ is significant and similar for both EDHSC and EDHCC thermal systems. However, as shown in Figures 4.13c and 4.13d, the mid-vertical θ remains almost constant, with minor variations with Ha, regardless of the system's geometric shape. This absence of thermal boundary layers is justified by the presence of adiabatic systems' walls.

The temperature profiles with γ in Figure 4.14a show minor changes, except for $\gamma = 90°$. Nevertheless, the changes in θ (dimensionless temperature ranging from 0

to 1) are markedly noted in Figures 4.14b to 4.14d due to the previously explained changes in their velocity profiles.

(a) Mid-horizontal θ for square cavity   (b) Mid-horizontal θ for circular cavity

(c) Mid-vertical θ for square cavity   (d) Mid-vertical θ for circular cavity
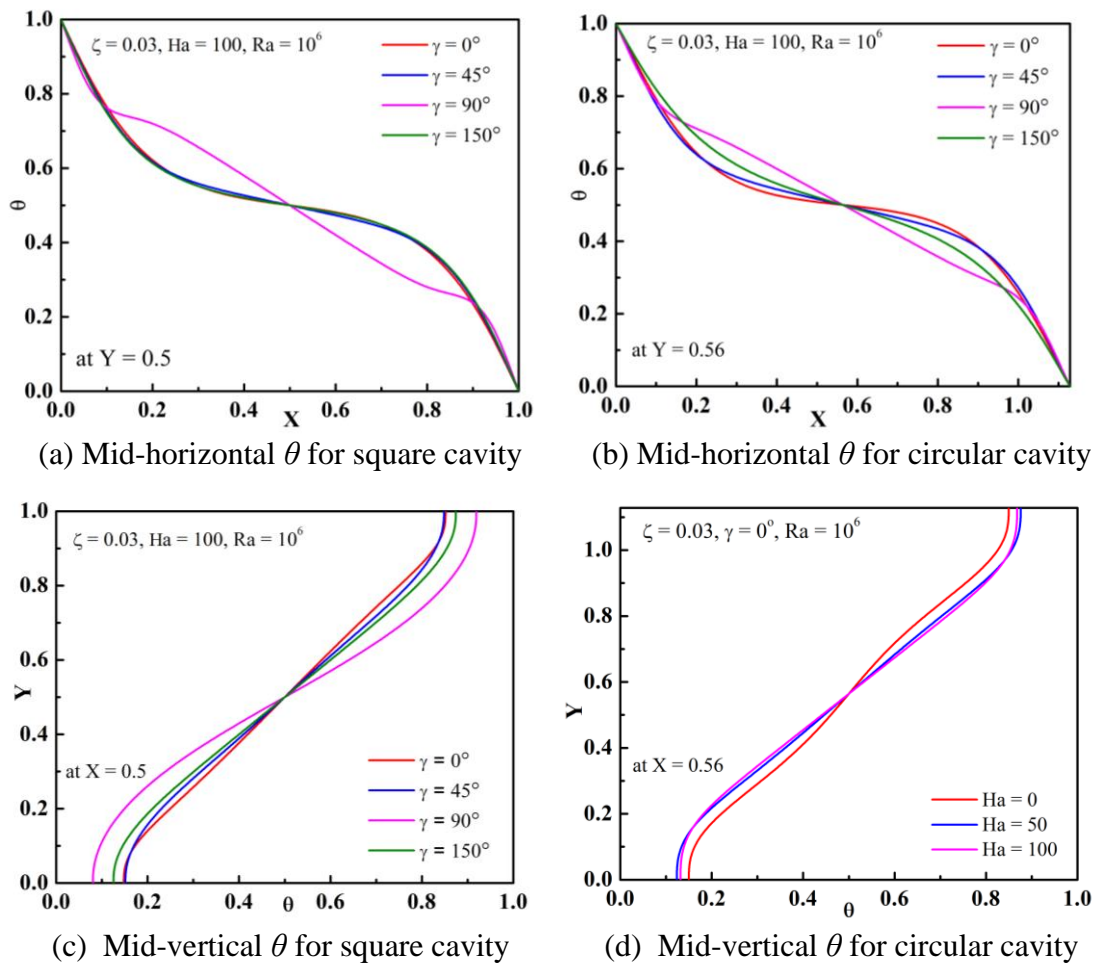
Figure 4.14 Effect of γ and cavity shape on sectional θ plots in EDHSC and EDHCC.

In summary, the sectional analyses of flow structures (U, V, θ) presented in this section provide valuable insights into the effects of magnetic field and field angle on the flow and thermal behaviors of the EDHSC and EDHCC thermal systems, showing significant impacts.
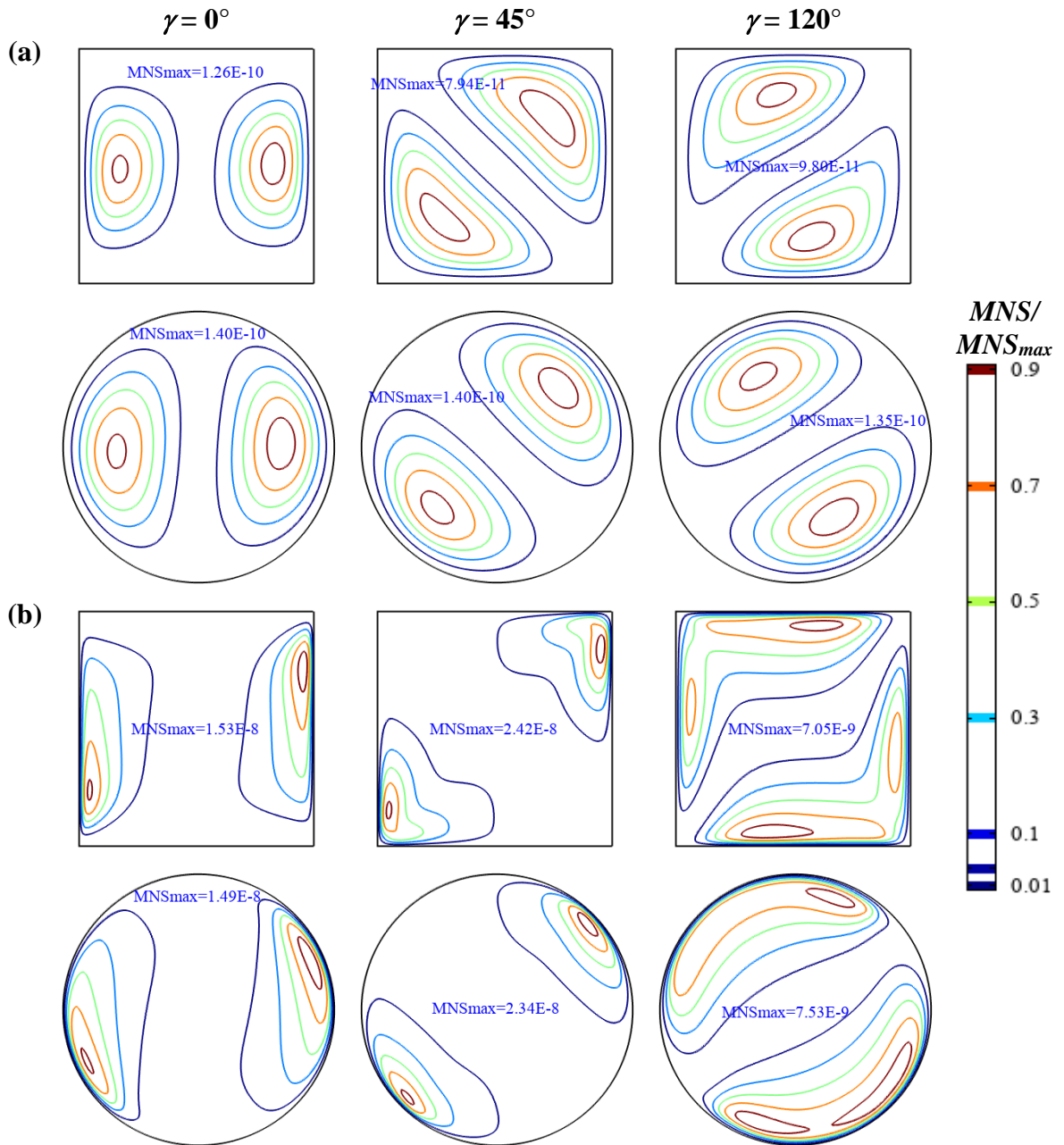
Figure 4.15 Magnetic field inclination effects on the magnetic contribution of irreversibility for ζ = 3%: (a) Ha = 05 and Ra = 10^3, (b) Ha = 70 and Ra = 10^5.

4.4.4 *Thermal systems' irreversibilities*

This section analyzes thermodynamic irreversibility generation in EDHSC and EDHCC in dimensionless form with the help of Figures 4.15 to 4.18 presenting normalized quantities. As previously discussed in Chapter 1, the entropy generation (EG) consists of three contributing physics: temperature gradient (NS_{tg}), viscous effect (NS_v), and magnetic field (NS_m). Figure 4.15 presents the impact of magnetic field inclination (at γ = 0, 45, and 120°) on magnetic entropy generation at ζ = 3% for two

sets of values: Ha = 05 and Ra = 10^3 in Figure 4.15a, and Ha = 70 and Ra = 10^5 in Figure 4.15b. The various orientations of NS_m contours reflect the significant impact of γ changes due to the sharing of the magnetic force in the horizontal and vertical directions. At $\gamma = 0°$, the localization of NS_m is noted at the sidewalls as the entire magnetic force, being the function of *V*-velocity only, is acting in the vertical direction opposing the buoyant force. At $\gamma \neq 0°$, both the components of magnetic force exist and they are a function of both *U*- and *V*-velocity; therefore, the orientation of NS_m localization becomes more or less diagonal at $\gamma = 45°$ and 120° (90°+30°) for the square thermal system. The same observations are noted for the circular thermal system with more uniform distributions of NS_m contours due to the conduction regime of heat transfer with a very weaker flow velocity at Ra = 10^3. However, this uniformity in distributions is substantially lost in Figure 4.15b, due to the evolved stronger convective velocity at Ra = 10^5 although the magnetic damping force at Ha = 70 is strong. The maximum NS_m values indicated in the figures reflect that the value of NS_m is very small.

Figure 4.16 presents the impact of Rayleigh numbers (10^3, 10^4, 10^5) on the viscous part of entropy generation at $\zeta = 3\%$ for two sets of values: $\gamma = 0°$ and Ha = 5 (Figure 4.16a), $\gamma = 120°$ and Ha = 30 (Figure 4.16b). The viscous entropy generation is observed to be located near all the walls for both the square and circular geometries. This is due to the formation of the velocity boundary layer where the velocity gradients are significantly stronger than in the central region of the fluid flow. At higher Rayleigh numbers, the localization of NS_v occurs over the active sidewalls. However, similar to NS_m, the magnitude of NS_v is also very small.

The orientation and distribution of NS_m contours are affected by changes in the magnetic field inclination, as both horizontal and vertical components of the magnetic force come into play. At a magnetic field inclination of 0 degrees, NS_m is localized at the sidewalls because the entire magnetic force, which is a function of *V*-velocity only, acts vertically against the buoyant force. At other magnetic field inclinations, the orientation of NS_m localization becomes more diagonal as both *U*- and *V*-velocity contribute to the magnetic force. This is observed at the field angles of 45 and 120 degrees for the square thermal system, as well as the circular thermal system with more uniform distributions of NS_m contours due to a weaker flow velocity at Ra = 10^3. However, this uniformity is lost in Figure 4.15b due to stronger convective velocity at

Ra = 10^5, despite the strong magnetic damping force at Ha = 70. It is also noted that NS_m values are very small, as indicated by the maximum NS_m values in the figures.
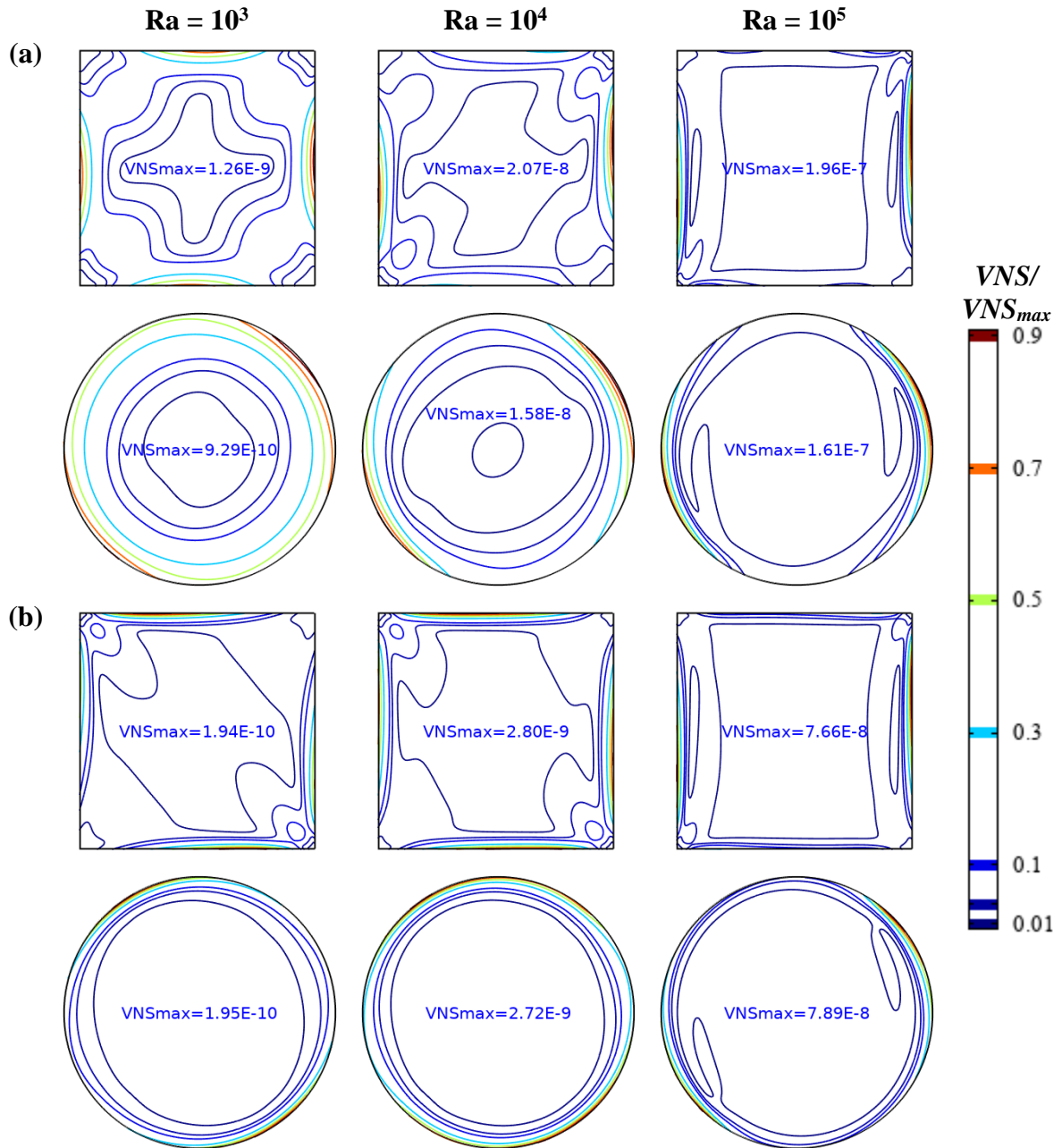
Figure 4.16 Effects of Ra-Ha-γ on viscous contribution of irreversibility (within square and circular domains) for ζ = 3%: (a) γ = 0° and Ha = 5, (b) γ = 120° and Ha = 30.

Figures 4.17 and 4.18 depict the total entropy generation (*NS* or *NS*$_l$) which equals the thermal contribution of EG, NS_{tg}. The magnitudes of the maximum local *NS* for γ = 90° and ζ = 1% are found to be significantly high compared to the magnitudes of NS_m and NS_v. The maximum NS_l is located where the temperature gradients are strongest, such as at the bottom of the left hot wall or the top of the right cold wall. In general, NS_{tg} or NS_l at higher Ra is densely distributed over the heated

and cooled sidewalls. For the circular geometry, the maximum NS_1 mentioned in the figures are very high due to a higher rate of heat transfer compared to their square geometry cases.
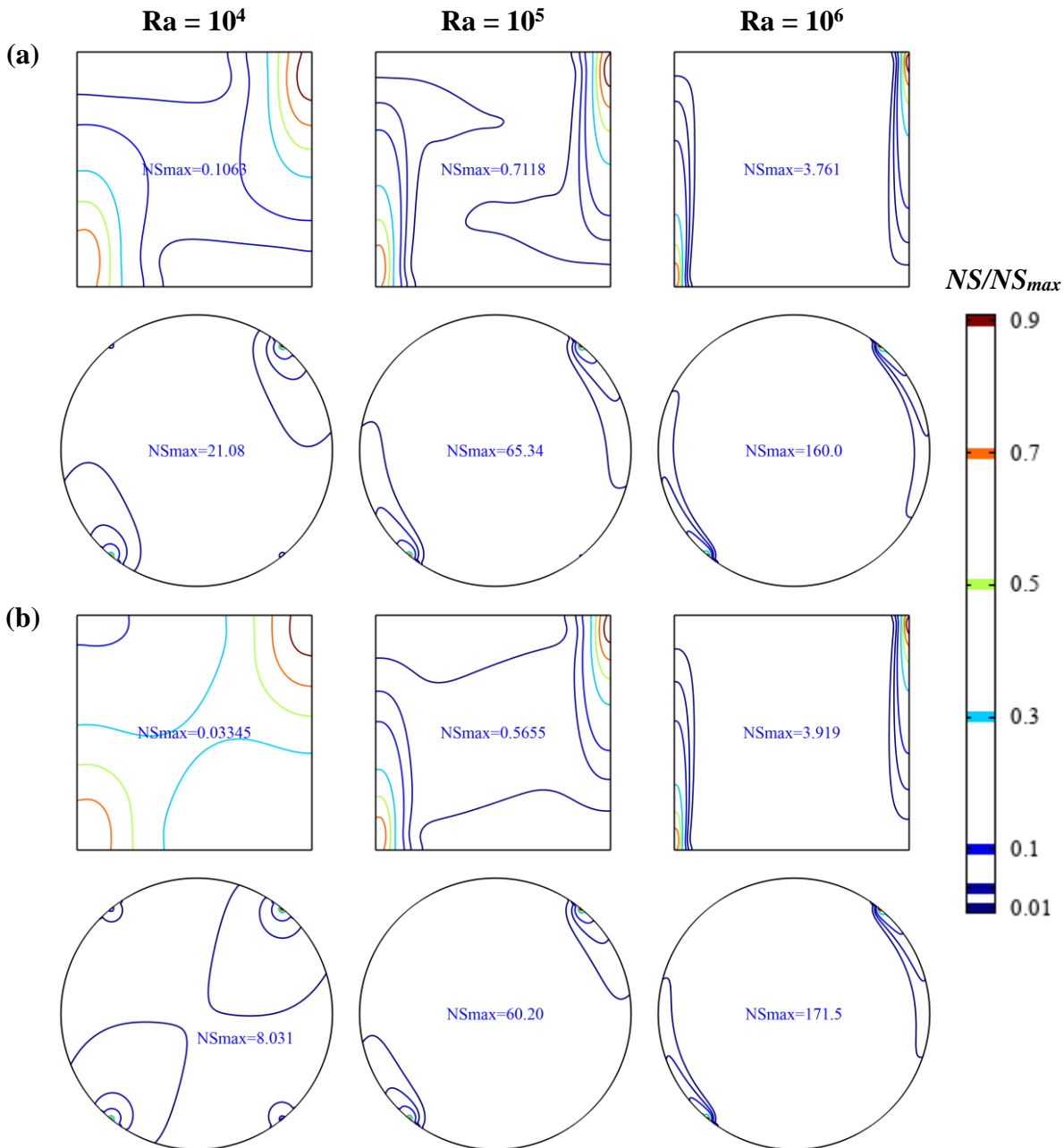
Figure 4.17 Effects of Ra on thermal systems' irreversibilities for $\gamma = 90°$ and $\zeta = 1\%$: (a) Ha = 10, and (b) Ha = 30.

Although the localization of NS_1 is markedly influenced by Ra values, as indicated in Figures 4.17a (for Ha = 10) and 4.17b (for Ha = 70), it appears almost invariant with the change of γ (0, 75, 120°) for Ha = 5 and Ra = 10^3 in Figure 4.18a (showing conduction regime) and Ha = 70 and Ra = 10^6 in Figure 4.18b (showing convection regime).
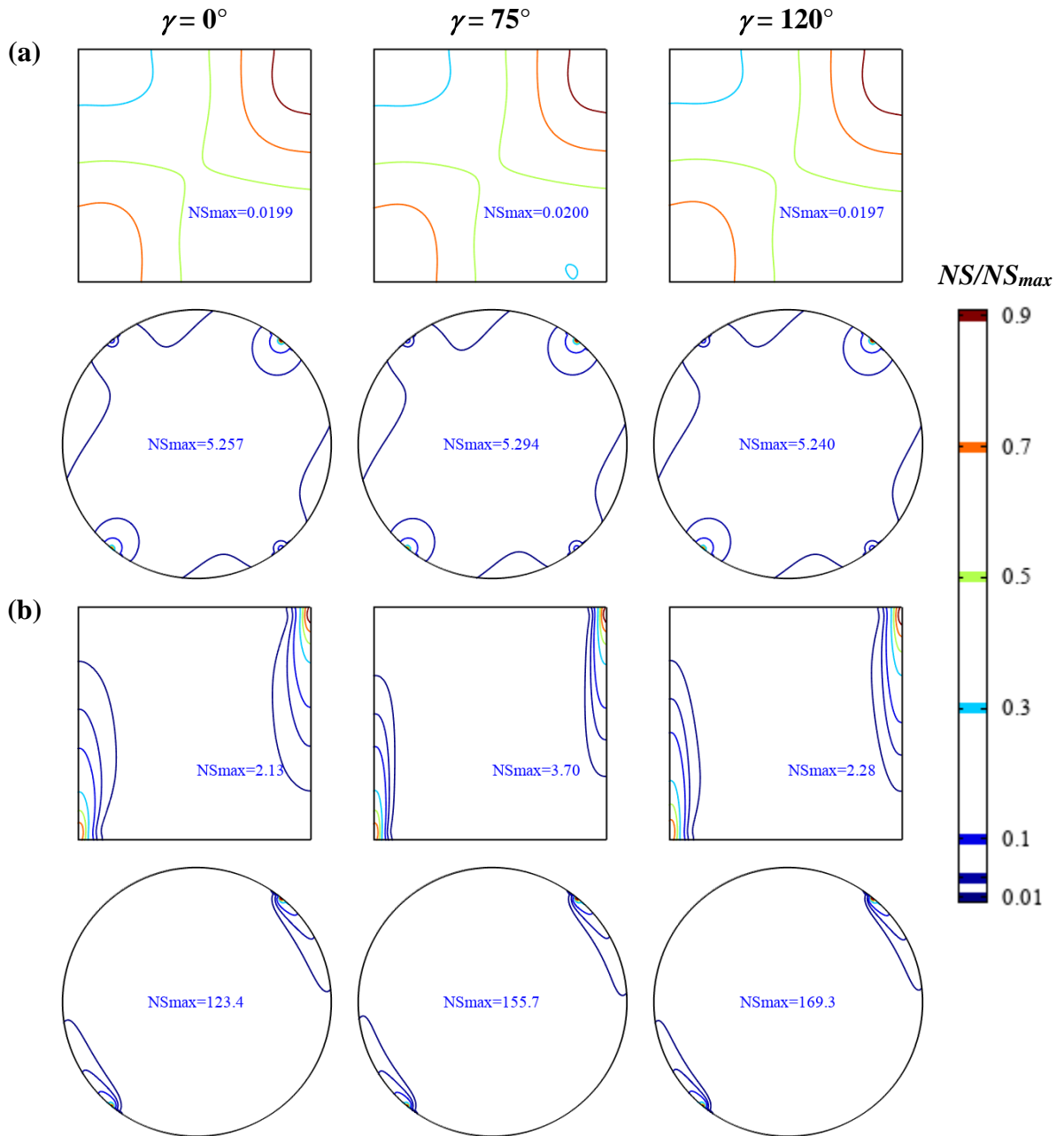
Figure 4.18 Ra effects on thermal systems' irreversibilities for $\zeta = 3\%$: (a) Ha = 05 and Ra = 10^3, (b) Ha = 70 and Ra = 10^6.

4.4.5 *Analysis of global parameters (Nu, ψ_{min})*

In this section, the global heat transfer and fluid flow characteristics of equivalent square and circular thermal systems are analyzed using the mean Nusselt number (Nu) and the maximum value of the streamfunction (ψ_{max}), as illustrated in Figures 4.19 and 4.20.

The impact of Ra on Nu in EDHSC and EDHCC is presented in Figure 4.19a for various Ha values ranging from 0 to 100 at fixed $\gamma = 0°$ and $\zeta = 3\%$. It is observed that for low Ra (= 10^3), the Nu is nearly equal to unity, indicating the conductive

mode of heat transfer. However, as Ra increases, the Nu also increases, and the thermal performance of EDHCC is found to be better than EDHSC for all cases, which is explained in detail in Chapter 3. Higher Ha values yield lower Nu for all Ra.

(a) Ra effect on Nu at different Ha   (b) Ra effect on Nu at different *γ*

(c) Ra effect on ψ_{min} at different Ha   (d) Ra effect on ψ_{min} at different *γ*
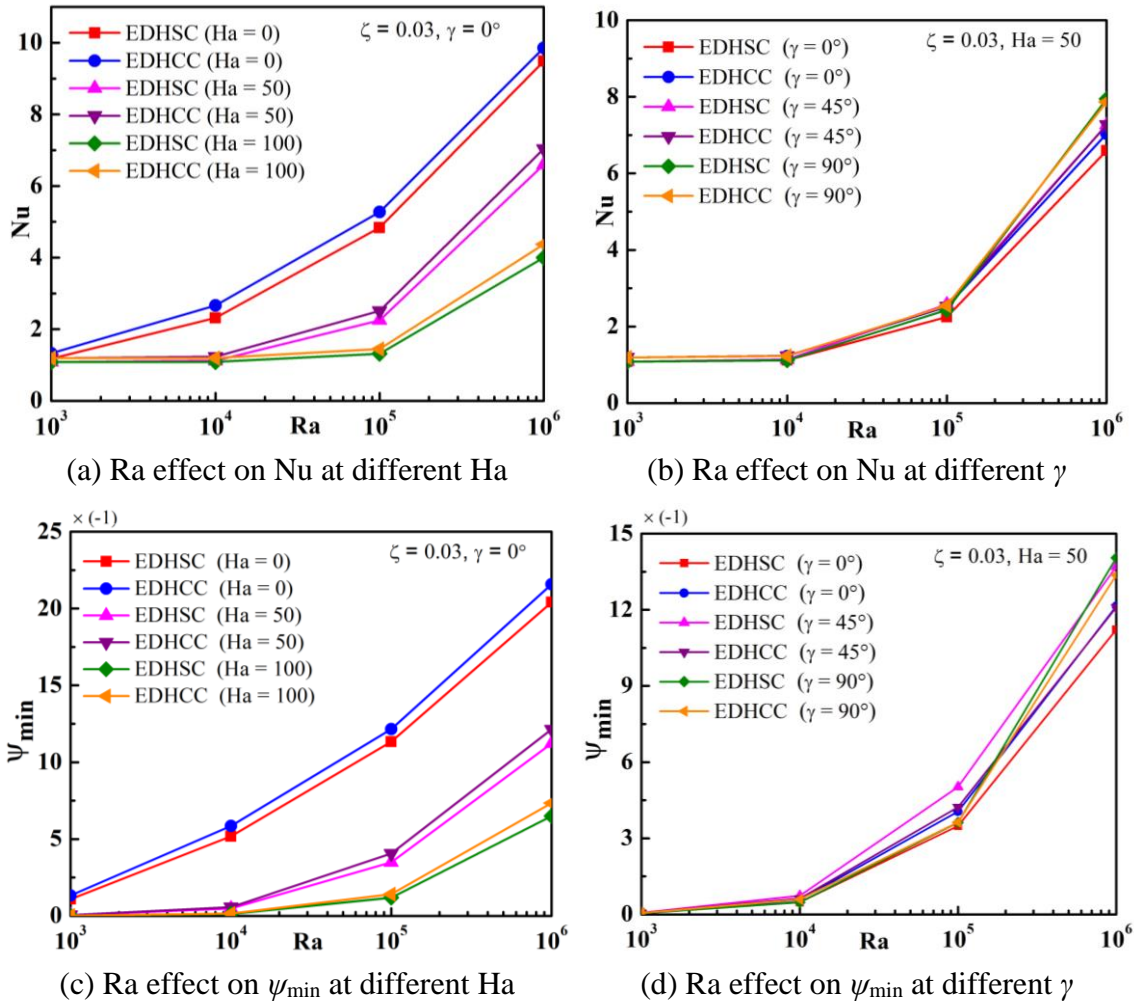
Figure 4.19 Variation of Nu (a-b) and ψ_{min} (c-d) with Ra for EDHSC and EDHCC at different Ha and *γ*.

Figure 4.19b illustrates the influence of Ra on Nu for EDHSC and EDHCC for various *γ* values ranging from 0° to 180° at fixed Ha = 50 and *ζ* = 3%. The effect of Ra on Nu is presented for distinct values of γ (= 0, 45, and 90°). It is observed that as *γ* varies, the component of Lorentz force varies along the horizontal and vertical directions, resulting in a variation of Nu. As Ra increases, the Nu monotonically increases for all values of γ, with the variation being more prominent at higher Ra due to the enhanced buoyant force.

The impact of Ra on ψ_{max} in EDHSC and EDHCC for various Ha (0−100) at fixed *γ* = 0° and *ζ* = 0.03 is presented in Figure 4.19c. It is noted that the strength of flow varies with Ra, Ha, and *γ* as the temperature and velocity are coupled in

buoyancy-induced flow. For low Ra, the flow strength is weak, indicating the conductive mode of heat transfer. As Ra increases, the flow strength increases, resulting in a rise in the value of ψ_{max}.

Figure 4.19d shows the effect of Ra on ψ_{max} for various γ at fixed Ha = 50 and ζ = 3%. As γ varies, the component of Lorentz forces also varies, resulting in a variation of ψ_{max}. It is observed that for all values of γ, the ψ_{max} monotonically increases with an increase in Ra due to the enhanced buoyant force. The effect of Ra on ψ_{max} is presented for distinct values of γ (= 0, 45, and 90°) to provide a clearer understanding of the variation.

The impacts of Ha and γ on Nu are demonstrated at different values of other parameters in Figure 4.20. In Figure 4.20a, the impact of Ha on Nu is shown for both EDHSC and EDHCC at various Ra values (ranging from 10^3 to 10^6) with fixed γ (0°) and ζ (3%). The application of a magnetic field to an electrically conducting fluid subjected to buoyancy-driven flow creates an opposing force known as the Lorentz force. As Ha increases, the Nu decreases for square and circular thermal systems, indicating that non-MHD flow has better thermal performance than MHD flow. This can be attributed to the opposing nature of the Lorentz force to the buoyant force.

In Figure 4.20b, the effect of Ha on Nu is depicted for different γ values (ranging from 0° to 90°) at a fixed Ra value of 10^6 and ζ value of 3%. The Nu peaks at Ha = 0 for all cases and increases in Ha result in a decrease in Nu due to the rise in the Lorentz force, which opposes the buoyant force and reduces heat transfer.

Figure 4.20c displays the impact of γ on Nu for various Ra values (ranging from 10^3 to 10^6) at fixed Ha (100) and ζ (3%). The value of Nu at γ = 0° and 180° is identical for all cases. The variation of Nu with γ is minimal at low Ra values (10^3 and 10^4) and becomes more prominent at high Ra values (10^5 and 10^6). The optimum heat transfer for EDHSC occurs at Ra = 10^6 and γ = 90° because the vertical component of the Lorentz force is zero at this angle. EDHCC generally has better thermal efficiency than EDHSC at γ = 0, 120, 150, and 180° for Ra = 10^6.

Finally, Figure 4.20d shows the effect of γ on Nu for various Ha values (ranging from 0 to 100) at a fixed Ra value of 10^6 and ζ value of 3%. At low Ha values (10), the variation of Nu with γ is insignificant but becomes more prominent at higher Ha values (50 and 100) due to the greater impact of the Lorentz force on the buoyant force.

(a) Ha effect on Nu at different Ra

(b) Ha effect on Nu at different γ

(c) γ effect on Nu at different Ra

(d)) γ effect on Nu at different Ha
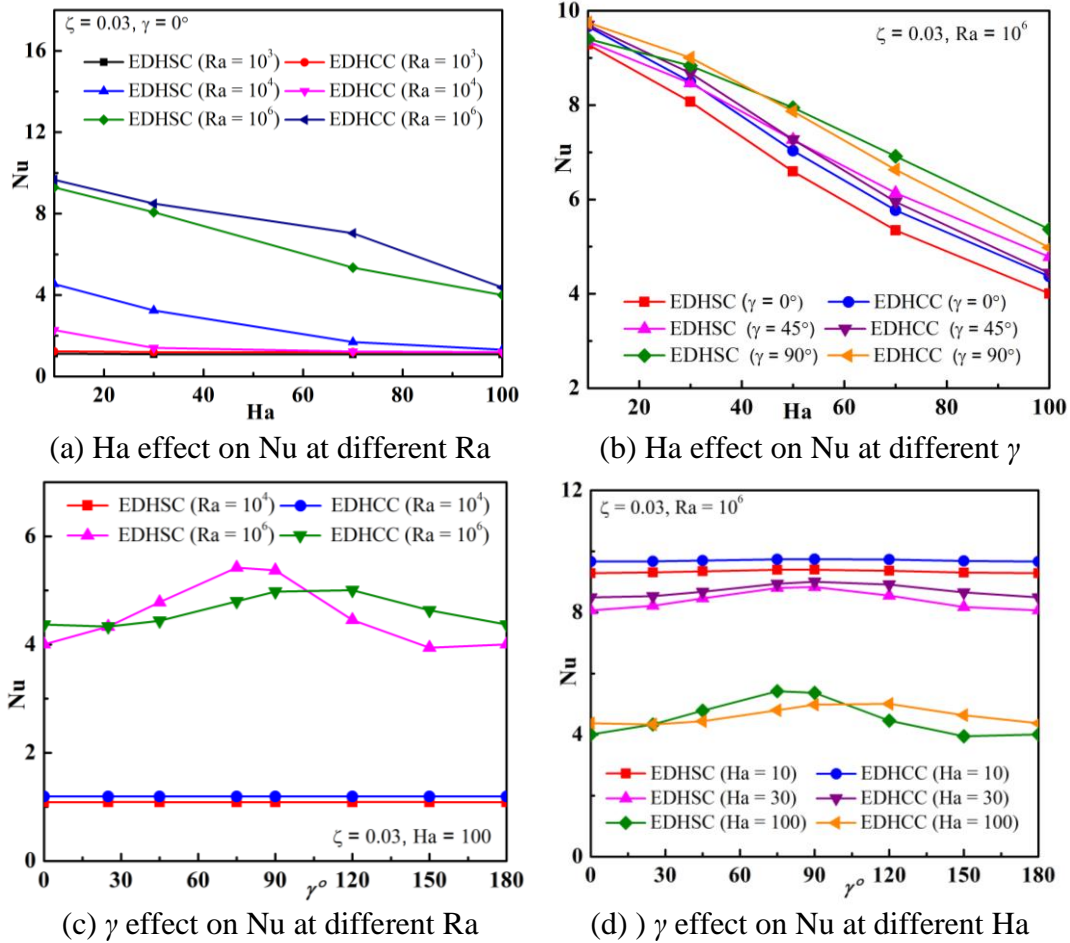
Figure 4.20 Variation of Nu with Ha (a-b) and Nu with γ (c-d) for EDHSC and EDHCC at different Ra, Ha, and γ.

4.5 Conclusions

In this study, a new approach for analyzing convective nanofluidic thermal systems in the presence of magnetic fields is presented to aid system developers in choosing between square and circular shapes of thermal system geometry based on superior thermal performance. Key observations and conclusions of the study are summarized as follows:

- This constraint-based study showcases a strong correlation between the shape of thermal systems and the flow behaviors that evolve as the flow structures adapt to the domain shape. The study highlights the significant impact of shape on the behavior of the heat flow in equivalent thermal systems.

- The circular geometry outperforms its equivalent square geometry in terms of heat flow, fluid flow, and heat transfer due to the following reasons:

1. The circular shape has a smaller wall perimeter, resulting in less surface frictional effects and improved convective flow, heat transport, and fluid and energy circulations.

2. Fluid flow can take smoother turns inside the circular thermal system, saving energy and enhancing the fluid flow and resulting heat transfer.

3. The maximum height of the circular geometry is higher, which enhances the buoyant force, thereby improving MHD nanofluidic thermal convection.

- The equivalent circular thermal system is more efficient with heat transfer enhancements of approximately 17.7% compared to the square geometry. Corresponding irreversibility production rate is also higher, which is up to 17.6%.

- An increase in the nanoparticle concentrations always enhances the heat transfer up to 4.7% (for circular system) and 5.3% (for the square system) compared to base fluid. Corresponding irreversibility production rate follows the similar patterns.

- Heatlines accurately depict the heat flow patterns in both thermal systems, which are strongly influenced by the Rayleigh number, Hartmann number, and cavity shape.

- The impact of viscous as well magnetic contributions to thermodynamic irreversibility generation is negligible. Therefore, the thermal contribution is mainly governed by the total entropy generation.

- The total EG increases with Ra and decreases with an increase in Ha.

- The effect of magnetic field orientation (γ) on total EG is minor.

- The local *NS* is markedly higher where temperature gradients are large, particularly at the bottom end of the heating wall and the top end of the cooling wall.

In summary, this study provides valuable insights into the choice of cavity shape for convective nanofluidic thermal systems in the presence of magnetic fields, with circular geometry being the more efficient choice for achieving superior heat transfer.

Chapter – 5

Heat transport and irreversibility during MHD nanofluid flow in the constraint-based analogous square, trapezoidal, and triangular thermal systems

5.1 Introduction

This chapter focuses on heat transport and irreversibility production during MHD nanofluid flow in the constraint-based analogous square, trapezoidal, and triangular thermal systems. The buoyancy-induced flow in these enclosures is diverse and multidisciplinary applications, incorporating aspects of fluid mechanics, heat transfer, and materials science. The findings of these studies can be applied to a wide range of engineering and industrial applications, from the design of cooling systems in electronics to the optimization of energy systems.

The study of buoyancy-driven convection in trapezoidal enclosures has been an interesting topic for many researchers, and there are several pioneering studies on the subject (Lee 1991; Perić 1993; Kuyper and Hoogendoorn 1995). Kuyper and Hoogendoorn (1995) found that the intersection angles of the isothermal and adiabatic walls affect fluid motion and heat transport at the enclosure's corners significantly. There are fundamental numerical research studies available, which provide a good insight into this field (Natarajan et al. 2008; Varol et al. 2009; da Silva et al. 2012; Saha 2019). Natarajan et al. (2008) observed that the Prandtl number (Pr) between 0.07 and 0.7 had a stronger influence on heat transfer than Pr between 10 and 100 on laminar buoyancy-driven convection in trapezoidal enclosures. There have been various experimental studies in the area of buoyancy-driven convection in trapezoidal enclosures (Iyican et al. 1980; Lam et al. 1989). Researchers have also looked into the effect of nanofluids on free convection in a trapezoidal enclosure (Saleh 2011; Akbarzadeh and Fardi 2018; Mahapatra et al. 2018). Saleh et al. (2011) found that increasing the concentration of nanoparticles and keeping a sharp sloping wall improves the thermal performance of a trapezoidal cavity filled with nanofluid. The effect of magnetic fields on thermal convection has also been investigated

(Hasanuzzaman et al. 2012; Hossain and Alim 2014). Hossain and Alim (2014) found that the highest heat transfer occurred when the side-inclination angle is 0°, using FEM to simulate MHD-based buoyancy-induced convection within a trapezoidal enclosure with a heated bottom wall.

Heat flow visualization in trapezoidal enclosures has also been studied using the heatline technique (Basak et al. 2009; Ramakrishna et al. 2013). Basak et al. (2009) investigated heat flow analysis for buoyancy-driven convection within trapezoidal enclosures using the heatline concept. Their results showed that the heatline is significantly dense at the cavity's central core, indicating improved heat transfer. This finding can be useful for the design of heat transfer systems, as it provides insight into the heat transfer mechanisms that occur within trapezoidal enclosures. Another important aspect of this research is the investigation of entropy generation, which has been explored in various articles. Mahmoudi et al. (2013) conducted a study on MHD-based natural convection and entropy generation in a trapezoidal enclosure using a Cu-water nanofluid. Their results showed that the inclusion of nanoparticles reduced entropy generation. This finding has important implications for the design of heat transfer systems, as reducing entropy generation can lead to improved system efficiency.

The study of buoyancy-driven convection in a triangular enclosure has also been an interesting topic for many researchers, and there have been several pioneering studies on the subject (Akinsete and Coleman 1982; Poulikakos and Bejan 1983; Campo and Ramos 1988; Karyakin et al. 1988; Salmun 1995). Akinsete and Coleman (1982) reported that the rate of heat transfer augments with Grashof number (Gr) values and falls with hypotenuse-to-base ratio values on laminar buoyancy-driven convection in a triangular enclosure. In addition to pioneering studies, there are various fundamental numerical research studies available (Basak et al. 2007; Fuad Kent et al. 2007; Kent 2009). Basak et al. (2007) found that Rayleigh number (Ra) has a more significant impact on heat transfer rate than Prandtl number (Pr) using the finite element method (FEM) to investigate the influence of Ra and Pr on laminar free convection in triangular enclosures. There is also a considerable amount of experimental work on this topic (Flack et al. 1979; Yesiloz and Aydin 2013). Yesiloz and Aydin (2013) studied buoyancy-driven convection in the triangular enclosure using both experimental and numerical methods and reported that the experimental and numerical results agreed reasonably well. The effect of nanofluids on free

convection in a triangular enclosure has been investigated by several authors (Aminossadati and Ghasemi 2011; Mahian et al. 2016) and magnetic fields (Mahmoudi et al. 2013; Afrand et al. 2020; Vahedi et al. 2022) on buoyancy-driven convection in triangular enclosures. Aminossadati and Ghasemi (2011) found that Ethylene Glycol-Cu nanofluid had a superior heat transfer performance than pure Ethylene Glycol. Additionally, the study revealed that enhanced heat transfer occurs as the concentration of nanoparticles and Ra value increase.

Entropy production in buoyancy-induced flow in triangular enclosures has been investigated in several articles (Varol et al. 2009; Bhardwaj and Dalal 2013; Rathnam et al. 2016). Varol et al. (2009) reported that the entropy production rate increases as Ra increases. Furthermore, several authors have studied heat flow visualization in triangular enclosures using the heatlines approach (Varol et al. 2008; Basak et al. 2009). Basak et al. (2009) used Bejan's heatline concept to illustrate heat transport due to natural convection within triangular enclosures and found that dense heatlines are observed near the bottom portion of slanted walls, indicating that a considerable amount of heat is transported from the bottom portion of the slanted walls. Finally, several review articles (Kamiyo et al. 2010; Saha and Khan 2011) provide in-depth knowledge of the topic, which can be useful for researchers working in this field.

While there have been numerous studies on buoyancy-driven convection in trapezoidal and triangular enclosures separately, a constraint-based study investigating the effects of enclosure shapes on MHD nanofluid flow, heat transport, and irreversibility is still lacking. This chapter aims to bridge this gap by investigating the MHD nanofluid flow, heat transport, and irreversibility in square, trapezoidal, and triangular enclosures with fluid volume constraints. The novelty of this study lies in comparing the effect of enclosure shape on MHD nanofluid flow and irreversibility by modifying the shape of the system's geometry. It can also be viewed as a series of several trapezoidal-shaped systems of identical fluid volume and heating load however varying cooling surfaces. Another important point of this study is viewing the triangular–shaped system as a special case of a trapezoidal-shaped system where one parallel length approaches zero. The findings of this study are expected to contribute to the understanding of the impact of enclosure shape on heat transfer performance in MHD nanofluid flow systems, which can have significant practical

implications in various fields, such as thermal management of electronic devices, energy systems, and heat exchangers.

5.2 Problem formulation and solutions

Figure 5.1 describes the present problem dealing with MHD nanofluid flow in the constraint-based analogous square, trapezoidal, and triangular thermal systems, keeping the fluid volume constant. Several trapezoidal systems have been examined by adjusting the ratio of the top wall length to cavity height while keeping the height (H or L_h) constant. Here, four different cases of trapezoidal-shaped flow geometries are considered with varying the length of the top wall, L_{top} being $0.1H$, $0.3H$, $0.5H$, and $0.7H$, which are also addressed as Cases 1, 2, 3, and 4, respectively. As the base case, a square configuration (shown in a dotted line on the figures) and as a special case, a triangular configuration ($L_{top} = 0$, not shown here but presented separately in Section 5.3.6 later) are also considered. For all these configurations, the equivalency statement is made on the basis of constant heating surfaces at the left wall ($L_h = H$) and fixed fluid flow volumes, however, allowing different cooling surfaces (at right). CuO-water nanofluid and magnetic field considered are acting in similar ways as discussed in previous Chapter 4.
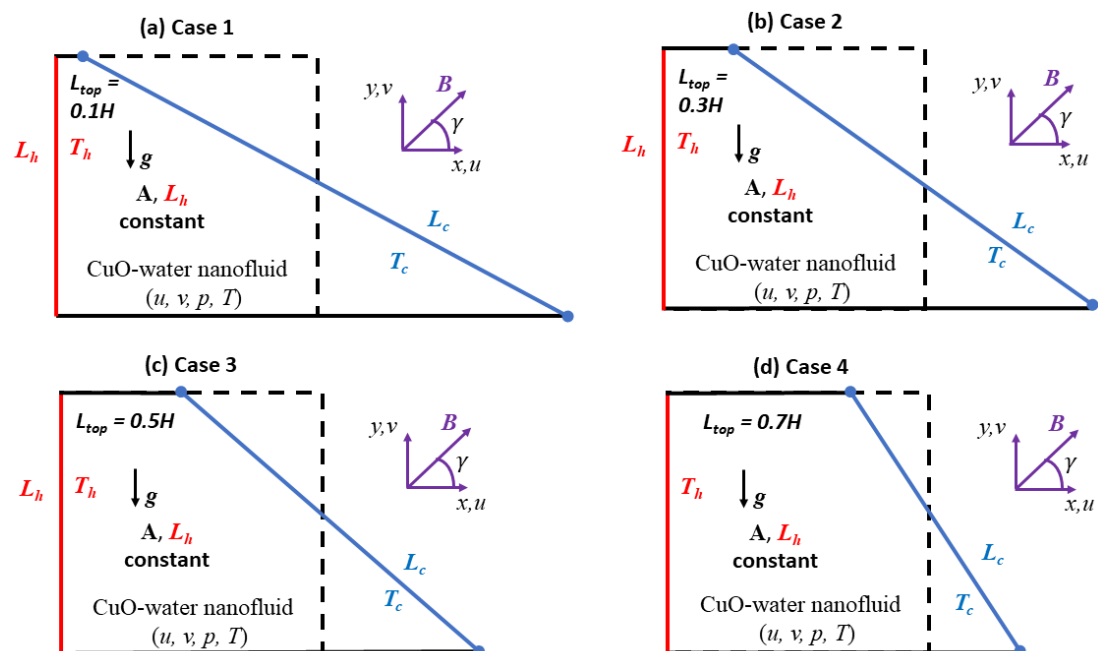
Figure 5.1 Problem description of equivalent trapezoidal systems with constant heat input ($L_h = H$) and fluid volume: (a) Case 1: $L_{top} = 0.1H$, (b) Case 2: $L_{top} = 0.3H$, Case 3: $L_{top} = 0.5H$, and (d) Case 4: $L_{top} = 0.7H$.

The mesh structures for triangular and trapezoidal enclosures are illustrated in Figures A1 (c) and (d), respectively (shown in Appendix). The mesh studies for triangular and trapezoidal enclosures, shown in Appendix, are summarised in Tables A1 (c) and (d).

The formulation and solution of the governing equations for MHD nanofluid flow in these systems are executed following the same techniques discussed in earlier chapters. The numerical simulation results for velocity, temperature, stream function, heat function, and entropy generation are presented, and the effects of various parameters such as the Rayleigh number, Hartmann number, magnetic field angle, and nanoparticle volume fraction are investigated systematically to explore the geometric shape impact on the system's thermal performance.

5.3 Results and Discussion

This section presents the findings and analyses of the constraint-based analogous square, trapezoidal, and triangular thermal systems with constant fluid volume. The subsections examine the effect of nanofluid concentration (ζ varying from 0 to 4%), Rayleigh number (Ra changing from 10^3 to 10^6), magnetic field (Ha = 0–100), magnetic field inclination (γ = 0–180°), and entropy production in the flow domains systematically in Sections 5.3.1 to 5.3.5. Section 5.3.6 extends the research to the special case of a triangular cavity. The local fluid flow and heat transfer characteristics are examined in Sections 5.3.1–5.3.3, while global heat transfer is computed using the mean Nusselt number in Section 5.3.7. These analyses are based on the theoretical discussion presented in previous chapters and the figures depicted in Figure 5.1 (constant fluid volume).

5.3.1 *Impact of nanofluid concentration (ζ)*

In this study, the impact of nanoparticle concentration (ζ) on non-MHD flow (Ha = 0) at a higher Rayleigh number (Ra = 10^6) is investigated. The reason for choosing higher Ra is that it leads to a stronger convective strength, making the effect of nanoparticle concentration more significant. The investigation is conducted using streamlines, isotherms, and heatlines, as shown in Figures 5.2, 5.3, and 5.4, respectively. The geometry consists of trapezoidal-shaped cavities with the fixed vertical left wall at a higher temperature than the slanted right wall, while the lengths of the top and bottom adiabatic walls are varied to meet the volume-constraint

requirement. As a result, fluid circulation cells, or convection cells, form inside the cavity, resembling the geometrical configuration's outline. The streamfunction is used to represent flow direction, with positive and negative signs indicating anticlockwise and clockwise movements, respectively. In all cases, the fluid moves from the heated left wall to the cold right wall, resulting in a clockwise motion.
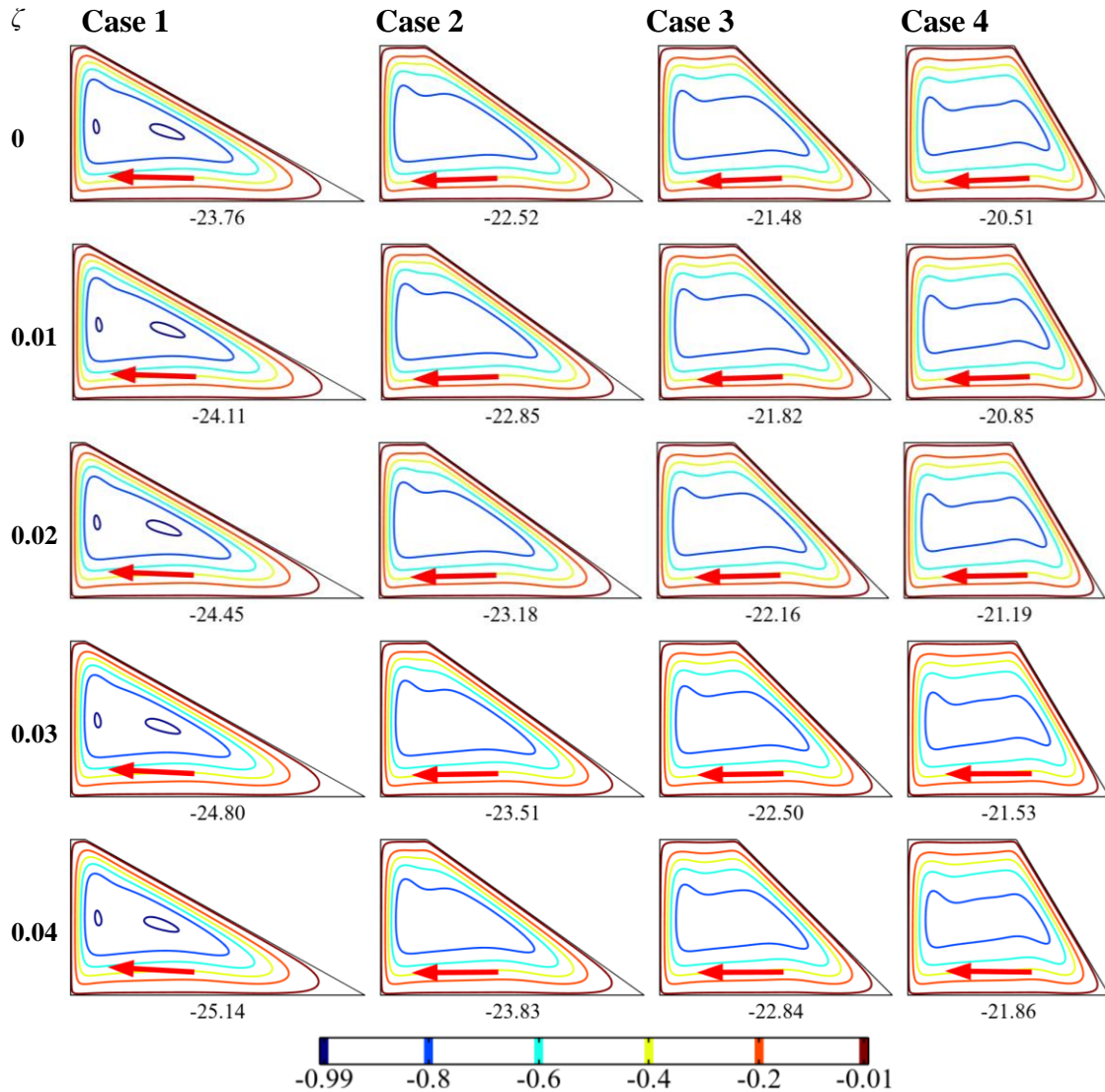
Figure 5.2 Nanofluid concentration (ζ) impact on flow patterns (streamlines) at Ra = 10^6.

The results reveal that increasing nanoparticle concentration enhances heat transfer (due to the improved thermal conductivity), which in turn boosts flow strength. This is apparent from the rise in the maximum value of streamfunction (ψ_{max}) with increasing ζ. Moreover, the thickness of the hydrodynamic boundary layer decreases with increasing ζ. The wall perimeter and cooling length increase when L_{top} decreases. However, an increase in wall perimeter causes higher fluid friction, thereby offering reduced flow strength or circulation. Furthermore, increasing the length of

the cooling wall causes more thermal energy to be extracted from the heated left wall, leading to a rise in heat transfer, which in turn increases flow strength. The overall effect of decreasing L_{top} increases the flow strength (Figure 5.2). Therefore, the results suggest that the flow strength increases with increasing nanoparticle concentration and decreases with increasing the top wall length to cavity height ratio.
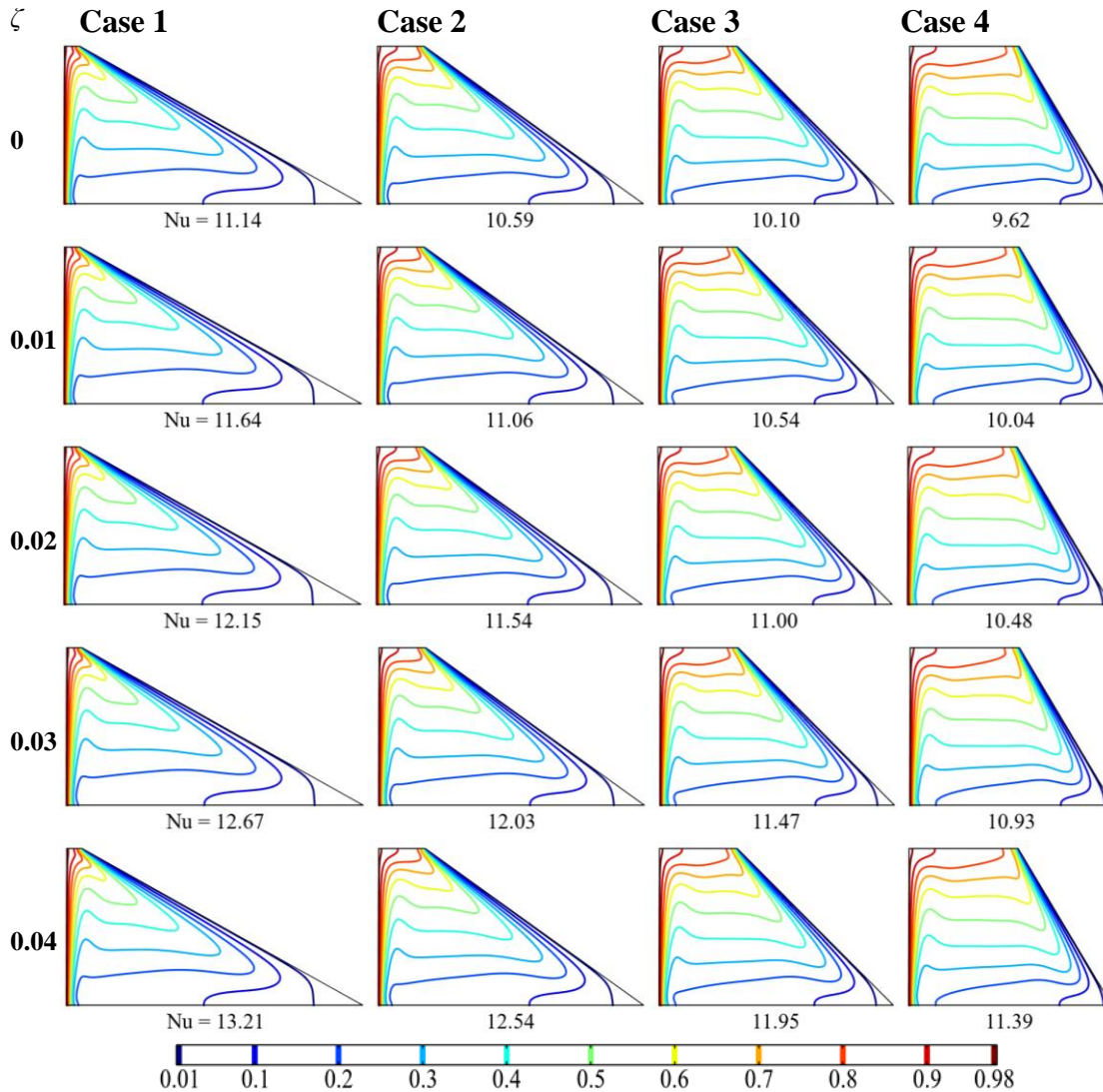
Figure 5.3 Nanofluid concentration (ζ) impact on temperature patterns (isotherms) at Ra = 10^6.

Isotherm profiles are presented in Figure 5.3 to demonstrate the effect of nanoparticle concentration on convective heat transfer. The isotherm profiles become more compact as nanoparticle concentration (ζ) increases from 0 to 0.04. However, the change in isotherm profiles is relatively small due to the coupling of velocity and temperature in buoyancy-driven convection. The increase in nanoparticle concentration leads to a higher convective heat transfer rate, which is reflected in the higher value of the Nusselt number (Nu). Moreover, reducing the top wall length to

enclosure height ratio enhances thermal energy transfer by increasing the length of the cooling wall. Therefore, it can be concluded that adding nanoparticles to the base fluid and reducing the top wall length to enclosure height ratio both contribute to improved convective heat transfer, and the maximum Nu is achieved in Case 1 at $\zeta =$ 0.04.
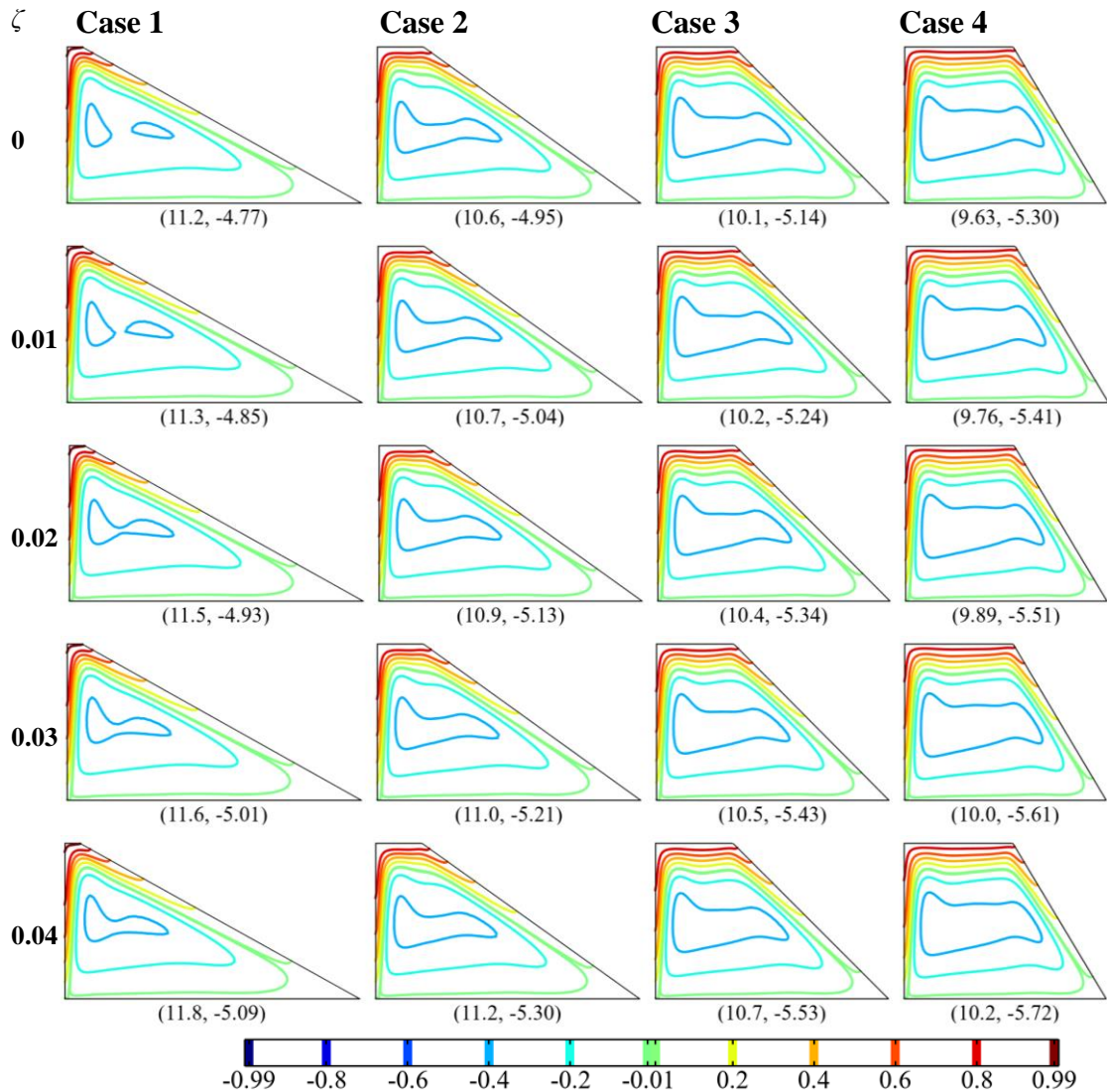
Figure 5.4 Nanofluid concentration (ζ) impact on heat flow patterns (heatlines) at Ra = 10^6.

Figure 5.4 depicts the influence of nanoparticle concentration on the heat flow pattern using heatlines. These lines, similar to streamlines, depict the direction of heat flow, originating from the hot left wall and extending towards the cold right wall, creating pathways of heat transport. The width of the heat flow corridors reflects the variation in local heat flux due to diffusion and convection, with constant thermal energy transfer rates within a corridor. As the hot working fluid circulates within an

enclosed system, heat flow with circulation cells develops. The heatline plots indicate two numerical values, the first being the highest value at the top adiabatic wall, and the second indicating the lowest value related to the clockwise rotation of heat flow. The influence of nanoparticle concentration on heat flow is examined at higher values of Ra ($=10^6$). As the concentration of nanoparticles increases, the passage between the heatlines shrinks, indicating an increase in heat flow intensity. This is also evident in the heatline plot's first numerical value, which indicates the maximum value at the left heating wall. Similarly, when the ratio of the top wall's length to the height of the cavity decreases, the gap between the heatlines shrinks, indicating an increase in heat flow, which is again supported by the first numerical value of the heatline plot. The quantitative values in the figure clearly indicate that the inclusion of nanoparticles and reducing the ratio of top wall length to cavity height can improve thermal performance in a trapezoidal cavity. For the presentation of parametric effects of Ra, Ha, etc. in the following subsections, the nanoparticle concentration is considered at ζ = 0.02.
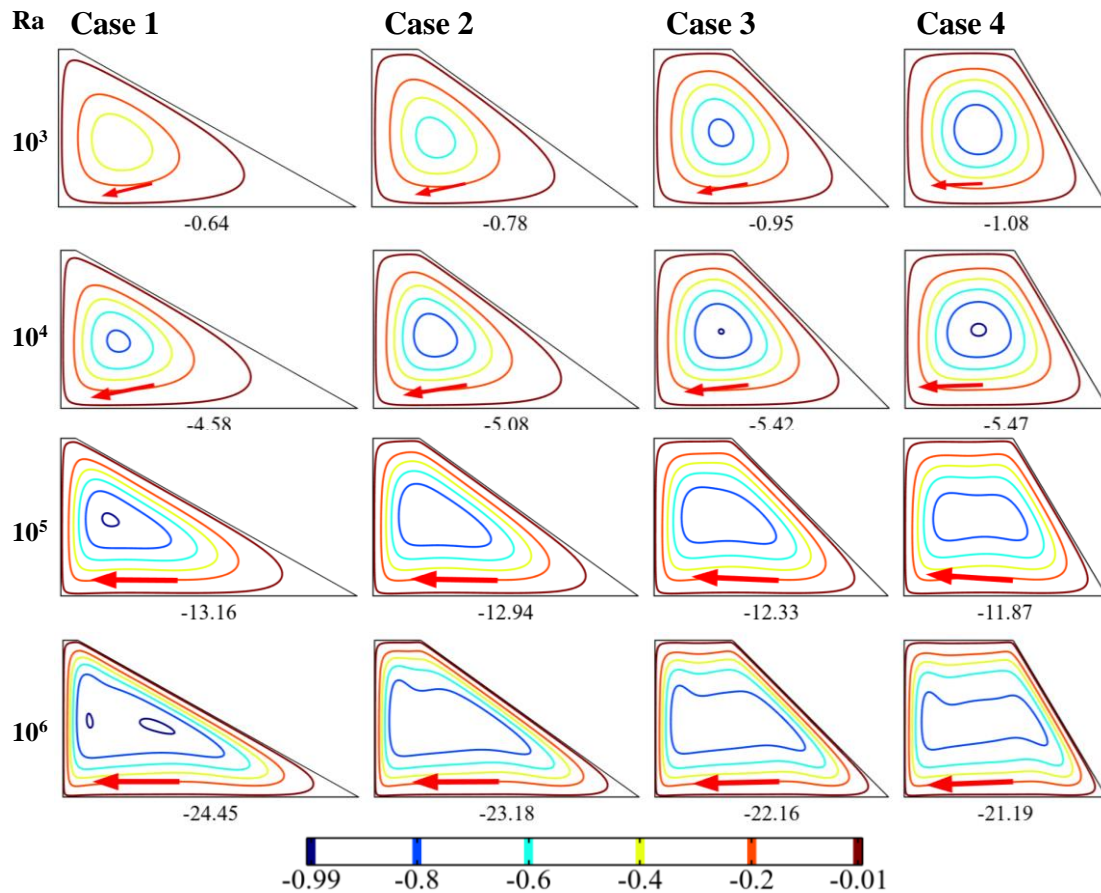
Figure – 5.5 Impact of Ra on flow patterns (streamlines) for non-MHD flow.

5.3.2 *Effects of Rayleigh numbers for non-MHD flow*

This section investigates the effects of varying Rayleigh numbers (Ra) on buoyancy-induced convection in non-MHD flow (Ha = 0) in trapezoidal thermal systems. Figures 5.5, 5.6, and 5.7 illustrate the impact of Ra on fluid motion, temperature distribution, and heat flow pattern, respectively. In Figure 5.5, the velocity of the fluid is low at lower Ra (10^3), and the fluid appears to be stagnant near the lower region of the cooling wall. However, as Ra increases, the circulation strength of convection cells increases, resulting in elongated cells horizontally towards the cold wall. Flow strength varies with the ratio of the top wall length to cavity height, where flow intensity is governed by the wall perimeter and length of the cooling wall. At low Ra (10^3 and 10^4), the flow strength increases as the ratio of top wall length to cavity height increases, but at high Ra values (10^4 and 10^5), flow strength decreases as the ratio of top wall length to cavity height increases. These results imply that flow strength increases as Ra increases, and for low Ra values, increasing the ratio of top wall length to cavity height improves flow strength, but for high Ra values, increasing this ratio decreases flow strength.
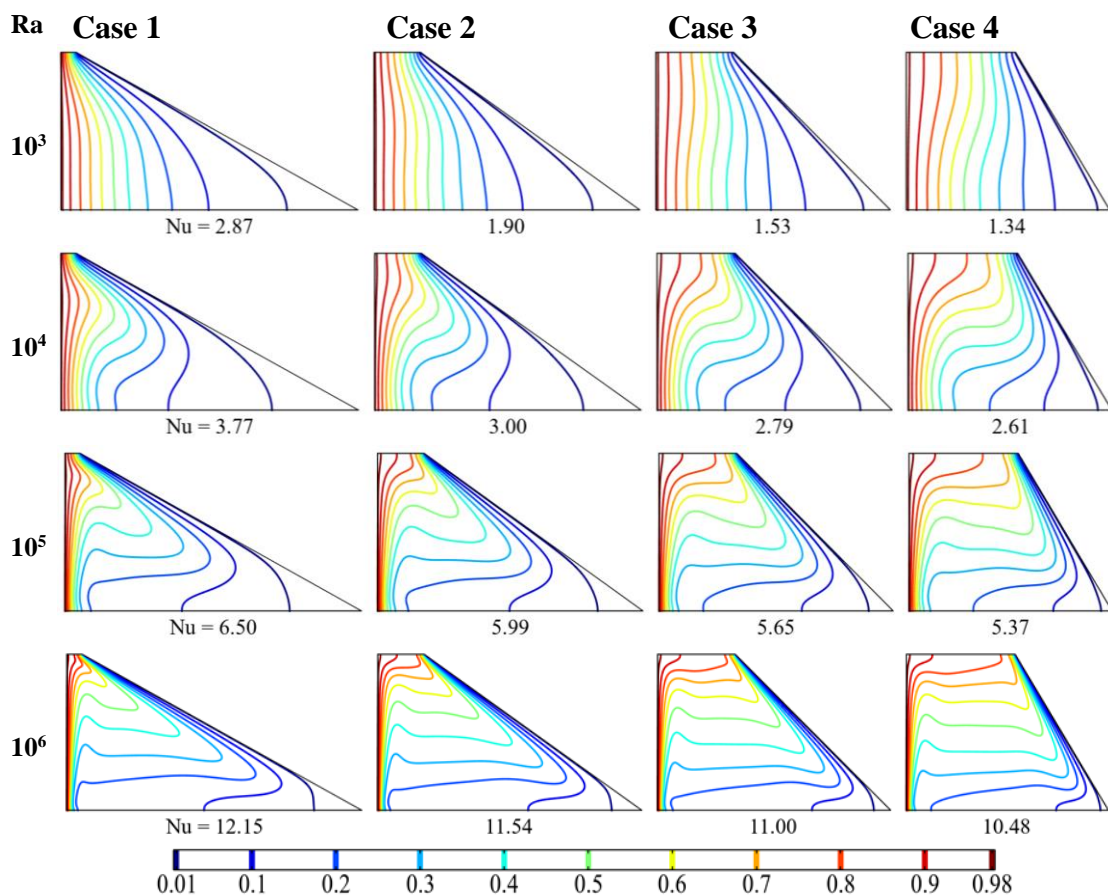
Figure 5.6 Impact of Ra on static temperature patterns (isotherms) for non-MHD flow.

The influence of Ra on the isotherm is illustrated in Figure 5.6. The flow strength varies with Ra and the geometrical arrangement of the trapezoidal system. In this problem, velocity and temperature are interlinked, as stated in Section 5.3.1, resulting in the variation of isotherm profiles as Ra and geometrical shape change. Due to the active non-parallel sidewalls of the trapezoidal enclosure, the isotherms appear distorted in the middle stretch and parallel adjacent to the sidewalls. At low Ra values ($\leq 10^3$), the isotherms take a nearly vertical orientation, indicating a conductive mode of thermal energy transport. However, as Ra approaches 10^4, the isotherms adopt an 'S' shape.
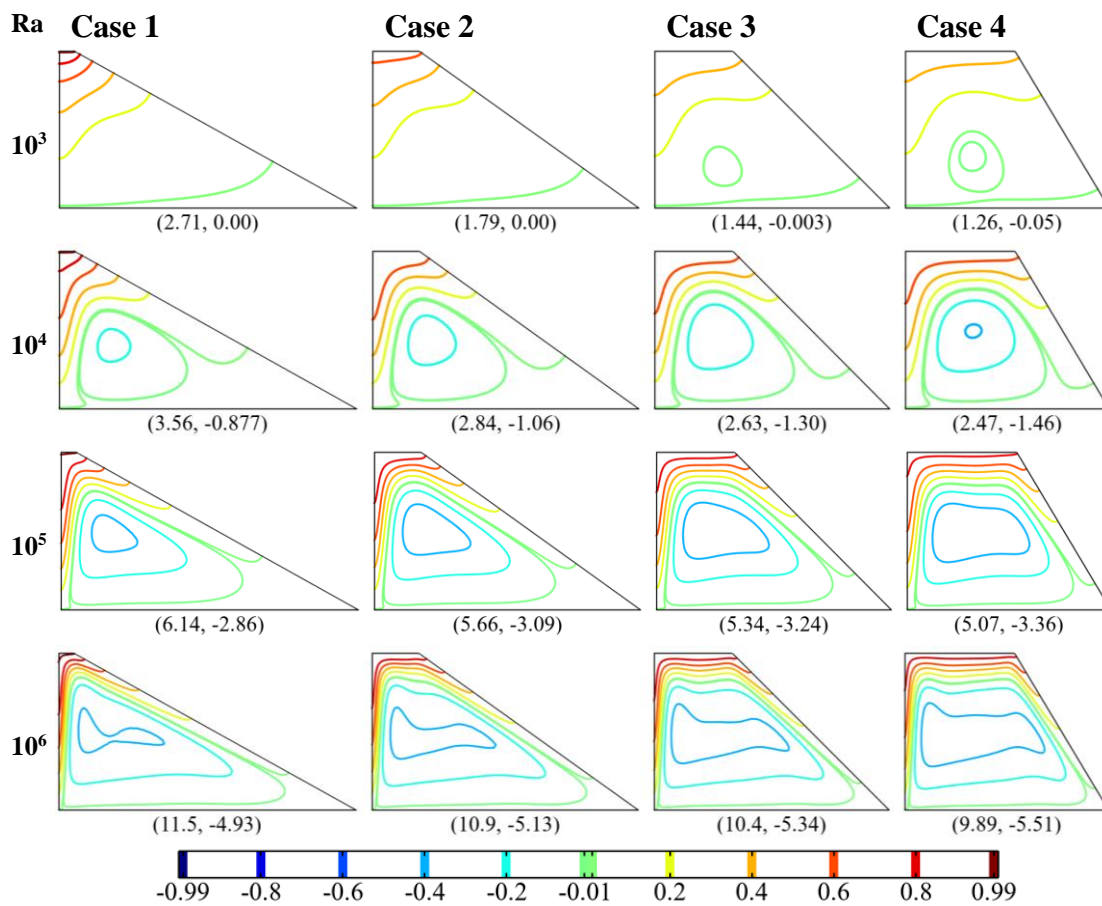
Figure 5.7 Impact of Ra on heat flow patterns (heatlines) for non-MHD flow.

The isotherm profiles are stretched along the active wall as Ra reaches higher values (10^5 and 10^6) due to the greater thermal gradient, resulting in greater deformation. Additionally, the isotherm lines become overcrowded near the active sidewalls, indicating a thinner thermal boundary layer thickness and a higher heat transfer rate at higher Ra. The isotherm profiles become more densely populated as the ratio of top wall length to cavity height decreases for all cases, as evidenced by the

increase in Nu value. This is due to the increase in the length of the cooling wall, as detailed in Section 5.3.1. It can be concluded that increasing Ra and decreasing the top wall-to-cavity height ratio can improve heat transfer.

Figure 5.7 presents the impact of Rayleigh number (Ra) on the heat flow pattern using Bejan's Heatlines (Kimura and Bejan, 1983). The results demonstrate that for low Ra (= 10^3), the heat flow is conducted from the hot left wall to the cold right wall. As Ra increases to 10^4, energy circulation cells are formed, and there is a rise in the convective mode of heat transfer. The strength of energy circulation cells further increases with a higher Ra value, which is evident from the maximum value at the left heating wall on the heatline plot. Additionally, the intensity of heat flow increases with a decrease in the cooling wall length to cavity height ratio. This is due to a thinner thermal boundary layer and higher heat transfer rate, which is explained in Section 5.3.1. Therefore, it can be concluded that increasing Ra and reducing the cooling wall length to cavity height ratio can enhance the intensity of heat flow.
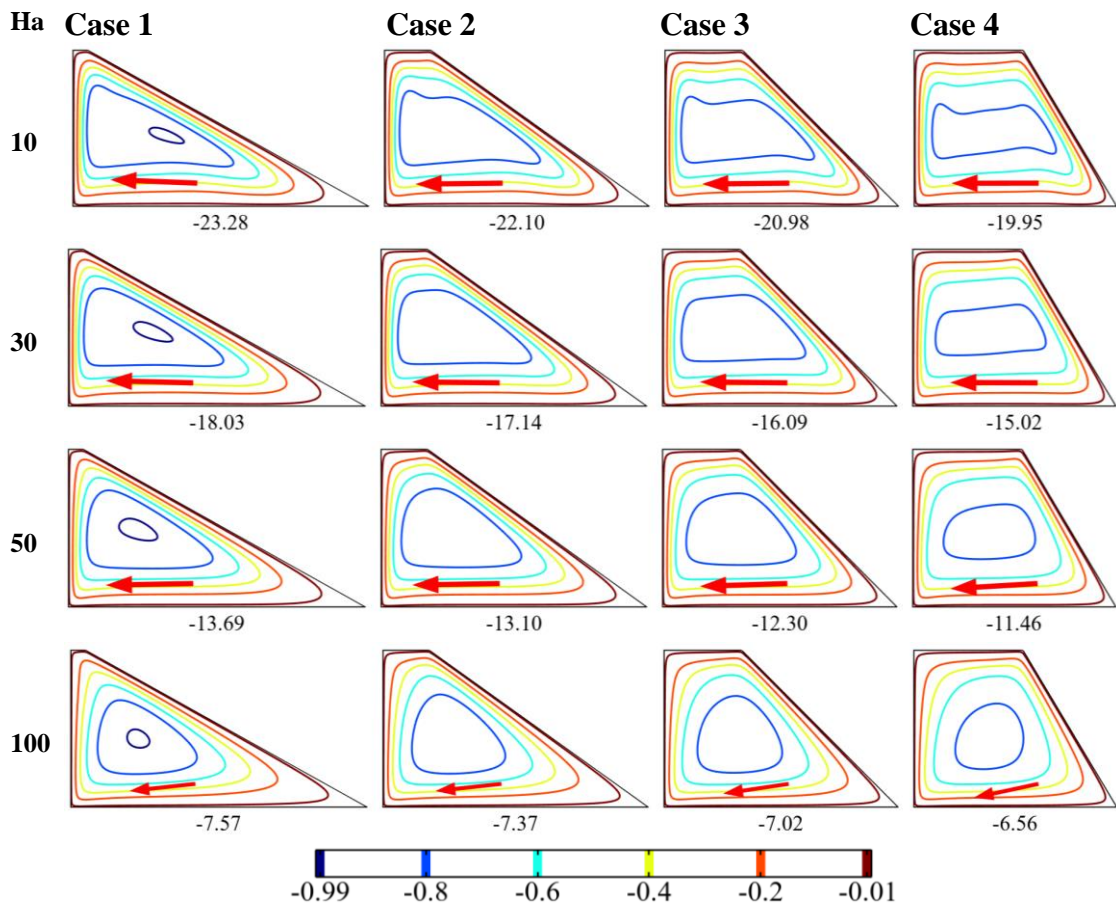
Figure 5.8 Ha impact on flow patterns (streamlines) at Ra = 10^6.

5.3.3 *Effects of Hartmann numbers*

The effect of the Hartmann number (Ha) on the flow structure, temperature distribution, and heat flow is investigated for fixed Ra = 10^6, $\gamma = 0°$, and $\zeta = 2\%$, and Ha varying from 0 to 100. The results are presented in Figures 5.8, 5.9, and 5.10.
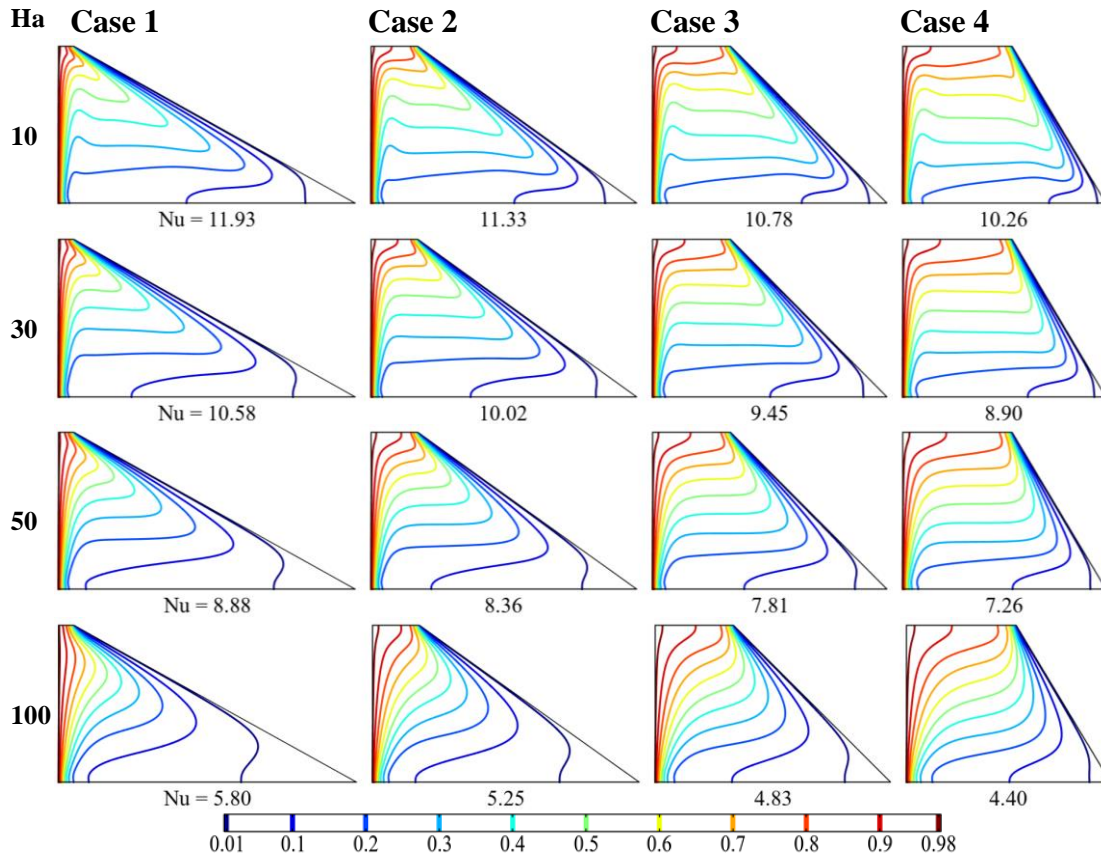
Figure 5.9 Ha impact on temperature patterns (isotherms) at Ra = 10^6.
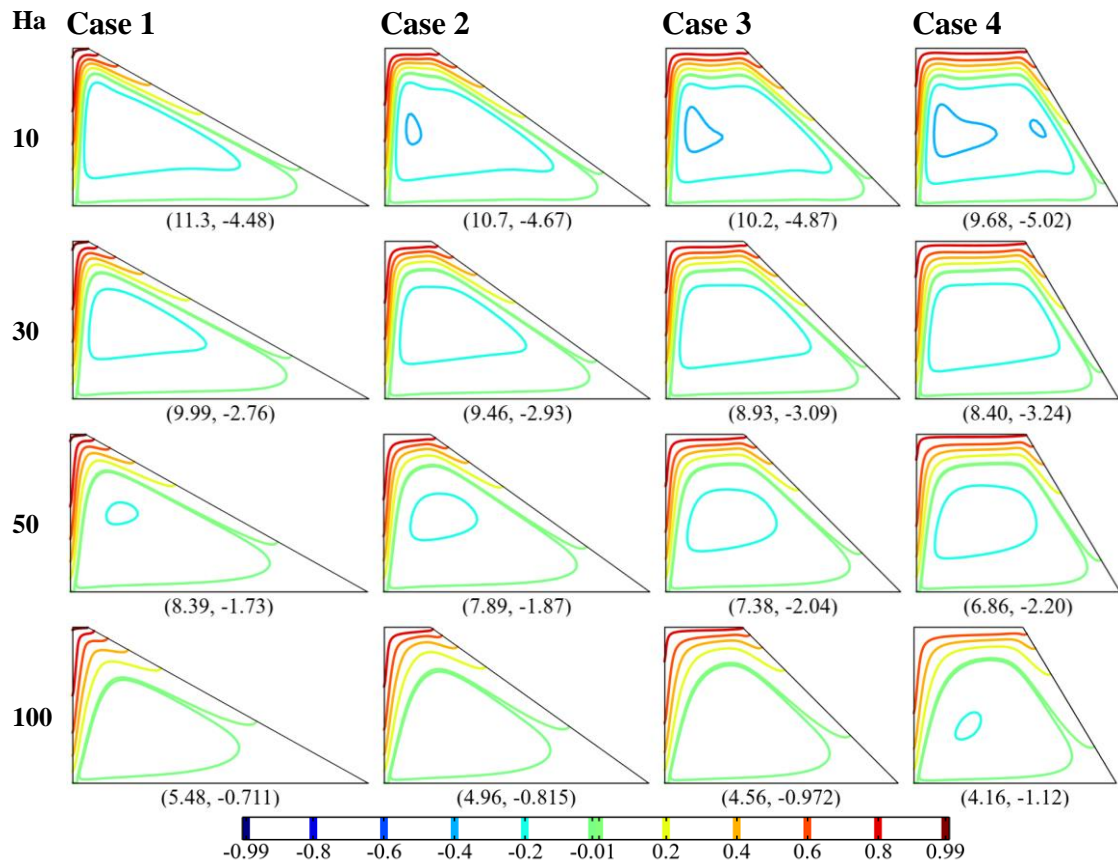
Figure 5.10 Ha impact on heat flow patterns (heatlines) at Ra = 10^6.

The flow structure for MHD flow in Figure 5.8 is found to be similar to non-MHD flow, with a quantitative change in the flow velocity indicated by the reduced values of the streamfunction. As Ha increases, the Lorentz force also increases, which leads to an increase in the hydrodynamic boundary layer and a decrease in fluid movement, as indicated by the decrease in the value of ψ_{max}. Similar to non-MHD flow, the flow strength is found to increase by decreasing the length of the top wall-to-cavity height ratio, which is explained in detail in Section 5.3.1.
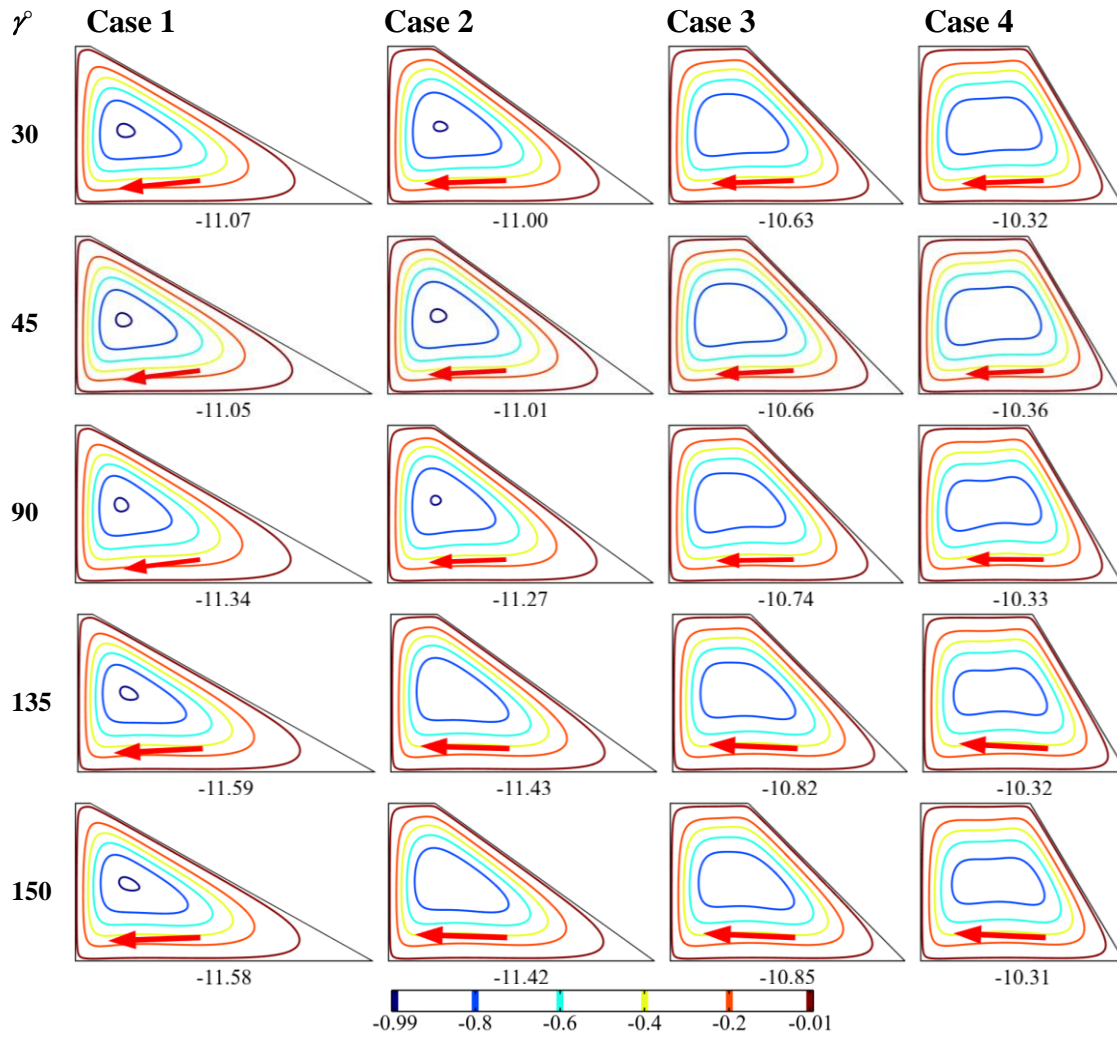
Figure 5.11 Magnetic field inclination (γ) impact on streamlines at Ha = 10 and Ra = 10^5.

Figure 5.9 shows the impact of the magnetic field on temperature distribution in the trapezoidal thermal system. The temperature distribution for MHD flow is similar to that of non-MHD flow. As Ha increases, the Lorentz force also increases, leading to a decrease in the net driving force. This results in less crowded isotherms as Lorentz forces rise, indicating a reduction in convective heat transfer. This is also evident from the decrease in the value of Nu. Similar to the non-MHD flow, the temperature gradient increases by reducing L_{top}, causing an increase in convective heat transfer.
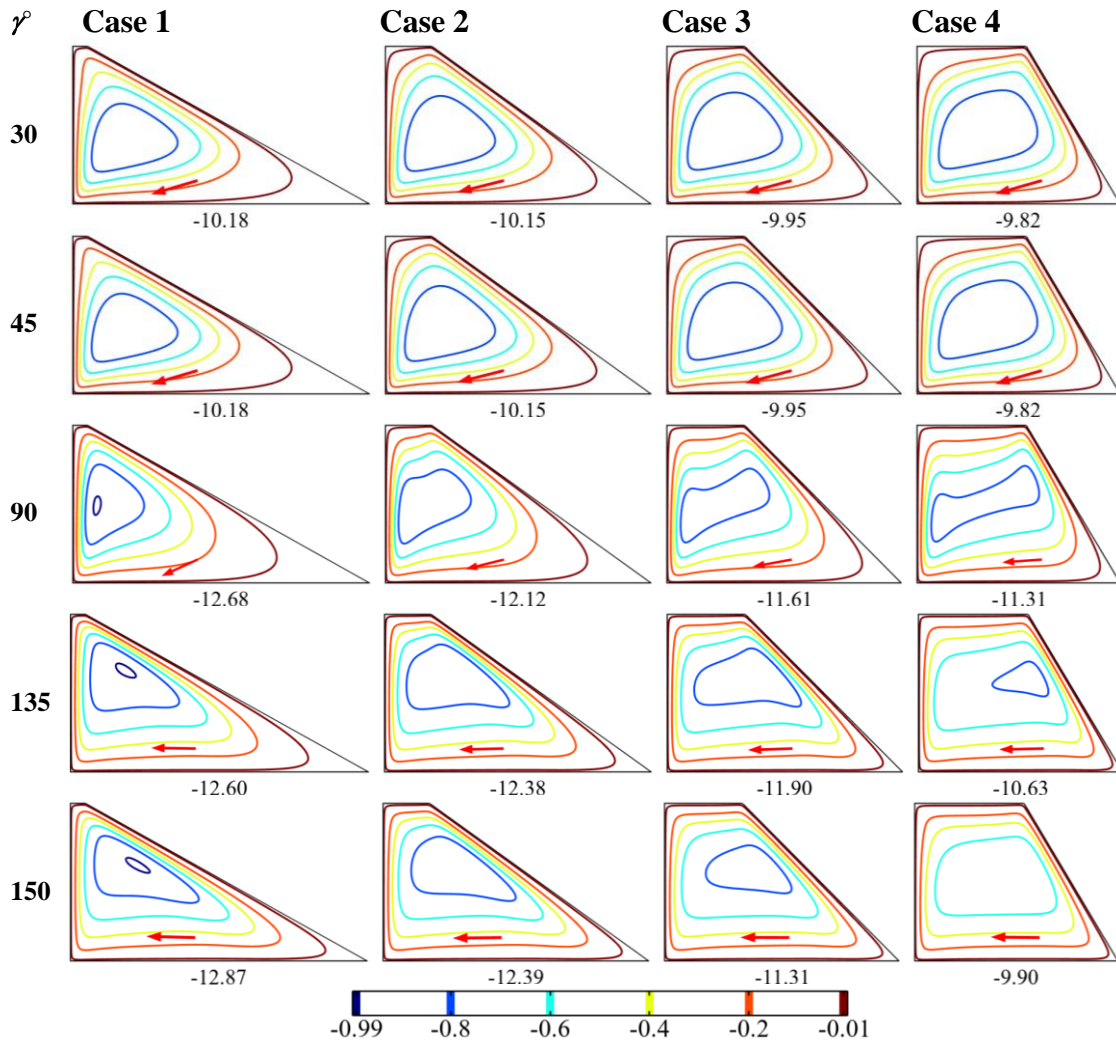
Figure 5.12 Magnetic field inclination (γ) impact on streamlines at Ha = 70 and Ra = 10^6.

In Figure 5.10, the impact of a magnetic field on the heat flow pattern is shown. The heat flow pattern of MHD flow is similar to that of non-MHD flow (Ha = 0). However, as the value of Ha increases, the Lorentz force counteracts the buoyant force. Therefore, the Lorentz force causes the dampening of the convective flow velocity, in turn, reduces the heat flow. As Ha increases, the passage between the heatlines widens, indicating a decrease in heat flux. Additionally, the number of energy circulation cells reduces as Ha increases. This is also evident from the numerical first value (the maximum value at the left heating wall) in the heatline figure. Similar to non-MHD flow, reducing the length of the top wall to cavity height ratio enhances heat flow intensity.

5.3.4 *Impact of magnetic field inclination (γ)*

In a trapezoidal thermal system exposed to thermal convection, the impact of magnetic field inclination (γ) ranging from 0° to 180° is examined. To keep the

discussion concise, results for $\gamma = 30, 45, 90, 135,$ and $150°$ are presented for two sets: $Ra = 10^5$, $Ha = 10$, and $\zeta = 2\%$ for the first set, and $Ra = 10^6$, $Ha = 70$, and $\zeta = 2\%$ for the second set.
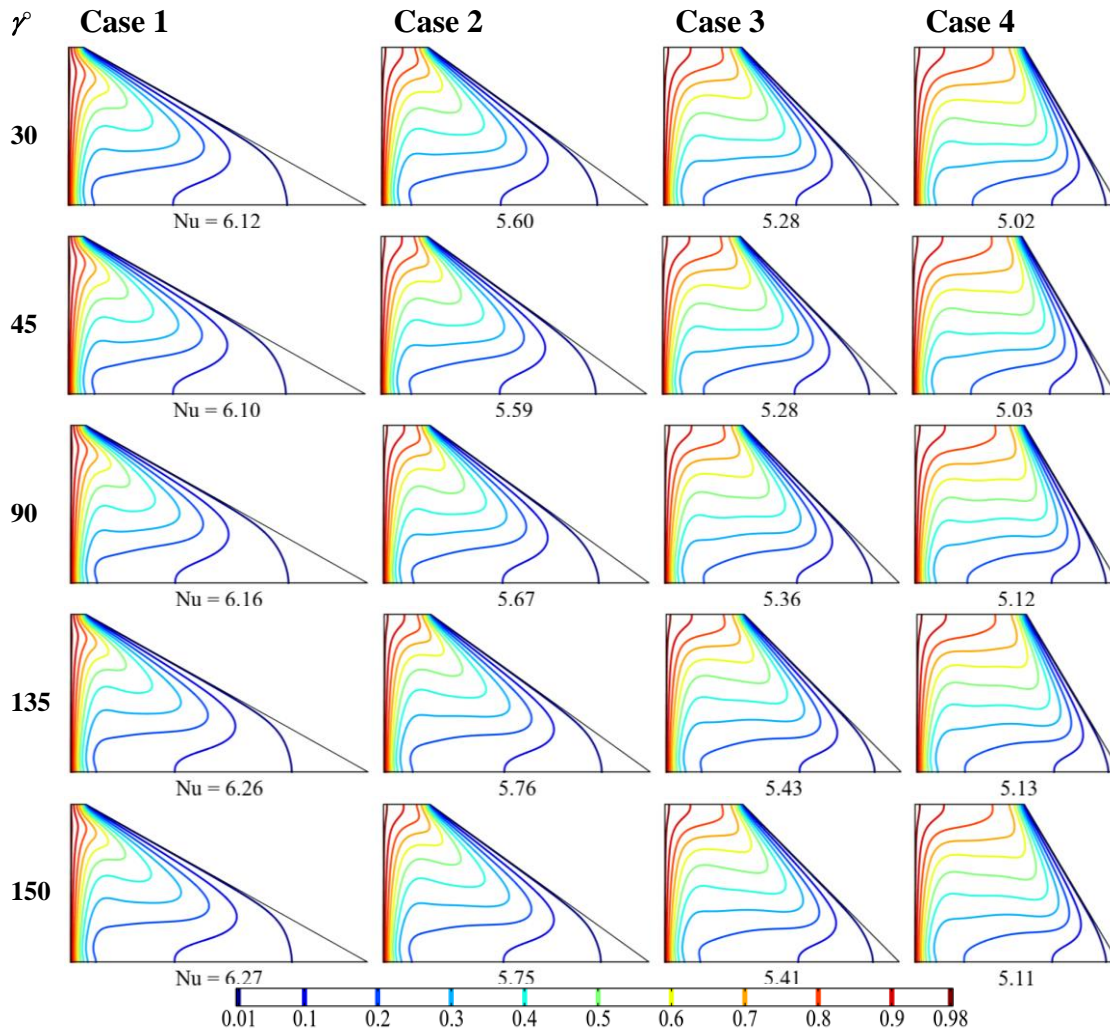
Figure 5.13 Magnetic field inclination (γ) impact on isotherms at Ha = 10 and Ra = 10⁵.

The impact of magnetic field inclination on the flow pattern is illustrated in Figures 5.11 and 5.12 considering two datasets (Ha = 10, Ra = 10^5; and Ha = 70, Ra = 10^6), respectively. The flow pattern is similar in all cases, with a slight variation in flow velocity due to the alteration of the magnetic field orientation affecting the Lorentz force contributions in the *X* and *Y* directions. However, the variation in flow velocity with γ is negligible. For all γ values, the hydrodynamic boundary layer thickness decreases as L_{top} decreases, indicating an increase in flow strength, as seen from the value of ψ_{max}. Furthermore, the results obtained from both sets show that similar flow strength can be obtained by adjusting the controlling parameters.

113
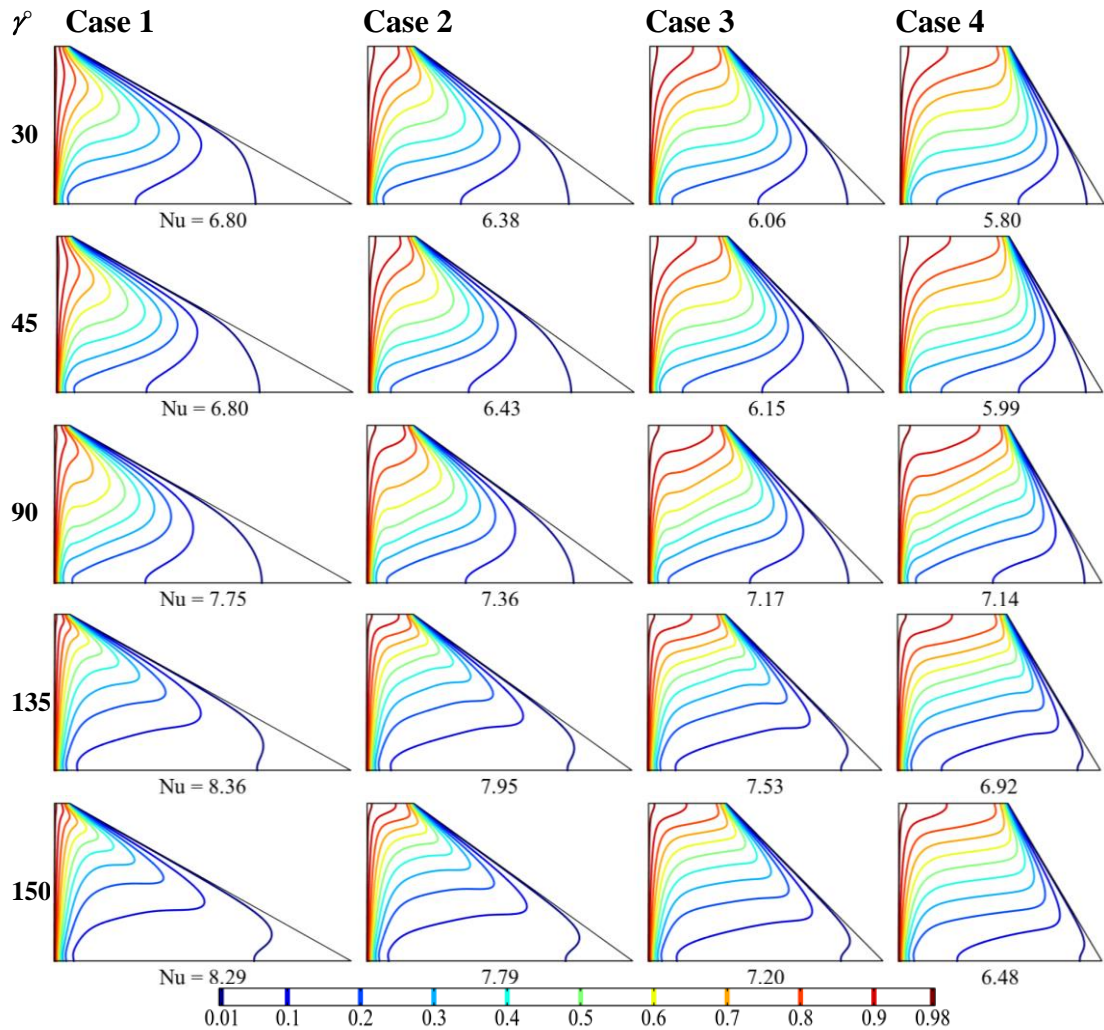
Figure 5.14 Magnetic field inclination (γ) impact on isotherms at Ha = 70 and Ra = 10⁶.

Figures 5.13 and 5.14 illustrate the γ-impact on isotherms in the first and second sets, respectively. In this problem, the velocity and temperature are coupled, resulting in changes to the temperature profiles as γ varies. The flow pattern is nearly identical for γ = 30, 45, 90, 135, and 150°, but there is a minor variation in the temperature gradient. A careful analysis of the isotherm profiles reveals that the temperature gradient is highest for γ = 135° because the Lorentz force moves the fluid toward the heated wall. As with γ = 0°, reducing L_{top} causes the isotherms to become more crowded there, indicating a rise in convective heat transfer, as evidenced by the Nu value. The results indicate that by adjusting the controlling parameters, the same level of heat transfer can be achieved. This information is beneficial for the design of a thermal system.
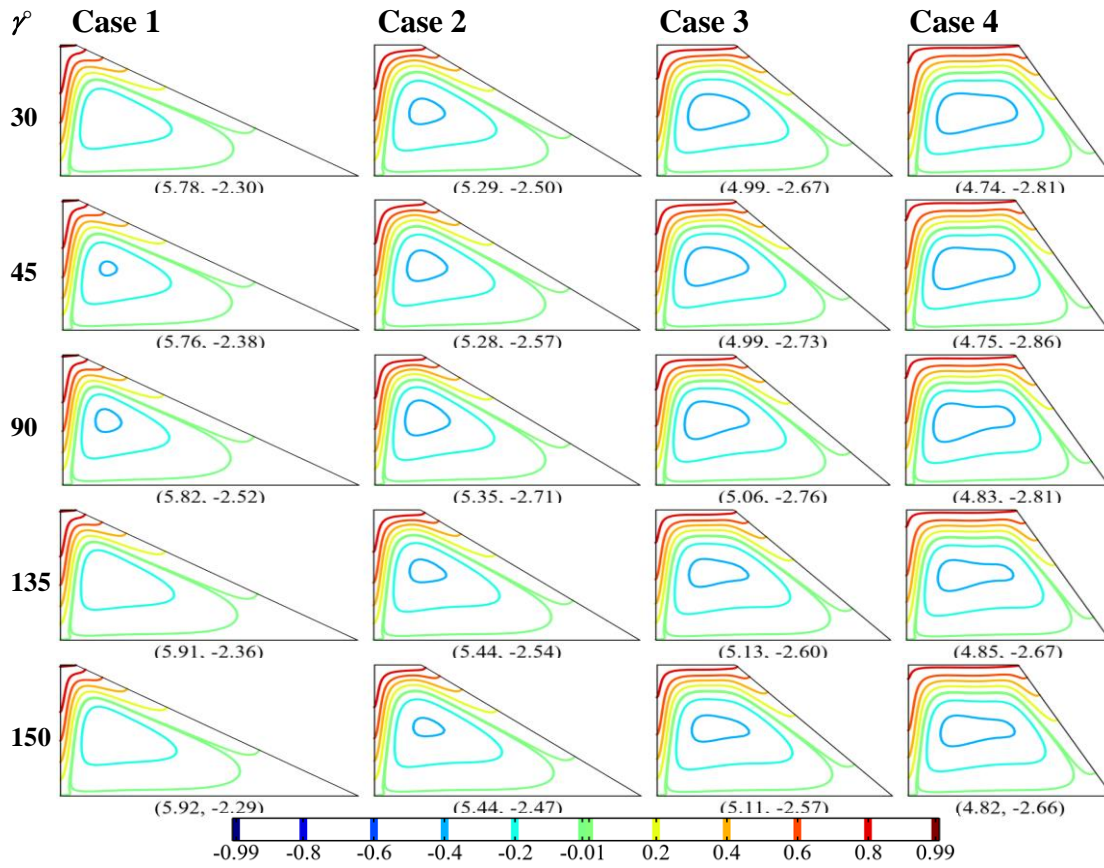
Figure 5.15 Magnetic field inclination (γ) impact on heatlines at Ha = 10 and Ra = 10^5.
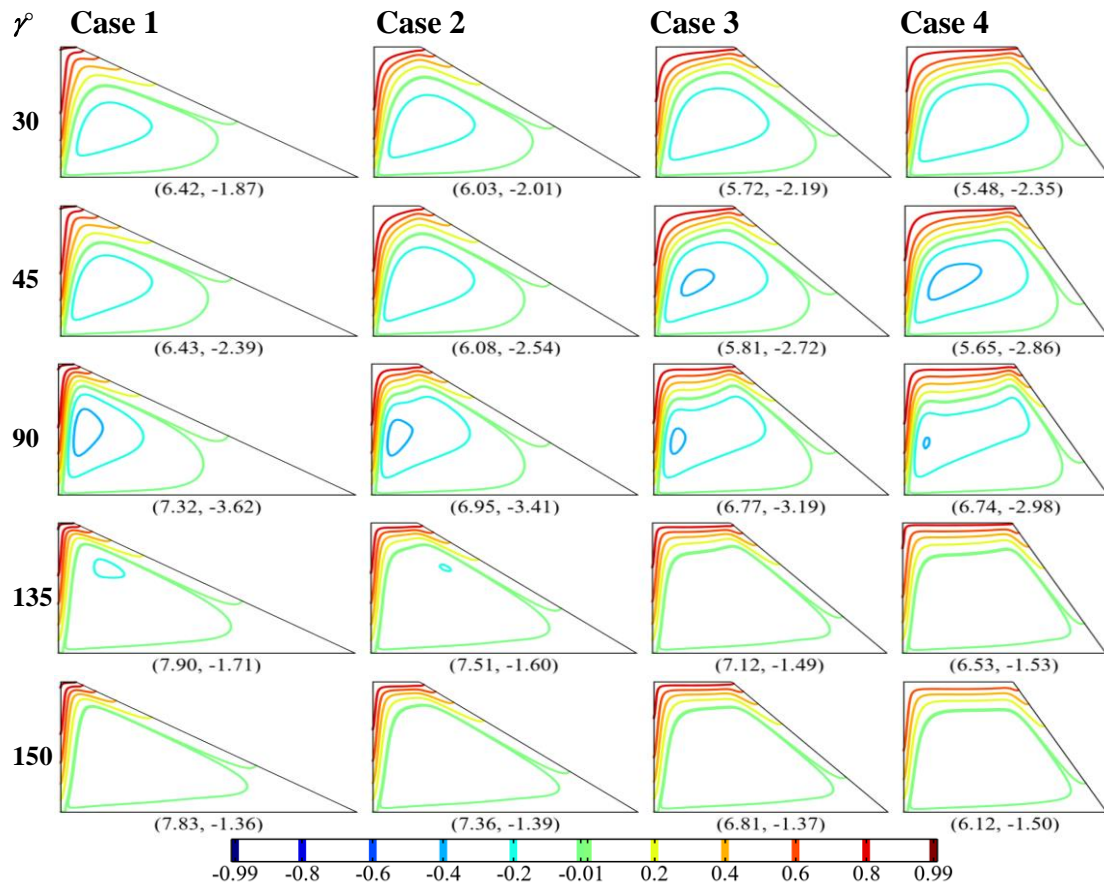
Figure 5.16 Magnetic field inclination (γ) impact on heatlines at Ha = 70 and Ra = 10^6.

The impact of γ on heatlines is also investigated and presented in Figures 5.15 and 5.16 for the first and second sets, respectively. Similar to streamlines and isotherms, the results of heatlines for $\gamma = 0°$ are given in Section 5.3.3 for different Ha, and the heat flow results for $\gamma = 0°$ and $180°$ are the same for all cases. For $\gamma = 30$, 45, 90, 135, and $150°$, there is a minor variation in heat flow intensity, but the overall heat flow pattern is similar. It is noteworthy that the maximum heat flow intensity is observed for $\gamma = 135°$, which is also explained earlier in this section. Moreover, as with $\gamma = 0°$, the tunnel between the heatlines becomes narrower as the length of the top wall to cavity height ratio decreases, indicating an increase in heat flux. This is supported by the first numerical value in the heatline contour. The presented findings indicate that by adjusting the controlling factors, similar heat transfer can be achieved, which can be useful in designing a thermal system.

5.3.5 *Parametric impacts on irreversibility generation*

The impact of flow parameters on thermodynamic irreversibility generation is investigated here, with the total entropy production (NS) comprising irreversibility induced by the temperature gradient (NS_{tg}), viscous effect (NS_v), and magnetic field (NS_m). Results are presented in normalized form, with Figures 5.17 and 5.18 showing the viscous and magnetic contributions of entropy generation (EG) first to illustrate their order of magnitude and localization.
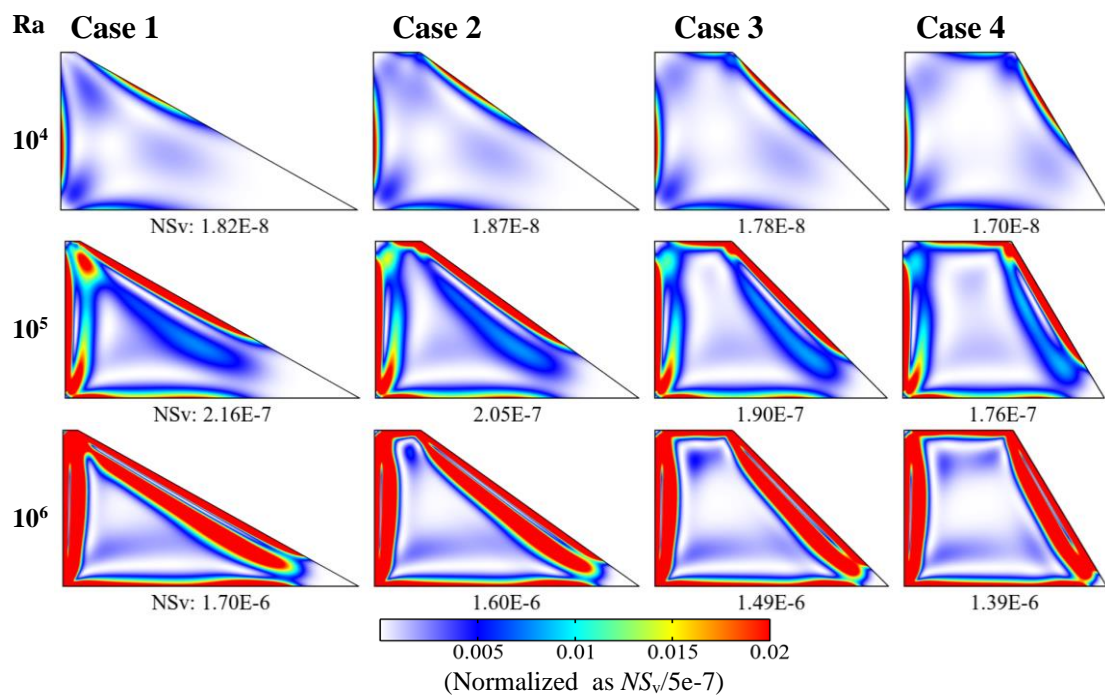
Figure 5.17 Viscous entropy generation at Ha = 10 for different Ra values.

Figure 5.17 presents the impact of varying Ra from 10^4 to 10^6 on NS_v for a specific value of Ha = 30 and ζ = 2% in four trapezoidal cases. The NS_v is found to be higher near the hot and cold walls due to the growth of a hydrodynamic boundary layer near the active walls, resulting in a high-velocity gradient in the region of the active walls. The NS_v is low for low Ra (= 10^4) due to the weak convective heat transmission, increasing as Ra and convective heat transport strength rise. Furthermore, the NS_v value increases as L_{top} falls, with Case 1 and Case 4 having the maximum and minimum NS_v values, respectively, and the other two cases lying between the two. However, the magnitude of NS_v is relatively very small compared to NS_{tg} in all the cases.

In Figure 5.18, the effect of changing Ra (10^4, 10^5, and 10^6) on magnetic EG (NS_m) is demonstrated with Ha = 10, γ = 0°, and ζ = 2%. The NS_m distribution is higher in the cavity region where the flow velocity is high and is concentrated near the hot and cold walls while being significantly less concentrated near the top and bottom adiabatic walls. At a low Ra value (10^4), NS_m is extremely small due to the weak convective mode of thermal transport and low fluid velocity. As Ra increases, the convective process of thermal energy transport becomes stronger, leading to an increase in NS_m with a rise in Ra. The order of magnitude of NS_m is nearly uniform for all cases and is very small; therefore, the total EG (NS_l) is mainly reflected by NS_{tg}.
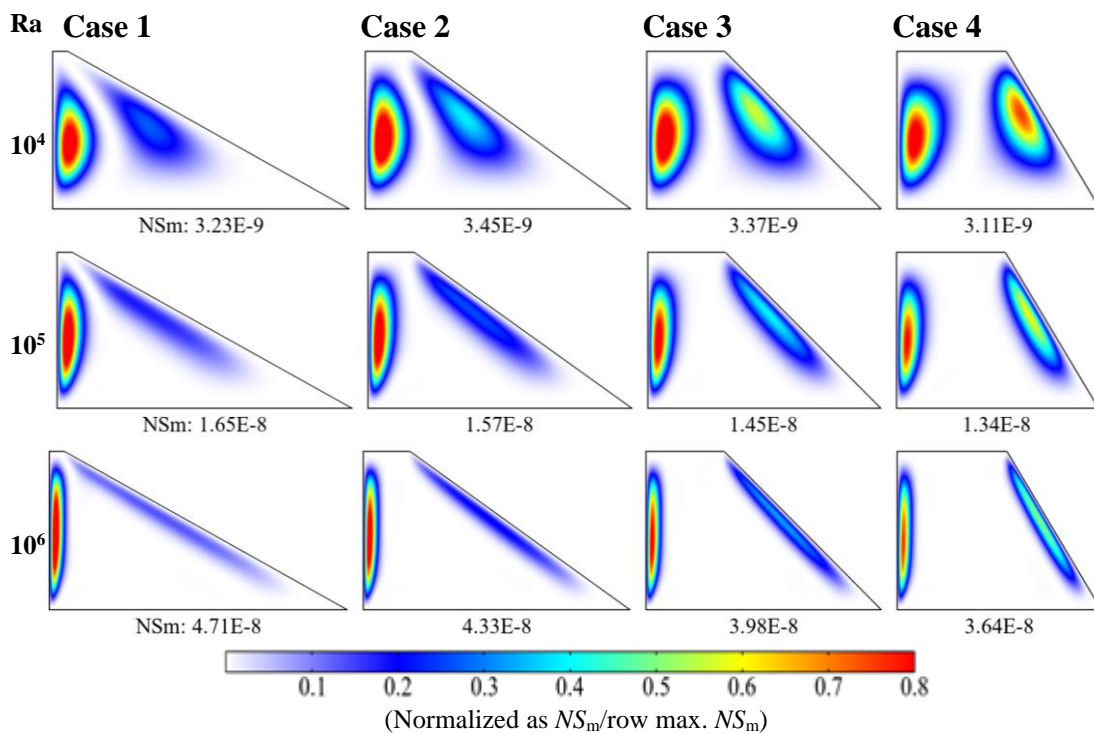
Figure 5.18 Magnetic entropy generation Ha = 10 for different Ra values.
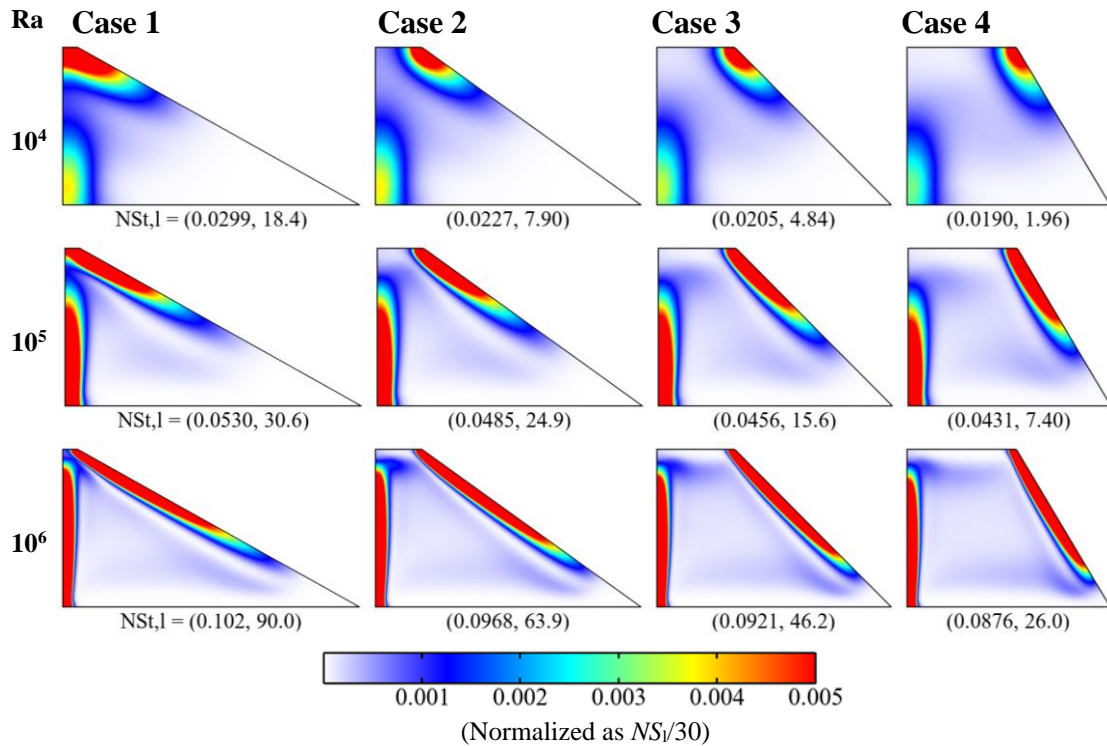
Figure 5.19 Total entropy generation at Ha = 10 for different Ra values.

The entropy generation due to temperature gradient (NS_{tg}) has a significant impact on the overall EG, and the values of NS_{tg} and overall EG are nearly the same (as other viscous and magnetic contributions are insignificant). Therefore, the total EG (NS or NS_l) is presented in subsequent figures. Figure 5.19 illustrates the effect of changing Ra from 10^4 to 10^6 on overall EG for a fixed Ha = 0 and ζ = 2% in four cases. The local NS value is higher in the lower region of the hot wall (source) and the upper region of the cold wall (sink) in accordance with the static temperature contour. A strong temperature gradient is observed in the area with high EG. The overall EG is lower for low Ra (= 10^4) due to weak convective heat transport, resulting in a lower thermal gradient. As Ra increases, the convective mechanism of thermal energy transfer intensifies, leading to a rise in temperature gradient and thereby NS_{tg} (or NS_l). Decreasing L_{top} increases the length of the cooling wall, resulting in a rise in temperature gradient and overall EG. Thus, the overall EG is minimum for Case 4 and maximum for Case 1, while the other two cases fall in between.

In Figure 5.20, the impact of Ha (= 0, 50, and 100) on overall EG is illustrated for a fixed Ra value of 10^6, γ = 0°, and ζ = 2% for four different cases. In all situations, the local NS is found to be high in the regions close to the lower area of the

heating wall (heat source) and the higher area of the cooling wall (heat sink). For non-MHD flow, i.e., Ha = 0, the value of local *NS* is high. As Ha increases, the Lorentz force also increases, which reduces the effect of buoyant force and results in a decrease in a temperature gradient. Therefore, as Ha increases, the overall EG decreases. Additionally, it is observed that decreasing the top length-to-height ratio leads to an increase in *NS*. Consequently, the overall EG is lowest in Case 4 and highest in Case 1. This is because decreasing the ratio increases the length of the cooling wall and, in turn, enhances heat transfer, resulting in a rise in a temperature gradient. It is worth noting that the area of each trapezoidal enclosure is constant in this analysis, so a rise in heat transfer causes an increase in a temperature gradient.
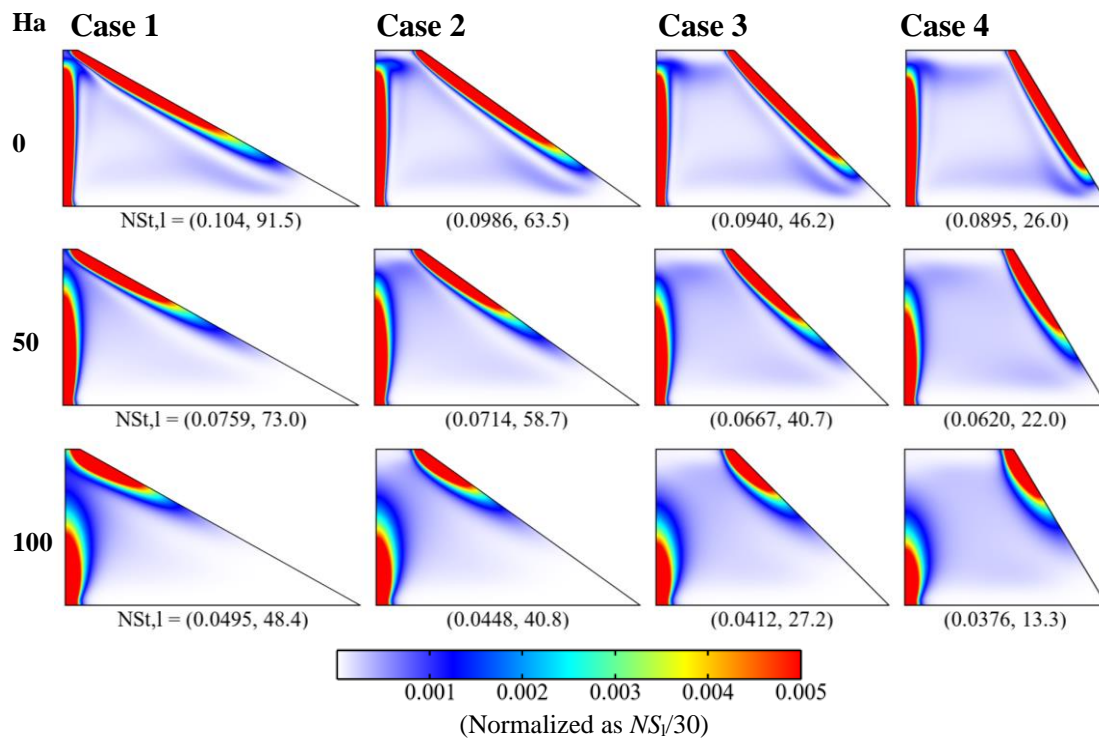
Figure 5.20 Total entropy generation at Ra = 10^6 for different Ha values.

Figure 5.21 depicts the impact of varying the magnetic field orientation (γ) from 0° to 180° on the total EG for four distinct cases, with Ra = 10^6, Ha = 70, and ζ = 2%. The allocation of Lorentz force in the *X* and *Y* directions alters as the magnetic field orientation changes, leading to changes in total EG. However, the effect of magnetic field orientation on total EG is minor. The lowest overall EG is observed for $\gamma = 30°$, while the highest is observed for $\gamma = 135°$. This is due to the fact that for $\gamma = 30°$, the Lorentz force drives the fluid toward the core region of the cavity, whereas

for $\gamma = 135°$, it moves the fluid toward the left wall (heat source). It is also observed that decreasing L_{top}, as in the case of non-MHD flow, increases the overall EG.
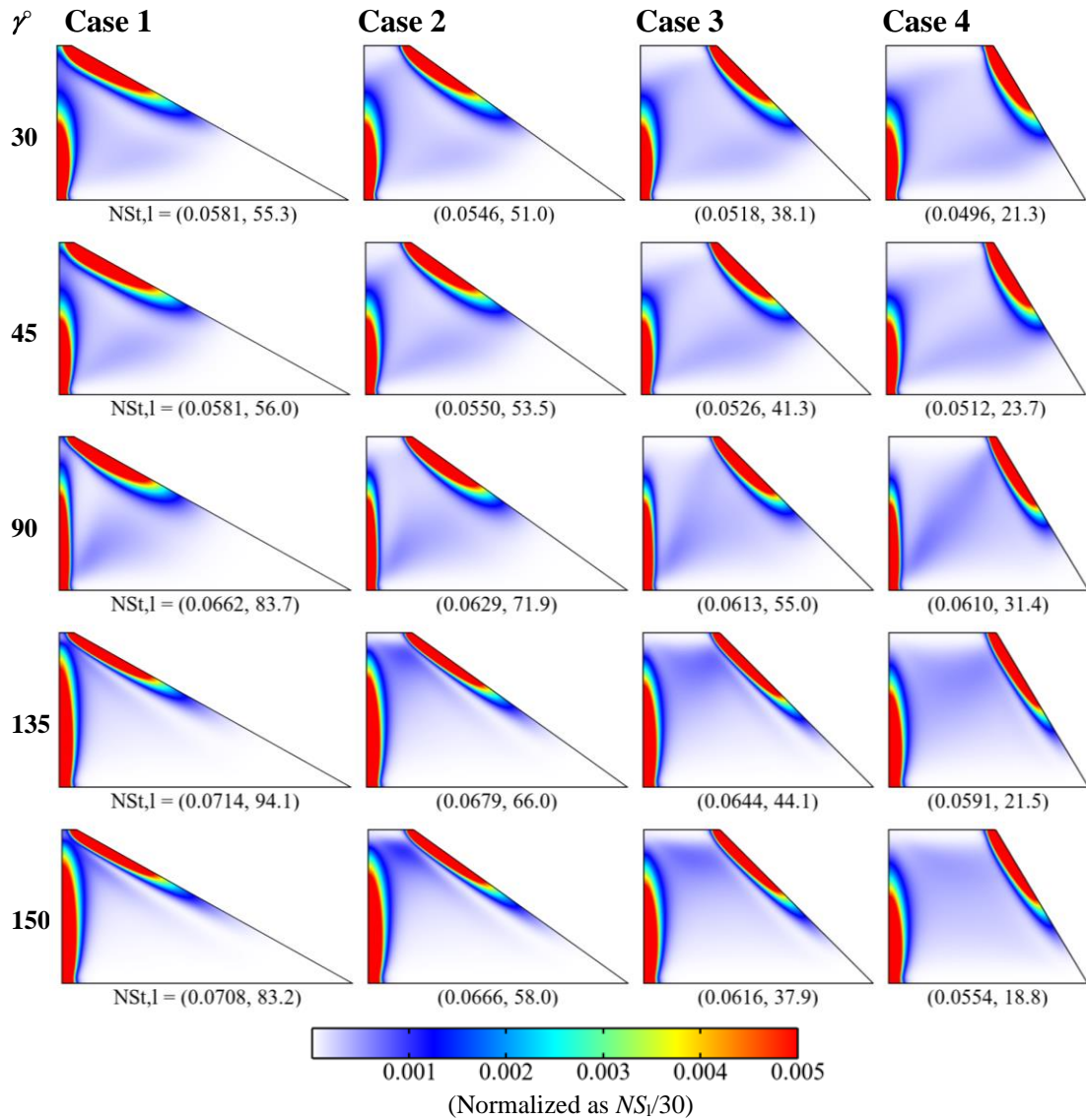
Figure 5.21 Total entropy generation at Ra = 10^6 and Ha = 70 for different γ values.

Furthermore, Figure 5.22 shows the effect of changing γ (= 30, 45, 90, 135, and 150°) on the magnetic EG (NS_m) for a specific value of Ra = 10^6, Ha = 10, and ζ = 2%. It is observed that for $\gamma < 90°$, the NS_m is high near both the hot and cold walls, whereas it is high close to the hot wall for $\gamma > 90°$. Notably, the order of magnitude of NS_m remains nearly identical in all cases, and its value is extremely low for the present problem.

Figure 5.22 Magnetic entropy generation at Ra = 10⁶ and Ha = 10 for different γ values.

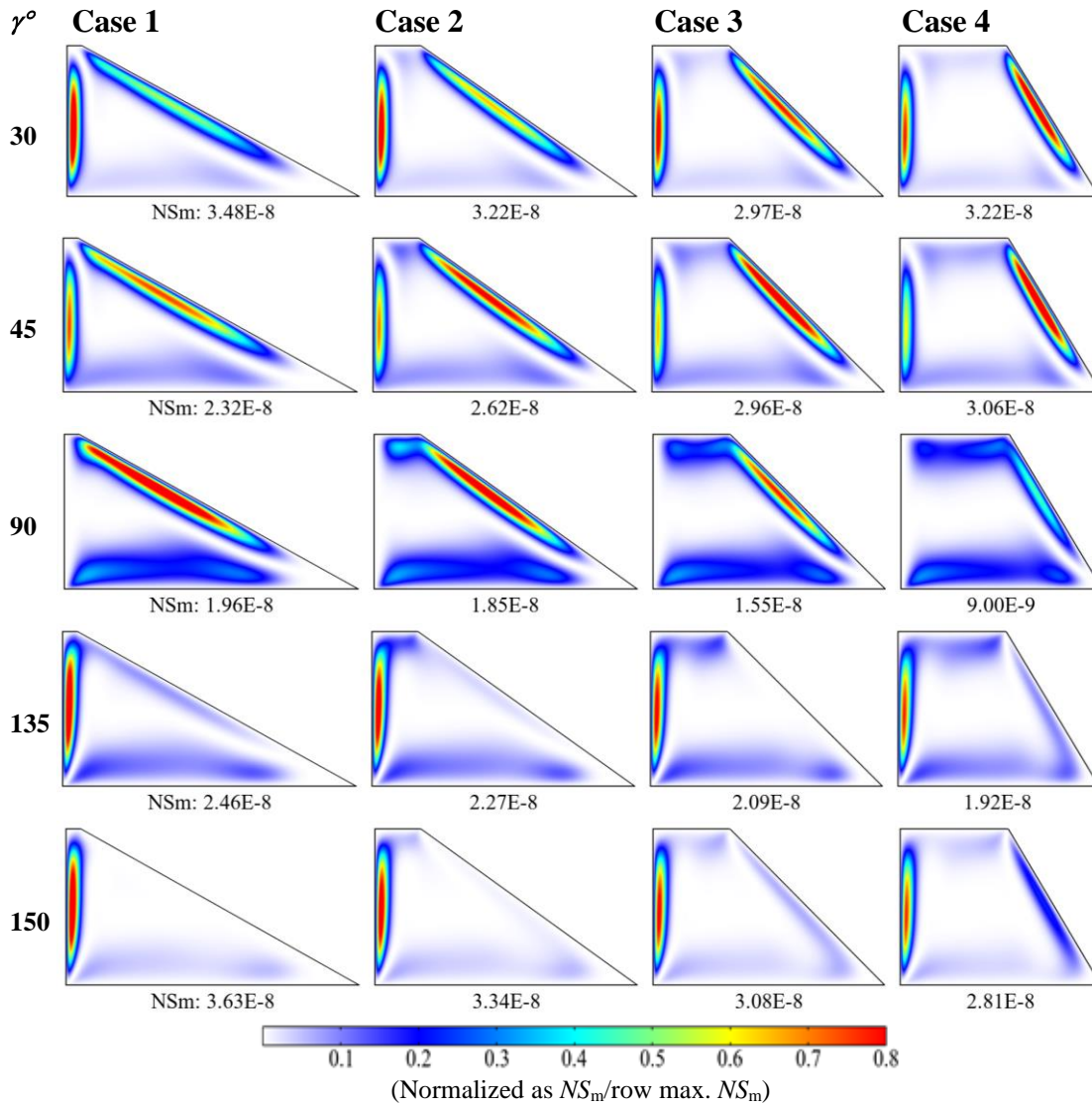
Figure 5.22 Magnetic entropy generation at $Ra = 10^6$ and $Ha = 10$ for different γ values.

5.3.6 *Flow patterns in an equivalent triangular system*

In this section, the study is extended for a special case of a trapezoidal geometry, namely a triangular geometry ($L_{top} = 0$). The corresponding results are presented systematically considering the streamlines, isotherms, heatlines, and entropy generation altogether to address the effects of Ra, Ha, and γ in Figures 5.23 to 5.25.

Figure 5.23 shows the impact of Rayleigh number (Ra) on thermo-fluid flow aspects in a non-MHD situation (Ha = 0). Figure 5.23a (first row) shows that as the Rayleigh number (Ra) increases, the flow pattern adopts the shape of the triangular cavity and the convection cells elongate towards the active wall, resulting in congestion of streamlines near the hot left and cold right walls. The strength of the flow increases with Ra, as indicated by an increase in the maximum value of the

stream function (ψ_{max}). Compared to a trapezoidal enclosure, the flow strength in a triangular enclosure is found higher. The temperature distribution is shown in Figure 5.23b (second row). As velocity and temperature are coupled in buoyancy-driven flow, the isotherm profiles change with varying Ra. The temperature gradient is highest at the junction of the hot and cold walls, and it increases with the Ra value. The increase in temperature gradient is evident from the rise in the Nusselt number (Nu).
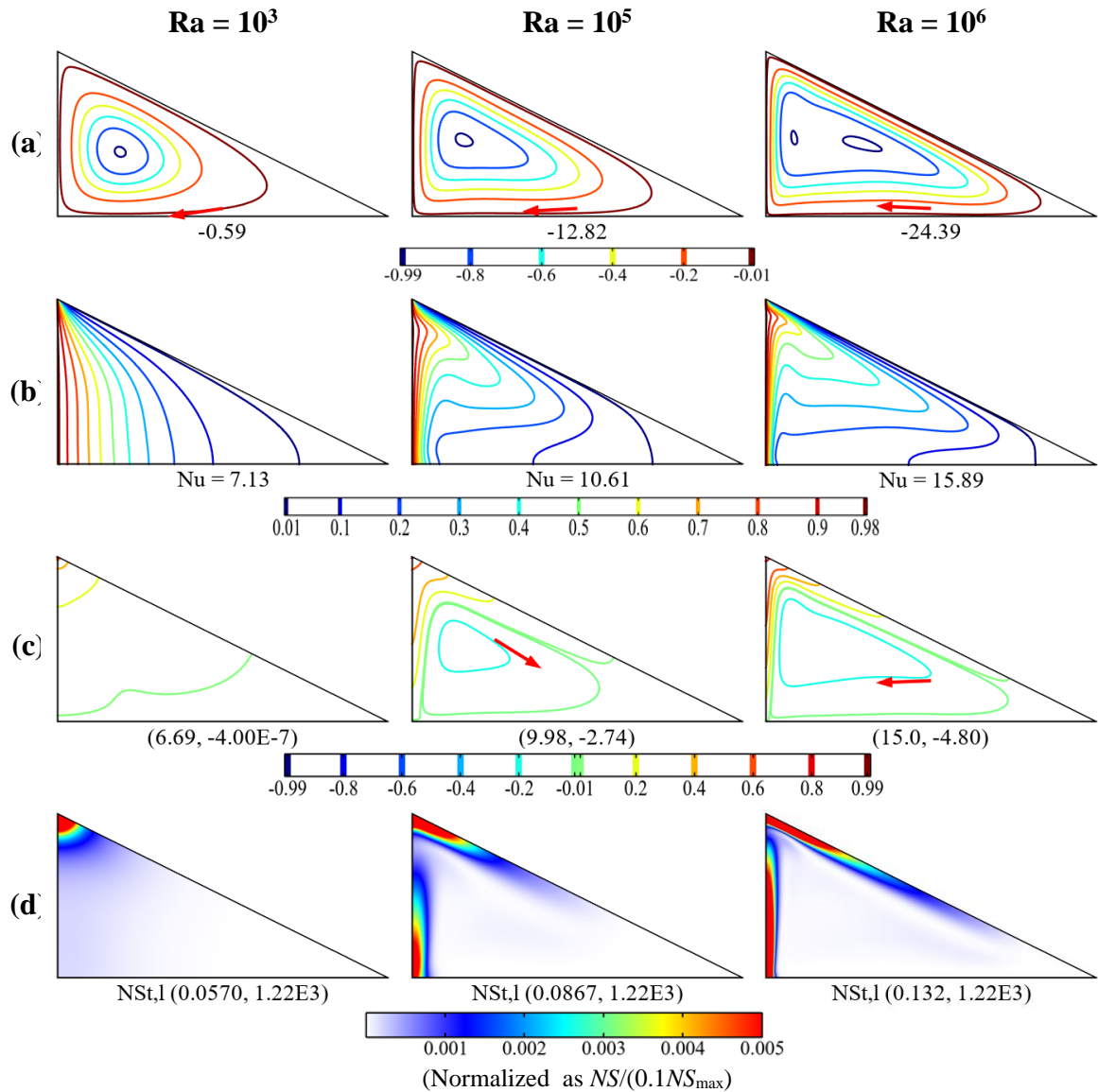
Figure 5.23 Effects of Ra on non-MHD (Ha = 0) flow patterns in the triangular system: (a) streamlines, (b) isotherms, (c) heatlines, (d) entropy generation (NS)

The impact of Ra on heat flow patterns is shown in Figure 5.23c (third row). When Ra is low (= 10^3), the thermal energy is directly transferred from the hot left wall to the cold right wall. However, as Ra increases, energy circulation cells appear and become stronger. This is evident from the highest value of the heat function at the

left hot wall, which increases with increasing Ra. Finally, Figure 5.23d (fourth row) depicts the effect of Ra on the irreversibility generation. It is observed that thermal irreversibility dominates over viscous and magnetic irreversibilities. Therefore, in this figure, the total entropy is presented. The local value of the entropy generation rate (NS_l) is higher in regions with a significant temperature gradient. As Ra increases, the overall irreversibility increases as well, as demonstrated by the first numerical value specified in the entropy generation (EG) contour. Therefore, it can be concluded that Ra enhances flow strength, heat transfer, and irreversibility.
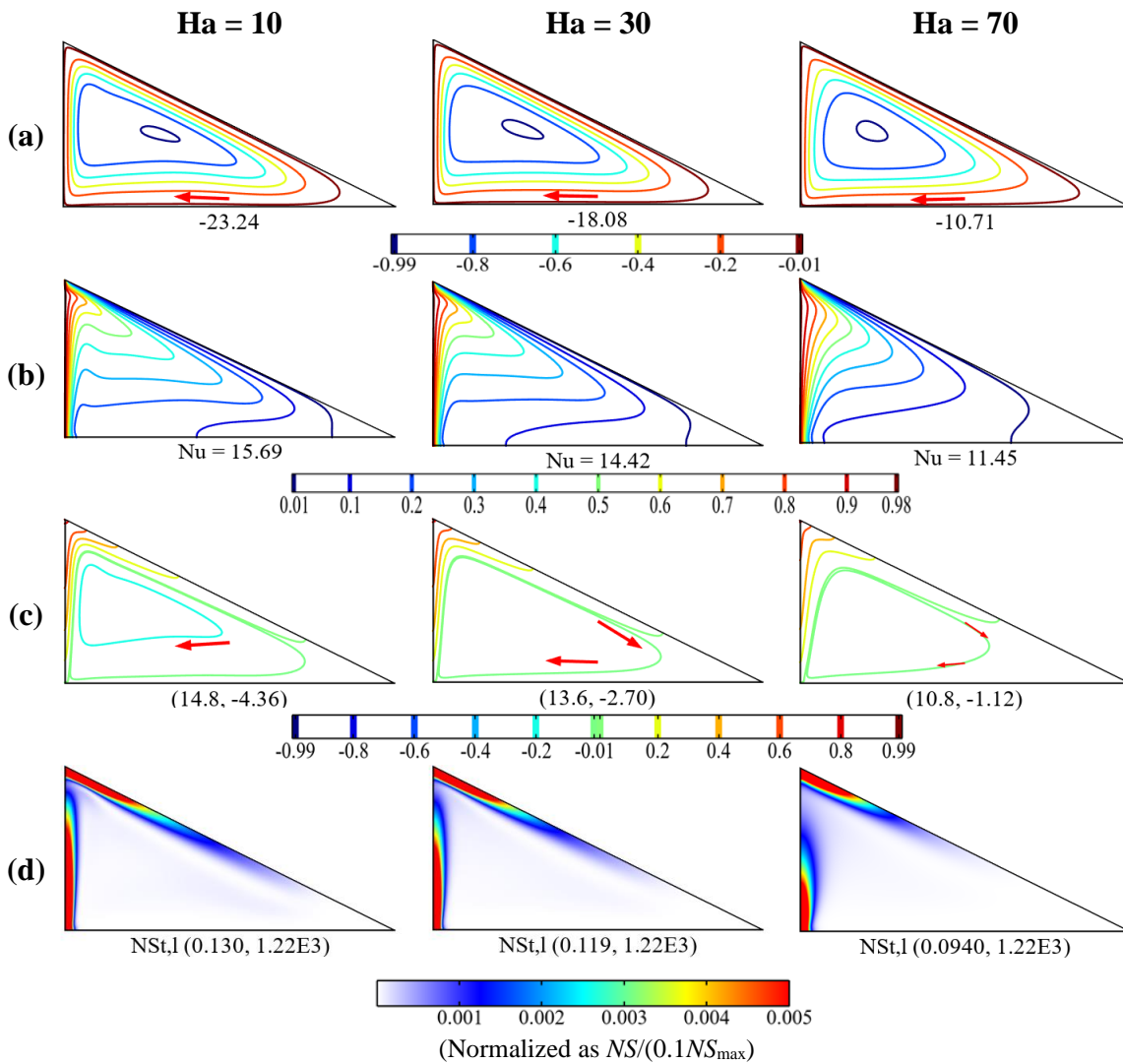
Figure 5.24 Effects of Ha on MHD flow patterns (Ha ≠ 0) in the triangular system at Ra = 10⁶: (a) streamlines, (b) isotherms, (c) heatlines, (d) entropy generation (*NS*).
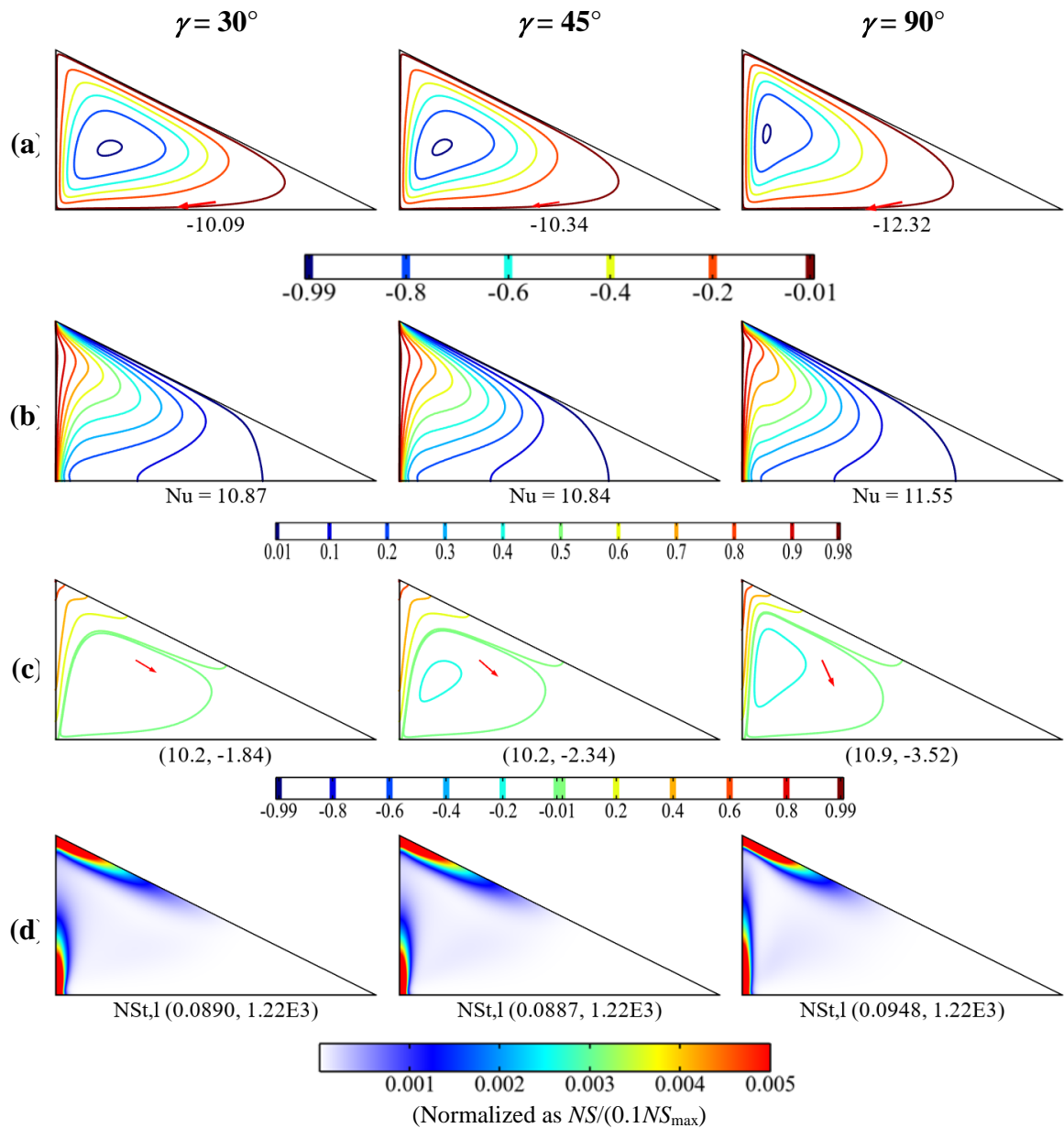
Figure 5.25 Effects of γ on MHD flow patterns (Ha ≠ 0) in the triangular system at Ha = 70 and Ra = 10^6: (a) streamlines, (b) isotherms, (c) heatlines, (d) entropy generation (*NS*).

In Figure 5.24, the effects of magnetic field strength (Ha) on the flow patterns, temperature distribution, heat flow pattern, and irreversibility of a triangular enclosure are investigated at Ra = 10^6. Figure 5.24a (first row) shows that the flow structure of MHD flow is similar to the non-MHD flow, with the exception of quantitative changes in flow velocity. As Ha increases, the convection cells become less congested near the active wall, indicating a decrease in flow strength. This is further confirmed by the decrease in the value of ψ_{max}. The impact of Ha on the temperature distribution is illustrated in Figure 5.24b (second row), where a rise in Ha results in a decrease in the temperature gradient, as shown by the increase in the value of Nu. The effect of

Ha on heat flow structure is demonstrated in Figure 5.24c (third row), where the thermal energy transport via direct mode and energy circulatory cells for low Ha (= 10) is reduced as Ha increases, leading to a decline in heat flux. The influence of Ha on irreversibility is presented in Figure 5.24d (fourth row), where a higher local value of *NS* is observed in regions with a significant temperature gradient. As Ha increases, there is a decrease in overall EG, as indicated by the first numerical value specified in the EG contour. The results suggest that an increase in Ha leads to a decline in flow strength, heat transfer, and irreversibility generation.

Finally, the impact of the inclination (γ) of the magnetic field is addressed in Figure 5.25. Figure 5.25a (first row) shows how the flow pattern is influenced by the change of γ. The study considers values of γ from 0° to 180°, with a specific focus on γ = 30, 45, and 90°. Results reveal that changes in the direction of the magnetic field lead to alterations in the flow structure. When γ = 90°, the hydrodynamic boundary layer's thickness is at a minimum, causing a rise in flow strength. This observation is supported by the increase in the value of ψ_{max}. The impact of magnetic field direction on temperature distribution is displayed in Figure 5.25b (second row). It is observed that the temperature gradient changes with varying γ, reaching its peak value at γ = 90°. This is supported by the increase in the value of Nu. Figure 5.25c (third row) demonstrates the impact of γ on the heat flow pattern. The thermal energy flow from the heat source to the heat sink occurs via direct mode and also via energy circulation cells for γ = 30°. However, for γ = 90°, heat transport through the energy circulatory cell increases. Additionally, the space between heatlines becomes thinner, indicating a rise in heat flux. This is further supported by the heatline contour's first numerical value (the highest value at the left hot wall). Figure 5.25d (fourth row) illustrates the effect of γ on EG. Results show that the value of *NS* is highest in areas with a strong temperature gradient, with a peak value at γ = 90°. The numerical value specified in the EG contour also supports this finding. In conclusion, variations in magnetic field inclination affect flow strength, heat transport, and irreversibility, with γ = 90° providing the highest flow strength, heat transfer, and irreversibility generation.

5.3.7 *Analysis of global thermal performance parameters (Nu, η)*

In order to understand how the overall thermal performance of a system is affected by its geometric design, the mean Nusselt number (Nu) is used to illustrate the variation in global heat transfer characteristics. The heat transfer performance

parameter (η) is then used to assess whether the geometric shape enhances or reduces thermal energy transport. It is calculated by taking the ratio of the difference in the Nu values of specific case and base case to the Nu value of the base case.

Figure 5.26a shows the effect of varying Ra from 10^3 to 10^6 on the Nu while maintaining Ha = 10, $\gamma = 0°$, and $\zeta = 2\%$ fixed for trapezoidal as well as triangular cases. The results indicate that the Nu is minimal for low Ra values (= 10^3) and increases monotonically as Ra rises due to an increase in the convective mechanism of heat transport irrespective of the system's geometrical shape. Moreover, the Nu curve of the trapezoidal system (Cases 1, 2, 3, and 4) is higher than that of the square system (Base case), which suggests that the thermal energy transport is greater in the former. It becomes magnificently highest for the equivalent triangular system. This is because the length of the cooling wall of the trapezoidal system increases as the top wall length-to-height ratio decreases, and as a result, it withdraws more amount of thermal energy from the heat source. As a limiting case, L_{top} tends to zero, and the evolved triangular thermal system provides maximum heat transfer.

(a)   (b)
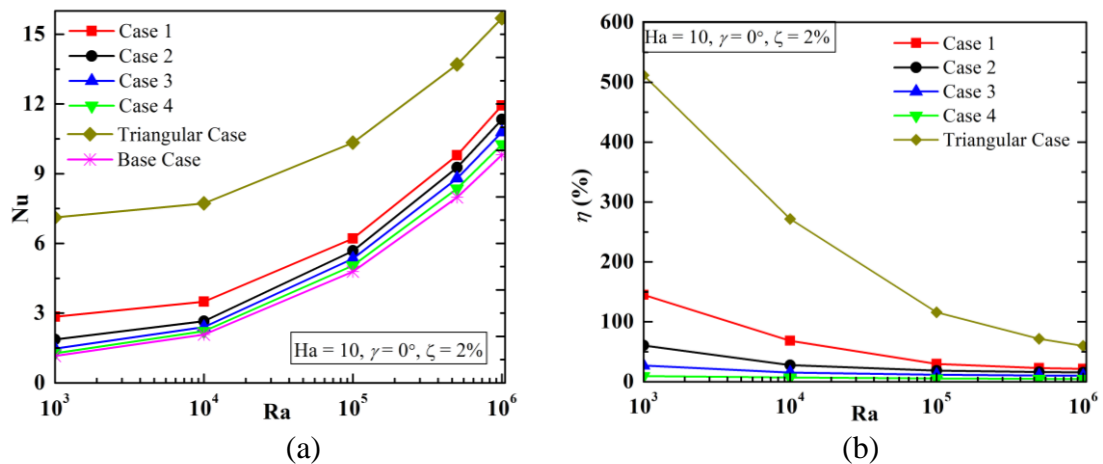
Figure 5.26 Variation of (a) Nu and (b) heat transfer enhancement (η) at Ha = 10, $\gamma = 0°$, $\zeta = 2\%$.

According to the results, after the triangular system, the Case 1 configuration of the trapezoidal thermal system can be employed as the optimal geometrical design to achieve superior heat transport. This is also evident from the heat transfer performance parameter (η) shown in Figure 5.26b, which demonstrates that for all cases, the heat transfer performance parameter shows a positive value indicating an enhancement in heat transfer, compared to their equivalent square base case. The maximum enhancement in heat transfer is noted for triangular case at low Ra values (= 10^3). The heat transfer performance parameter (η) curve indicates that enhancement in thermal energy transport reduces as Ra increases and remains almost constant at

higher Ra values ($\geq 10^5$). For non-MHD flow (Ha = 0), these observations are almost the same except for a minor change in the values.

It is further noted from Figure 5.26a, the Nu value increases monotonically in all cases. It is also noted that the Nu curves of cases 1, 2, 3, 4, and the triangular case are almost parallel to the base case (square cavity). It is evident from the figure that the difference of Nu is almost fixed, and the value of the Nu for the base case grows as Ra increases. As a result, the heat transfer enhancement diminishes as Ra increases (as shown in Figure 5.26b).
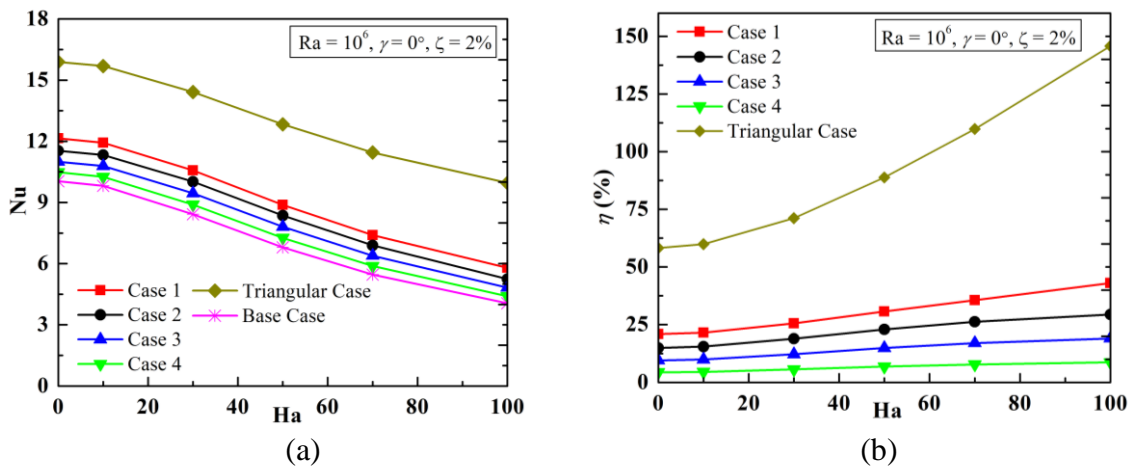
Figure 5.27 Variation of (a) Nu and (b) heat transfer enhancement (η) at Ra = 10^6, and ζ = 2%.

Figure 5.27a displays the impact of varying Ha from 0 to 100 on the Nu for all the scenarios studied here, while keeping Ra = 10^6, $\gamma = 0°$, and $\zeta = 2\%$ constant. The rise in Ha leads to an increase in the Lorentz force and a subsequent reduction in fluid movement and heat transfer, causing Nu to decrease monotonically. For the trapezoidal systems, Case 1 exhibits a higher Nu curve as compared to other trapezoidal cases due to the maximum length of the cooling wall, which draws more heat from the source and improves heat transfer. For the same reason, the triangular thermal system can cause maximum heat transfer. Figure 5.27b demonstrates the effect of Ha on the heat transfer performance parameter (η). In all cases, the value of η is positive, indicating an increase in heat transfer. The rise in Ha results in an augmentation of heat transfer performance parameter, after the triangular case, with Case 1 displaying the highest enhancement and Case 4 the least. The other two cases exhibit an improvement in heat transfer between these two extremes. The enhancement in heat transfer, compared to the base case (square geometry), is found more as Ha increases. This MHD flow result is consistent with the non-MHD flow, with a quantitative variation in η value.

127

Figure 5.28a shows the impact of magnetic field inclination (γ) on thermal energy transfer. As γ changes, the Lorentz forces' horizontal and vertical components vary, resulting in changes in the buoyant force. The magnetic field inclination ranges from 0 to 180°, and the values of Nu at $\gamma = 0°$ and 180° are identical in all the cases. At $\gamma = 90°$, heat transfer is expected to be at its maximum, but the results show that Nu reaches its peak value at $\gamma = 135°$. This is because, at $\gamma = 135°$, the Lorentz force component moves the fluid toward the heated wall. In other inclinations, the sharing of the Lorentz force changes in the X and Y directions, causing Nu to vary. However, there is almost no effect on Nu results of the triangular system, although it is the most superior.

(a)   (b)
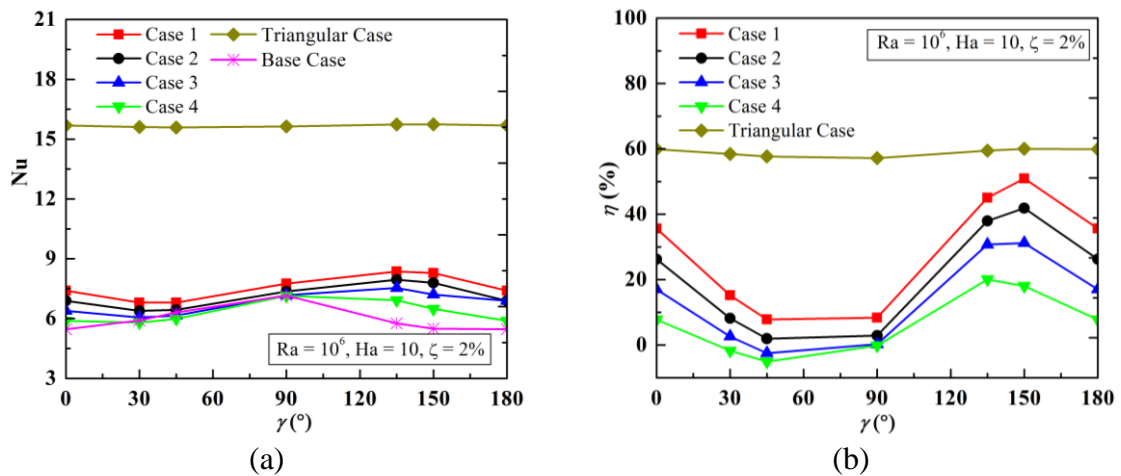
Figure 5.28 Variation of (a) Nu and (b) heat transfer enhancement (η) at Ra = 10^6, and Ha = 10.

(a)   (b)
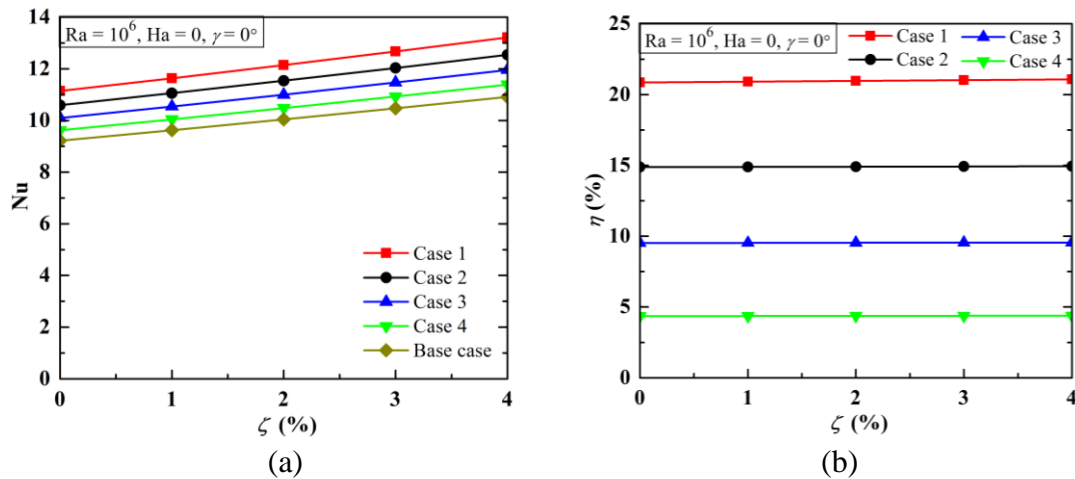
Figure 5.29 Variation of (a) Nu and (b) heat transfer enhancement (η) at Ra = 10^6, Ha = 0.

Figure 5.28b illustrates the effect of magnetic field inclination on the heat transfer performance parameter. All cases, except for Case 4, exhibit a positive value for η. The negative η observed in Case 4 for $\gamma = 30°$ and 45° is due to the cooling wall length, in this case, being similar to that of the base case. The enhancement is noted for the triangular system, and Cases 1, 2, 3, and 4. The results indicate that the Case 1 configuration of the

trapezoidal system is the optimal geometrical design for achieving maximum enhancement for MHD flow.

Finally, to investigate the impact of varying volumetric concentrations of CuO nanoparticles on global thermal performance, only trapezoidal cases are examined. The variation in Nu values for different ζ values ranging from 0 to 4% while maintaining Ra = 10^6 and Ha = 0 is shown in Figure 5.29a. The addition of nanoparticles in the base fluid (water) increases the effective thermal conductivity of the working fluid, resulting in improved thermal convection and enhanced thermal energy transport. This is evidenced by the increase in Nu as ζ rises. However, the heat transfer performance parameter (η) curve in Figure 5.29b remains horizontal; indicating that the heat transfer performance parameter remains constant with changing ζ. The maximum enhancement is observed for Case 1, and the minimum enhancement is noted for Case 4. The findings suggest that Case 1 is the optimal choice to achieve maximum heat transfer enhancement.

5.4 Conclusions

This study compared the trapezoidal, triangular, and square thermal systems under constraint-based equivalency. By altering the ratio of the top wall length to cavity height, the effects of Rayleigh number (Ra), Hartmann number (Ha), magnetic field orientation (γ), and nanoparticle concentration (ζ) on heat transfer and thermodynamic irreversibility are analyzed by taking four distinct cases of the trapezoidal system and one triangular. The key findings are summarized as follows:

- The geometrical design influences fluid velocity, heat transfer, and irreversibility.
- The thermal performance of a trapezoidal system is superior to a square system, and the triangular system can be used to achieve optimal enhancement.
- Decreasing the top wall length to cavity height ratio of the equivalent trapezoidal thermal system leads to increased flow strength.
- The nanoparticle concentration (ζ) enhances heat transfer and flow strength at higher Ra.
- Increasing Ra improves thermal performance and flow strength.
- The magnetic field intensity (Ha) has a significant impact on fluid flow and heat transport in natural convection, and increasing Ha reduces flow strength ($\psi_{\max}$) and heat transfer (Nu). In the case of a triangular cavity, heat transfer reaches a maximum at $\gamma = 90°$.

- Thermodynamic entropy generation (EG) is mainly governed by the thermal effect (or temperature gradient), with the effects of viscous and magnetic EG being minimal.

- Total EG increases with Ra and ζ and decreases with increasing Ha.

- Lowering the ratio of hot wall length to cavity height increases the overall EG of a trapezoidal system.

Chapter – 6

Heat transport and accompanying irreversibility during MHD nanofluid flow in constraint-based analogous square and circular annular systems

6.1 Introduction

Annular systems have been widely researched in terms of their application in heat-exchanging devices, particularly buoyancy-driven convection. Understanding the effects of various non-dimensional parameters on fluid flow, thermal energy transport, and entropy generation is important from the application viewpoint. Several numerical and experimental studies on this topic have been conducted. Here, a brief literature review is presented addressing several pioneering works, fundamental studies, and current research trends. Many numerical pioneering studies have been published investigating the influence of non-dimensional parameters on fluid flow and thermal energy transport in the circular annulus (Mack and Bishop 1968; Custer and Shaughnessy 1977; Projahn et al. 1981; Wang and Bau 1988; Kumar 1988; Lee 1992). The effect of Ra was studied by various authors (Mack and Bishop 1968; Wang and Bau 1988), and the impact of Pr was studied by several researchers (Custer and Shaughnessy 1977; Lee 1992).

Furthermore, the impact of the concentric and eccentric position of the inner cylinder was studied by Projahn et al. (1981). Kumar (1988) numerically investigated the effect of constant heat flux and isothermal heating in a horizontal annulus and discovered that constant heat flux has a higher rate of heat transport than isothermal heating when the temperature difference is the same in both cases. Fundamental numerical research on this topic is also available in abundance (Yoo 1998; Mizushima et al. 2001; Shi et al. 2006; Alipour et al. 2013; Seyyedi et al. 2015; Yuan et al. 2015). Yoo (1998) studied free and mixed convection in a differentially heated horizontal concentric cylinder and discovered a sharp decline in heat transfer as the rotation of the inner cylinder increased. Mizushima et al. (2001) numerically investigated buoyancy-driven flow and heat transport in a horizontal cylindrical annulus and found that dual stable steady solutions can be obtained for Ra higher than a threshold value.

131

Yuan et al. (2015) studied the effect of varying inner cylinder shapes (cylindrical, elliptical, square, or triangular) in a concentric cylinder annulus and found that thermal performance was better in square, triangular, and elliptical annuli compared to the cylindrical annulus. Alipour et al. (2013) investigated the effect of radius ratio on free convection in a concentric annulus. Limited experimental work is available on this topic in addition to fundamental numerical research (Powe et al. 1969; Kuehn and Goldstein 1976). Kuehn and Goldstein (1976) conducted comprehensive experiments to examine fluid flow and heat transfer in buoyancy-driven flow inside a horizontal annulus. They used a Mach-Zehnder interferometer to evaluate temperature distributions and local heat-transfer coefficients experimentally. A numerical analysis was also performed to supplement the experimental data. Furthermore, they found that the present experimental and numerical results are in excellent agreement. Their findings served as a benchmark for subsequent research in this area.

Recent research has shifted from traditional fluids to improved heat transfer fluids, known as nanofluids. Numerous researchers have investigated the effects of nanofluid on free convection in circular annuli, including Tayebi and Chamkha (2017) and Saha et al. (2020), who have reported that introducing nanoparticles into the base fluid enhances flow strength while significantly improving heat transfer. With advancements in technology, research has shifted towards magnetohydrodynamics (MHD)-based buoyancy-driven convection. Many authors, including Sheikholeslami et al. (2014) and Aboud et al. (2020), have examined the influence of a magnetic field on heat convection in circular annuli and found that flow strength, and heat transport decrease as the magnetic field's intensity increases.

A few studies on entropy generation (EG), which is crucial in assessing irreversibility in thermodynamic systems, have been published in the literature for buoyancy-driven convection in circular annuli, including Shahsavar et al. (2018) and Tayebi and Öztop (2020). Shahsavar et al. (2018) observed that as Ra values increase, the rate of thermal, viscous, and total entropy generation increases, with the rate of thermal EG being significantly higher than the rate of viscous EG. The heatline approach has been employed by a few authors, including Waheed (2007) and Sheikholeslami et al. (2013), to study heat flow visualization in circular annuli. Waheed (2007) used the heat function technique to study the combined effect of Ra, Pr, and gap width on buoyancy-induced flow in the horizontal cylindrical annulus and found that the heat function profiles depend on these parameters.

132

Compared to circular annuli, limited research has been conducted on square annuli. Asan (2000) investigated the effects of dimension ratio and Ra on flow pattern and thermal energy transport, found that multiple cells are developed as the dimension ratio increases. Arefmanesh et al. (2012) numerically investigated the impact of Ra, aspect ratio (*A*), and nanoparticle concentration (ζ) on thermal convection in a differentially-heated square duct filled with nanofluid and reported that eddies develop as the Ra value increases, and the mean Nusselt number (Nu) increases as ζ increases. Few papers have been published on buoyancy-driven convection in triangular annular systems. Shadlaghani et al. (2019) investigated the impact of fins on natural convection in concentric and eccentric annuli with varying cross-sections (square, circular, and triangular) and found that the reverse triangular annulus with fins installed on the inner wall has the best heat transfer rate, and eccentric annulus has a higher heat transfer rate than concentric annulus. Other important works, including Mahapatra et al. (2013), Datta et al. (2016), Biswas and Manna (2017a), Chatterjee et al. (2022), and Chatterjee et al. (2023), indirectly present annulus-type flows by placing solid obstructions in the flow domains. In addition to computational and experimental studies, Ahmed and Ahmed (2017) presented a review paper on the thermal performance of annulus systems. A review of the literature reveals that there is a limited amount of research on buoyancy-driven convection in an annular configuration, with studies exploring flow and heat transport in various annular systems explicitly.

The present study aims to fill the gap in the literature on research on square and circular annuli by comprehensively comparing their thermal performance in the presence of a magnetic field and a nanofluid. Although there have been several studies on buoyancy-induced convection in circular and square annuli, there is a dearth of research on the impact of a nanofluidic magnetic field on heat convection and entropy generation in these geometries. On a circular annulus, one systematic study conducted by Saha et al. 2022a recently establishes enhanced heat transfer in the presence of an adiabatic block, which serves as an initial effort on the present annular problem. This present study takes a more comprehensive approach by conducting a comparative analysis of different annular systems using a novel constraint-based approach. This approach considers the matching of flow areas or cooling lengths, while the heating length remains identical in all three cases consisting of a square annulus (base case) and two circular annuli (one on matching flow areas

or the other on matching cooling lengths). This fundamental research aims to comprehend the influence of geometrical shapes on the thermal performance of real systems, which will assist in determining the thermal system with superior performance, along with valuable insights into the effects of various parameters on fluid flow and heat transfer in two distinct shapes of the annular geometries. Thus, the novelty of this study lies in its comprehensive approach and the use of a constraint-based methodology to analyze the impact of a magnetic field on heat transport and accompanying irreversibility during MHD nanofluid flow in constraint-based analogous square and circular annular systems.
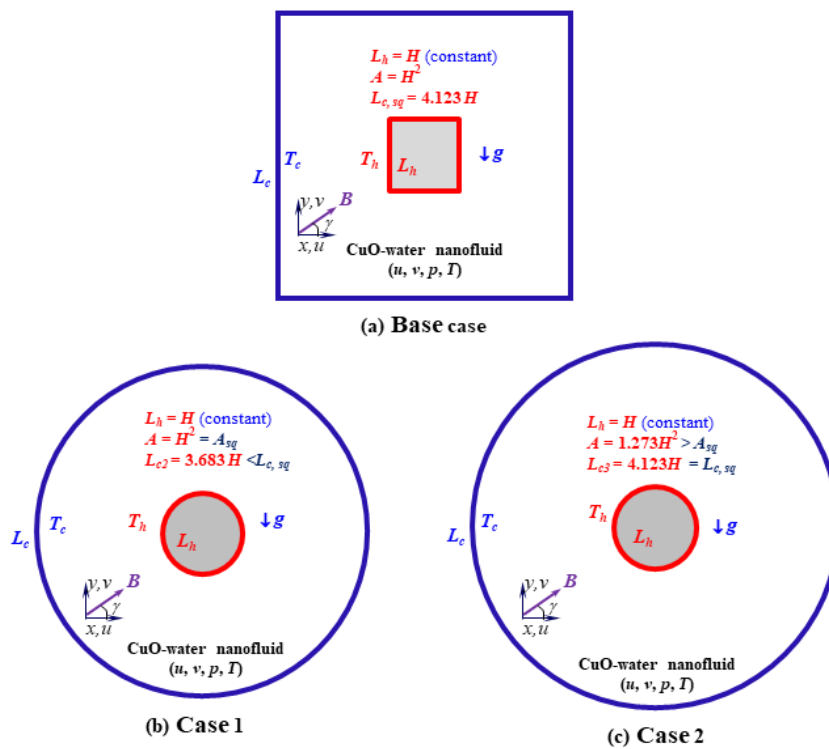
Figure 6.1 Problem description: (a) square annulus (base case), (b) circular annulus with volume constraint (Case 1), and (c) circular annulus with length constraint (Case 2).

6.2 Problem formulation and numerical solutions

Figure 6.1 describes analogous circular annular systems derived from a square annular system. The study explores three different cases based on constraints: (i) the Base case, represented by the square annular system; (ii) Case 1, which represents a circular annular system with identical flow area or volume as the Base case; and (iii) Case 2, which represents a circular annular configuration with the same cooling length as the Base case. The heating length for Cases 1 and 2 is equivalent to that of the Base case and set to $L_h = H$ for circular geometries. Our analysis reveals that for

Case 1, the cooling length of the circular annular system ($L_c = 3.683H$) is smaller than that of the square annular system ($L_{c,sq} = 4.123H$). Similarly, for Case 2, the flow area of the circular annular system ($A_{cir} = 1.273H^2$) is greater than the square annular system ($A_{sq} = H^2$). Despite the different geometrical configurations, the circular annuli can be considered equivalent to the square annular system under the mentioned constraints. The study aims to examine the impact of geometrical design on thermal performance and flow features driven by buoyancy-induced convection, following the numerical methodology, and simulation technique as discussed in Chapter 2.

The mesh arrangements for the square annulus (Base case) are depicted in Figure A1 (e), and the mesh architectures for the equivalent circular annulus (Cases 1 and 2) are displayed in Figures A1 (f) and (g) in the Appendix. Table A1 (e) shows the mesh specifications for the square annulus (Base case), while Tables A1 (f) and (g) provide the mesh information for the equivalent circular annulus (Cases 1 and 2).

6.3 Results and Discussion

The current study's results and analyses are presented methodically in the following subsections, based on the theoretical discussion detailed in the preceding chapters. Section 6.3.1 examines the impact of Rayleigh number (Ra ranging from 10^3 to 10^6) on three distinct cases consisting of (i) square annulus (Base case), (ii) volume-constraint circular annulus (Case 1), and (iii) cooling length constraint circular annulus (Case 2). Section 6.3.2 analyzes the effect of nanoparticle concentration (with ζ ranging from 0 to 4%) on all the annuli (Base case, Cases 1 and 2). In Sections 6.3.3 and 6.3.4, the effects of the magnetic field (with Ha ranging from 0 to 100) and magnetic field inclination (with γ varying from 0° to 180°) are analyzed. In Section 6.3.5, irreversibility in the flow domain is studied using entropy generation (EG). The local behaviors of fluid flow and heat transfer are analyzed using streamlines and isotherms in Sections 6.3.1 to 6.3.4, parametric impacts on entropy generation are presented in 6.3.5, while global heat transfer is calculated using the average Nusselt number (Nu), presented in Section 6.3.6. This systematic and comprehensive approach aims to provide valuable insights into the effects of various parameters on fluid flow and heat transfer in different equivalent annular geometries, thereby facilitating the determination of thermal systems with superior performance.

6.3.1 *Effects of various Rayleigh numbers*

This study investigates buoyancy-induced convection in non-MHD flow (Ha = 0) within different annular thermal systems, considering different Rayleigh numbers (Ra) ranging from 10^3 to 10^6 and nanofluid concentration, $\zeta = 0.02$. The influence of Ra on the flow patterns is studied through the visualization of streamlines and isotherms, presented in Figures 6.2 and 6.3, respectively. In all cases, the inner wall is kept hotter than the outer cylinder, causing the fluid to absorb heat and move upwards along the vertical centerline; while rejecting heat to the cold outer wall and moving downwards, resulting in fluid circulation within the annular region. The streamlines in Figure 6.2 reveal the formation of a pair of counter-rotating kidney-shaped cells, symmetric about the vertical plane through the annulus centerline, and equidistant from it. The vertical plane acts as a virtual wall, with $\psi = 0$, prohibiting flow across it. The overall flow pattern is similar for all the cases; however, flow velocities vary with different Ra values, and the counter-clockwise and clockwise rotations are represented by positive and negative stream function values, respectively.
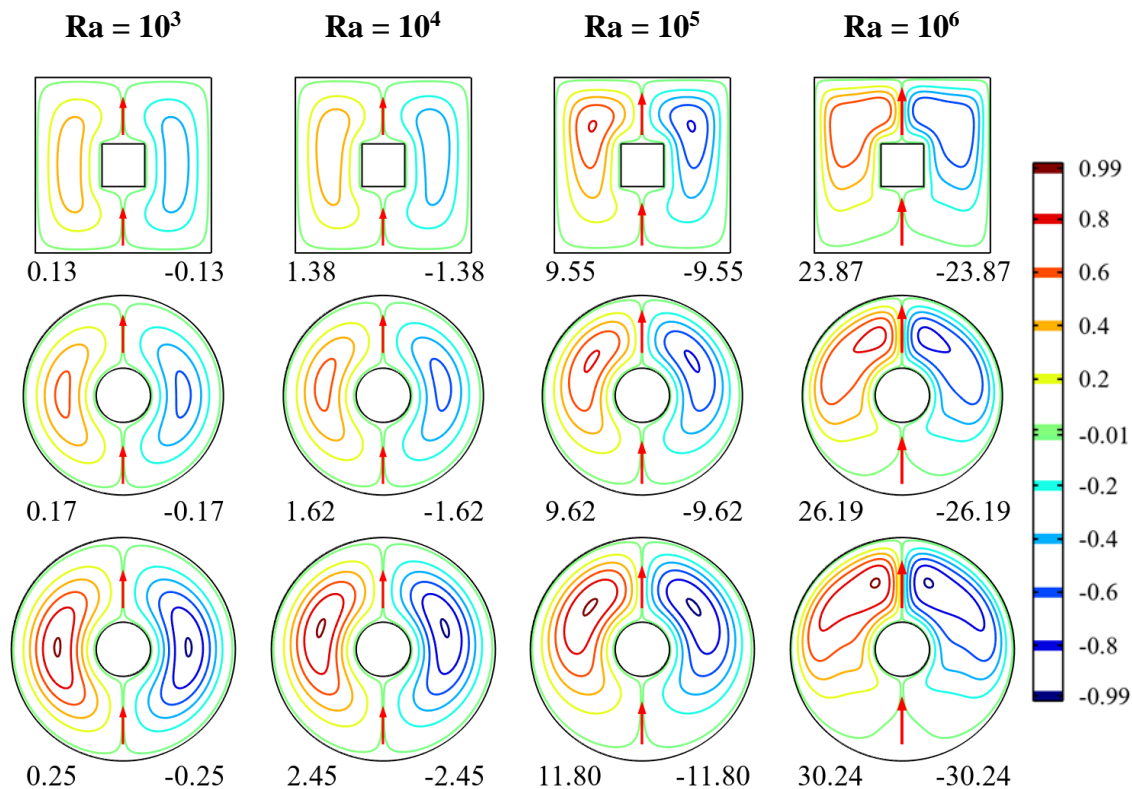
Figure 6.2 Streamlines for non-MHD flow (Ha = 0) at different Ra values.

At Ra (= 10^3), the velocity of flow is relatively low which is indicated by the ψ_{max} values. According to Figure 6.2 (first column), the values of ψ_{max} for Ra = 10^3

are 0.13, 0.17, and 0.25 respectively for the base case, and Cases 1 and 2. Whereas at higher Ra values (10^4 and 10^5), the improved buoyant convection leads to increased circulation strength and upward movement of the convection cells as indicated by the contours of stream function for Ra = 10^4 and 10^5. It creates a stagnation zone in the lower part of the annulus; however, streamlines are crowded at the upper portion of the annulus. At higher Ra = 10^6, a significant increase in flow velocity is observed, which is evident by the value of higher ψ_{max}. The values of ψ_{max} at Ra = 10^6 are 23.87, 26.19, and 30.24 for the Base case, and Cases 1 and 2, respectively (as illustrated in the last column in Figure 6.2).

The study finds that the circular annuli (Cases 1 and 2) have stronger flow than the square annulus (Base case). It happens due to a smoother flow path and reduced fluid friction, resulting in enhanced buoyant forces. Case 2, which has a larger flow volume, results in greater buoyant force and fluid motion.
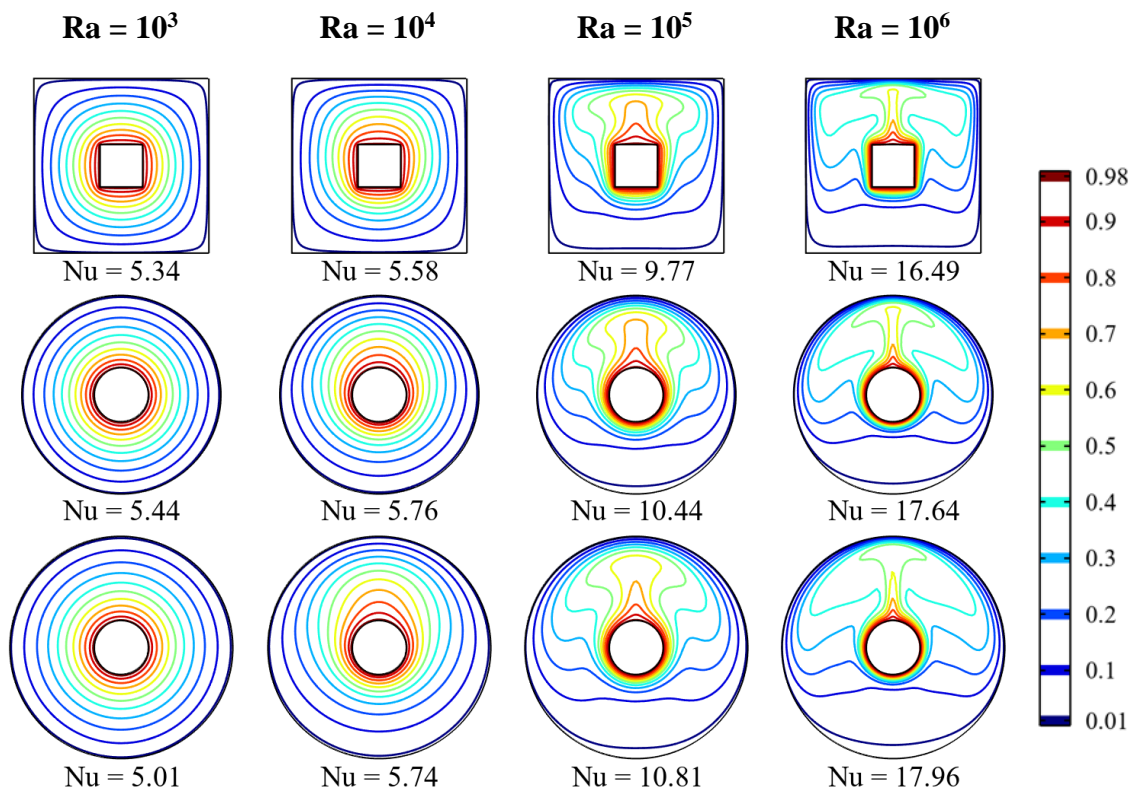
Figure 6.3 Temperature profile for non-MHD flow (Ha = 0) at different Ra values.

In Figure 6.3, the temperature profiles for non-MHD flow (Ha = 0) at different Ra values are shown. The magnitudes of the isotherm contours decrease towards the outer cold wall. It can be observed that the isotherm profiles around the inner heated blocks are almost identical in all the investigating cases. At low Ra (= 10^3), the

isotherms appear as concentric circles, indicating that heat transport is mostly due to pure conduction. These isotherms deviate slightly from the concentric circles and become eccentric circles at the onset of convective flow at $Ra = 10^4$. As Ra increases to 10^5 or 10^6, the convection cells move upwards due to the higher buoyancy force. The isotherms become crowded near the bottom portion of the inner wall and the top portion of the outer wall, forming a heated plume-like structure in the annulus's upper section. The isotherms get distorted more with increasing Ra. For $Ra = 10^4$ and 10^5, the isotherm features lie in between the limiting cases of $Ra = 10^3$ and 10^6. Additionally, for higher Ra values, such as $Ra = 10^5$ and 10^6, the radial temperature inversion appears, resulting in the separation of the thermal boundary layer at the inner and outer walls. This observation is similar to Kuehn and Goldstein (1976). As Ra increases, convective heat transfer enhances, as shown by the increased value of the mean Nusselt number (Nu) in Figure 6.3 (below individual snapshots). It is also observed that circular annular systems (Cases 1 and 2) benefit from curved heating and cooling walls, which produce less restriction to fluid flow velocity, resulting in stronger buoyancy-induced convection compared to a square annular system (Base case). Moreover, Case 2 (last row in Figure 6.3), cooling length constraint circular annulus, exhibits the highest convective heat transport, which is attributed to the higher buoyant force caused by the increased flow area.

6.3.2 *Impact of nanoparticle concentrations (ζ)*

In this section, the impact of nanoparticle concentration ($\zeta = 0$ to 0.04) is investigated on local fluid motion and heat transfer behaviors at higher Ra ($= 10^6$), as shown in Figures 6.4 and 6.5, respectively. The overall flow pattern is the same as described in the previous section, with the value of ψ_{max} gradually increasing from 23.48 ($\zeta = 0$) to 24.44 ($\zeta = 0.04$) as the concentration of nanoparticles increases. It is also worth mentioning here that the flow strength of the circular annuli (Cases 1 and 2) is higher than that of the square annulus (Base case), which is discussed in detail in Section 6.3.1. Examining the isotherm profiles shown in Figure 6.5, it is observed that the isotherms become more crowded as the concentration of nanoparticles (ζ) increases from 0 to 0.04. Moreover, the thermal energy transport of the circular annular systems (Cases 1 and 2) exceeds that of the square annular system (Base case), with the maximum thermal energy transport occurring in Case 2.

$\zeta = 0$ $\zeta = 0.01$ $\zeta = 0.02$ $\zeta = 0.04$
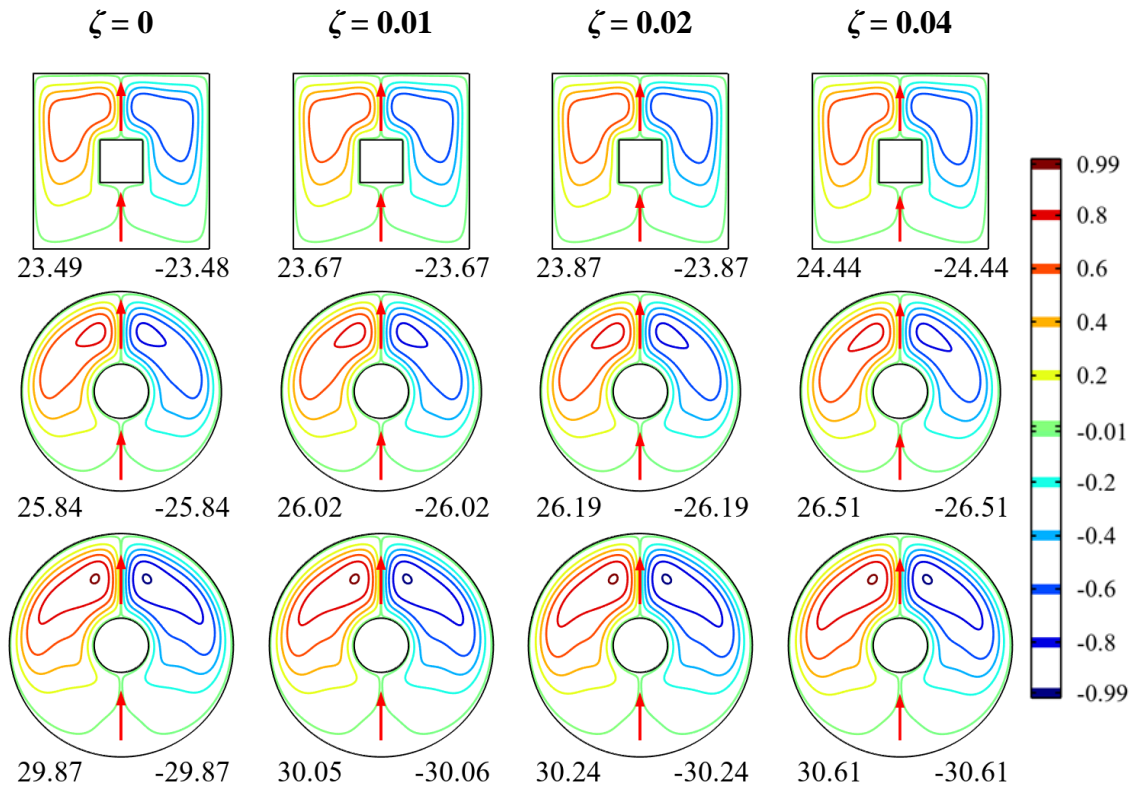
Figure 6.4 Nanofluid concentration (ζ) impact on non-MHD streamlines at Ra = 10^6.

$\zeta = 0$ $\zeta = 0.01$ $\zeta = 0.02$ $\zeta = 0.04$
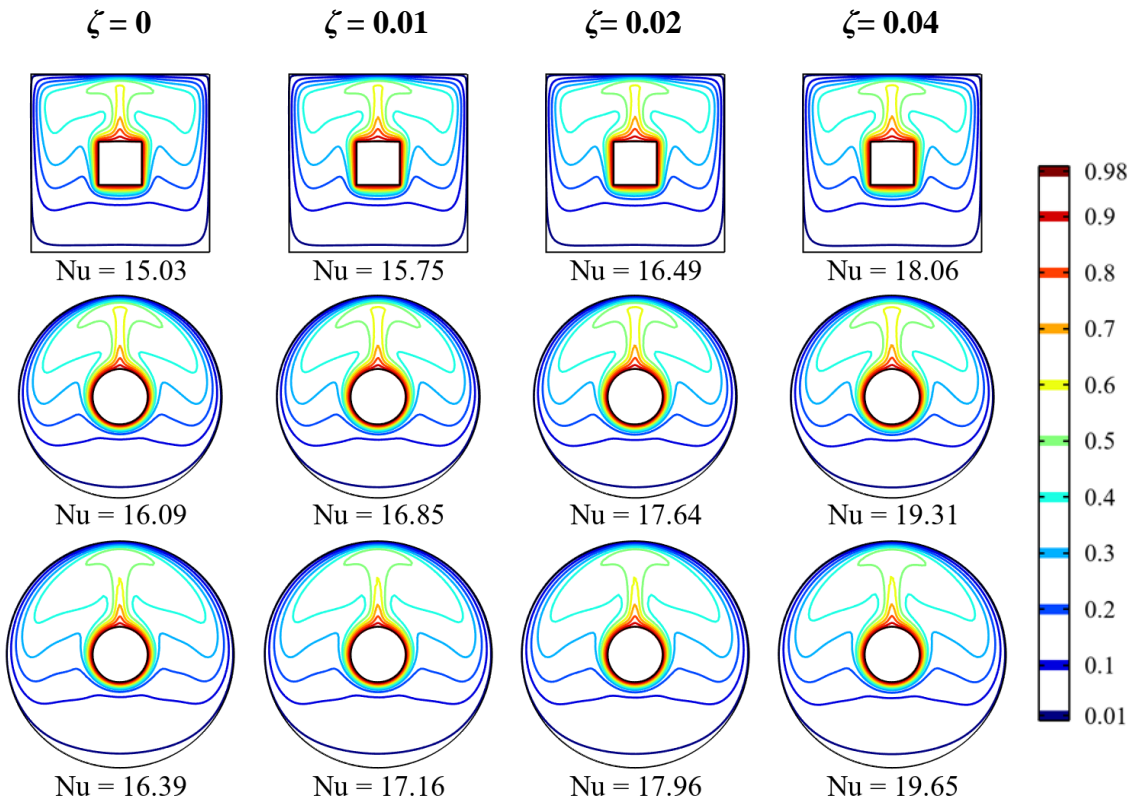
Figure 6.5 Nanofluid concentration (ζ) impact on non-MHD isotherms at Ra = 10^6.

6.3.3 *Effects of various Hartmann numbers*

In this section, the effects of the Hartmann number (Ha) on fluid flow and heat transfer for three different cases are studied in detail. The presence of a magnetic field in a buoyancy-driven flow of an electrically conducting fluid induces an electric current in the flow domain. This current is generated due to the relative motion between the magnetic field and velocity, and it acts normal direction to both velocity and the applied magnetic field. The interaction of this induced electric current with the applied magnetic field leads to the development of an electromagnetic force, which is commonly referred to as the Lorentz force. This force acts in a direction perpendicular to the direction of the induced electric current and applied magnetic field. Thus, in the case of MHD-based natural convection, the fluid motion and heat transfer are controlled by buoyant and electromagnetic forces. It is important to note that the Lorentz force opposes the fluid motion and heat transfer, and its strength is dependent on the strength of the magnetic field, as measured by the value of Ha. It has a significant influence on the local fluid velocity and temperature in the annuli. The Lorentz force, which is acting opposite to the buoyant force, controls fluid motion and heat transfer in the case of MHD-based natural convection. The investigation is carried out here for Ha varying from 0 to 100 and fixed values of Ra = 10^6, $\gamma = 0°$, and $\zeta = 0.02$. At $\gamma = 0°$, the Lorentz force and buoyant force are acting in opposite directions, affecting the flow pattern of the fluid. The flow characteristics and temperature distribution for Ha = 0 are discussed in Section 6.3.1. It is worth noting that the flow pattern of fluid for MHD-based flow is similar to the non-MHD flow (Ha = 0) as discussed earlier.

The influence of magnetic field strength on flow structure and isotherms is represented in Figures 6.6 and 6.7, respectively, for distinct values of Ha (10, 30, 50, and 70). As shown in Figure 6.6, with an increase in Ha, the concentration of the streamlines nearer to the active walls reduces, implying a decrease in fluid velocity (indicated by the value of ψ_{max}). This is due to the increase in Lorentz force along the vertical direction. Furthermore, it is noted that for MHD-based buoyancy-driven flow, the flow velocity of the circular annular system (Cases 1 and 2) is higher than that of a square annular system (Base case). The reason for this finding is discussed in detail in Section 6.3.1.

Ha = 10 **Ha = 30** **Ha = 50** **Ha = 70**

22.18   -22.18   16.22   -16.22   11.61   -11.61   8.40   -8.40

23.68   -23.68   16.19   -16.19   11.55   -11.55   8.41   -8.41

26.56   -26.55   17.41   -17.41   12.49   -12.48   9.18   -9.18
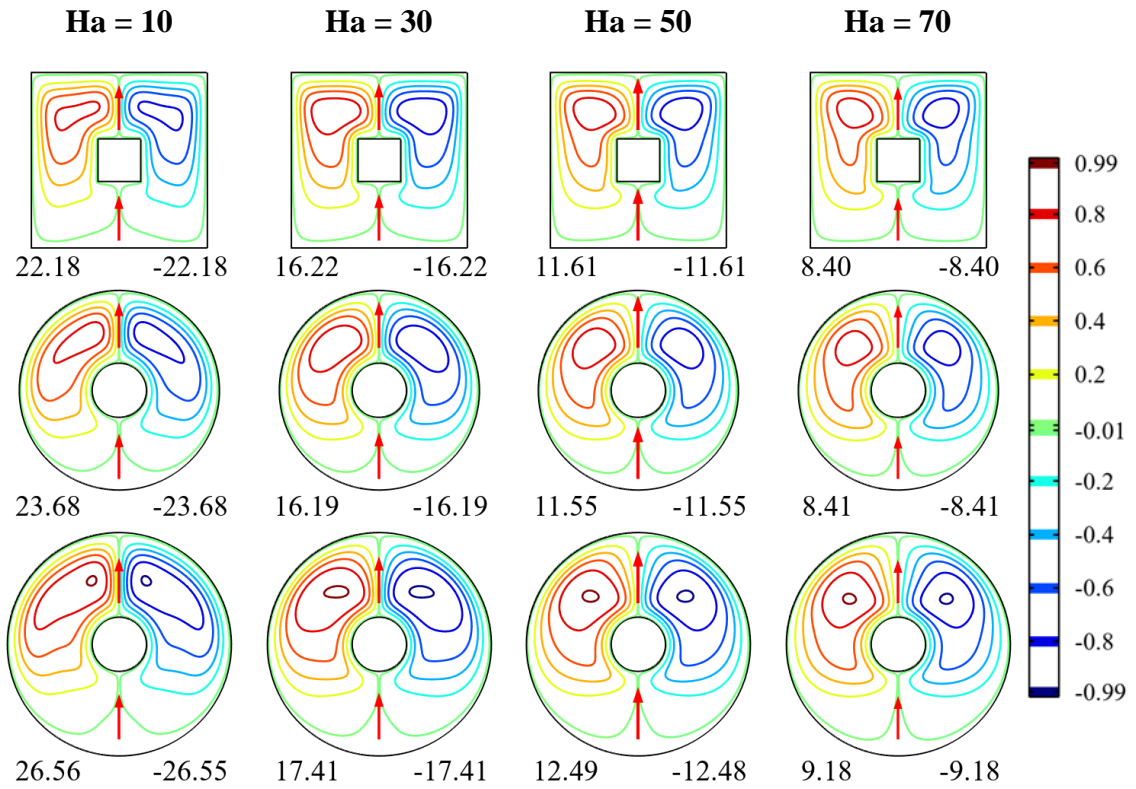
Figure 6.6 Streamlines at Ra = 10^6 for different Ha values.

Ha = 10 **Ha = 30** **Ha = 50** **Ha = 70**

Nu = 16.25   Nu = 14.64   Nu = 12.48   Nu = 10.48

Nu = 17.37   Nu = 15.65   Nu = 13.38   Nu = 11.23

Nu = 17.68   Nu = 15.94   Nu = 13.68   Nu = 11.50
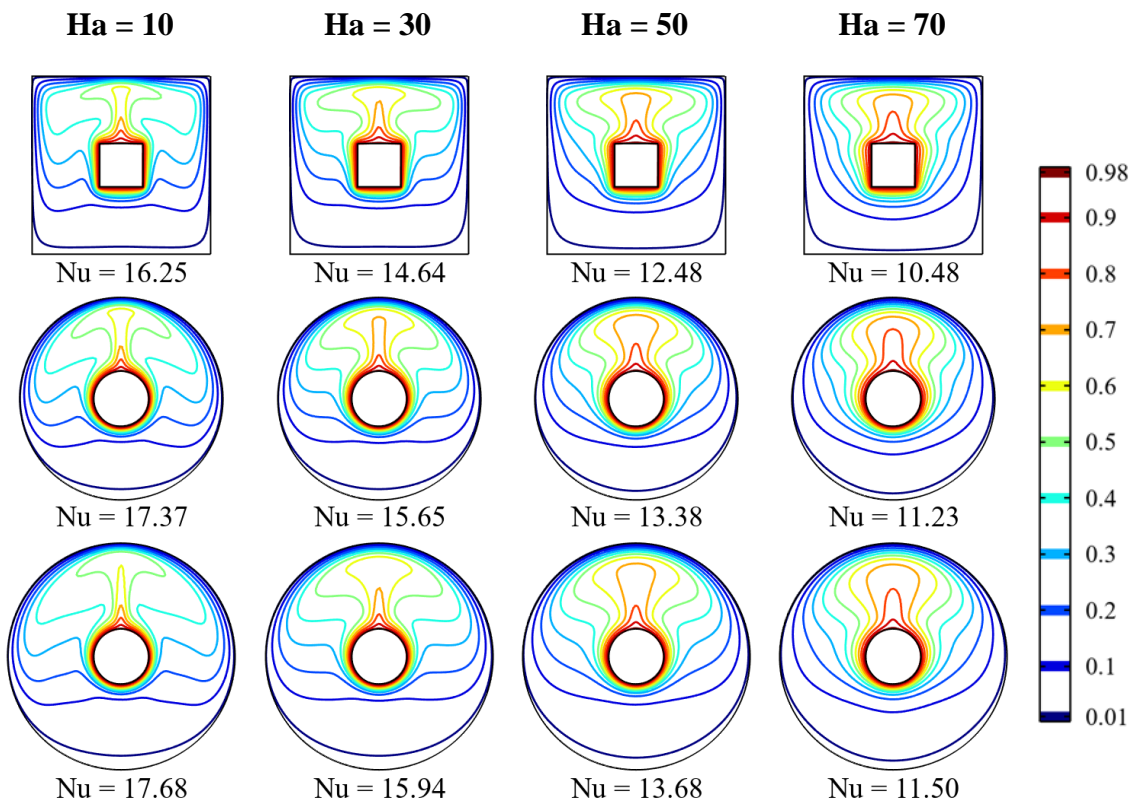
Figure 6.7 Temperature profile at Ra = 10^6 for different Ha values.

Figure 6.7 displays the impact of the magnetic field on the isotherm. The isotherm profiles of MHD-based flow resemble those of non-MHD flow (Ha = 0). However, as Ha increases, the concentration of the isotherm near the active walls decreases, indicating a decrease in buoyancy-driven heat transfer (indicated by the value of Nu at the bottom of individual snapshots). This is due to an increase in the Lorentz force in the vertical direction, which suppresses the influence of the buoyant force (driving force). The clustering of the isotherms adjacent to the hot wall decreases, signifying an increase in the thickness of thermal boundary layers. This indicates that the convective heat transfer decreases with an increase in magnetic field for all the cases investigated.
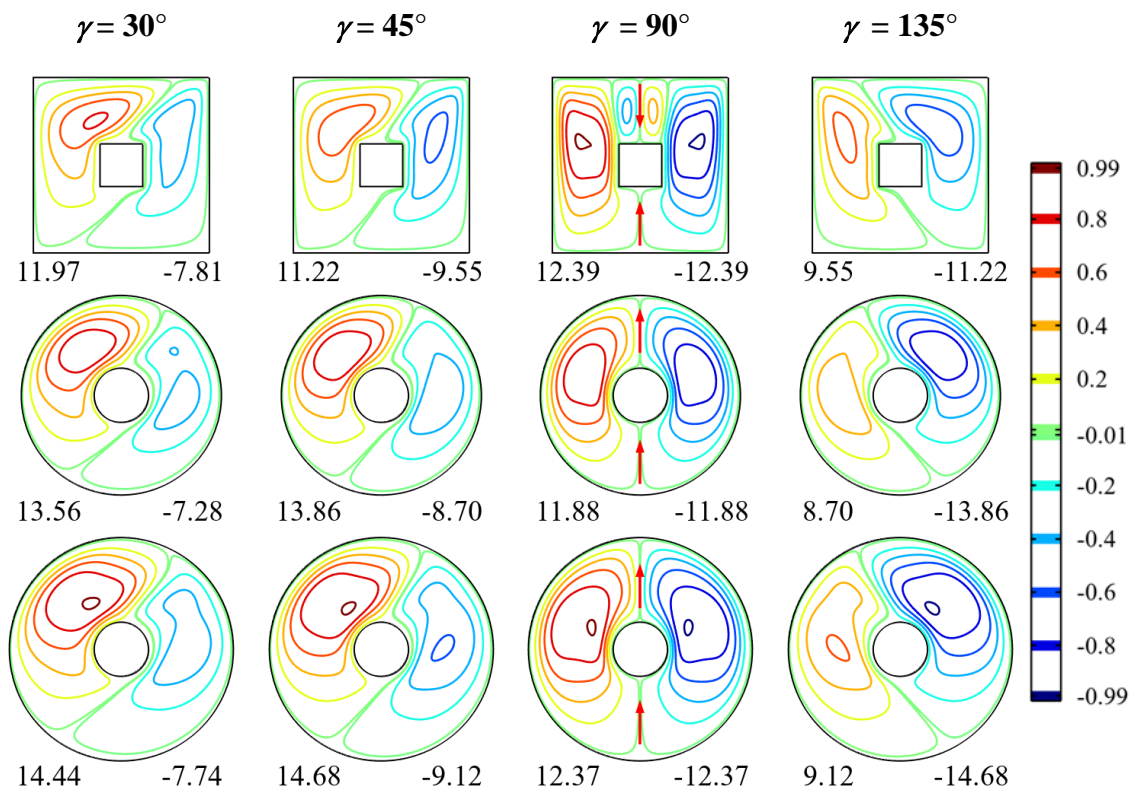
Figure 6.8 Magnetic field inclination (γ) impact on streamlines at Ha = 70 and Ra = 10^6.

6.3.4 *Impact of magnetic field inclination (γ)*

The influence of magnetic field orientation (γ) on the flow pattern and temperature distribution is examined for Ra = 10^6, Ha = 70, $\zeta = 0.02$, and varying γ from 0° to 180° in Figures 6.8 and 6.9. The direction of the magnetic force has a significant impact on local fluid velocity and temperature, as the component of Lorentz force changes in both *X* and *Y* directions with changing γ. The results of the flow pattern and temperature distribution for γ = 0° and 180° are identical, but they

vary for other specific values of γ. The flow structure and isotherm profile for $\gamma = 0°$ are discussed earlier in Section 6.3.3. Hence, the results corresponding to $\gamma = 30, 45, 90,$ and $135°$ are presented in Figures 6.8 and 6.9.

In Figure 6.8, the symmetric pattern of the streamlines is lost when $\gamma = 30, 45,$ and $135°$, with the convection cells tilting to the right for $\gamma = 30$ and $45°$ and to the left for $\gamma = 135°$. In the case of the circular annuli (Cases 1 and 2), the flow pattern for $\gamma = 90°$ is similar to $\gamma = 0°$, but a pair of secondary cells are found at the top of the vertical mid-plane for the square annular system (Base case). It is also found that the flow strength reaches its peak at $\gamma = 90°$, where the Lorentz force acts normally to buoyant force, implying that the component of Lorentz force opposing buoyant force is zero. The sharing of Lorentz force alters in both X and Y directions with a change in γ, resulting in a change in flow strength for different γ (30, 45, and 135°).
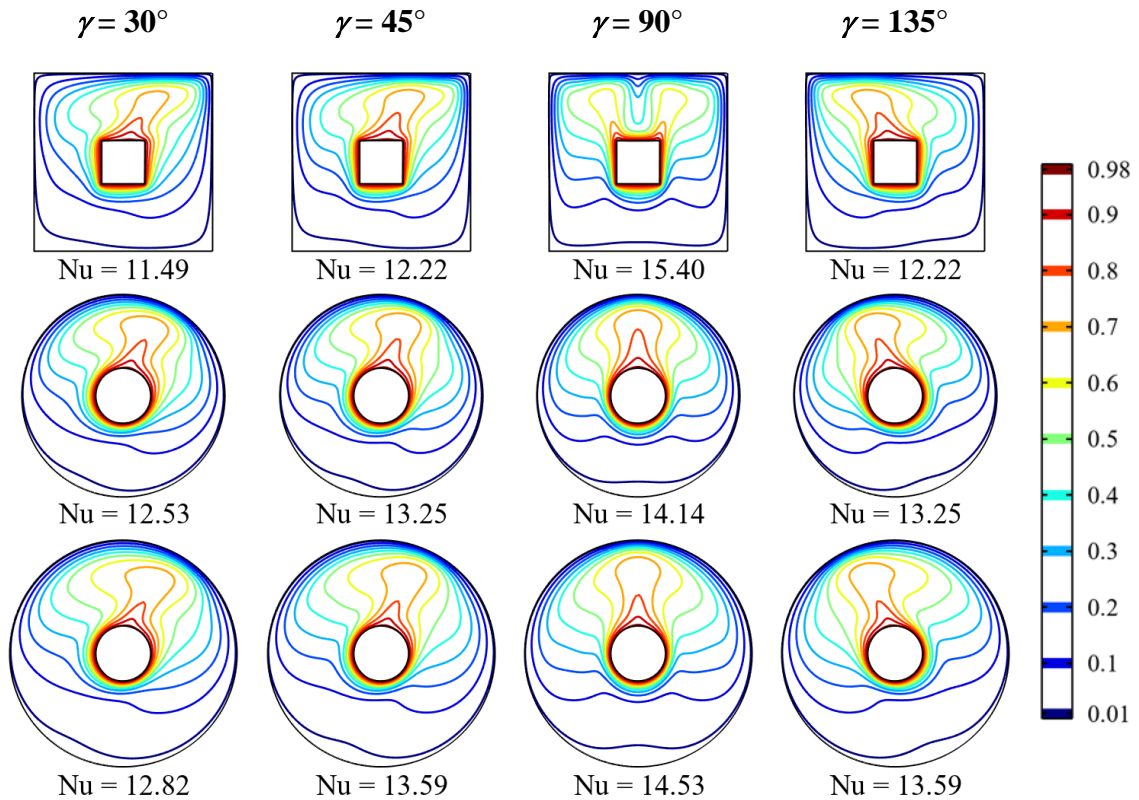
Figure 6.9 Magnetic field inclination (γ) impact on isotherms at Ha = 70 and Ra = 10^6.

The orientation of the magnetic field (γ) has a significant impact on the rate of heat transfer that can be realized from the distribution of isotherms shown in Figure 6.9. In buoyancy-driven convection, the velocity and temperature are interrelated, and thus, the isotherm profiles lose their mid-vertical symmetric pattern except for $\gamma = 0,$ 90, and 180° (Figure 6.9). The isotherm profiles for all cases resemble a plume-like

structure. At $\gamma = 90°$, the plume-like structure remains vertical and symmetric about the vertical mid-plane. However, when γ changes, the distribution of the Lorentz force also changes in the X and Y directions, and it causes changes in the isotherm profiles. The plume-like structure tilts to the right at $\gamma = 30$ and $45°$, and the left at $\gamma = 135°$. In the case of the circular annular system (Case 1 and 2), the isotherm profiles for $\gamma = 90°$ are similar to those for $\gamma = 0°$, while for the square annular system (Base case), a pair of plume-like structures are formed at $\gamma = 90°$ due to the secondary convection cells formed at the upper portion of the system (ref. Figure 6.8). It is worth noting that the heat transfer is maximum when $\gamma = 90°$, as the Lorentz force acts horizontally, resulting in a zero component of Lorentz force acting in the vertical direction. This minimal resistance offered by Lorentz force to buoyancy force (the driving force) leads to maximum heat transport at $\gamma = 90°$. As the value of γ changes, the component of Lorentz force alters in both the horizontal and vertical directions, resulting in a change in thermal energy transportation.

6.3.5 *Parametric impacts on entropy generation*

This section investigates the impact of various parameters on entropy generation (EG) in buoyancy-induced MHD nanofluidic convection, which is crucial to determine the irreversibility in a thermodynamic system. The total local EG (NS_l) comprises irreversibility caused by the temperature gradient (NS_{tg}), viscous effect (NS_v), and magnetic field (NS_m). All these entropy quantities are taken in dimensionless form for the parametric analysis. Contour plots are used to present the results in normalized values as indicated in individual figures in Figures 6.10–6.16. The results show that NS_v and NS_m have insignificant contributions to total EG when compared to NS_{tg}. Therefore, NS_{tg} has a significant impact on total EG, and their values are almost equal. For brevity, the results of NS_{tg} are not reported here. The effects of Ra, Ha, and γ parameters on the total local distribution of EG are depicted in Figures 6.10 to 6.12, respectively. Thereafter, the viscous and magnetic entropy generation components are presented in Figures 6.13 to 6.16. The quantitative information is mentioned below each parametric figure as ($NS_{t,l}$) that indicates the total EG over the entire domain (NS_t) and the local maximum NS (NS_l).

Ra = 10^3 **Ra = 10^4** **Ra = 10^5** **Ra = 10^6**

NSt,l (0.0456, 5.47) NSt,l (0.0477, 8.23) NSt,l (0.0835, 27.6) NSt,l (0.141, 62.1)

NSt,l (0.0465, 0.224) NSt,l (0.0493, 0.382) NSt,l (0.0892, 1.40) NSt,l (0.151, 3.88)

NSt,l (0.0428, 0.198) NSt,l (0.0491, 0.414) NSt,l (0.0924, 1.43) NSt,l (0.153, 3.95)

0.002 0.004 0.006 0.008 0.01 0.012 0.014 0.016 0.018
(Normalized as NS_l/column max. NS_l)
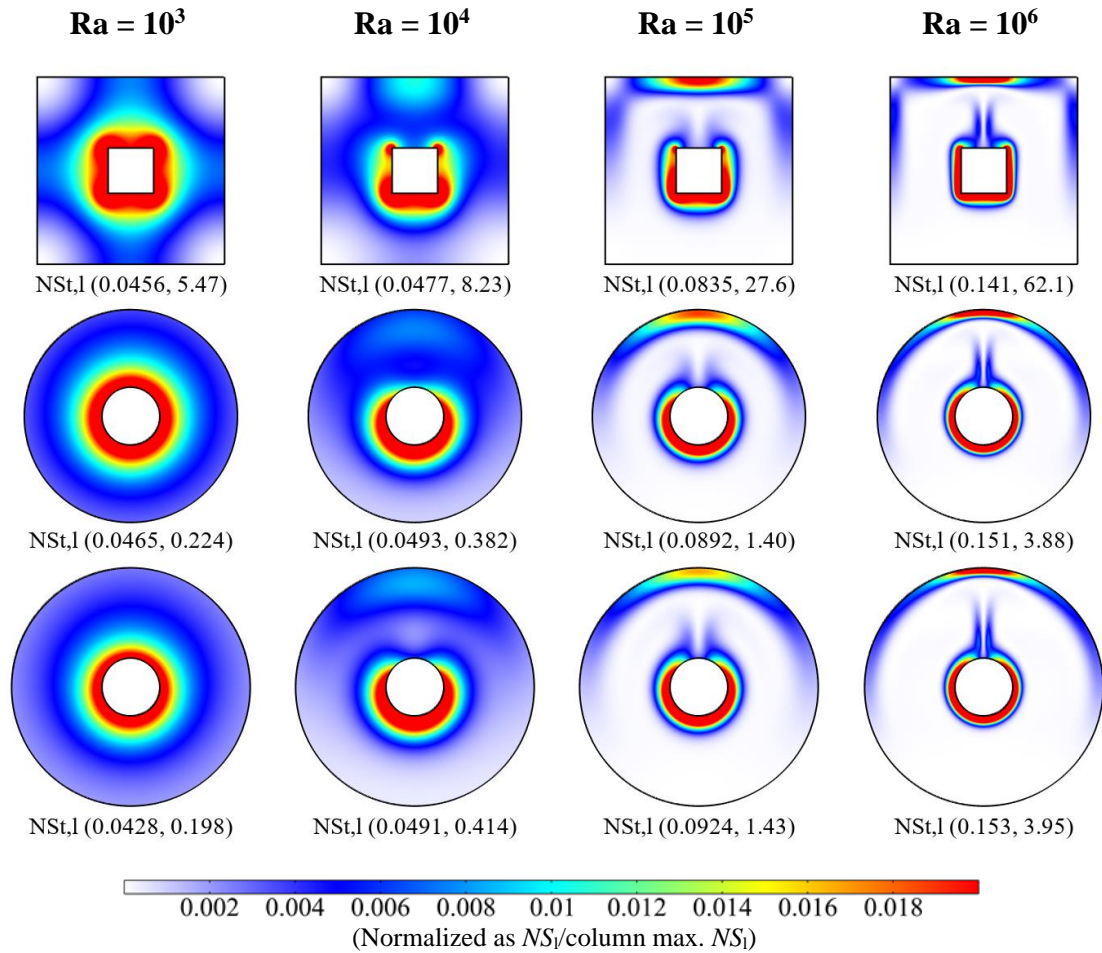
Figure 6.10 Entropy generation at Ha = 0 for different Ra values.

Figure 6.10 demonstrates the effect of varying Ra from 10^3 to 10^6 on the total local EG for a fixed value of Ha = 0, and $\zeta = 2\%$ for three distinct cases (Base case, Case 1, and Case 2). Upon analysis, it is discovered that the local EG (NS_l) values below the inner wall as well as the top portion of the outer wall is higher, a finding that aligns with the static temperature contour represented in Figure 6.3. It is worth noting here that the temperature gradient is strong near the region with high EG around the inner heaters. The overall EG value is observed to be lower for low Ra ($\leq 10^4$) because the thermal gradient is reduced at low Ra values. However, with an increase in Ra value, the convective mode dominates the conductive mode of thermal energy transfer, increasing a temperature gradient. Thus, the value of NS_{tg} and NS_l increases with a rise in Ra, leading to an increase in total EG. Due to the presence of sharp corners, the maximum value of NS_l is higher for the square base case than its alternative circular annuli (Cases 1 and 2). However, the integrated value of NS_l over the entire flow domain, which is indicated by NS_t, shows relatively higher values for the circular cases, particularly at higher Ra (10^5, 10^6), due to the higher rate of heat

transfer resulting from a higher temperature gradient. From the graphical results, it is very clear that the entropy production is intensely localized near the sharp corners of the inner square walls that act as a heating source for the square annular thermal system.

<table>
<tr><td>**Ha = 10**</td><td>**Ha = 30**</td><td>**Ha = 50**</td><td>**Ha = 70**</td></tr>
</table>

NSt,l (0.0787, 24.9)   NSt,l (0.0596, 14.1)   NSt,l (0.0496, 8.85)   NSt,l (0.0469, 7.00)

NSt,l (0.0841, 1.32)   NSt,l (0.0629, 0.845)   NSt,l (0.0514, 0.528)   NSt,l (0.0481, 0.390)

NSt,l (0.0869, 1.36)   NSt,l (0.0638, 0.881)   NSt,l (0.0497, 0.525)   NSt,l (0.0450, 0.369)

0.002 0.004 0.006 0.008 0.01 0.012 0.014 0.016 0.018
(Normalized as NS_l/column max. NS_l)
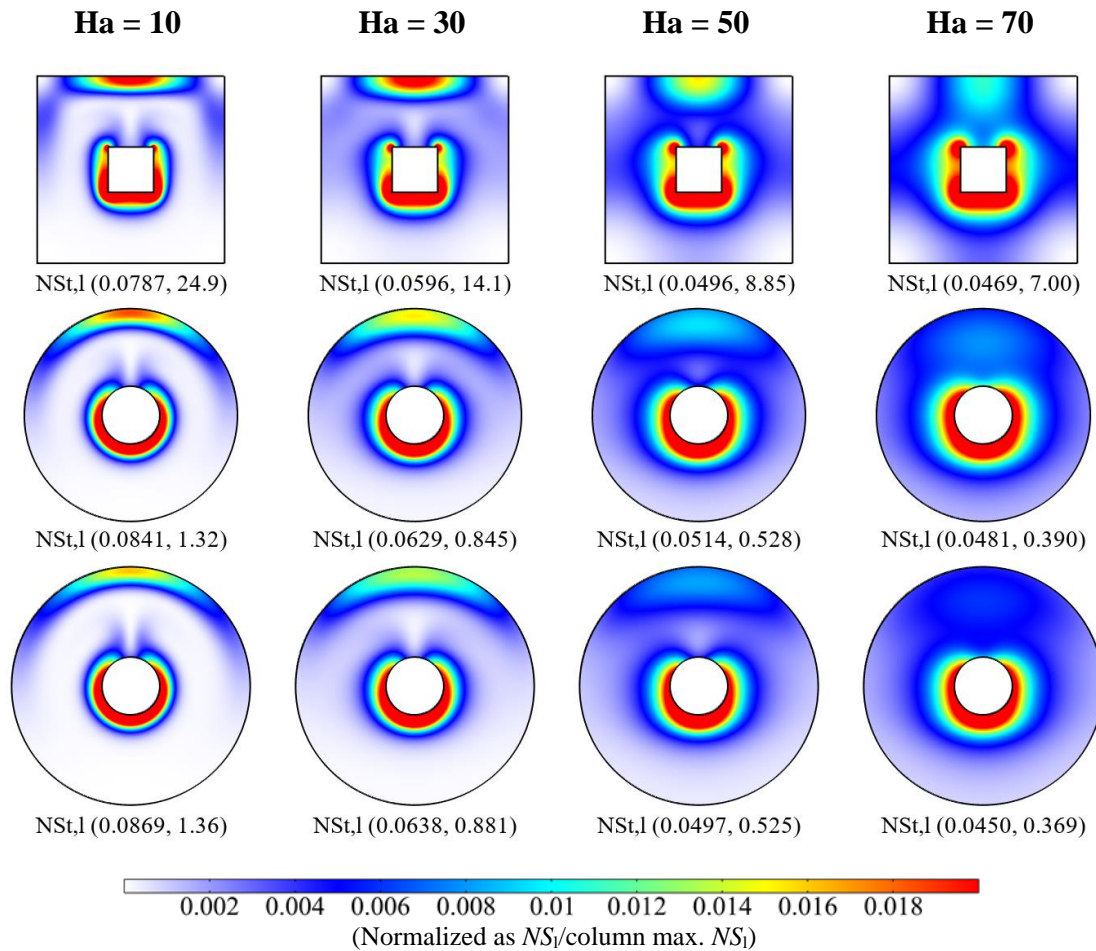
Figure 6.11 Entropy generation at Ra = 10^5 for different Ha values.

Figure 6.11 displays the effect of varying Ha (10, 30, 50, and 70) on the total EG for three distinct cases (Base case, Case 1, and Case 2), with a fixed value of Ra = 10^5, $\gamma = 0°$, and $\zeta = 2\%$. For low Ha (= 10), the local *NS* value is high adjacent to the lower region of the inner wall and the upper region of the outer wall, irrespective of different configurations. However, for high Ha (= 100), the value of local *NS* is high at the lower part of the inner wall. The EG distribution for Ha (= 30 and 50) falls between the two extremes. These results for total EG (NS_l) are consistent with the isotherm profile shown in Figure 6.7. The temperature gradient is high in the region with high EG, as seen in the figure. As the Ha value increases, so does the Lorentz force, which suppresses the impact of buoyant force, resulting in less heat transport for a given temperature difference. Consequently, the total EG value decreases as Ha

values increase. Notably, for MHD-based flow, the *NS* value of the circular annuli (Cases 1 and 2) is higher than that of the square annulus (Base case), which is also found for the non-MHD flow situation (Ha = 0). It is also worth mentioning that the *NS* values of circular annular systems are nearly equal.

$\gamma = 30°$	$\gamma = 45°$	$\gamma = 90°$	$\gamma = 135°$
NSt,l (0.0982, 40.6)	NSt,l (0.104, 51.9)	NSt,l (0.132, 64.9)	NSt,l (0.104, 51.7)
NSt,l (0.107, 3.08)	NSt,l (0.113, 3.21)	NSt,l (0.121, 2.83)	NSt,l (0.113, 3.21)
NSt,l (0.110, 3.15)	NSt,l (0.116, 3.29)	NSt,l (0.124, 2.94)	NSt,l (0.116, 3.29)

0.002 0.004 0.006 0.008 0.01 0.012 0.014 0.016 0.018
(Normalized as NS_l/column max. NS_l)
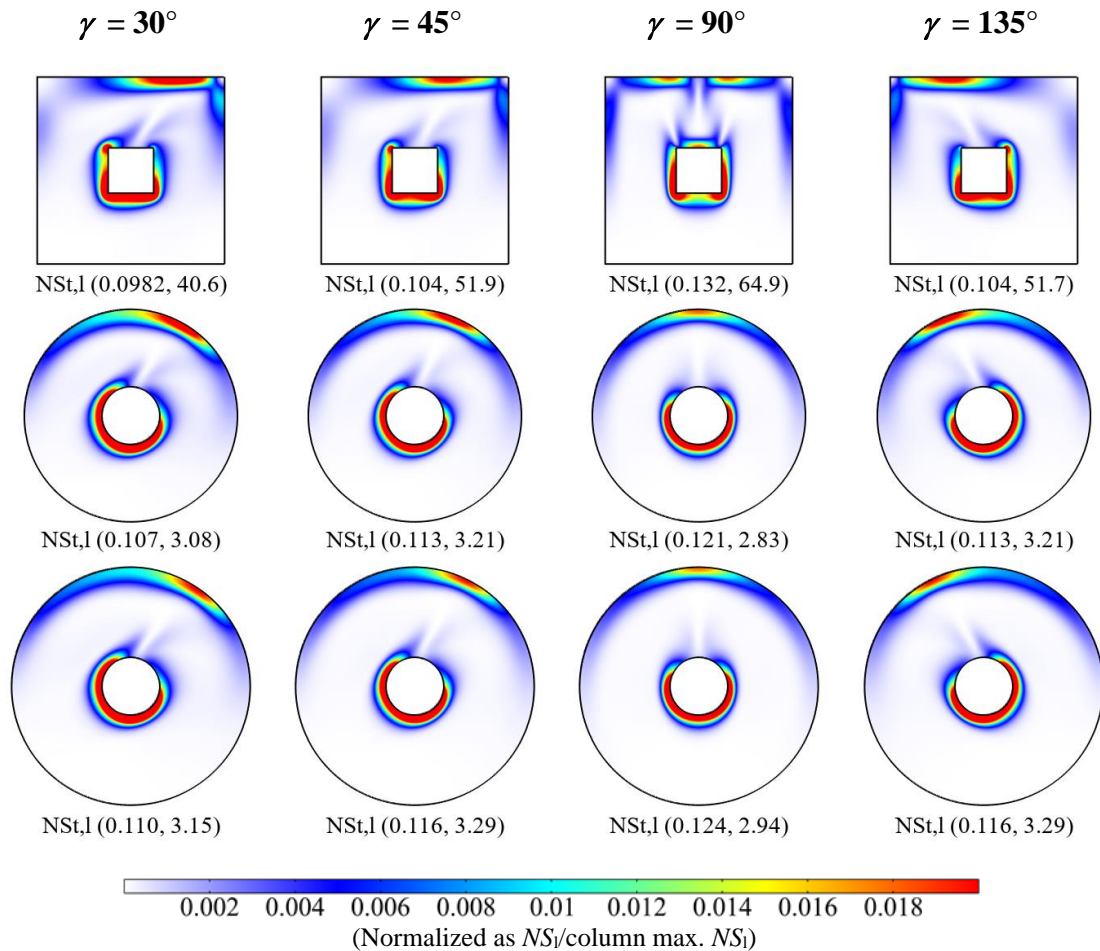
Figure 6.12 Total entropy generation at Ra = 10^6 and Ha = 70 for different γ values.

Figure 6.12 illustrates the impact of varying the angle of inclination, *γ* (= 30, 45, 90, and 135°), on the total EG for a fixed value of Ra = 10^6, Ha = 70, and ζ = 2% for three distinct cases (Base case, Case 1, and Case 2). At *γ* = 90°, the contours of *NS* remain symmetrical about the vertical mid-plane, which is consistent with the results obtained at *γ* = 0°. However, as the magnetic field's orientation changes, the distribution of the Lorentz force in the *X* and *Y* directions changes, which results in non-symmetric profiles. A closer examination of the contour of local *NS* reveals that when *γ* < 90°, the contour of *NS* tilts to the right, whereas when *γ* > 90°, the contour of *NS* tilts to the left. Similar to the situation at *γ* = 0°, the value of *NS* of the circular annuli (Cases 1 and 2) is less than that of the square annulus (Base case). Moreover, the value of *NS* is almost the same for both cases of the circular annular system.

The impact of varying Ra from 10^3 to 10^6 on the viscous EG (NS_v) is illustrated in Figure 6.13 for a fixed value of Ha = 30, $\gamma = 0°$, $\zeta = 2\%$. The local NS_v value is observed to be higher near the annulus's inner and outer walls due to the development of a hydrodynamic boundary layer. NS_v is also found to be higher near regions of the strong velocity gradient. The NS_v value is extremely low for low Ra (= 10^3) due to the prevalence of conductive mode of thermal energy transfer resulting in very weak fluid velocity. However, with increasing Ra, the convective mechanism of thermal energy transfer dominates, enhancing flow velocity, and leading to an increase in NS_v value.
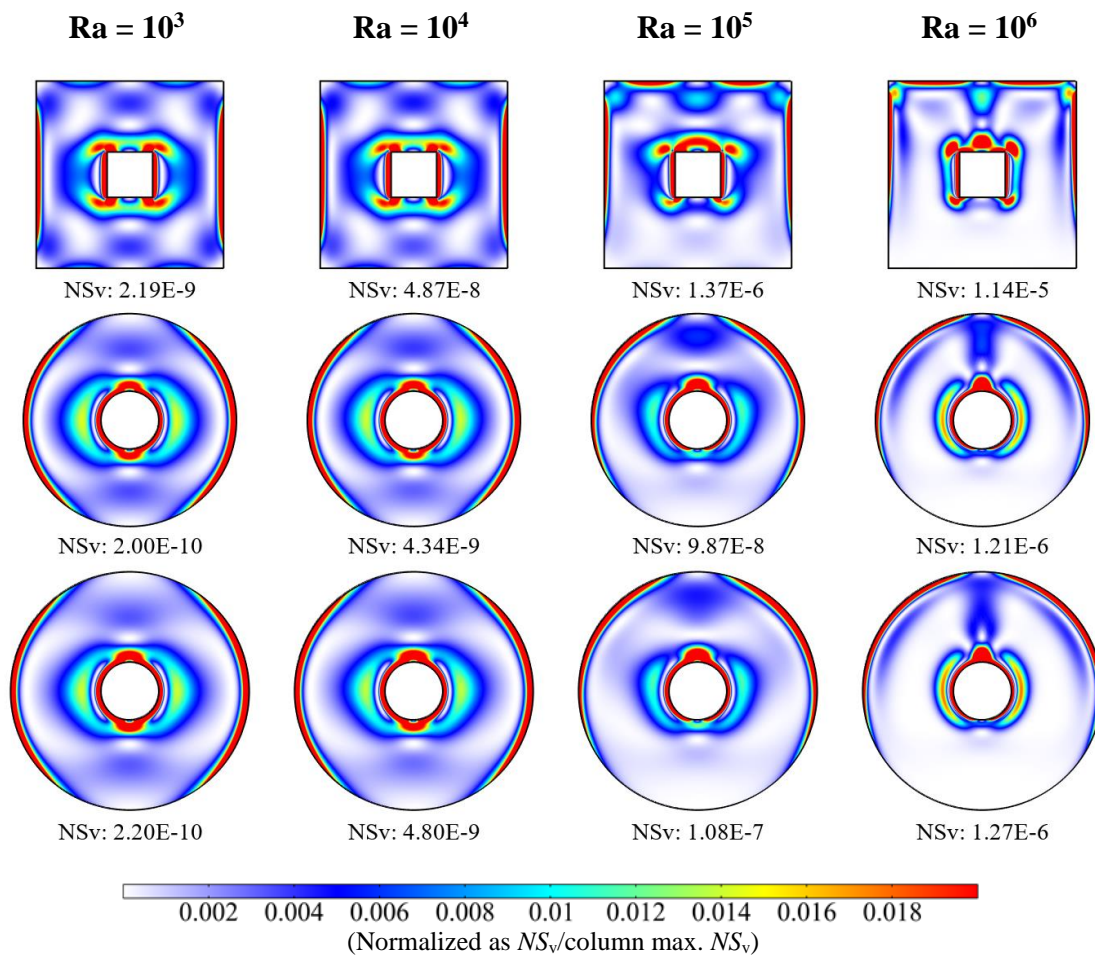
Figure 6.13 Viscous entropy generation at Ha = 30 for different Ra values.

Additionally, it is observed that NS_v values for circular annuli (Cases 1 and 2) are lower than that of a square annular system (Base case) due to the smoother turning along the curved surface of circular annuli, reducing fluid friction. It is noteworthy that the order of magnitude of NS_v is almost the same in both cases of circular annular systems. Despite this, the NS_v order of magnitude is found to be relatively minimal in

comparison to total EG (NS_t). Hence, NS_v can be ignored in comparison to NS_t, irrespective of the cases.
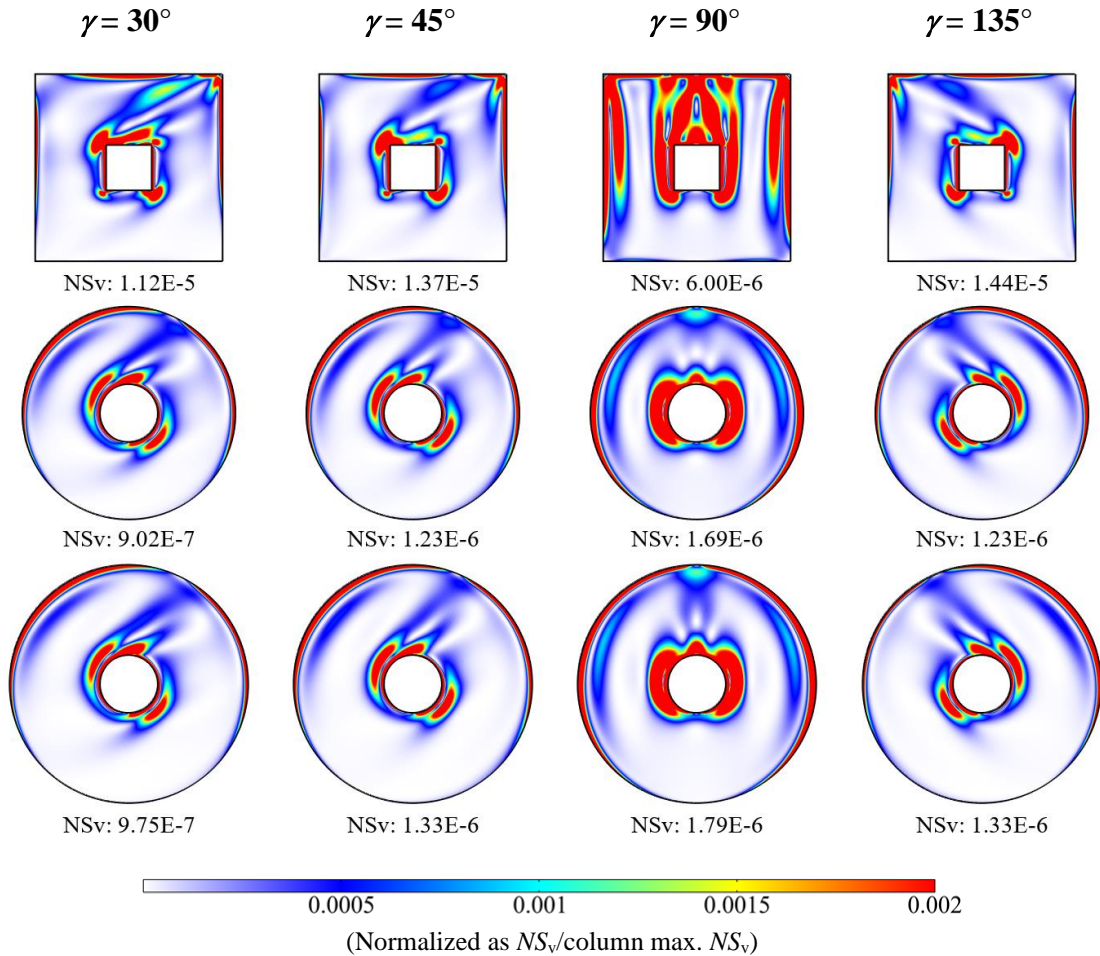
Figure 6.14 Viscous entropy generation at Ra = 10^6 and Ha = 70 for different γvalues.

In Figure 6.14, the impact of changing γ (= 30, 45, 90, and 135°) on the viscous EG (NS_v) is presented for a constant value of Ra = 10^6, Ha = 70, and ζ = 2% for the studied three different cases. The local NS_v value is higher in the vicinity of the annulus's inner and outer walls where the velocity gradient is strong, as observed for γ = 0°. This is due to the presence of a hydrodynamic boundary layer close to the walls. At γ = 90°, the contour of NS_v is symmetric about the vertical mid-plane, similar to that at γ = 0°. When the orientation of the magnetic field changes, the Lorentz force distribution changes in the *X* and *Y* directions, leading to non-symmetric NS_v contours. The contour of local NS reveals that the minimum value of NS_v occurs at γ = 90°. This is because, at γ = 90°, the Lorentz force component that opposes the buoyant force is zero, resulting in less resistance to fluid motion and a lower NS_v value. For other values of γ (= 30, 45, and 135°), the NS_v value is lower for circular annular systems

(Cases 1 and 2) than that for a square annular system (Base case), owing to the reduced fluid friction resulting from the smooth turning on the curved surface of the circular annular system. The NS_v order of magnitude is the same for both circular annular thermal cases. Regardless of the cases, the variation of NS_v with γ is found to be insignificant.
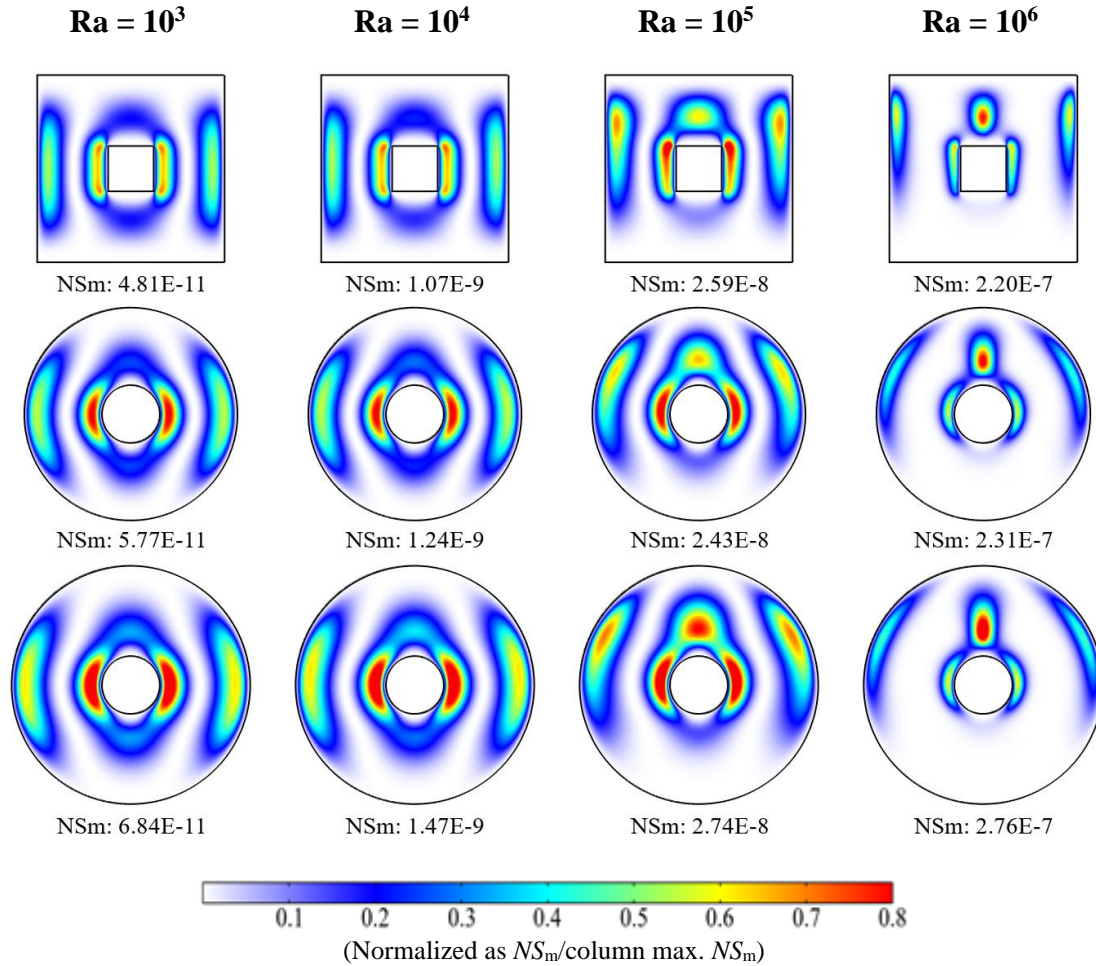
Figure 6.15 Magnetic entropy generation Ha = 10 for different Ra values.

In Figure 6.15, the impact of changing Ra (10^3, 10^4, 10^5, and 10^6) on the magnetic EG (NS_m) is presented for a chosen value of Ha = 10, $\gamma = 0°$, $\zeta = 2\%$. The local NS_m value is observed to be higher in the annulus region where the fluid velocity is high. It is primarily concentrated at the inner (heat source) and outer walls (heat sink). For low Ra (= 10^3), the NS_m value is exceptionally low. This is because, at low Ra values, heat transfer occurs due to the conductive mode leading to low fluid velocity. With an increase in Ra, the convective mechanism of thermal energy transfer improves, which enhances flow velocity. As a result, the NS_m value increases with increasing Ra. Regardless of the cases, the order of magnitude of NS_m is nearly the

same. Furthermore, when compared to NS_l, the order of magnitude of NS_m is significantly small.

$$\gamma = 30° \qquad \gamma = 45° \qquad \gamma = 90° \qquad \gamma = 135°$$

NSm: 2.32E-7   NSm: 2.31E-7   NSm: 1.53E-7   NSm: 2.31E-7

NSm: 1.95E-7   NSm: 1.92E-7   NSm: 1.85E-7   NSm: 1.92E-7

NSm: 2.11E-7   NSm: 2.11E-7   NSm: 1.79E-7   NSm: 2.11E-7

0.1 0.2 0.3 0.4 0.5 0.6 0.7 0.8

(Normalized as NS_m/column max. NS_m)
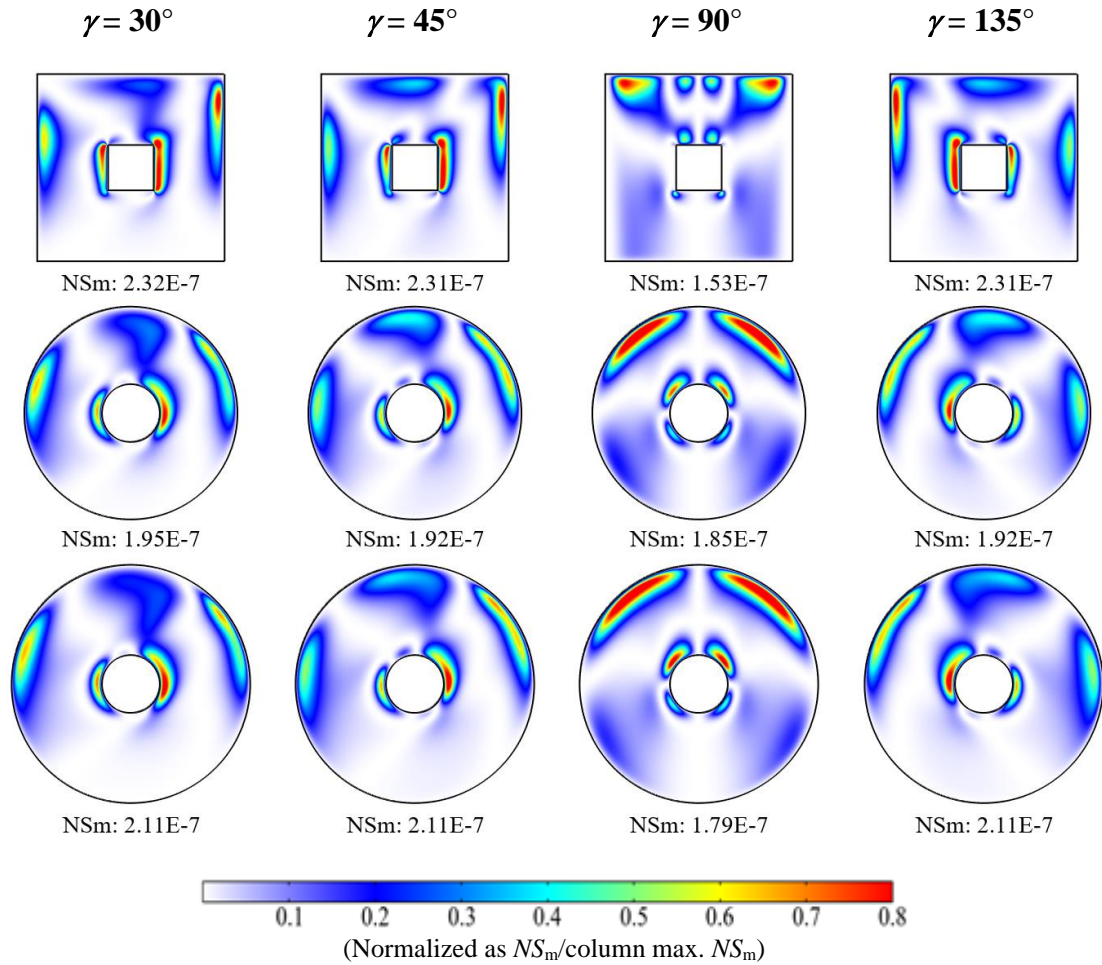
Figure 6.16 Magnetic entropy generation at Ra = 10^6 and Ha = 70 for different γ values.

Figure 6.16 illustrates the impact of altering γ (30, 45, 90, and 135°) on the magnetic EG (NS_m) for a specific value of Ra = 10^6, Ha = 70, and $\zeta = 2\%$ for three distinct cases. Local NS_m values are found to be higher in the annulus region where the flow velocity is high, similar to the case of $\gamma = 0°$. The flow velocity is observed to be higher after a little away from the active walls following the growth of the hydrodynamic boundary layer and it is reducing towards cores of flow circulations. At $\gamma = 90°$, the NS_m contour is symmetric about the vertical mid-plane, consistent with the NS_m contour at $\gamma = 0°$. As the magnetic field's inclination changes, the Lorentz force distribution in the X and Y directions changes, resulting in non-symmetric NS_m contours. A detailed examination of the local NS_m contour reveals that NS_m is lowest at $\gamma = 90°$. This is due to the Lorentz force component opposing buoyant force being zero at $\gamma = 90°$, resulting in less resistance to fluid flow and lower NS_m. Although the

order of magnitude of NS_m is the same in all cases, its value is very low. Additionally, in all cases, the variation of NS_m with γ is insignificant.

6.3.6 *Analysis of global thermal performance parameters (Nu, η)*

To assess the impact of geometrical shape on the overall thermal performance, the global heat transfer characteristics are computed. For this, the average Nusselt number (Nu), and the heat transfer enhancement/deterioration from the base case are evaluated. A heat transfer performance parameter (η) is defined as the ratio of the Nu difference to the Nu of the base case. The effect of varying Ra from 10^3 to 10^6 on the Nu is shown in Figure 6.17a while maintaining Ha = 0, and $\zeta = 2\%$ fixed for three distinct cases (Base case, Cases 1, and 2). For all the cases, the Nu curves exhibit minor variation for Ra value up to 10^4, owing to the prevalence of the conduction mechanism of heat transport. However, when Ra exceeds 10^4, the value of Nu monotonically increases, indicating that the convective mechanism surpasses the conductive mechanism, resulting in superior thermal energy transport. At higher Ra values, the Nu curve of the circular annular system (Cases 1 and 2) is higher than that of the square annular system (Base case). This is also evident from the heat transfer parameter (η) shown in Figure 6.17b.

(a)   (b)
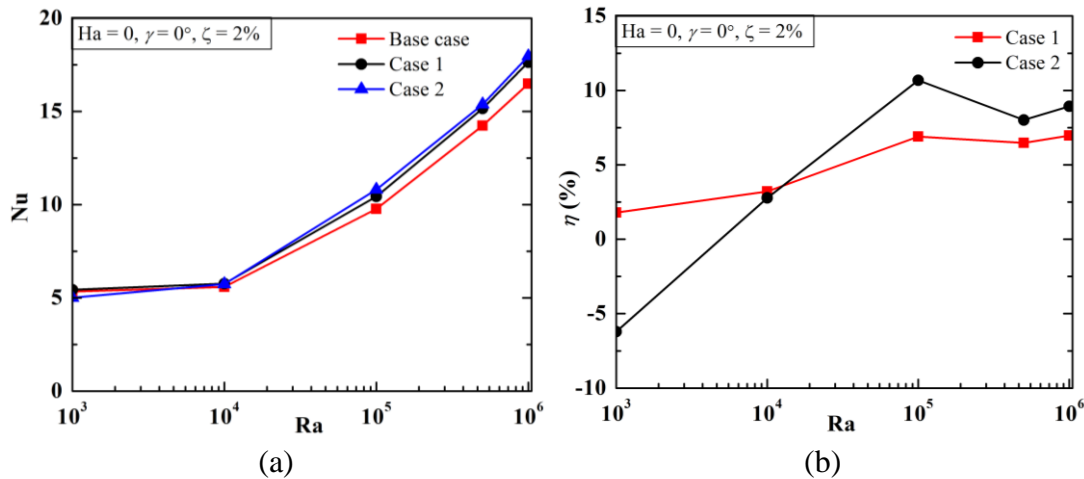
Figure 6.17 Impact of Ra on (a) Nusselt number (Nu) and (b) heat transfer parameter (η).

The heat transfer parameter for circular annuli (Cases 1 and 2) shows a positive value for a higher value of Ra ($\geq 10^4$), indicating an enhancement in heat transfer. The maximum value of heat transfer noted for Case 1 and Case 2 are ~7% and ~11%, respectively, at Ra = 10^5. This shows that Case 2 has the highest heat transfer enhancement and can be employed as the optimal thermal system to achieve

superior heat transport for non-MHD flow (Ha = 0). This is because Case 2 has a greater flow area or volume than the other cases.
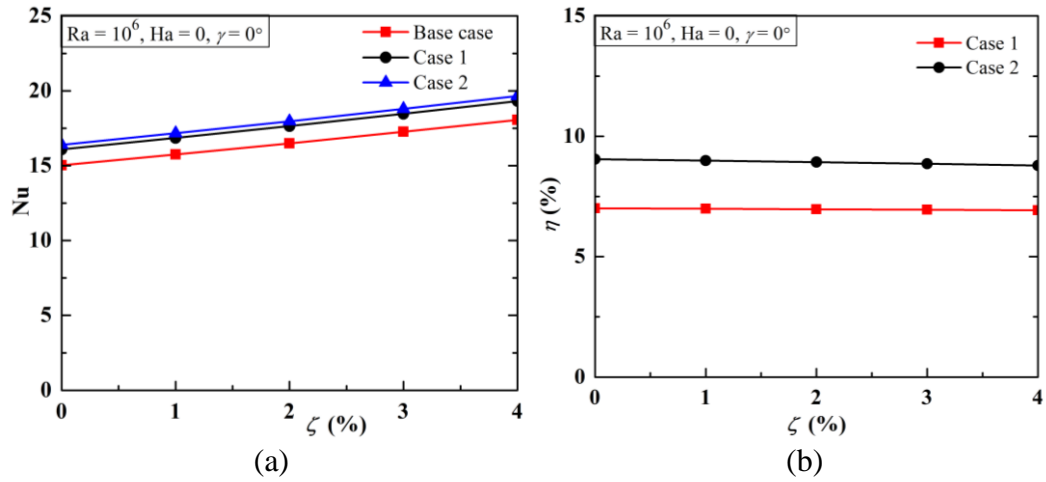
Figure 6.18 Impact of ζ at Ra = 10⁶ and Ha = 0 on (a) Nu and (b) η.

In this study, the effect of volumetric concentrations (ζ) of CuO nanoparticles on global thermal performance is investigated for all three cases. Figure 6.18a displays the Nu values for different ζ values (0–4%) with Ra = 10⁶ and Ha = 0. The inclusion of nanoparticles in water, the base fluid, enhances the effective thermal conductivity of the working fluid. This leads to increased thermal convection and a stronger buoyant force, which results in improved thermal energy transport. As shown in Figure 6.18a, Nu increases with increasing ζ, however, η remains almost constant (Figure 6.18b), indicating that η remains unchanged as ζ varies. However, as expected, the heat transfer enhancement of Case 2 is greater than that of Case 1, with maximum values of enhancement of ~7 % and ~ 9 % for Cases 1 and 2, respectively.
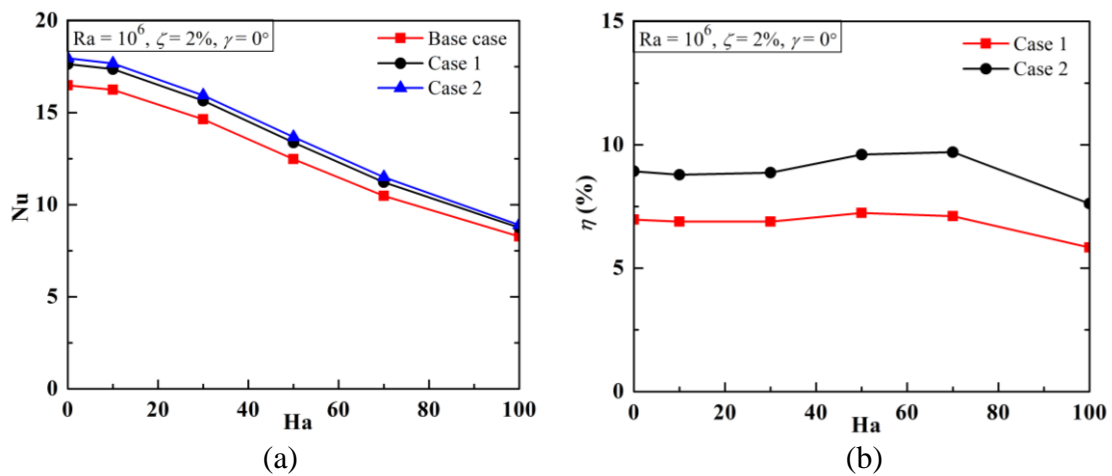
Figure 6.19 Influence of Ha at Ra = 10⁶, γ = 0°, ζ = 2% on (a) Nu and (b) η.

The impact of Ha (from 0 to 100) on the global thermal performance of three different scenarios (Base case, Case 1, and 2) is presented in Figure 6.19, keeping Ra $= 10^6$, $\gamma = 0°$, and $\zeta = 2\%$ fixed. It is observed that the presence of a magnetic field in a moving electrically conducting fluid produces an electromagnetic force, which affects the fluid velocity and heat transfer in MHD-based thermal convection. As the value of Ha increases, the retarding force increases, resulting in a decrease in the value of Nu. This is due to the reduction in the influence of the buoyant force.

Figure 6.19b depicts the variation of the heat transfer parameter (η) with Ha for both Cases 1 and 2. The η curve remains horizontal for both cases, indicating that the heat transfer parameter remains constant with varying Ha. However, as Ha increases, there is a significant decrease in heat transfer owing to the sharp increase in the Lorentz force at Ha = 100. Similar to the non-MHD flow case, the value of η is positive for both cases, indicating that the circular annuli (Cases 1 and 2) have superior thermal performance compared to the square annulus (Base case). It is further observed that Case 2 has the highest value of η among the three cases, indicating that it is the most effective geometrical design for MHD flow (Ha $\neq$ 0).

(a)   (b)
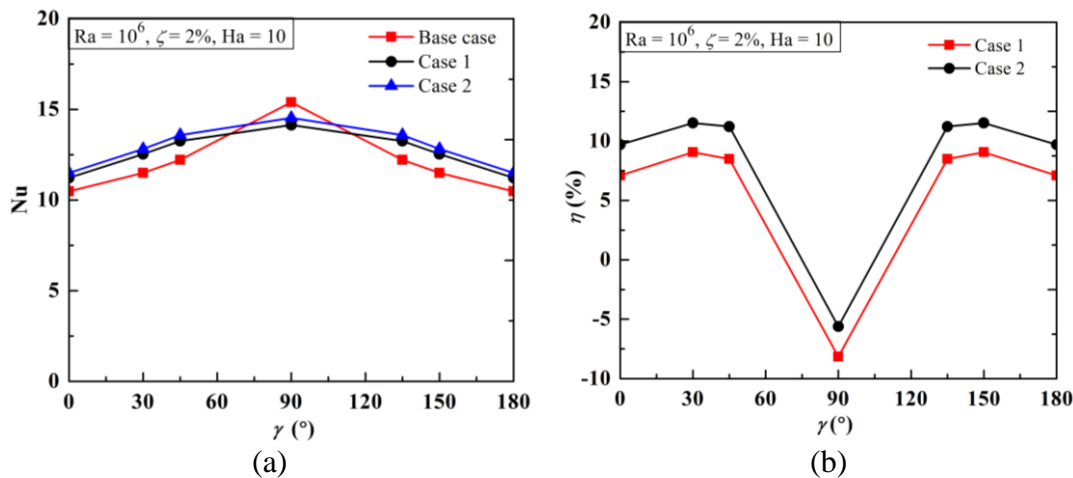
Figure 6.20 Effect of γ at Ra = 10^6, Ha = 10, ζ = 2% on (a) Nu and (b) η.

Finally, the influence of magnetic field orientation on the thermal performance of the circular and square annular systems is investigated. Figure 6.20a displays the variation in Nu with γ ($= 0-180°$) for three different scenarios (Base case, Case 1, and 2) while keeping Ra = 10^6, Ha = 20, and $\zeta = 2\%$ fixed. The effect of Lorentz forces on buoyant force changes as the orientation of the magnetic field changes from 0 to 180°, causing the Nu values to vary. The results show that the Nu values at $\gamma = 0°$ and 180° are the same for all the cases. However, at $\gamma = 90°$, Nu reaches its maximum value due

to the normal orientation of the Lorentz force with the buoyant force. The value of Nu for the base case is higher at $\gamma = 90°$ compared to Cases 1 and 2 due to the formation of a pair of secondary cells observed for the square annular system, as shown in Figure 6.8.

Figure 6.20b illustrates the influence of γ on the heat transfer parameter (η). At $\gamma = 90°$, the value of η is negative, indicating that the thermal performance of the square annular system is better than that of the circular annular system. This observation is consistent with the Nu values obtained at $\gamma = 90°$ for all the cases shown in Figure 6.20a. The magnitude and direction of the Lorentz force acting both horizontally and vertically vary as the orientation of the magnetic field changes from 0 to 180°, affecting its opposition to the buoyant force. Therefore, the component of Lorentz force acting on the buoyant force varies with the orientation of the magnetic field, causing the Nu and η values to change accordingly.

6.4 Conclusions

In this study, the thermal equivalence of the square annular system to its circular annular counterpart is examined, based on certain constraints. Three different cases are analyzed, including the Base case, represented by the square annular system, Case 1, which represents a circular annular system with the same flow area or volume as the Base case, and Case 2, which represents a circular annular system with the same cooling length as the Base case. The impact of various parameters, including Rayleigh number (Ra), Hartmann number (Ha), magnetic field orientation (γ), and nanoparticle concentration (ζ), on heat transfer and irreversibility, is investigated for the different annular systems. The main findings of the study can be summarized as follows:

- The shape of the geometry has a significant influence on fluid velocity, heat transfer, and irreversibility.
- It is concluded that the thermal performance of a circular annular system is superior to that of a square annular system. Case 2 is found to be the optimal geometrical design for achieving better thermal performance.
- The addition of nanoparticles to the working fluid leads to a significant improvement in heat transfer. At $Ra = 10^6$, $Ha = 0$, $\zeta = 4\%$, the highest enhancement in heat transfer is noted, compared to pure fluid ($\zeta = 0$).
- The magnetic field intensity plays a crucial role in controlling fluid flow and heat transfer in buoyancy-driven convection. Increasing the value of

Ha decreases the flow strength (ψ_{max}) and heat transfer (Nu). Additionally, the orientation of the magnetic field plays a significant role in determining the overall rate of heat transfer. Notably, the total heat transfer rate reaches its maximum at $\gamma = 90°$ for a specific combination of Ra, Ha, and ζ values.

- The impact of viscous EG and magnetic EG is negligible compared to thermal EG. Therefore, the primary reason for thermodynamic irreversibility is thermal EG for this type of annular thermal system.

- The total EG increases with Ra and ζ and decreases with an increase in Ha. The effect of magnetic field orientation (γ) on total EG is minor.

- The integrated EG (total EG) of a square annular system is lower than that of a circular annular system; however, the local *NS* is markedly higher due to the presence of corner heating points.

Outcome summary, Contributions and Future scope

7.1 Overall outcomes of the present investigations

The overall observations of constraint-based performance analysis are presented in Tables 7.1 to 7.3.

Table 7.1 Performance analysis of the equivalent square and circular enclosures.

Ra	ξ	Ha	$\gamma°$	Nu_{sq}	$(-\psi_{min})_{sq}$	η_{cir} (%)	χ_{cir} (%)
10^4	0.03	10	150	1.97	3.68	15	12
	0.01	10	150	1.93	3.64	15	12
	0.03	10	180	1.99	3.81	15	12
	0.01	10	180	1.95	3.78	15	12
	0.03	10	120	1.96	3.62	14	12
	0.01	10	120	1.93	3.57	14	11
	0.03	10	90	1.98	3.68	13	11
	0.03	10	25	2.01	3.95	13	10
	0.01	10	90	1.95	3.63	13	11
	0.01	10	25	1.98	3.93	13	9
	0.03	10	75	2.00	3.78	13	10
	0.01	10	75	1.97	3.74	13	9
	0.03	10	45	2.02	3.96	13	8
	0.01	10	45	1.99	3.94	12	8
	0.01	30	180	1.21	1.20	12	16
	0.03	30	180	1.26	1.22	12	16
	0.03	30	90	1.25	1.18	11	18
	0.01	30	90	1.21	1.16	11	18
	0.03	30	75	1.27	1.29	10	12
	0.01	30	150	1.21	1.27	10	4
	0.03	30	150	1.26	1.29	10	4
	0.03	30	120	1.26	1.27	10	5
	0.01	30	75	1.22	1.27	10	12
	0.01	30	120	1.21	1.25	10	5
	0.01	100	90	1.03	0.13	10	23
	0.03	100	90	1.09	0.13	10	23
	0.03	100	75	1.09	0.14	10	18
	0.01	100	75	1.03	0.13	10	18
	0.03	100	180	1.09	0.13	10	17
	0.01	100	180	1.03	0.13	10	17
	0.03	100	25	1.09	0.15	10	-1
	0.03	100	120	1.09	0.16	10	-3
	0.01	100	25	1.03	0.15	10	-1
	0.01	100	120	1.03	0.16	10	-3
	0.03	100	150	1.09	0.16	10	-7
	0.01	100	150	1.03	0.16	10	-6
	0.03	100	45	1.09	0.21	10	-22
	0.01	100	45	1.03	0.21	10	-22
	0.03	30	25	1.29	1.45	9	3
	0.01	30	25	1.24	1.45	9	3
	0.03	30	45	1.32	1.61	7	-5
	0.01	30	45	1.27	1.61	7	-6

Ra	ξ	Ha	γ	Nu_{sq}	$(-\psi_{min})_{sq}$	η_{cir} (%)	χ_{cir} (%)
10^6	0.03	100	150	3.94	6.16	17	17
	0.01	100	120	4.37	6.27	12	13
	0.03	100	180	4.00	6.49	9	13
	0.01	100	180	3.90	6.30	9	13
	0.03	30	150	8.18	14.81	6	8
	0.01	30	150	8.01	14.39	6	8
	0.03	30	180	8.07	14.62	5	6
	0.01	30	180	7.90	14.16	5	6
	0.03	30	120	8.55	15.98	4	6
	0.03	10	150	9.31	19.39	4	6
	0.03	10	180	9.29	19.29	4	6
	0.01	30	120	8.39	15.58	4	6
	0.03	10	120	9.36	19.76	4	5
	0.01	10	150	9.13	18.87	4	6
	0.03	0	0	9.48	20.41	4	6
	0.03	10	25	9.31	19.50	4	5
	0.01	10	180	9.11	18.75	4	6
	0.03	30	25	8.22	15.54	4	0
	0.03	10	45	9.35	19.78	4	4
	0.01	10	120	9.19	19.26	4	5
	0.01	10	25	9.14	18.97	4	5
	0.01	0	0	9.31	19.87	4	6
	0.03	10	75	9.40	20.04	4	4
	0.03	10	75	9.40	20.05	4	4
	0.01	30	25	8.05	15.06	4	0
	0.01	10	45	9.18	19.26	4	4
	0.01	10	90	9.23	19.55	4	4
	0.01	10	75	9.22	19.55	3	4
	0.03	30	45	8.46	16.59	3	-4
	0.01	30	45	8.29	16.13	2	-5
	0.03	30	90	8.83	17.30	2	-1
	0.01	30	90	8.67	16.92	2	-1
	0.03	30	75	8.80	17.48	2	-4
	0.01	30	75	8.64	17.08	1	-4
	0.03	100	25	4.33	8.03	0	-7
	0.01	100	25	4.22	7.76	0	-7
	0.03	100	45	4.78	9.21	-7	-22
	0.03	100	90	5.37	8.29	-7	-11
	0.01	100	45	4.67	8.94	-7	-22
	0.01	100	90	5.30	8.14	-8	-12
	0.03	100	75	5.42	8.81	-11	-19
	0.01	100	75	5.33	8.64	-12	-20

Table 7.2 Performance analysis of the equivalent square, trapezoidal and triangular enclosures.

Trapezoidal Cavity (Case 1) $\xi = 0.02$

Ra	Ha	$\gamma°$	Nu_{sq}	$(-\psi_{min})_{sq}$	Nu	η (%)	χ (%)
10^3	100	0	1.13	0.01	2.84	151	42
10^3	50	0	1.13	0.04	2.84	151	23
10^3	30	0	1.13	0.12	2.84	151	2
10^4	50	0	1.16	0.44	2.86	147	23
10^3	10	0	1.16	0.59	2.85	145	-31
10^3	0	0	1.24	1.12	2.87	132	-43
10^4	30	0	1.29	1.13	2.96	129	5
10^5	100	0	1.35	1.09	3.04	126	33
10^5	70	0	1.71	1.99	3.36	96	25
10^5	50	0	2.28	3.26	3.87	69	19
10^4	10	0	2.08	3.73	3.50	68	-9
10^4	0	0	2.46	5.21	3.77	53	-12
10^5	30	0	3.34	5.68	4.87	46	16
10^6	100	0	4.05	6.14	5.80	43	23
10^6	70	0	5.46	8.51	7.40	36	25
5×10^5	50	0	5.02	8.05	6.80	36	24
10^6	50	0	6.80	10.80	8.88	31	27
10^5	10	0	4.79	9.76	6.21	30	16
5×10^5	30	0	6.52	11.07	8.38	28	25
10^5	0	0	5.13	11.29	6.50	27	24
10^6	30	0	8.42	14.18	10.58	26	27
5×10^5	0	0	8.24	17.19	10.04	22	19
10^6	10	0	9.81	19.02	11.93	22	22
10^6	0	0	10.04	20.24	12.15	21	21
10^5	70	150	1.69	2.10	3.51	107	40
10^5	70	135	1.71	2.18	3.51	106	28
10^5	70	90	1.77	2.12	3.41	93	-3
10^5	70	30	1.90	3.00	3.23	70	-57
10^6	70	150	5.49	8.24	8.29	51	195
10^5	10	150	4.80	9.52	6.27	31	389
10^5	10	135	4.82	9.50	6.26	30	352
10^5	10	90	4.91	9.81	6.16	26	252
10^5	10	45	4.87	10.08	6.10	25	78
10^6	10	150	9.84	19.14	11.99	22	584
10^6	10	135	9.87	19.34	12.00	22	526
10^6	10	90	9.94	19.86	11.90	20	358
10^6	70	30	5.90	10.39	6.80	15	97
10^6	70	90	7.15	10.92	7.75	8	976
10^6	70	45	6.31	11.15	6.80	8	475

Triangular Cavity $\xi = 0.02$

Ra	Ha	$\gamma°$	Nu_{sq}	$(-\psi_{min})_{sq}$	η (%)	χ (%)
10^3	100	0	1.13	0.01	530	44
10^3	50	0	1.13	0.04	530	23
10^3	30	0	1.13	0.12	529	1
10^4	100	0	1.13	0.12	529	43
10^4	50	0	1.16	0.44	514	23
10^3	10	0	1.16	0.59	512	-35
10^3	0	0	1.24	1.12	477	-47
10^4	30	0	1.29	1.13	459	4
10^5	100	0	1.35	1.09	442	35
10^5	70	0	1.71	3.26	345	27
10^5	50	0	2.28	5.21	256	20
10^4	0	0	2.46	3.98	224	-16
5×10^5	100	0	2.80	5.68	209	24
10^5	30	0	3.34	6.00	172	15
5×10^5	70	0	3.89	6.14	151	24
10^6	100	0	4.05	8.05	146	24
5×10^5	50	0	5.02	9.76	118	25
10^5	10	0	4.79	8.51	116	14
10^6	70	0	5.46	11.07	110	26
10^5	0	0	5.13	11.29	107	14
10^6	50	0	6.80	10.80	89	27
10^6	30	0	8.24	14.18	71	28
10^6	10	0	9.81	19.02	60	22
10^6	0	0	10.04	20.24	58	20
10^5	70	150	1.69	2.10	356	43
10^5	70	135	1.71	2.18	351	37
10^5	70	90	1.77	2.12	330	44
10^5	70	30	1.90	3.00	295	-24
10^6	70	150	5.49	8.24	120	54
10^5	10	150	4.80	9.52	116	19
10^5	10	135	4.82	9.50	115	19
10^5	10	45	4.87	10.81	110	7
10^5	10	90	4.91	9.81	109	12
10^6	70	30	5.90	10.39	84	-3
10^6	70	45	6.31	11.15	72	-7
10^6	70	90	7.15	10.92	62	13
10^6	10	150	9.84	19.14	60	23
10^6	10	135	9.87	19.33	59	21
10^6	10	90	9.94	19.86	57	16

All these tables indicate Nu and circulation strength (ψ) of the base case (square system) and the percentage of enhancement/decrement of Nu and ψ of the alternative systems are presented by heat transfer performance parameter (η) and fluid-flow performance parameter (χ). The performance parameters are described in Section 2.3. In Table 7.1, MHD nanofluid flow at Ra = 10^4 and 10^6 clearly shows the enhancement in heat transfer in the circular thermal system are significant for certain values of other operating parameters such as Ha, γ, and ζ.

Similar observations are noted in Tables 7.2 and 7.3 for trapezoidal and triangular systems as well as annular systems. The heat transfer enhancement is magnificent for the triangular system in almost all ranges of operating parameters. The thermal performance of cooling length constraint circular annulus is relatively good compared to volume constraint circular annulus. These outcome observations help to identify the optimal geometric shape for superior performance of different thermal systems taken for this investigation.

Table 7.3 Performance analysis of the equivalent square, and circular annular enclosures.

Annular Cavity									$\xi = 0.02$	
Ra	**Ha**	**$\gamma°$**	**Nu_{sq}**	**Nu_{SqAn}**	**$(-\psi_{min})_{SqAn}$**	**η_{cAn1} (%)**	**χ_{cAn1} (%)**	**η_{cAn2} (%)**	**χ_{cAn2} (%)**	**$\eta_{SqAn/Sq}$ (%)**
10^5	0	0	5.13	9.77	9.55	7	24	11	1	90
10^5	10	0	4.79	9.21	8.16	7	22	10	1	92
10^6	70	0	5.46	10.48	8.40	7	9	10	0	92
10^6	50	0	6.80	12.48	11.61	7	8	10	0	84
5×10^5	50	0	5.02	9.67	7.68	7	10	9	0	93
10^6	0	0	10.04	16.49	23.87	7	27	9	10	64
10^6	30	0	8.42	14.64	16.22	7	7	9	0	74
10^6	10	0	9.81	16.25	22.18	7	20	9	7	66
5×10^5	30	0	6.52	11.94	11.76	7	9	9	0	83
10^6	0	0	8.24	14.24	19.48	6	19	8	2	73
10^6	100	0	4.05	8.27	5.26	6	13	8	2	104
10^5	30	0	3.34	6.97	3.93	6	22	7	3	109
10^4	0	0	2.46	5.58	1.38	3	78	3	18	127
10^5	50	0	2.28	5.80	1.73	4	30	0	9	154
10^4	10	0	2.08	5.48	1.01	3	66	-2	18	164
10^5	70	0	1.71	5.49	0.90	3	35	-4	14	220
10^5	100	0	1.35	5.38	0.45	2	35	-6	15	299
10^4	30	0	1.29	5.36	0.32	2	45	-6	17	314
10^3	0	0	1.24	5.34	0.13	2	93	-6	25	332
10^4	50	0	1.16	5.34	0.14	2	41	-6	18	360
10^3	10	0	1.16	5.34	0.10	2	73	-6	23	359
10^3	30	0	1.13	5.34	0.03	2	45	-6	18	373
10^3	50	0	1.13	5.34	0.01	2	41	-6	19	373
10^3	100	0	1.13	5.34	0.00	2	36	-6	17	373
10^6	70	30	5.90	11.49	11.97	9	21	12	13	95
10^6	70	150	5.49	11.49	7.81	9	-1	12	-7	109
10^6	70	45	6.31	12.22	11.22	8	31	11	4	94
10^5	10	45	4.87	9.39	8.64	7	31	11	8	93
10^5	10	135	4.82	9.39	8.27	7	13	11	-4	95
10^5	10	150	4.80	9.30	8.12	7	14	11	-4	94
10^5	10	90	4.91	9.56	8.81	6	21	10	1	95
10^6	10	150	9.84	16.29	21.82	7	15	9	3	66
10^6	10	135	9.87	16.34	21.79	7	16	9	3	66
10^6	10	90	9.94	16.42	22.23	7	23	9	8	65
10^5	70	135	1.71	5.78	1.67	7	43	4	27	239
10^5	70	150	1.69	5.64	1.22	5	50	1	33	233
10^5	70	30	1.90	5.64	1.63	5	62	1	37	197
10^5	70	90	1.77	6.74	3.42	-3	2	-4	-9	281
10^6	70	90	7.15	15.40	12.39	-8	0	-6	-4	115

7.2 Contributions and future of the present work

In this section, we summarize the original contributions of this thesis work and discuss its future implications. The following contributions are highlighted:

- A novel constraint-based methodology is developed to investigate and compare the thermal performance of dissimilar cavities.

- The constraint-based thermal analysis approach is utilized to investigate various thermal systems of square, circular, trapezoidal, triangular, and annulus geometries. The heat transfer and fluid flow of the alternative constraint-based equivalent geometries are generally found to be higher than the base square geometry case, indicating an enhanced heat transfer for the equivalent alternative thermal systems.

- The order of heat transfer enhancement depends on the parametric values, which are detailed in the previous section in tabular form. This dataset could be directly useful for thermal system engineers and researchers when they utilize similar geometrical shapes.

- The study reveals that the rate of heat transfer and associated transport flow structures can be modulated by controlling magnetic field parameters, with the magnetic field strength playing a strong role and the field inclination playing a significant role only at certain values of operating parameters.

- The findings of this work could be utilized to better design thermal systems and enrich the knowledge in this field. The constraint-based analysis approach could potentially be useful for designing the optimal thermal-performing shape of cavities for specific applications.

- This concept of improving heat transfer can be extended to other geometry configurations and multi-physical flow scenarios as future research.

Overall, the contributions of this work have advanced our understanding of thermal systems and their performance. The findings could be utilized to improve the design of energy-efficient devices and contribute to the development of more sustainable technologies. In future research, this approach of constraint-based analysis could be applied to other geometry configurations and multi-physical flow scenarios to investigate their thermal performance.

References

Alipour, M., Hosseini, R. and Rezania, A., 2013. Radius ratio effects on natural heat transfer in concentric annulus. *Experimental Thermal and Fluid Science*, *49*, pp.135-140.

Ho, C.J., Liu, W.K., Chang, Y.S. and Lin, C.C., 2010. Natural convection heat transfer of alumina-water nanofluid in vertical square enclosures: an experimental study. *International Journal of Thermal Sciences*, *49*(8), pp.1345-1353.

Lukose, L. and Basak, T., 2019. Numerical heat flow visualization analysis on enhanced thermal processing for various shapes of containers during thermal convection. *International Journal of Numerical Methods for Heat & Fluid Flow*, *30*(7), pp. 3535-3583.

Abdulkadhim, A., Abed, I.M. and Mahjoub Said, N., 2021. Review of natural convection within various shapes of enclosures. *Arabian Journal for Science and Engineering*, *46*(12), pp.11543-11586.

Abouali, O. and Falahatpisheh, A., 2009. Numerical investigation of natural convection of Al_2O_3 nanofluid in vertical annuli. *Heat and mass transfer*, *46(1)*, pp.15-23.

Aboud, E.D., Rashid, H.K., Jassim, H.M., Ahmed, S.Y., Khafaji, S.O.W., Hamzah, H.K. and Ali, F.H., 2020. MHD effect on mixed convection of annulus circular enclosure filled with Non-Newtonian nanofluid. *Heliyon*, 6(4), p. e03773.

Abu-Nada, E. and Chamkha, A.J., 2010. Effect of nanofluid variable properties on natural convection in enclosures filled with a CuO–EG–water nanofluid. *International Journal of Thermal Sciences*, *49*(12), pp.2339-2352.

Abu-Nada, E. and Oztop, H.F., 2009. Effects of inclination angle on natural convection in enclosures filled with Cu–water nanofluid. *International Journal of Heat and Fluid Flow*, *30*(4), pp.669-678.

Afrand, M., Pordanjani, A.H., Aghakhani, S., Oztop, H.F. and Abu-Hamdeh, N., 2020. Free convection and entropy generation of a nanofluid in a tilted triangular cavity exposed to a magnetic field with sinusoidal wall temperature distribution considering radiation effects. *International Communications in Heat and Mass Transfer*, *112*, p.104507.

Ahmed, H.E. and Ahmed, M.I., 2017. Thermal performance of annulus with its applications; A review. *Renewable and Sustainable Energy Reviews*, *71*, pp.170-190.

Akbarinia, A. and Laur, R., 2009. Investigating the diameter of solid particles effects on a laminar nanofluid flow in a curved tube using a two phase approach. *International Journal of Heat and Fluid Flow*, *30*(4), pp.706-714.

Akbarzadeh, P. and Fardi, A.H., 2018. Natural convection heat transfer in 2D and 3D trapezoidal enclosures filled with nanofluid. *Journal of Applied Mechanics and Technical Physics*, *59*(2), pp.292-302.

Akinsete, V.A. and Coleman, T.A., 1982. Heat transfer by steady laminar free convection in triangular enclosures. *International Journal of Heat and Mass Transfer*, 25(7), pp.991-998.

Aminossadati, S.M. and Ghasemi, B., 2009. Natural convection cooling of a localised heat source at the bottom of a nanofluid-filled enclosure. *European Journal of Mechanics-B/Fluids*, *28*(5), pp.630-640.

Aminossadati, S.M. and Ghasemi, B., 2011. Enhanced natural convection in an isosceles triangular enclosure filled with a nanofluid. *Computers and Mathematics with Applications*, 61(7), pp.1739-1753.

Ampofo, F. and Karayiannis, T.G., 2003. Experimental benchmark data for turbulent natural convection in an air filled square cavity. *International Journal of Heat and Mass Transfer*, *46(19)*, pp.3551-3572.

Arefmanesh, A., Amini, M., Mahmoodi, M. and Najafi, M., 2012. Buoyancy-driven heat transfer analysis in two-square duct annuli filled with a nanofluid. European *Journal of Mechanics-B/Fluids*, *33*, pp.95-104.

Asan, H., 2000. Natural convection in an annulus between two isothermal concentric square ducts. *International Communications in Heat and Mass Transfer, 27*(3), pp.367-376.

Ashorynejad, H.R. and Hoseinpour, B., 2017. Investigation of different nanofluids effect on entropy generation on natural convection in a porous cavity. *European Journal of Mechanics-B/Fluids*, *62*, pp.86-93.

Ayyaswamy P.S., Catton I., 1973. The boundary-layer regime for natural convection in a differentially heated, tilted rectangular cavity. *Journal of Heat Transfer*, *95(4)*, pp. 543-545.

Badruddin, I.A., Al-Rashed, A.A., Ahmed, N.S., Kamangar, S. and Jeevan, K., 2012. Natural convection in a square porous annulus. *International Journal of Heat and Mass Transfer*, *55*(23-24), pp.7175-7187.

Balla, C.S., Kishan, N., Gorla, R.S. and Gireesha, B.J., 2017. MHD boundary layer flow and heat transfer in an inclined porous square cavity filled with nanofluids. *Ain Shams Engineering Journal*, *8*(2), pp.237-254.

Banerjee A., Manna N.K., Mukhopadhyay A., Sen S., 2013, Effects of Flow and Fluid Properties and Geometries on the Dispersion of Particles Stream in Quiescent Liquid, Proceedings of the Fortieth National Conference on Fluid Mechanics and Fluid Power December 12-14, 2013, NIT Hamirpur, Himachal Pradesh, India.

Banerjee, S., Banik, S., Mondal, C., Sarkar, S. and Manna, N.K., 2021. Mixed Convective Power-Law Fluid Flow and Heat Transfer Characteristics Past a Semi-circular Cylinder Mounted with a Splitter Plate. In *Theoretical, Computational, and Experimental Solutions to Thermo-Fluid Systems.* pp. 219-226. Springer, Singapore.

Banerjee, S., Mukhopadhyay, A., Sen, S. and Ganguly, R., 2008. Natural convection in a bi-heater configuration of passive electronic cooling. *International Journal of Thermal Sciences*, *47*(11), pp.1516-1527.

Basak, T., Aravind, G. and Roy, S., 2009. Visualization of heat flow due to natural convection within triangular cavities using Bejan's heatline concept. *International Journal of Heat and Mass Transfer*, *52*(11-12), pp.2824-2833.

Basak, T., Roy, S. and Pop, I., 2009b. Heat flow analysis for natural convection within trapezoidal enclosures based on heatline concept. *International Journal of Heat and Mass Transfer*, *52*(11-12), pp.2471-2483.

Basak, T., Roy, S. and Thirumalesha, C., 2007. Finite element analysis of natural convection in a triangular enclosure: effects of various thermal boundary conditions. *Chemical Engineering Science*, 62(9), pp.2623-2640.

Batchelor, G.K., 1977. The effect of Brownian motion on the bulk stress in a suspension of spherical particles. *Journal of fluid mechanics*, *83*(1), pp.97-117.

Batyas A.C., 2000. Entropy generation for natural convection in an inclined porous cavity. *International Journal of Heat and Mass Transfer*, *43*, pp. 2089-2099.

Bejan, A., 1979. A study of entropy generation in fundamental convective heat transfer. *Journal of Heat Transfer*, *101(4)*, pp. 718-725.

Bejan, A., Dincer, I., Lorente, S., Miguel, A. and Reis, H., 2004. *Porous and complex flow structures in modern technologies*. Springer Science & Business Media.

Bhardwaj, S. and Dalal, A., 2013. Analysis of natural convection heat transfer and entropy generation inside porous right-angled triangular enclosure. *International Journal of Heat and Mass Transfer*, *65*, pp.500-513.

Bianco, V., Manca, O. and Nardini, S., 2011. Numerical investigation on nanofluids turbulent convection heat transfer inside a circular tube. *International Journal of Thermal Sciences*, *50*(3), pp.341-349.

Biswal P., Basak T., 2017. Entropy generation vs energy efficiency for natural convection based energy flow in enclosures and various applications: A review, *Renewable and Sustainable Energy Reviews*, *80*, pp.1412-1457.

Biswas, N. and Manna, N.K., 2017a. Enhanced convective heat transfer in lid-driven porous cavity with aspiration. *International Journal of Heat and Mass Transfer*, *114*, pp.430-452.

Biswas, N. and Manna, N.K., 2017b. Transport phenomena in a sidewall-moving bottom-heated cavity using heatlines. *Sādhanā*, *42*(2), pp.193-211.

Biswas, N. and Manna, N.K., 2018. Magneto-hydrodynamic Marangoni flow in bottom-heated lid-driven cavity. *Journal of Molecular Liquids*, *251*, pp.249-266.

Biswas, N., Chamkha, A.J. and Manna, N.K., 2020. Energy-saving method of heat transfer enhancement during magneto-thermal convection in typical thermal cavities adopting aspiration. *SN Applied Sciences*, *2*(11), pp.1-25.

Biswas, N., Datta, A., Manna, N.K., Mandal, D.K. and Gorla, R.S.R., 2020b. Thermo-bioconvection of oxytactic microorganisms in porous media in the presence of magnetic field. *International Journal of Numerical Methods for Heat & Fluid Flow*, *31*(5), pp. 1638-1661.

Biswas, N., Kumar Manna, N., Mukhopadhyay, A. and Sen, S., 2012. Numerical simulation of laminar confined radial flow between parallel circular discs. *Journal of fluids engineering*, *134*(1). pp. 011205.

Biswas, N., Mahapatra, P.S. and Manna, N.K., 2015. Mixed convection heat transfer in a grooved channel with injection. *Numerical Heat Transfer, Part A: Applications*, *68*(6), pp.663-685.

Biswas, N., Mahapatra, P.S. and Manna, N.K., 2015. Thermal management of heating element in a ventilated enclosure. *International Communications in Heat and Mass Transfer*, *66*, pp.84-92.

Biswas, N., Mahapatra, P.S. and Manna, N.K., 2016. Buoyancy-driven fluid and energy flow in protruded heater enclosure. *Meccanica*, *51*(9), pp.2159-2184.

Biswas, N., Mahapatra, P.S., Manna, N.K. and Roy, P.C., 2016a. Influence of heater aspect ratio on natural convection in a rectangular enclosure. *Heat Transfer Engineering*, *37*(2), pp.125-139.

Biswas, N., Mandal, D.K., Manna, N.K. and Benim, A.C., 2022. Magneto-hydrothermal triple-convection in a W-shaped porous cavity containing oxytactic bacteria. *Scientific Reports*, *12*(1), pp.1-30.

Biswas, N., Mandal, D.K., Manna, N.K. and Benim, A.C., 2023. Enhanced energy and mass transport dynamics in a thermo-magneto-bioconvective porous system containing oxytactic bacteria and nanoparticles: Cleaner energy application. Energy, 263, Part B, pp.125775.

Biswas, N., Mandal, D.K., Manna, N.K., Gorla, R.S.R. and Chamkha, A.J., 2021. Magnetohydrodynamic thermal characteristics of water-based hybrid nanofluid-filled non-Darcian porous wavy enclosure: effect of undulation. *International Journal of Numerical Methods for Heat & Fluid Flow*. 32(5), pp. 1742-1777.

Biswas, N., Manna, N.K. and Chamkha, A.J., 2021a. Effects of half-sinusoidal nonuniform heating during MHD thermal convection in Cu–Al2O3/water hybrid nanofluid saturated with porous media. *Journal of Thermal Analysis and Calorimetry*, *143*(2), pp.1665-1688.

Biswas, N., Manna, N.K. and Mahapatra, P.S., 2016. Enhanced thermal energy transport using adiabatic block inside lid-driven cavity. *International Journal of Heat and Mass Transfer*, *100*, pp.407-427.

Biswas, N., Manna, N.K. and Mahapatra, P.S., 2016. Merit of non-uniform over uniform heating in a porous cavity. *International Communications in Heat and Mass Transfer*, *78*, pp.135-144.

Biswas, N., Manna, N.K., Chamkha, A.J. and Mandal, D.K., 2021a. Effect of surface waviness on MHD thermo-gravitational convection of Cu−Al2O3−water hybrid nanofluid in a porous oblique enclosure. *Physica Scripta*, *96*(10), p.105002.

Biswas, N., Manna, N.K., Datta, A., Mandal, D.K. and Benim, A.C., 2020. Role of aspiration to enhance MHD convection in protruded heater cavity. *Progress in Computational Fluid Dynamics, an International Journal*, *20*(6), pp.363-378.

Biswas, N., Manna, N.K., Datta, P. and Mahapatra, P.S., 2018. Analysis of heat transfer and pumping power for bottom-heated porous cavity saturated with Cu-water nanofluid. *Powder technology*, *326*, pp.356-369.

Biswas, N., Manna, N.K., Mandal, D.K. and Gorla, R.S.R., 2021b. Magnetohydrodynamic mixed bioconvection of oxytactic microorganisms in a nanofluid-saturated porous cavity heated with a bell-shaped curved bottom. *International Journal of Numerical Methods for Heat and Fluid Flow*, 31(12), pp. 3722-3751.

Biswas, N., Manna, N.K., Mandal, D.K. and Gorla, R.S.R., 2021c. Magnetohydrodynamic bioconvection of oxytactic microorganisms in porous media saturated with Cu–water nanofluid. *International Journal of Numerical Methods for Heat and Fluid Flow*, 31(11), pp. 3461-3489.

Biswas, N., Mondal, M.K., Mandal, D.K., Manna, N.K., Gorla, R.S.R. and Chamkha, A.J., 2022. A narrative loom of hybrid nanofluid-filled wavy walled tilted porous enclosure imposing a partially active magnetic field. *International Journal of Mechanical Sciences*, *217*, p.107028.

Biswas, N., Mondal, M.K., Manna, N.K., Mandal, D.K. and Chamkha, A.J., 2022. Implementation of partial magnetic fields to magneto-thermal convective systems operated using hybrid-nanoliquid and porous media. *Proceedings of the Institution of Mechanical Engineers, Part C: Journal of Mechanical Engineering Science*, *236*(10), pp.5687-5704.

Biswas, N., Sarkar, U.K., Chamkha, A.J. and Manna, N.K., 2021. Magneto-hydrodynamic thermal convection of Cu–Al2O3/water hybrid nanofluid saturated with porous media subjected to half-sinusoidal nonuniform heating. *Journal of Thermal Analysis and Calorimetry*, *143*(2), pp.1727-1753.

Bondareva, N.S., Sheremet, M.A. and Pop, I., 2015. Magnetic field effect on the unsteady natural convection in a right-angle trapezoidal cavity filled with a nanofluid: Buongiorno's mathematical model. *International Journal of Numerical Methods for Heat and Fluid Flow*. 25 (8), pp. 1924-1946.

Bourantas, G.C. and Loukopoulos, V.C., 2014. MHD natural-convection flow in an inclined square enclosure filled with a micropolar-nanofluid. International Journal of Heat and Mass Transfer, *79*, pp.930-944.

Brinkman, H.C., 1952. The viscosity of concentrated suspensions and solutions. The *Journal of chemical physics*, *20(4)*, pp.571-571.

Buongiorno, J., 2006. Convective transport in nanofluids. *Journal of Heat Transfer*, *128(3)*, pp. 240-250.

Campo, E.M.D., Sen, M. and Ramos, E., 1988. Analysis of laminar natural convection in a triangular enclosure. *Numerical Heat Transfer, Part A Applications*, 13(3), pp.353-372.

Catton, I., Ayyaswamy, P.S. and Clever, R.M., 1974. Natural convection flow in a finite, rectangular slot arbitrarily oriented with respect to the gravity vector. *International Journal of Heat and Mass Transfer*, *17*(2), pp.173-184.

Chakravarty, A., Biswas, N., Ghosh, K., Manna, N.K., Mukhopadhyay, A. and Sen, S., 2021. Impact of side injection on heat removal from truncated conical heat-generating porous bed: thermal non-equilibrium approach. *Journal of Thermal Analysis and Calorimetry*, *143*(5), pp.3741-3760.

Chatterjee, D., Biswas, N., Manna, N.K. and Mandal, D.K., 2023. Effect of Bottom Wall Curvature on Thermal Convection of Air/ Nanofluid in a Differentially Heated Cavity Subjected to a Magnetic Field. In *Recent Advancements in Mechanical Engineering*. pp. 255-271. Springer, Singapore.

Chatterjee, D., Biswas, N., Manna, N.K. and Sarkar, S., 2022. Effect of discrete heating-cooling on magneto-thermal-hybrid nanofluidic convection in cylindrical system. *International Journal of Mechanical Sciences*, pp.107852.

Chatterjee, D., Biswas, N., Manna, N.K., Mandal, D.K. and Chamkha, A.J., 2023. Magneto-nanofluid flow in cylinder-embedded discretely heated-cooled annular thermal systems: conjugate heat transfer and thermodynamic irreversibility. *Journal of Magnetism and Magnetic Materials*, p.170442.

Chatterjee, D., Manna, N.K. and Biswas, N., 2022. Thermo-magnetic convection of nanofluid in a triangular cavity with a heated inverted triangular object. *Materials Today: Proceedings*, *52*, pp.427-433.

Cho, C.C., 2014. Heat transfer and entropy generation of natural convection in nanofluid-filled square cavity with partially-heated wavy surface. *International Journal of Heat and Mass Transfer*, *77*, pp.818-827.

Cho, C.C., 2020. Effects of porous medium and wavy surface on heat transfer and entropy generation of Cu-water nanofluid natural convection in square cavity containing partially-heated surface. *International Communications in Heat and Mass Transfer*, *119*, pp.104925.

Choi, S.K. and Kim, S.O., 2012. Turbulence modeling of natural convection in enclosures: A review. *Journal of Mechanical Science and Technology*, *26(1)*, pp.283-297.

Choi, S.U. and Eastman, J.A., 1995. *Enhancing thermal conductivity of fluids with nanoparticles* (No. ANL/MSD/CP-84938; CONF-951135-29). Argonne National Lab.(ANL), Argonne, IL (United States).

Chon, C.H., Kihm, K.D., Lee, S.P. and Choi, S.U., 2005. Empirical correlation finding the role of temperature and particle size for nanofluid (Al2O3) thermal conductivity enhancement. *Applied Physics*

Letters, *87*(15), p.153107.

Costa, V.A.F., 1999. Unification of the streamline, heatline and massline methods for the visualization of two-dimensional transport phenomena. *International Journal of Heat and Mass Transfer*, *42(1)*, pp.27-33.

Custer, J.R. and Shaughnessy, E.J., 1977. Thermoconvective motion of low Prandtl number fluids within a horizontal cylindrical annulus. *Journal of Heat Transfer*, *99*(4), pp. 596-602.

da Silva, A., Fontana, É., Mariani, V.C. and Marcondes, F., 2012. Numerical investigation of several physical and geometric parameters in the natural convection into trapezoidal cavities. *International Journal of Heat and Mass Transfer*, *55*(23-24), pp.6808-6818.

Dalal, A. and Das, M.K., 2008. Heatline method for the visualization of natural convection in a complicated cavity. *International Journal of Heat and Mass Transfer*, *51*(1-2), pp.263-272.

Das, A., Nandy, S., Das, S., Biswas, N. and Manna, N.K., 2021. Magnetohydrodynamic Convection in a Grooved Channel Embedded with a Conducting Cylinder. In *Proceedings of the 26thNational and 4th International ISHMT-ASTFE Heat and Mass Transfer Conference December 17-20, 2021, IIT Madras, Chennai-600036, Tamil Nadu, India*. Begel House Inc..

Das, D. and Basak, T., 2017. Role of discrete heating on the efficient thermal management within porous square and triangular enclosures via heatline approach. *International Journal of Heat and Mass Transfer*, *112*, pp.489-508.

Das, D. and Basak, T., 2017b. Role of distributed/discrete solar heaters for the entropy generation studies in the square and triangular cavities during natural convection. *Applied Thermal Engineering*, *113*, pp.1514-1535.

Das, D., Roy, M. and Basak, T., 2017a. Studies on natural convection within enclosures of various (non-square) shapes–A review. International Journal of Heat and Mass Transfer, *106*, pp.356-406.

Datta, A., Biswas, N. and Manna, N.K., 2020. Magneto-Convective Heat Transfer in a Cavity Under Partial Magnetic Fields. In *International Conference on Thermal Engineering and Management Advances.* pp. 117-130. Springer, Singapore.

Datta, A., Biswas, N., Manna, N.K. and Mandal, D.K., 2022. Thermal Management of Nanofluid Filled Porous Cavity Utilized for Solar Heating System. *Journal of The Institution of Engineers (India): Series C*, *103*(2), pp.207-221.

Datta, P., Mahapatra, P.S., Ghosh, K., Manna, N.K. and Sen, S., 2016. Heat transfer and entropy generation in a porous square enclosure in presence of an adiabatic block. *Transport in Porous Media*, *111*(2), pp.305-329.

de Vahl Davis, G. and Jones, I., 1983. Natural convection in a square cavity: a comparison exercise. *International Journal for numerical methods in fluids*, *3*(3), pp.227-248.

Ding, Y. and Wen, D., 2005. Particle migration in a flow of nanoparticle suspensions. Powder Technology, 149(2-3), pp.84-92.

Dogonchi, A.S., Chamkha, A.J. and Ganji, D.D., 2019. A numerical investigation of magneto-hydrodynamic natural convection of Cu–water nanofluid in a wavy cavity using CVFEM. *Journal of Thermal Analysis and Calorimetry*, *135*(4), pp.2599-2611.

Dogonchi, A.S., Sheremet, M.A., Pop, I. and Ganji, D.D., 2018. MHD natural convection of Cu/H2O nanofluid in a horizontal semi-cylinder with a local triangular heater. *International Journal of Numerical Methods for Heat and Fluid Flow*, *28*(12), pp. 2979-2996.

Dropkin, D. and Somerscales, E., 1965. Heat transfer by natural convection in liquids confined by two parallel plates which are inclined at various angles with respect to the horizontal. *Journal of Heat Transfer. 87(1)*, pp. 77-82.

Dutta, S., Goswami, N., Biswas, A.K. and Pati, S., 2019. Numerical investigation of magnetohydrodynamic natural convection heat transfer and entropy generation in a rhombic enclosure filled with Cu-water nanofluid. *International Journal of Heat and Mass Transfer*, *136*, pp.777-798.

El Omari, K., Kousksou, T. and Le Guer, Y., 2011. Impact of shape of container on natural convection and melting inside enclosures used for passive cooling of electronic devices. *Applied Thermal Engineering*, *31*(14-15), pp.3022-3035.

ElSherbiny, S.M., Raithby, G.D. and Hollands, K.G.T., 1982. Heat transfer by natural convection

across vertical and inclined air layers. *Journal of heat transfer*, *104*, pp.96-102.

Esmaeilpour, M. and Abdollahzadeh, M., 2012. Free convection and entropy generation of nanofluid inside an enclosure with different patterns of vertical wavy walls. *International Journal of Thermal Sciences*, *52*, pp.127-136.

Faraji, H., Faraji, M. and El Alami, M., 2020. Numerical survey of the melting driven natural convection using generation heat source: application to the passive cooling of electronics using nano-enhanced phase change material. *Journal of Thermal Science and Engineering Applications*, *12*(2), p.021005.

Flack, R.D., Konopnicki, T.T. and Rooke, J.H., 1979. The measurement of natural convective heat transfer in triangular enclosures. *Journal of Heat Transfer*,101(4): 648-654

Fuad Kent, E., Asmaz, E. and Ozerbay, S., 2007. Laminar natural convection in right triangular enclosures. *Heat and Mass Transfer*, 44(2), pp.187-200.

Gadoin, E., Le Quéré, P. and Daube, O., 2001. A general methodology for investigating flow instabilities in complex geometries: application to natural convection in enclosures. *International Journal for Numerical methods in fluids*, *37*(2), pp.175-208.

Ghalambaz, M., Mehryan, S.A.M., Izadpanahi, E., Chamkha, A.J. and Wen, D., 2019. MHD natural convection of Cu–Al2O3 water hybrid nanofluids in a cavity equally divided into two parts by a vertical flexible partition membrane. *Journal of Thermal Analysis and Calorimetry*, *138*(2), pp.1723-1743.

Ghalambaz, M., Sabour, M., Sazgara, S., Pop, I. and Trâmbiţaş, R., 2020. Insight into the dynamics of ferrohydrodynamic (FHD) and magnetohydrodynamic (MHD) nanofluids inside a hexagonal cavity in the presence of a non-uniform magnetic field. *Journal of Magnetism and Magnetic Materials*, *497*, p.166024.

Ghasemi, B., Aminossadati, S.M. and Raisi, A., 2011. Magnetic field effect on natural convection in a nanofluid-filled square enclosure. *International Journal of Thermal Sciences*, *50*(9), pp.1748-1756.

Ghosh, A., Sen, D., Manna, N.K. and Sarkar, S., 2021, February. Multiphase dynamics in a three dimensional branching network. In *IOP Conference Series: Materials Science and Engineering*. 1080(1), pp. 012041. IOP Publishing.

Giwa, S.O., Sharifpur, M. and Meyer, J.P., 2020a. Effects of uniform magnetic induction on heat transfer performance of aqueous hybrid ferrofluid in a rectangular cavity. *Applied Thermal Engineering*, *170*, p.115004.

Giwa, S.O., Sharifpur, M., Ahmadi, M.H. and Meyer, J.P., 2020b. Magnetohydrodynamic convection behaviours of nanofluids in non-square enclosures: A comprehensive review. *Mathematical Methods in the Applied Sciences*.

Giwa, S.O., Sharifpur, M., Ahmadi, M.H. and Meyer, J.P., 2021. A review of magnetic field influence on natural convection heat transfer performance of nanofluids in square cavities. *Journal of Thermal Analysis and Calorimetry*, *145*(5), pp.2581-2623.

Globe, S. and Dropkin, D., 1959. Natural-convection heat transfer in liquids confined by two horizontal plates and heated from below. *Journal of Heat Transfer*, *81(1)*, pp.24-28.

Gokulavani, P., Muthtamilselvan, M. and Abdalla, B., 2022. Impact of injection/suction and entropy generation of the porous open cavity with the hybrid nanofluid. *Journal of Thermal Analysis and Calorimetry*, *147*(4), pp.3299-3312.

Gokulavani, P., Muthtamilselvan, M., Al-Mdallal, Q.M. and Doh, D.H., 2020. Effects of orientation of the centrally placed heated baffle in an alternative configured ventilation cavity. *The European Physical Journal Plus*, *135*(1), p.23.

Gupta, A., Midya, S., Biswas, N. and Manna, N.K., 2018, January. Impact of Magnetic Field on Thermal Convection in a Linearly Heated Porous Cavity. In *International Conference on Mechanical Engineering* (pp. 503-522). Springer, Cham.

Haddad, Z., Oztop, H.F., Abu-Nada, E. and Mataoui, A., 2012. A review on natural convective heat transfer of nanofluids. *Renewable and Sustainable Energy Reviews*, *16*(7), pp.5363-5378.

Hamzah, H., Albojamal, A., Sahin, B. and Vafai, K., 2021. Thermal management of transverse magnetic source effects on nanofluid natural convection in a wavy porous enclosure. *Journal of*

Thermal Analysis and Calorimetry, *143*(3), pp.2851-2865.

Hasanuzzaman, M., Öztop, H.F., Rahman, M.M., Rahim, N.A., Saidur, R. and Varol, Y., 2012. Magnetohydrodynamic natural convection in trapezoidal cavities. *International Communications in Heat and Mass Transfer*, *39*(9), pp.1384-1394.

Hazra, C., Biswas, N. and Manna, N.K., 2020. Thermal magneto-hydrodynamics in a ventilated porous enclosure. *Sādhanā*, *45*(1), pp.1-12.

Hemmat Esfe, M., Afrand, M. and Esfandeh, S., 2020. Investigation of the effects of various parameters on the natural convection of nanofluids in various cavities exposed to magnetic fields: a comprehensive review. *Journal of Thermal Analysis and Calorimetry*, *140*(5), pp.2055-2075.

Henderson, D., Junaidi, H., Muneer, T., Grassie, T. and Currie, J., 2007. Experimental and CFD investigation of an ICSSWH at various inclinations. *Renewable and Sustainable Energy Reviews*, *11*(6), pp.1087-1116.

Ho, C.J., Liu, W.K., Chang, Y.S. and Lin, C.C., 2010. Natural convection heat transfer of alumina-water nanofluid in vertical square enclosures: an experimental study. *International Journal of Thermal Sciences*, *49(8)*, pp.1345-1353.

Hollands, K.G.T. and Konicek, L., 1973. Experimental study of the stability of differentially heated inclined air layers. *International Journal of Heat and Mass Transfer*, *16(7)*, pp.1467-1476.

Hollands, K.G.T., Unny, T.E., Raithby, G.D. and Konicek, L., 1976. Free convective heat transfer across inclined air layers. *Journal of Heat Transfer*, *98(2)*, pp.189-193.

Hossain, M.S. and Alim, M.A., 2014. MHD free convection within trapezoidal cavity with non-uniformly heated bottom wall. *International Journal of Heat and Mass Transfer*, 69, pp.327-336.

Hu, Y., He, Y., Qi, C., Jiang, B. and Schlaberg, H.I., 2014. Experimental and numerical study of natural convection in a square enclosure filled with nanofluid. *International Journal of Heat and Mass Transfer*, *78*, pp.380-392.

Huminic, G. and Huminic, A., 2020. Entropy generation of nanofluid and hybrid nanofluid flow in thermal systems: a review. *Journal of Molecular Liquids*, *302*, p.112533.

Hussain, S. and Öztop, H.F., 2021. Impact of inclined magnetic field and power law fluid on double diffusive mixed convection in lid-driven curvilinear cavity. *International Communications in Heat and Mass Transfer*, *127*, p.105549.

Hussein, A.K., Bakier, M.A.Y., Hamida, M.B.B. and Sivasankaran, S., 2016. Magneto-hydrodynamic natural convection in an inclined T-shaped enclosure for different nanofluids and subjected to a uniform heat source. *Alexandria Engineering Journal*, *55*(3), pp.2157-2169.

Hussien, A.A., Al-Kouz, W., El Hassan, M., Janvekar, A.A. and Chamkha, A.J., 2021. A review of flow and heat transfer in cavities and their applications. *The European Physical Journal Plus*, *136*(4), p.353.

Ilis, G.G., Mobedi, M. and Sunden, B., 2008. Effect of aspect ratio on entropy generation in a rectangular cavity with differentially heated vertical walls. *International Communications in Heat and Mass Transfer*, *35*(6), pp.696-703.

Incropera, F.P., 1988. Convection heat transfer in electronic equipment cooling. *Journal of Heat Transfer*, *110*(4b), pp.1097-1111.

Iyican, L., Bayazitoglu, Y. and Witte, L.C., 1980. An analytical study of natural convective heat transfer within a trapezoidal enclosure. *Journal of Heat Transfer*, 102(4), pp. 640-647.

Jang, S.P. and Choi, S.U., 2004. Role of Brownian motion in the enhanced thermal conductivity of nanofluids. *Applied physics letters*, *84*(21), pp.4316-4318.

Jou, R.Y. and Tzeng, S.C., 2006. Numerical research of nature convective heat transfer enhancement filled with nanofluids in rectangular enclosures. *International Communications in Heat and Mass Transfer*, *33*(6), pp.727-736.

Kabeel, A.E., El-Said, E.M. and Dafea, S.A., 2015. A review of magnetic field effects on flow and heat transfer in liquids: present status and future potential for studies and applications. *Renewable and Sustainable Energy Reviews*, *45*, pp.830-837.

Kamiyo, O.M., Angeli, D., Barozzi, G.S., Collins, M.W., Olunloyo, V.O.S. and Talabi, S.O., 2010. A comprehensive review of natural convection in triangular enclosures. *Applied Mechanics Reviews*, 63(6), p. 060801.

Karimi, S. and Ghasemi, B., 2012. Water-Alumina natural convection heat transfer in an inclined L shape cavity. *Modares Mechanical Engineering*, *13*(2), pp.133-144.

Karki, P., Perumal, D.A. and Yadav, A.K., 2022. Comparative studies on air, water and nanofluids based Rayleigh–Benard natural convection using lattice Boltzmann method: CFD and exergy analysis. *Journal of Thermal Analysis and Calorimetry*, *147*(2), pp.1487-1503.

Karyakin, Y.E., Sokovishin, Y.A. and Martynenko, O.G., 1988. Transient natural convection in triangular enclosures. *International Journal of Heat and Mass Transfer*, 31(9), pp.1759-1766.

Keblinski, P., Phillpot, S.R., Choi, S.U.S. and Eastman, J.A., 2002. Mechanisms of heat flow in suspensions of nano-sized particles (nanofluids). *International Journal of Heat and Mass Transfer*, 45(4), pp.855-863.

Kefayati, G.R., 2014. Effect of a magnetic field on natural convection in a nanofluid-filled enclosure with a linearly heated wall using LBM. *Arabian Journal for Science and Engineering*, *39*(5), pp.4151-4163.

Kefayati, G.R., 2015. FDLBM simulation of entropy generation due to natural convection in an enclosure filled with non-Newtonian nanofluid. *Powder Technology*, *273*, pp.176-190.

Kent, E.F., 2009. Numerical analysis of laminar natural convection in isosceles triangular enclosures for cold base and hot inclined walls. *Mechanics Research Communications*, 36(4), pp.497-508.

Khan, Z.H., Khan, W.A., Sheremet, M.A., Hamid, M. and Du, M., 2021. Irreversibilies in natural convection inside a right-angled trapezoidal cavity with sinusoidal wall temperature. *Physics of Fluids*, 33(8), p.083612.

Khanafer, K., Vafai, K. and Lightstone, M., 2003. Buoyancy-driven heat transfer enhancement in a two-dimensional enclosure utilizing nanofluids. *International journal of heat and mass transfer*, *46*(19), pp.3639-3653.

Kimura, S. and Bejan, A., 1983. The "heatline" visualization of convective heat transfer. *Journal of Heat Transfer*, *105(4)*, pp. 916-919.

Kolsi, L., Kalidasan, K., Alghamdi, A., Borjini, M.N. and Kanna, P.R., 2016. Natural convection and entropy generation in a cubical cavity with twin adiabatic blocks filled by aluminum oxide–water nanofluid. *Numerical Heat Transfer, Part A: Applications*, *70*(3), pp.242-259.

Kuehn, T.H. and Goldstein, R.J., 1976. An experimental and theoretical study of natural convection in the annulus between horizontal concentric cylinders. *Journal of Fluid mechanics*, *74*(4), pp.695-719.

Kumar, R., 1988. Study of natural convection in horizontal annuli. *International Journal of Heat and Mass Transfer*, 31(6), pp.1137-1148.

Kuyper, R.A. and Hoogendoorn, C.J., 1995. Laminar natural convection flow in trapezoidal enclosures. *Numerical Heat Transfer, Part A: Applications*, *28*(1), pp.55-67.

Lam, S.W., Gani, R. and Symons, J.G., 1989. Experimental and numerical studies of natural convection in trapezoidal cavities. *Journal of Heat Transfer*, *111(2)*, pp. 372-377.

Lartigue, B., Lorente, S. and Bourret, B., 2000. Multicellular natural convection in a high aspect ratio cavity: experimental and numerical results. *International Journal of Heat and Mass Transfer*, *43(17)*, pp.3157-3170.

Lee, S., Choi, S.S., Li, S.A. and Eastman, J.A., 1999. Measuring thermal conductivity of fluids containing oxide nanoparticles. *Journal of Heat Transfer*, *121(2)*, pp. 280-289.

Lee, T.S., 1992. Laminar fluid convection between concentric and eccentric heated horizontal rotating cylinders for low-Prandtl-number fluids. *International Journal for Numerical Methods in Fluids*, *14*(9), pp.1037-1062.

Mack, L.R. and Bishop, E.H., 1968. Natural convection between horizontal concentric cylinders for low Rayleigh numbers. *The Quarterly Journal of Mechanics and Applied Mathematics*, *21*(2), pp.223-

241.

Mahapatra, P.S., Chatterjee, S., Mukhopadhyay, A., Manna, N.K. and Ghosh, K., 2016. Proper orthogonal decomposition of thermally-induced flow structure in an enclosure with alternately active localized heat sources. *International Journal of Heat and Mass Transfer*, *94*, pp.373-379.

Mahapatra, P.S., De, S., Ghosh, K., Manna, N.K. and Mukhopadhyay, A., 2013. Heat transfer enhancement and entropy generation in a square enclosure in the presence of adiabatic and isothermal blocks. *Numerical Heat Transfer, Part A: Applications*, *64*(7), pp.577-596.

Mahapatra, P.S., Manna, N.K. and Ghosh, K., 2014. Analysis of entropy generation during the convective quenching of a cluster of balls. *Numerical Heat Transfer, Part A: Applications*, *66*(6), pp.689-711.

Mahapatra, P.S., Manna, N.K. and Ghosh, K., 2015. Effect of active wall location in a partially heated enclosure. *International Communications in Heat and Mass Transfer*, *61*, pp.69-77.

Mahapatra, P.S., Manna, N.K., Ghosh, K. and Mukhopadhyay, A., 2015. Heat transfer assessment of an alternately active bi-heater undergoing transient natural convection. *International Journal of Heat and Mass Transfer*, *83*, pp.450-464.

Mahapatra, P.S., Mukhopadhyay, A., Manna, N.K. and Ghosh, K., 2018. Heatlines and other visualization techniques for confined heat transfer systems. *International Journal of Heat and Mass Transfer*, *118*, pp.1069-1079.

Mahian, O., Kianifar, A., Heris, S.Z. and Wongwises, S., 2016. Natural convection of silica nanofluids in square and triangular enclosures: theoretical and experimental study. *International Journal of Heat and Mass Transfer*, 99, pp.792-804.

Mahian, O., Kianifar, A., Sahin, A.Z. and Wongwises, S., 2014. Entropy generation during Al_2O_3/water nanofluid flow in a solar collector: Effects of tube roughness, nanoparticle size, and different thermophysical models. *International Journal of Heat and Mass Transfer*, *78*, pp.64-75.

Mahmoodi, M. and Sebdani, S.M., 2012. Natural convection in a square cavity containing a nanofluid and an adiabatic square block at the center. *Superlattices and Microstructures*, *52*(2), pp.261-275.

Mahmoudi, A.H., Pop, I. and Shahi, M., 2012. Effect of magnetic field on natural convection in a triangular enclosure filled with nanofluid. International *Journal of Thermal Sciences*, *59*, pp.126-140.

Mahmoudi, A.H., Pop, I., Shahi, M. and Talebi, F., 2013. MHD natural convection and entropy generation in a trapezoidal enclosure using Cu–water nanofluid. *Computers and Fluids*, 72, pp.46-62.

Maitra, S., Biswas, N., Manna, N.K. and Mandal, D.K., 2023. Curvature Effect of Heated Sidewall During Heat Transport of Different Prandtl Number Fluids in a Square Enclosure in the Presence of a Magnetic Field. In *Recent Advancements in Mechanical Engineering*. pp. 239-254. Springer, Singapore.

Maitra, S., Mandal, D.K., Biswas, N., Datta, A. and Manna, N.K., 2022. Hydrothermal performance of hybrid nanofluid in a complex wavy porous cavity imposing a magnetic field. *Materials Today: Proceedings*, *52*, pp.419-426.

Maitra, S., Manna, N.K., Mandal, D.K. and Biswas, N., 2021. Thermal convection in an inclined cavity under the influence of partial magnetic field. In *IOP Conference Series: Materials Science and Engineering*. 1080(1), pp. 012029. IOP Publishing.

Malik, S. and Nayak, A.K., 2017. MHD convection and entropy generation of nanofluid in a porous enclosure with sinusoidal heating. *International Journal of Heat and Mass Transfer*, *111*, pp.329-345.

Mallick, H., Mondal, H., Biswas, N. and Manna, N.K., 2021. Buoyancy driven flow in a parallelogrammic enclosure with an obstructive block and magnetic field. *Materials Today: Proceedings*, *44*, pp.3164-3171.

Mamourian, M., Shirvan, K.M. and Pop, I., 2016. Sensitivity analysis for MHD effects and inclination angles on natural convection heat transfer and entropy generation of Al_2O_3-water nanofluid in square cavity by response surface methodology. *International Communications in Heat and Mass Transfer*, *79*, pp.46-57.

Mandal, D.K., Biswas, N., Manna, N.K., Gayen, D.K., Gorla, R.S.R. and Chamkha, A.J., 2022. Thermo-fluidic transport process in a novel M-shaped cavity packed with non-Darcian porous medium and hybrid nanofluid: Application of artificial neural network (ANN). *Physics of Fluids*, *34*(3),

p.033608.

Mandal, D.K., Biswas, N., Manna, N.K., Gorla, R.S.R. and Chamkha, A.J., 2021. Role of surface undulation during mixed bioconvective nanofluid flow in porous media in presence of oxytactic bacteria and magnetic fields. *International Journal of Mechanical Sciences*, *211*, pp.106778.

Mandal, D.K., Biswas, N., Manna, N.K., Gorla, R.S.R. and Chamkha, A.J., 2022. Hybrid nanofluid magnetohydrodynamic mixed convection in a novel W-shaped porous system. *International Journal of Numerical Methods for Heat & Fluid Flow*,

Mandal, D.K., Biswas, N., Manna, N.K., Gorla, R.S.R. and Chamkha, A.J., 2022. Magneto-hydrothermal performance of hybrid nanofluid flow through a non-Darcian porous complex wavy enclosure. *The European Physical Journal Special Topics*, 231, pp. 2695–2712.

Mandal, D.K., Mondal, M.K., Biswas, N., Manna, N.K., Gorla, R.S.R. and Chamkha, A.J., 2022. Nanofluidic thermal-fluid transport in a split-driven porous system working under a magnetic environment. *International Journal of Numerical Methods for Heat & Fluid Flow*, *32*(7), pp.2543-2569.

Manna, N.K. and Biswas, N., 2021b. Magnetic force vectors as a new visualization tool for magnetohydrodynamic convection. *International Journal of Thermal Sciences*, *167*, p.107004.

Manna, N.K., Biswas, N. and Mahapatra, P.S., 2019. Convective heat transfer enhancement: effect of multi-frequency heating. *International Journal of Numerical Methods for Heat & Fluid Flow*, *29*(10), pp. 3822-3856

Manna, N.K., Biswas, N., Mandal, D.K., Sarkar, U.K., Öztop, H.F. and Abu-Hamdeh, N., 2023. Impacts of heater-cooler position and Lorentz force on heat transfer and entropy generation of hybrid nanofluid convection in quarter-circular cavity. *International Journal of Numerical Methods for Heat & Fluid Flow*, *33*(3), pp.1249-1286.

Manna, N.K., Mondal, C., Biswas, N., Sarkar, U.K., Öztop, H.F. and Abu-Hamdeh, N.H., 2021a. Effect of multibanded magnetic field on convective heat transport in linearly heated porous systems filled with hybrid nanofluid. *Physics of Fluids*, *33*(5), p.053604.

Manna, N.K., Mondal, M.K. and Biswas, N., 2021. A novel multi-banding application of magnetic field to convective transport system filled with porous medium and hybrid nanofluid. *Physica Scripta*, *96*(6), p.065001.

Mansour, M.A. and Bakier, M.A.Y., 2015. Influence of thermal boundary conditions on MHD natural convection in square enclosure using Cu–water nanofluid. *Energy Reports*, *1*, pp.134-144.

Mansour, M.A., Bakeir, M.A. and Chamkha, A., 2014. Natural convection inside a C-shaped nanofluid-filled enclosure with localized heat sources. *International Journal of Numerical Methods for Heat and Fluid Flow*. *24 (8)*, pp.1954-1978.

Maxwell, J.C., 1873. *A treatise on electricity and magnetism* (Vol. 1). Clarendon press.

Mejri, I., Mahmoudi, A., Abbassi, M.A. and Omri, A., 2014. Magnetic field effect on entropy generation in a nanofluid-filled enclosure with sinusoidal heating on both side walls. *Powder Technology*, *266*, pp.340-353.

Mizushima, J., Hayashi, S. and Adachi, T., 2001. Transitions of natural convection in a horizontal annulus. *International Journal of Heat and Mass Transfer*, 44(6), pp.1249-1257.

Mliki, B., Abbassi, M.A., Omri, A. and Belkacem, Z., 2017. Lattice Boltzmann analysis of MHD natural convection of CuO-water nanofluid in inclined C-shaped enclosures under the effect of nanoparticles Brownian motion. *Powder Technology*, *308*, pp.70-83.

Mliki, B., Abbassi, M.A., Omri, A. and Zeghmati, B., 2016. Effects of nanoparticles Brownian motion in a linearly/sinusoidally heated cavity with MHD natural convection in the presence of uniform heat generation/absorption. *Powder Technology*, *295*, pp.69-83.

Molana, M., Zarrinderafsh, V., Chamkha, A.J., Izadi, S. and Rafizadeh, S., 2020. Magnetohydrodynamics convection in nanofluids-filled cavities: A review. *Heat Transfer*, *49*(3), pp.1418-1443.

Mondal, C., Sarkar, R., Sarkar, S., Biswas, N. and Manna, N.K., 2020. Magneto-thermal convection in lid-driven cavity. *Sādhanā*, *45*(1), pp.1-16.

Mondal, M.K., Biswas, N. and Manna, N.K., 2019. MHD convection in a partially driven cavity with

corner heating. *SN Applied Sciences*, *1*(12), pp.1-19.

Mondal, M.K., Biswas, N., Datta, A., Mandal, D.K. and Manna, N.K., 2023. Magneto-hydrothermal convective dynamics of hybrid nanofluid-packed partially cooled porous cavity: effect of half-sinusoidal heating. *Journal of Thermal Analysis and Calorimetry*, pp.1-26.

Mondal, M.K., Biswas, N., Datta, A., Manna, N.K. and Mandal, D.K., 2023. Effects of Thermal Aspect Ratio on MHD Thermal Convection of Cu–Water Nanofluid Saturated Porous Cavity. In *Recent Advancements in Mechanical Engineering*. pp. 127-143. Springer, Singapore.

Mondal, M.K., Biswas, N., Datta, A., Sarkar, B.K. and Manna, N.K., 2022. Positional impacts of partial wall translations on hybrid nanofluid flow in porous media: real coded genetic algorithm (RCGA). *International Journal of Mechanical Sciences*, *217*, pp.107030.

Mondal, M.K., Biswas, N., Mandal, D.K., Manna, N.K. and Chamkha, A.J., 2022. Assessment of thermal performance of hybrid nanofluid flow in a tilted porous enclosure by imposing partial magnetic fields. *Waves in Random and Complex Media*, pp.1-34.

Mondal, M.K., Biswas, N., Manna, N.K. and Chamkha, A.J., 2021. Enhanced magnetohydrodynamic thermal convection in a partially driven cavity packed with a nanofluid-saturated porous medium. *Mathematical Methods in the Applied Sciences*, pp.1–28.

Mukherjee, S., Biswas, N. and Manna, N.K., 2018. MHD Convection with Heat Generation in a Porous Cavity. In *International Conference on Mechanical Engineering* (pp. 547-569). Springer, Cham.

Mukhopadhyay, A., 2010. Analysis of entropy generation due to natural convection in square enclosures with multiple discrete heat sources. *International Communications in Heat and Mass Transfer*, *37*(7), pp.867-872.

Natarajan, E., Basak, T. and Roy, S., 2008. Natural convection flows in a trapezoidal enclosure with uniform and non-uniform heating of bottom wall. *International Journal of Heat and Mass Transfer*, *51*(3-4), pp.747-756.

Natarajan, E., Roy, S. and Basak, T., 2007. Effect of various thermal boundary conditions on natural convection in a trapezoidal cavity with linearly heated side wall (s). *Numerical Heat Transfer, Part B: Fundamentals*, 52(6), pp.551-568.

Nemati, H., Farhadi, M., Sedighi, K., Ashorynejad, H.R. and Fattahi, E.J.S.I., 2012. Magnetic field effects on natural convection flow of nanofluid in a rectangular cavity using the Lattice Boltzmann model. *Scientia Iranica*, *19*(2), pp.303-310.

Nia, S.N., Rabiei, F., Rashidi, M.M. and Kwang, T.M., 2020. Lattice Boltzmann simulation of natural convection heat transfer of a nanofluid in a L-shape enclosure with a baffle. *Results in Physics*, *19*, p.103413.

Oliveski, R.D.C., Macagnan, M.H. and Copetti, J.B., 2009. Entropy generation and natural convection in rectangular cavities. *Applied Thermal Engineering*, *29(8-9)*, pp.1417-1425.

Ostrach, S., 1988. Natural convection in enclosures. *Journal of Heat Transfer*,*110*(4b), pp.1175-1190.

Ozoe, H., Sayama, H. and Churchill, S.W., 1975. Natural convection in an inclined rectangular channel at various aspect ratios and angles—experimental measurements. *International Journal of Heat and Mass Transfer*, *18*(12), pp.1425-1431.

Oztop, H.F. and Abu-Nada, E., 2008. Numerical study of natural convection in partially heated rectangular enclosures filled with nanofluids. *International journal of heat and fluid flow*, *29(5)*, pp.1326-1336.

Oztop, H.F. and Al-Salem, K., 2012. A review on entropy generation in natural and mixed convection heat transfer for energy systems. *Renewable and Sustainable Energy Reviews*, *16*(1), pp.911-920.

Öztop, H.F., Estellé, P., Yan, W.M., Al-Salem, K., Orfi, J. and Mahian, O., 2015. A brief review of natural convection in enclosures under localized heating with and without nanofluids. *International Communications in Heat and Mass Transfer*, *60*, pp.37-44.

Oztop, H.F., Mobedi, M., Abu-Nada, E. and Pop, I., 2012. A heatline analysis of natural convection in a square inclined enclosure filled with a CuO nanofluid under non-uniform wall heating condition. *International Journal of Heat and Mass Transfer*, *55*(19-20), pp.5076-5086.

Pak, B.C. and Cho, Y.I., 1998. Hydrodynamic and heat transfer study of dispersed fluids with submicron metallic oxide particles. *Experimental Heat Transfer an International Journal*, *11*(2),

pp.151-170.

Patterson, J. and Imberger, J., 1980. Unsteady natural convection in a rectangular cavity. *Journal of Fluid Mechanics*, *100(1)*, pp.65-86.

Perić, M., 1993. Natural convection in trapezoidal cavities. *Numerical Heat Transfer, Part A: Applications*, *24*(2), pp.213-219.

Poulikakos, D. and Bejan, A., 1983. The fluid dynamics of an attic space. *Journal of Fluid Mechanics*, *131*, pp.251-269.

Powe, R.E., Carley, C.T. and Bishop, E.H., 1969. Free convective flow patterns in cylindrical annuli. *Journal of Heat Transfer*, *91*(3), pp. 310-314.

Projahn, U., Rieger, H. and Beer, H., 1981. Numerical analysis of laminar natural convection between concentric and eccentric cylinders. *Numerical Heat Transfer*, *4*(2), pp.131-146.

Putra, N., Roetzel, W. and Das, S.K., 2003. Natural convection of nano-fluids. *Heat and Mass Transfer*, *39(8)*, pp.775-784.

Rahimi, A., Saee, A.D., Kasaeipoor, A. and Malekshah, E.H., 2018. A comprehensive review on natural convection flow and heat transfer: the most practical geometries for engineering applications. *International Journal of Numerical Methods for Heat & Fluid Flow*. 29(3), pp.834-877.

Rahman, M.M., 2016. Influence of oriented magnetic field on natural convection in an equilateral triangular enclosure filled with water-and kerosene-based ferrofluids using a two-component nonhomogeneous thermal equilibrium model. *Cogent Physics*, *3(1)*, p.1234662.

Ramakrishna, D., Basak, T. and Roy, S., 2013. Analysis of heatlines and entropy generation during free convection within trapezoidal cavities. *International Communications in Heat and Mass Transfer*, *45*, pp.32-40.

Rashmi, W., Ismail, A.F., Khalid, M. and Faridah, Y., 2011. CFD studies on natural convection heat transfer of Al_2O_3-water nanofluids. *Heat and Mass Transfer*, *47(10)*, pp.1301-1310.

Rathnam, V.M., Roy, M. and Basak, T., 2016. Analysis of entropy generation during natural convection in tilted triangular enclosures with various base angles. *Numerical Heat Transfer, Part A: Applications*, *69*(12), pp.1332-1354.

Saghir, M.Z., Ahadi, A., Yousefi, T. and Farahbakhsh, B., 2016. Two-phase and single phase models of flow of nanofluid in a square cavity: comparison with experimental results. *International Journal of Thermal Sciences*, *100*, pp.372-380.

Saha, A., Biswas, N., Ghosh, K. and Manna, N.K., 2022b. Thermal management with localized heating on enclosure's wall during thermal convection using different fluids. *Materials Today: Proceedings*, *52*, pp.391-397.

Saha, A., Biswas, N., Manna, N.K. and Ghosh, K., 2022. Thermal analysis of buoyancy-driven flow in a square enclosure filled with porous medium. Materials Today: Proceedings. 63, pp 185-191.

Saha, A., Biswas, N., Manna, N.K. and Ghosh, K., 2022c. Effect of non-uniform heating on thermal performance of an enclosure filled with nanofluid. *Materials Today: Proceedings*, *56*, pp.179-185.

Saha, A., Chakravarty, A., Ghosh, K., Biswas, N. and Manna, N.K., 2022a. Role of obstructing block on enhanced heat transfer in a concentric annulus. *Waves in Random and Complex Media*, pp.1-25.

Saha, A., Ghosh, K. and Manna, N.K., 2021. Analysis of nanofluid based natural convection in a square cavity applying corner heating and cooling. In *IOP Conference Series: Materials Science and Engineering*. 1080(1), pp. 012049. IOP Publishing.

Saha, A., Manna, N.K. and Ghosh, K., 2021. Thermal Hydraulic Analysis of Natural Convection in a Solar Collector Filled with Nanofluid. In *2021 Innovations in Energy Management and Renewable Resources (52042)* (pp. 1-6). IEEE.

Saha, A., Manna, N.K. and Ghosh, K., 2023. Influence of Non-uniform Heating Profiles on Free Convection Entropy Generation Inside an Enclosure Filled with Nanofluid. In *Recent Advancements in Mechanical Engineering*. pp. 1-13. Springer, Singapore.

Saha, A., Manna, N.K., Ghosh, K. and Biswas, N., 2022. Analysis of geometrical shape impact on thermal management of practical fluids using square and circular cavities. *The European Physical Journal Special Topics*, pp.1-29.

Saha, L.K., Bala, S.K. and Roy, N.C., 2020. Natural convection of dusty nanofluids within a concentric annulus. *The European Physical Journal Plus*, *135*(9), pp.1-20.

Saha, S.C. and Khan, M.M.K., 2011. A review of natural convection and heat transfer in attic-shaped space. *Energy and Buildings*, *43*(10), pp.2564-2571.

Saha, S.K., 2019. Numerical study of laminar natural convection heat transfer in inclined trapezoidal enclosure. *Journal of Thermal Science and Engineering Applications*, *11*(6). p. 061021.

Şahin, B., 2020. Effects of the center of linear heating position on natural convection and entropy generation in a linearly heated square cavity. *International Communications in Heat and Mass Transfer*, *117*, p.104675.

Sahoo, R.K., Sarkar, A. and Sastri, V.M.K., 1993. Effect of an Obstruction on Natural Convection Heat Transfer in Vertical Channels—a Finite Element Analysis. *International Journal of Numerical Methods for Heat & Fluid Flow*, *3*(3), pp.267-276.

Saleh, H., Roslan, R. and Hashim, I., 2011. Natural convection heat transfer in a nanofluid-filled trapezoidal enclosure. *International Journal of Heat and Mass Transfer*, *54*(1-3), pp.194-201.

Salmun, H., 1995. Convection patterns in a triangular domain. *International Journal of Heat and Mass Transfer*, 38(2), pp.351-362.

Sarkar, J., Ghosh, P. and Adil, A., 2015. A review on hybrid nanofluids: recent research, development and applications. *Renewable and Sustainable Energy Reviews*, *43*, pp.164-177.

Sarkar, U.K., Biswas, N. and Öztop, H.F., 2021. Multiplicity of solution for natural convective heat transfer and entropy generation in a semi-elliptical enclosure. *Physics of Fluids*, *33*(1), p.013606.

Sarma, S., 2014. *Study of Premixing Phase of Fuel Coolant Interaction in Nuclear Reactor* (Doctoral dissertation).

Sciacovelli, A., Verda, V. and Sciubba, E., 2015. Entropy generation analysis as a design tool—A review. *Renewable and Sustainable Energy Reviews*, *43*, pp.1167-1181.

Selimefendigil, F. and Öztop, H.F., 2015. Natural convection and entropy generation of nanofluid filled cavity having different shaped obstacles under the influence of magnetic field and internal heat generation. *Journal of the Taiwan Institute of Chemical Engineers*, *56*, pp.42-56.

Sen, D., Ghosh, A., Chakravarty, A., Sarkar, S., Manna, N.K., Ghosh, K. and Mukhopadhyay, A., 2021. Forced convection and entropy generation past a series of porous bodies with internal heat generation. *Physica Scripta*, *96*(12), pp.125009.

Sen, G. and Inam, M.I., 2021. Numerical Analysis of Natural Convection Heat Transfer Inside an Inverted T-Shaped Cavity Filled with Nanofluid. *Journal of Engineering Advancements*, *2(04)*, pp.180-188.

Sen, K., Biswas, N., Sarkar, S. and Manna, N.K., 2023. Transport Phenomena in a Double Driven Cavity Involving Buoyancy, Magnetic Field and Nanofluid. In *Recent Advancements in Mechanical Engineering.* pp. 223-237. Springer, Singapore.

Sen, K., Manna, N.K. and Biswas, N., 2022. Thermo-fluidic transport process in a double-driven cavity with triangular adiabatic obstacles. *Materials Today: Proceedings*, *52*, pp.524-531.

Sen, N., Nag, S., Bamboowala, H.T., Manna, N.K., Biswas, N. and Mandal, D.K., 2022. Magnetohydrodynamic thermal behavior of nanofluid flow in a trapezoidal cavity subjected to non-uniform heating. Materials Today: Proceedings. 63. pp. 320-327.

Seyyedi, S.M., Dayyan, M., Soleimani, S. and Ghasemi, E., 2015. Natural convection heat transfer under constant heat flux wall in a nanofluid filled annulus enclosure. *Ain Shams Engineering Journal*, *6*(1), pp.267-280.

Shadlaghani, A., Farzaneh, M., Shahabadi, M., Tavakoli, M.R., Safaei, M.R. and Mazinani, I., 2019. Numerical investigation of serrated fins on natural convection from concentric and eccentric annuli with different cross sections. *Journal of Thermal Analysis and Calorimetry*, *135*, pp.1429-1442.

Shahriari, A., Ashorynejad, H.R. and Pop, I., 2019. Entropy generation of MHD nanofluid inside an inclined wavy cavity by lattice Boltzmann method. *Journal of Thermal Analysis and Calorimetry*, *135(1)*, pp.283-303.

Shahsavar, A., Sardari, P.T. and Toghraie, D., 2018. Free convection heat transfer and entropy generation analysis of water-Fe3O4/CNT hybrid nanofluid in a concentric annulus. *International*

Journal of Numerical Methods for Heat & Fluid Flow, 29 (3), pp. 915-934.

Sharma, A., Mahapatra, P.S., Manna, N.K., Ghosh, K., Wahi, P. and Mukhopadhyay, A., 2016. Thermal instability-driven multiple solutions in a grooved channel. *Numerical Heat Transfer, Part A: Applications*, *70*(7), pp.776-790.

Sharma, A.K., Mahapatra, P.S., Manna, N.K. and Ghosh, K., 2015. Mixed convection heat transfer in a grooved channel in the presence of a baffle. *Numerical Heat Transfer, Part A: Applications*, *67*(10), pp.1097-1118.

Sharma, A.K., Mahapatra, P.S., Manna, N.K. and Ghosh, K., 2015. Mixed convection in a baffled grooved channel. *Sadhana*, *40*(3), pp.835-849.

Sheikholeslami, M., Bandpy, M.G., Ellahi, R. and Zeeshan, A., 2014. Simulation of MHD CuO–water nanofluid flow and convective heat transfer considering Lorentz forces. *Journal of Magnetism and Magnetic Materials*, *369*, pp.69-80.

Sheikholeslami, M., Bandpy, M.G., Ellahi, R., Hassan, M. and Soleimani, S., 2014. Effects of MHD on Cu–water nanofluid flow and heat transfer by means of CVFEM. *Journal of Magnetism and Magnetic Materials*, *349*, pp.188-200.

Sheikholeslami, M., Gorji-Bandpy, M. and Soleimani, S., 2013. Two phase simulation of nanofluid flow and heat transfer using heatline analysis. *International Communications in Heat and Mass Transfer*, *47*, pp.73-81.

Sheikholeslami, M., Gorji-Bandpy, M., Ganji, D.D. and Soleimani, S., 2014. Natural convection heat transfer in a cavity with sinusoidal wall filled with CuO–water nanofluid in presence of magnetic field. *Journal of the Taiwan Institute of Chemical Engineers*, *45(1)*, pp.40-49.

Sheikholeslami, M., Gorji-Bandpy, M., Ganji, D.D., Soleimani, S. and Seyyedi, S.M., 2012. Natural convection of nanofluids in an enclosure between a circular and a sinusoidal cylinder in the presence of magnetic field. *International Communications in Heat and Mass Transfer*, *39(9)*, pp.1435-1443.

Shi, Y., Zhao, T.S. and Guo, Z.L., 2006. Finite difference-based lattice Boltzmann simulation of natural convection heat transfer in a horizontal concentric annulus. *Computers & Fluids*, *35*(1), pp.1-15.

Shukla, R.K. and Dhir, V.K., 2008. Effect of Brownian motion on thermal conductivity of nanofluids. *Journal of Heat Transfer*, 130(4), pp. 042406.

Sojoudi, A., Saha, S.C., Gu, Y. and Hossain, M.A., 2013. Steady natural convection of non-Newtonian power-law fluid in a trapezoidal enclosure. *Advances in Mechanical Engineering*, *5*, p.653108.

Suresh, S., Venkitaraj, K.P., Selvakumar, P. and Chandrasekar, M., 2012. Effect of Al2O3–Cu/water hybrid nanofluid in heat transfer. *Experimental Thermal and Fluid Science*, *38*, pp.54-60.

Tayebi, T. and Chamkha, A.J., 2017. Natural convection enhancement in an eccentric horizontal cylindrical annulus using hybrid nanofluids. *Numerical Heat Transfer, Part A: Applications*, *71*(11), pp.1159-1173.

Tayebi, T. and Chamkha, A.J., 2020. Entropy generation analysis due to MHD natural convection flow in a cavity occupied with hybrid nanofluid and equipped with a conducting hollow cylinder. *Journal of Thermal analysis and Calorimetry*, *139*(3), pp.2165-2179.

Tayebi, T. and Öztop, H.F., 2020. Entropy production during natural convection of hybrid nanofluid in an annular passage between horizontal confocal elliptic cylinders. *International Journal of Mechanical Sciences*, *171*, p.105378.

Tayebi, T., Öztop, H.F. and Chamkha, A.J., 2020b. Natural convection and entropy production in hybrid nanofluid filled-annular elliptical cavity with internal heat generation or absorption. *Thermal Science and Engineering Progress*, *19*, p.100605.

Tayebi, T., Öztop, H.F. and Chamkha, A.J., 2021. MHD natural convection of a CNT-based nanofluid-filled annular circular enclosure with inner heat-generating solid cylinder. *The European Physical Journal Plus*, *136*(2), p.150.

Tian, Y. and Zhao, C.Y., 2013. A review of solar collectors and thermal energy storage in solar thermal applications. *Applied energy*, *104*, pp.538-553.

Torki, M. and Etesami, N., 2020. Experimental investigation of natural convection heat transfer of SiO_2/water nanofluid inside inclined enclosure. *Journal of Thermal Analysis and Calorimetry*, *139*(2),

pp.1565-1574.

Vahedi, S.M., Aghakhani, S., Pordanjani, A.H. and Azaiez, J., 2022. A comprehensive parametric study on heat transfer optimization of a triangular enclosure subjected to a magnetic field using neural network machine learning. *Engineering Analysis with Boundary Elements*, *145*, pp.173-186.

Varol, Y., Oztop, H.F. and Pop, I., 2009. Entropy generation due to natural convection in non-uniformly heated porous isosceles triangular enclosures at different positions. *International Journal of Heat and Mass Transfer*, 52(5-6), pp.1193-1205.

Varol, Y., Oztop, H.F. and Pop, I., 2009. Natural convection in right-angle porous trapezoidal enclosure partially cooled from inclined wall. *International Communications in Heat and Mass Transfer*, *36*(1), pp.6-15.

Varol, Y., Oztop, H.F., Mobedi, M. and Pop, I., 2008. Visualization of natural convection heat transport using heatline method in porous non-isothermally heated triangular cavity. *International Journal of Heat and Mass Transfer*, 51(21-22), pp.5040-5051.

Waheed, M.A., 2007. An approach to the simulation of natural-convective heat transfer between two concentric horizontal cylindrical annuli. *Numerical Heat Transfer, Part A: Applications*, *53*(3), pp.323-340.

Wang, L., Chai, Z. and Shi, B., 2017. Lattice Boltzmann simulation of magnetic field effect on natural convection of power-law nanofluids in rectangular enclosures. *Advances in Applied Mathematics and Mechanics*, *9*(5), pp.1094-1110.

Wang, X., Xu, X. and Choi, S.U., 1999. Thermal conductivity of nanoparticle-fluid mixture. *Journal of Thermophysics and Heat Transfer*, *13*(4), pp.474-480.

Wang, X.Q. and Mujumdar, A.S., 2007. Heat transfer characteristics of nanofluids: a review. *International Journal of Thermal Sciences*, *46*(1), pp.1-19.

Wang, Y. and Bau, H.H., 1988. Low Rayleigh number convection in horizontal, eccentric annuli. *The Physics of fluids*, *31*(9), pp.2467-2473.

Yadav, C.K., Dey, K., Manna, N.K. and Biswas, N., 2022. Low Reynolds number MHD mixed convection of nanofluid in a corner heated grooved cavity. Materials Today: Proceedings. 63, pp. 170-175.

Yadav, C.K., Halder, A., Mukherjee, S., Manna, N.K., Biswas, N. and Mandal, D.K., 2022. Effect of sinusoidal heating and Hartmann number on nanofluid based heat flow evolution in a cavity. Materials Today: Proceedings. 63, pp. 157-163

Yao, L.S., 2006. Natural convection along a vertical complex wavy surface. *International Journal of Heat and Mass Transfer*, *49*(1-2), pp.281-286.

Yesiloz, G. and Aydin, O., 2013. Laminar natural convection in right-angled triangular enclosures heated and cooled on adjacent walls. *International Journal of Heat and Mass Transfer*, 60, pp.365-374.

Yin, S.H., Wung, T.Y. and Chen, K., 1978. Natural convection in an air layer enclosed within rectangular cavities. *International Journal of Heat and Mass Transfer*, *21*(3), pp.307-315.

Yoo J.-S.,1998, Mixed convection of air between two horizontal concentric cylinders with a cooled rotating outer cylinder. *International Journal of Heat Mass Transfer*, 41, pp. 293-302.

Yu, W. and Choi, S.U.S., 2003. The role of interfacial layers in the enhanced thermal conductivity of nanofluids: a renovated Maxwell model. *Journal of nanoparticle research*, *5*(1), pp.167-171.

Yuan, X., Tavakkoli, F. and Vafai, K., 2015. Analysis of natural convection in horizontal concentric annuli of varying inner shape. *Numerical Heat Transfer, Part A: Applications*, *68*(11), pp.1155-1174.

Zhang, T. and Che, D., 2016. Double MRT thermal lattice Boltzmann simulation for MHD natural convection of nanofluids in an inclined cavity with four square heat sources. *International Journal of Heat and Mass Transfer*, *94*, pp.87-100.

APPENDIX

Grid independence test

The grid independence test was conducted to ensure that the numerical simulations were not significantly affected by the mesh size. This test is crucial to ensure the accuracy and reliability of the simulations. Mesh generation in two-dimensional problems was executed using the Finite Element Method (FEM), and the mesh structures for various geometries are shown in Figure A1. The details of the mesh studies are indicated in Table A1.

(a)   (b)

(c)

_____

(d)

(e)

(f)

(g)
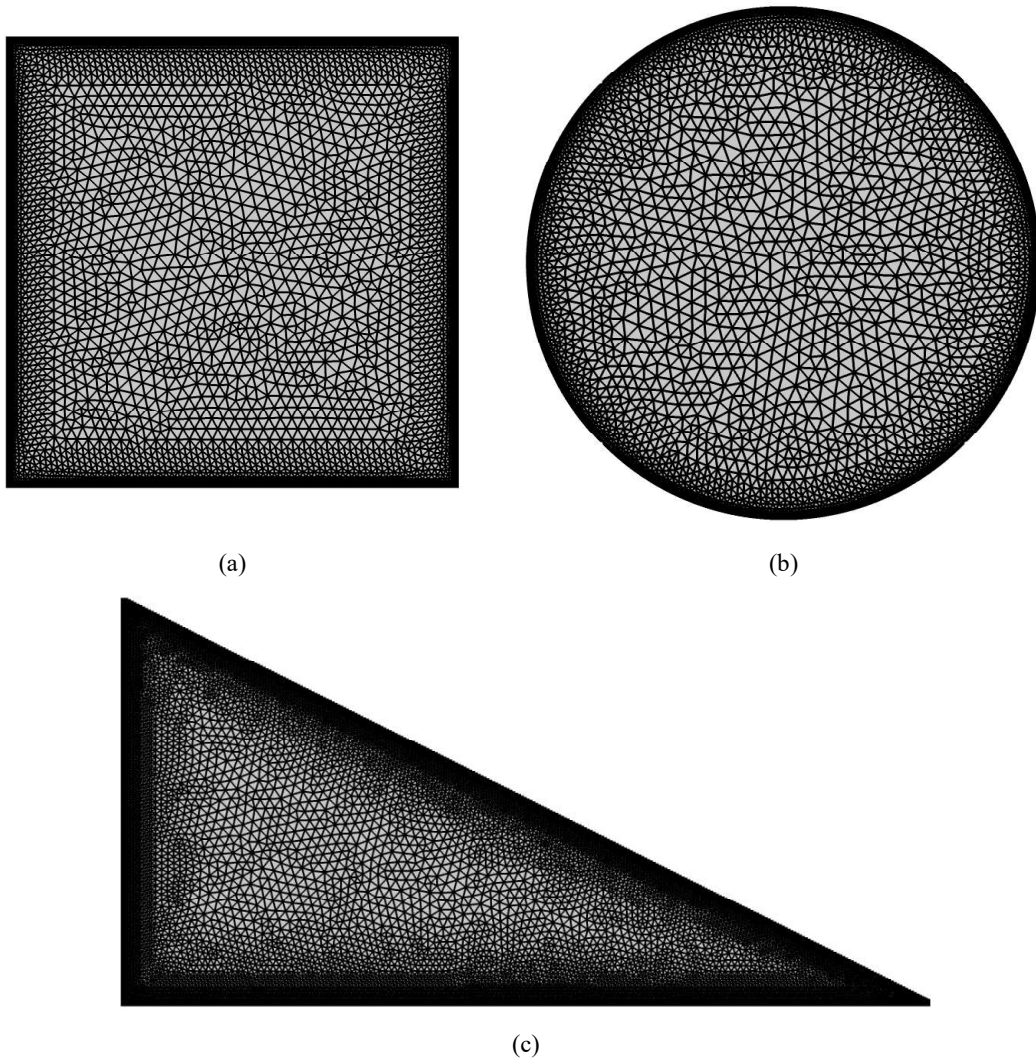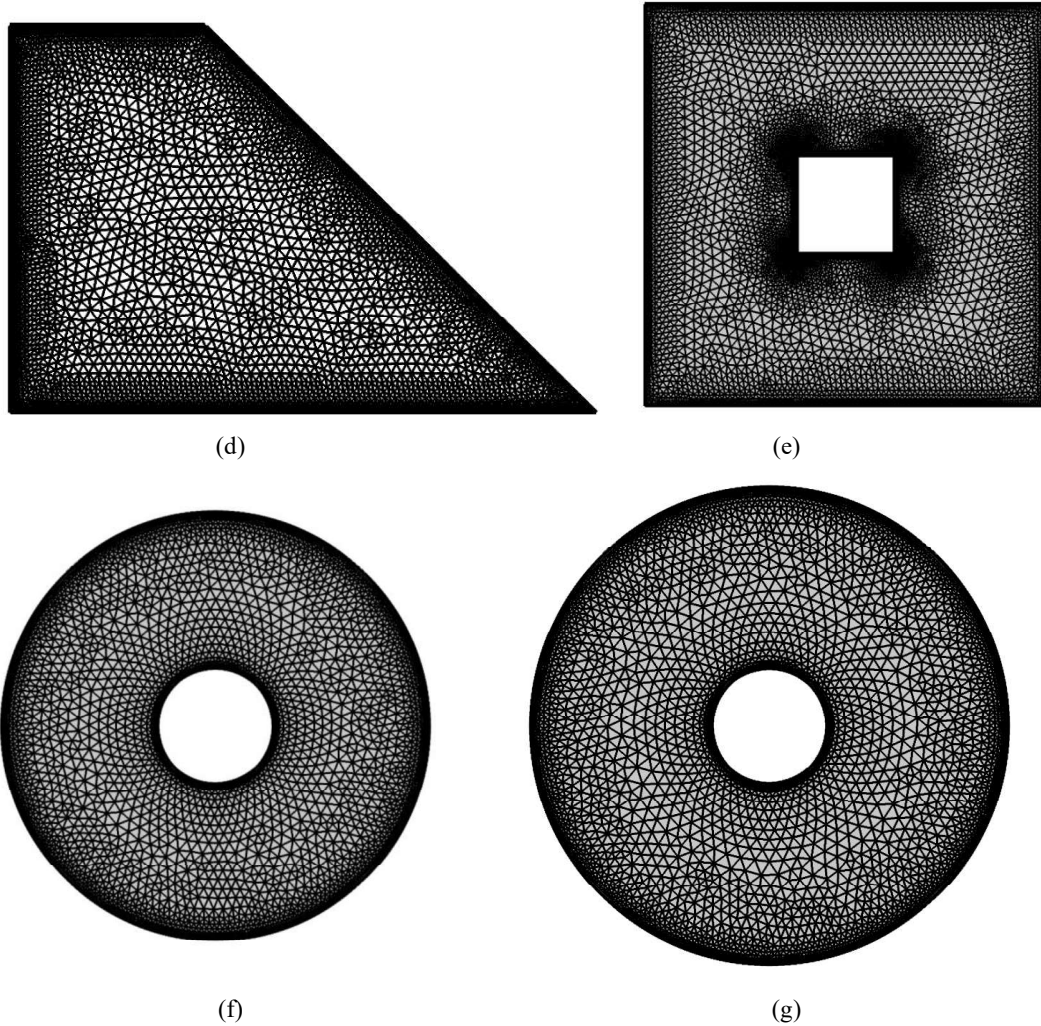
Figure A1. Mesh structures for various geometries with Mesh 3: (a) Square geometry (Base case), (b) Equivalent circular geometry, (c) Triangular geometry, (d) Trapezoidal geometry, (e) Square annulus (Base case), (f) Equivalent circular annulus I (volume constraint), and (g) Equivalent circular annulus II (cooling length constraint).

Table A1. Mesh independence study results with Pr = 5.83, ζ = 0.01, Ra = 10^6.

Mesh & global parameters	Mesh 1	Mesh 2	Mesh 3	Mesh 4
(a) Square geometry (base case) (with Ha = 0)				
Total elements	1000	1538	6524	16966
Element size: min.-max.	0.004 – 0.087	0.003 – 0.067	0.001 – 0.035	0.0004 – 0.028
Avg. Nu	9.6253	9.6233	9.6244	9.6241
ψ_{min}	-19.985	-19.941	-19.923	-19.920
(b) Equivalent circular geometry (with Ha = 0)				
Total elements	730	1210	5292	13434
Element size: min.-max.	0.00451–0.0982	0.00339–0.0756	0.00113–0.0395	0.000451–0.0316
Avg. Nu	9.9778	9.9884	9.9821	9.9776
ψ_{min}	-21.260	-21.134	-21.073	-21.059
(c) Equivalent triangular geometry (with Ha = 30)				
Total elements	934	1484	6920	19606
Element size: min.-max.	0.009–0.196	0.00675–0.151	0.00225–0.0788	0.0009–0.063
Avg. Nu	11.544	11.748	12.582	13.223
ψ_{min}	-18.399	-18.292	-17.960	-17.950
(d) Equivalent trapezoidal geometry (with Ha = 30) (Case 3)				
Total elements	1038	1578	6939	18140
Element size: min.-max.	0.004–0.087	0.003–0.067	0.001–0.035	0.0004 –0.028
Avg. Nu	9.0985	9.0984	9.0966	9.0964
ψ_{min}	-16.034	-15.978	-15.950	-15.950
(e) Square annular geometry (with Ha = 30)				
Total elements	1867	2801	10837	27025
Element size: min.-max.	0.00412–0.0897	0.00309–0.0691	0.00103–0.0361	0.000412–0.0289
Avg. Nu	14.074	14.057	14.044	14.041
ψ_{min}	-16.190	-16.177	-16.158	-16.156
(f) Equivalent circular annular geometry I (with Ha = 30) (volume constraint)				
Total elements	1056	1462	6090	16840
Element size: min.-max.	0.00469–0.102	0.00352–0.0786	0.00117–0.041	0.000469–0.0328
Avg. Nu	15.008	15.004	15.016	15.013
ψ_{min}	-16.212	-16.155	-16.139	-16.135
(g) Equivalent circular annular geometry II (with Ha = 30) (cooling length constraint)				
Total elements	1068	1398	5974	16646
Element size: min.-max.	0.00525–0.114	0.00394–0.0879	0.00131–0.0459	0.000525–0.0367
Avg. Nu	15.304	15.305	15.296	15.293
ψ_{min}	-17.398	-17.383	-17.336	-17.337

These results provide information about the mesh size, average Nusselt number (Nu) and minimum stream function (ψ_{min}) for different meshes and geometries. Mesh 3 is often selected for the present simulations as it provides a balance between accuracy and computational resources. This rigorous grid independence testing ensures the reliability of the numerical simulations conducted in the study.

Abhinav Saha
09/03/2023